DISSERTATION

A MEASUREMENT OF THE DOUBLE-DIFFERENTIAL ELECTRON ANTINEUTRINO CHARGED-CURRENT INCLUSIVE CROSS SECTION IN THE NOVA NEAR DETECTOR

Submitted by

Derek Doyle

Department of Physics

In partial fulfillment of the requirements

For the Degree of Doctor of Philosophy

Colorado State University

Fort Collins, Colorado

Summer 2023

Doctoral Committee:

Advisor: Norm Buchanan

Martin Gelfand
John Harton
Andrew Norman
Louis-Noël Pouchet

ABSTRACT

A MEASUREMENT OF THE DOUBLE-DIFFERENTIAL ELECTRON ANTINEUTRINO CHARGED-CURRENT INCLUSIVE CROSS SECTION IN THE NOVA NEAR DETECTOR

The neutrino is a fundamental particle of the universe that was first hypothesized in 1930 by Wolfgang Pauli to explain the observed energy distribution of outgoing electrons produced from beta-decay. Since then, it has been discovered that there are at least three types, or flavors, of neutrinos and that they oscillate between these flavors as they travel through space and time. This discovery proved that neutrinos have a non-zero mass and positioned neutrino oscillations to provide a window into understanding the matter/antimatter asymmetry in the universe.

Principle to all neutrino measurements is an accurate and robust interaction model over a large range of energies, and measurements to support the model. Of particular importance to the NuMI Off-axis ν_e Appearance (NOvA) neutrino oscillation experiment is the energy range from 1 to 10 GeV, where Quasi-Elastic (QE), Meson-Exchange Current (MEC), and Deep Inelastic Scattering (DIS) interactions all contribute significantly. Using neutrinos from the Neutrinos at the Main Injector (NuMI) beam and the NOvA near detector, the first double-differential electron antineutrino charged-current inclusive cross section is measured and compared to various interaction models implemented within the GENIE Generator framework, version 3. Good agreement is observed between measurement and a GENIE model tuned to NOvA data.

ACKNOWLEDGEMENTS

The journey that I end with this thesis would not have been possible without the love, support, and friendship of more people than I can mention, but I will do my best...

My partner Kalyn Bonn. For the last four years, she has been my most stubborn supporter and very best friend. She has sacrificed an amazing job and life in Colorado to follow me across the country so that I might finish my thesis. Her unwavering love and companionship has kept me afloat throughout this journey.

My friends and family back home. My parents for their love and for providing me with the opportunities and tools to be successful. My friends for helping me cope with a life in a new state and for giving me much needed breaks from physics.

The friends I made at CSU. David Marchfield, Ryan LaZur, and Justin Mueller for their friendship and game nights. Steven Calvez and Matt Judah for their significant contributions to this thesis and for the many games of billiards. My office-mate and friend, Paul Rojas, for discussions about movies over pub trivia. Connor Johnson for welcoming me to the Buchanan group and for their valuable insights. The faculty of the CSU physics department for empowering my curiosity. Especially my advisor, Norm Buchanan, for his physics, professional, and personal mentorship that has prepared me for life after graduate school.

The friends I made on the NOvA and SciDAC-4 collaborations. The NOvA Near Detector group conveners for their guidance throughout the development of my cross section analysis: Mathew Muether, Jonathan Paley, Linda Cremonesi, Leonidas Aliaga Soplin, Matthew Judah, Gregory Pawolkowski, and Matthew Wetstein. Jim Kowalkowsi, Marc Paterno, and Saba Sehrish from SciDAC-4 for teaching me all I know of scientific computing. In particular, Andrew Norman, for his many hours of mentorship and advice.

TABLE OF CONTENTS

ABSTRACT ii

ACKNOWLEDGEMENTS iii

LIST OF TABLES viii

LIST OF FIGURES x

Chapter 1. Introduction 1

Chapter 2. Motivation and Neutrino Physics 4

2.1. Neutrinos and the Standard Model of Particle Physics 5

2.2. Neutrino Oscillation 8

2.3. Neutrino-Matter Interactions 11

2.3.1. Neutrino-Nucleus Interactions 13

2.4. Importance of Electron Antineutrino Cross-section Measurements 20

2.4.1. Relevant Measurements 20

Chapter 3. The NOvA Experiment 23

3.1. The NuMI Beam 23

3.2. Off-axis Design 27

3.3. Neutrino Flux at the NOvA ND 29

3.4. The NOvA Detectors 32

3.4.1. Detector Calibration 36

Chapter 4. NOvA Software and Simulation 40

4.1. Simulation of the NuMI neutrino beam 40

4.2. Simulation of Neutrino Interactions . . . 41
4.2.1. Model Tuning . . . 44
4.3. Simulation of Particle Transport and Detector Response . . . 46
4.4. Reconstruction of Neutrino Interactions . . . 46
4.5. Estimation of Electron Kinematics . . . 50
4.6. Estimation of Neutrino Energy . . . 53
4.7. Analysis Software . . . 56

Chapter 5. The $\bar{\nu}_e$-CC Inclusive Cross Section Analysis . . . 60
5.1. Signal Definition . . . 61
5.2. Event Selection . . . 62
5.2.1. Data Quality . . . 62
5.2.2. Number of Planes from the Front of the Detector . . . 64
5.2.3. Number of Hits in Slice . . . 64
5.2.4. Containment Volume . . . 65
5.2.5. Selection Optimization Procedure . . . 65
5.2.6. Fiducial Volume . . . 68
5.2.7. Electron Phase Space . . . 69
5.2.8. Muon Rejection . . . 69
5.3. Cut Flow and Composition of Analysis Sample . . . 72
5.4. Systematic Uncertainties . . . 73
5.4.1. Flux Uncertainties . . . 75
5.4.2. Cross-section Modeling Uncertainties . . . 76
5.4.3. Detector Uncertainties . . . 79

5.4.4. Neutron Uncertainties . . . 85
5.5. Signal Estimation . . . 87
5.5.1. Particle Identification with a Convolutional Neural Network . . . 87
5.5.2. Identification of $\bar{\nu}_e$-CC Interactions . . . 98
5.5.3. Template Fit Overview . . . 101
5.5.4. Global Template Fit Overview . . . 110
5.5.5. A Simultaneous Two-sample Global Template Fit . . . 111
5.5.6. Application of Two-sample Global Template Fit to Fake Data . . . 117
5.5.7. Purity Correction . . . 122
5.6. Correcting for Detector Effects . . . 123
5.6.1. Unfolding . . . 123
5.6.2. Efficiency . . . 127
5.7. Target Count . . . 136
5.8. Fake Data Studies . . . 136
5.8.1. Analysis Self-consistency . . . 137
5.8.2. Statistical Fluctuations . . . 138
5.8.3. Modified Neutrino Interaction and Flux Model . . . 140

Chapter 6. Results of the $\bar{\nu}_e$-CC Inclusive Cross Section Measurement . . . 154

Chapter 7. The SciDAC Project and High Performance Computing . . . 165
7.1. An Analysis Workflow for High Performance Computing . . . 165
7.1.1. Event Selection Scaling of the HDF5 Data Format . . . 167
7.1.2. Demonstration of Workflow Scaling . . . 170

Chapter 8. Conclusion . . . 173

BIBLIOGRAPHY 174

LIST OF ACRONYMS 189

LIST OF TABLES

4.1 Best fit parameters that define the second-order polynomial surface of the FHC and RHC neutrino energy estimators [1]. 55

4.2 NOvA dataset statistics 58

5.1 Overall efficiency and signal purity as stages of the selection criteria are applied to an Reverse Horn Current (RHC) Monte Carlo (MC) sample normalized to 12.6×10^{20} Protons on Target (POT). 73

5.2 Parameters of the Neutrinos at the Main Injector (NuMI) beam simulation and associated uncertainties from [2]. Decay Pipe B_i is the magnetic field along the i axis of the decay pipe 79

5.3 Upper-bound momenta used to simulate freely propagating particles. 91

5.4 Percent of surviving muons, pions, and protons after the containment filter. 91

5.5 Prong Convolutional Vision Network (CVN) training hyperparameters optimized by grid search. 94

5.6 Conditioning (ϕ_1) and complementary (ϕ_2) samples listed for each component of the simultaneous template fit. The "Other" component is held fixed at the nominal prediction during the fit. 115

5.7 Optimal unfolding iterations found by minimization of $\langle$MSE$\rangle$. 127

5.8 Materials and mass contributions of the fiducial volume of the NOvA ND. 136

5.9 Elements and mass contributions of the fiducial volume of the NOvA ND. 137

6.1 Contributions to the average uncertainty on the measured double-differential cross section. 155

6.2 χ^2 values comparing model predictions to the measured cross sections and uncertainties. Degrees of freedom ($d.f.$) for each measurement are also shown. 156

7.1 Data analyzed to perform a realistic neutrino cross-section analysis using the High Performance Computing (HPC) analysis workflow described in Section 7.1. The Nominal sample was used to predict the cross section. The $\pm 1\sigma$ Calibration samples were compared to the Reference Nominal to estimate error due to calibration uncertainty. 171

LIST OF FIGURES

2.1 Average electron energy distribution measured by Ellis and Wooster [3] from radium β-decay. 4

2.2 The Standard Model of particle physics. 6

2.3 Fundamental vertices of the weak interaction involving fermions. The W bosons couple to leptons (left) and quarks (right), exchanging electric charge. The Z boson couples to all fermions (middle), exchanging no electric charge. Antifermion vertices are constructed by twisting the diagrams about the vertical axis. 12

2.4 Neutrino cross section divided by neutrino energy as a function of neutrino energy [4]. For energies relevant to oscillation experiments, typically $1\,\mathrm{GeV}$ to $10\,\mathrm{GeV}$, Quasi-Elastic (QE), Resonant (RES), and Deep Inelastic Scattering (DIS) occur at comparable rates for both neutrinos (left) and antineutrinos (right). 14

2.5 Feynman diagram of resonant single-pion production. 17

2.6 Double-differential ν_e-CC inclusive cross section measured with the NuMI Off-axis ν_e Appearance (NOvA) experiment [5] and compared to neutrino generator predictions. . 22

3.1 Diagram of the Fermilab accelerator complex [6]. 24

3.2 Daily exposure of the NuMI neutrino beam (orange) and antineutrino beam (blue) from the start of commissioning to March 2020. Lines indicate cumulative exposure for neutrino-mode (dark blue), antineutrino-mode (dark orange), and the total (dark gray) [7]. 25

3.3 The NuMI beamline [8]. 26

3.4 Schematic of the NuMI magnetic focusing horn system [8]. 26

3.5 Neutrino energy as a function of parent-pion energy and off-axis angle [9]. The NOvA detectors are placed $14\,\mathrm{mrad}$ off-axis resulting in $\langle E_\nu \rangle = 2\,\mathrm{GeV}$. 28

3.6 Energy distribution of pion-decay neutrinos at various off-axis positions (area normalized) [9]. The NOvA detectors are placed $14\,\mathrm{mrad}$ off-axis resulting in $\langle E_\nu \rangle = 2\,\mathrm{GeV}$. 29

3.7 The affect of off-axis positioning on background Neutral-Current (NC) interactions [9]. Although NCπ^0 interactions can mimic the topological signal of ν_e Charged-Current (CC) interactions, the visible energy deposited by these interactions is significantly lower. 30

3.8 Neutrino flux from NuMI at the NOvA Near Detector (ND) broken down by neutrino flavor for forward (A) and reverse (B) NuMI horn configurations [10]. 30

3.9 Direct lineage of the neutrinos incident on the NOvA ND from collisions between Main Injector (MI) protons and the NuMI target for NuMI forward (A) and reverse (B) horn configurations [10]. 31

3.10 Photograph of the ND at Fermilab. The detector dimensions are $4.2\,\mathrm{m} \times 4.2\,\mathrm{m} \times 15.8\,\mathrm{m}$. The camera is pointed toward the beam direction. 33

3.11 Photograph of the Far Detector (FD) in Ash River, Minnesota. The detector dimensions are $15.6\,\mathrm{m} \times 15.6\,\mathrm{m} \times 63.0\,\mathrm{m}$. The camera is pointed toward the beam direction. 33

3.12 A cell of the NOvA detectors. Cells are filled with liquid scintillator that emits light when charged particles propagate through. The scintillation light is carried to Avalanche Photo Diodes (APDs) by wavelength-shifting fiber, which is looped to maximize collection efficiency [9]. 34

3.13 A schematic of the NOvA ND showing logical segmentation along the beam axis. Alternating planes span the length of the detector. Colors indicate veto (red), fiducial (green), shower containment (yellow), and muon catcher (black) regions of the detector [9]. The real muon catcher is two-thirds the height of the standard modules. . 35

3.14 Time of hits relative to the start of the NuMI beam spill window illustrating ND timing resolution capabilities and NuMI beam structure. 36

3.15 An event display of neutrino event occurring in the NOvA ND [11]. Color represents relative timing of detector hits. 37

3.16 Average corrected detector response per unit length as a function of distance from the end of stopped muon tracks [12] 39

4.1 Flowchart of the NOvA simulation. The hadron production and transportation from the NuMI beam is simulated with G4NUMI. Neutrinos produced from G4NUMI interact with the detector material as simulated by the GENIE generator. Detector response is simulated with custom NOvA software and takes into account real detector running conditions, noise, and dead detector material. 40

4.2 Corrected neutrino fluxes at the NOvA ND. Panels A and B show the ν_μ and ν_e flux in the Forward Horn Current (FHC) beam mode samples, respectively [13, 10]. Panels C and D show the $\bar{\nu}_\mu$ and $\bar{\nu}_e$ flux in the RHC beam mode samples, respectively. Error bands include data-constrained uncertainty on hadron production models. Flux ratio is the corrected flux divided by the uncorrected flux. 42

4.3 NOvA ND data compared to simulation before and after NOvA MEC and FSI tune [14]. 45

4.4 Slicing is performed on a $550\,\mu$s readout window of the NOvA FD. Colors represent different slices [15]. 47

4.5 Reconstruction chain after slicing. An interaction vertex is found via a Hough Transform algorithm and prongs are formed to represent particle trajectories by a fuzzy k-means algorithm [16]. 48

4.6 Completeness (A) and purity (B) of prong clustering of visible lepton energy [16]. 49

4.7 Electron $\cos\theta$ bias of the reconstructed prong angle. A plot of true versus reconstructed electron angle (A) shows that the relationship closely follows a line with slope of 1 (dashed red line). Overall fractional bias (B) is shown to be essential 0% with 2% resolution. 51

4.8 Bias of the calorimetric energy estimation from the clustered electron prong. True electron energy versus calorimetric energy (A) shows the slope clearly deviating from 1 (dotted red line). Overall fractional bias (B) is shown to underestimate true electron energy by 10% with a resolution of 16%. 51

4.9 Polynomials are fit to calorimetric energy bias as a function of calorimetric energy within the range $0 \leq E_{\text{cal}}\,(\text{GeV}) \leq 6$. 52

4.10 Absolute bias (A) and resolution (B) of polynomial-corrected electron energy estimators as a function of true electron energy. 53

4.11 Bias of the 2^{nd}-order polynomial electron energy estimator. A plot of true versus reconstructed electron energy (A) shows the relationship closely follows a line with slope of 1 (dashed red line). Overall fractional bias (B) is shown to be roughly 1% with 14% resolution, reduced from 16%. 54

4.12 Average energy of true ν_e-CC interactions selected from FHC simulation as a function of E_{EM} and E_{Had} [1]. 55

4.13 Reconstructed neutrino energy bias as a function of true neutrino energy for simulated ν_e-CC events in FHC (left) and $\bar{\nu}_e$-CC events in RHC (right) [1]. 56

4.14 A simplified illustration of the nested-tree structure of slice in the CAF format. Every slice contains a collection of prongs, tracks, and a tree of MC truth information. Each slice can contain any number of prongs or tracks indicated by the dotted lines. Each prong contains features that describe the prong. Each track contains features that describe the track. Tree leaves are indicated by a square end point. A closed circle indicates a branching point. An open circle indicates a branching point that potentially contains many nested branches that are not shown in the diagram. 57

5.1 Distance from the closest clustered energy deposition to the walls of the detector for RHC data and MC events. Arrows indicate containment cuts optimized for the ν_e-CC analysis [17]. Good agreement is shown between data and MC beyond the optimized containment cut values. 66

5.2 Fractional uncertainty on the total cross section as a function of upper and lower bounds of the x- (A), y- (B), and z-coordinates (C) defining the fiducial volume. Dashed lines indicate the optimal bounds of the ν_e-CC inclusive analysis [17] defined in (5.14). The surface of fractional uncertainty is smooth near the optimal bounds. 70

5.3 Reconstructed vertex x- (A), y- (B), and z-coordinates (C) from RHC data and MC. Agreement is observed between the optimal fiducial bounds (5.14). 71

5.4 Maximum MuonID classification score per slice of simulated RHC events, broken down by CC flavor and NC. Clear separation is observed between interactions with and without a true muon in the final state. 72

5.5 Fractional uncertainty on total cross section as a function of MuonID cut value. The optimal cut is found to be MuonID < -0.55. 72

5.6 Selected events from the nominal RHC (left) and FHC (right) MC samples broken down by CC flavor and NC interactions. 74

5.7 Hadron production uncertainties on FHC ν_μ (A) and RHC $\bar{\nu}_\mu$ (B) from [13]. The dominant source (nucleon-A) is from nucleon interactions with targets not covered by data. 77

5.8 Ensemble of Package to Predict the Flux (PPFX) universes of selected events in bins of reconstructed electron energy (top) and scattering angle (bottom). 78

5.9 Top: Electron antineutrino flux at the NOvA ND. Bottom: Flux uncertainties from beam focusing and hadron production. 80

5.10 Fractional change in all signal (A) and selected signal (B) event rate due to varying individual GENIE parameters $\pm 1\sigma$, broken down by final-state pion multiplicity. The 40 knobs with the largest impact on signal rate are shown. 81

5.11 GENIE multiverse of selected signal events in bins of reconstructed electron energy (top) and scattering angle (bottom). 82

5.12 Profile of the Cherenkov scaling factor of the NOvA light model [18]. The 3σ interval is conservatively chosen to represent the uncertainty in Cherenkov photon production. 83

5.13 Profile of the F_{XZ} (ND X) and F_{YZ} (ND Y) scaling factors of the NOvA light yield model [18]. The 3σ region is conservatively chosen to represent the uncertainty in the overall scaling of photon production. 84

5.14 Corrected photoelectrons deposited per particle path length as a function of distance from center of the cell length is measured in data and simulation [19]. A line is fit to the Data/MC ratio between $-160 < W < 160$, which is used to derive a systematic uncertainty on the calibration procedure. Lines are also fit near the edges (not shown). 84

5.15 Prong energy distributions from a sample of neutron prong candidates in RHC beam mode [20]. The MC is broken down by the type of particle the parent neutron interacted with that is clustered into a prong. Comparisons to data show that the simulation significantly over-estimates the number of low-energy neutron prong candidates. 86

5.16 Calorimetric energy of 2- and 3-dimensional prongs (Summed 2D+3D) after modification by neutron-daughter prong energy scaling factor of $S = 3.6$ and probability of $P = 0.33$ [21]. 87

5.17 Pixel maps of simulated charged particles propagating in the NOvA ND. 90

5.18 Particle kinematics of Prong CVN training sample. 93

5.19 Particles in the Prong CVN training sample 94

5.20 Diagram of the Prong CVN architecture [22] based on MobileNetV2. 95

5.21 Training accuracy and loss as a function of epoch. Solid lines indicate the data sample used to minimize the loss and dashed lines indicate the statistically-independent data sample used evaluate over-fitting. 96

5.22 ROC curves for the Prong CVN classification of GENIE prongs. 97

5.23 Confusion matrices for the Prong CVN evaluated on GENIE prongs. 97

5.24 Prong CVN electron and photon scores decomposed into true particle species. The left column shows the full range of the scores ([0-1]) and the right column is zoomed in to [0.5-1]. 99

5.25 Prong CVN muon and hadron scores decomposed into true particle species. The left column shows the full range of the scores ([0-1]) and the right column is zoomed in to [0.5-1]. 100

5.26 NueID training variables where "signal" is defined as true ν_e-CC or $\bar{\nu}_e$-CC interactions that pass the analysis preselection criteria. 102

5.27 Correlation between NueID input variables showing only small correlations between shower width and dE/dx log-likelihood ratio. Correlations between these variables are shown for signal (top) and background (bottom) events. 103

5.28 NueID distributions broken down by type of neutrino interaction for FHC (top) and RHC (bottom) samples showing good separation between signal and background in both beam-modes. 104

5.29 NueID distributions broken down by interaction mode of ν_e CC and $\bar{\nu}_e$ CC events for FHC (top) and RHC (bottom) samples. 105

5.30 On the left, a 1σ enhancement of the RHC $\bar{\nu}_e$-CC component is shown by the solid blue line. Equation (5.39) is used to calculate the most likely FHC $\bar{\nu}_e$-CC distribution given the 1σ enhancement in the RHC sample. The result is shown on the right in the dashed blue line and compared to the 1σ error band on the FHC $\bar{\nu}_e$-CC component. Because normalization uncertainties are highly correlated between the RHC and FHC

samples, the predicted FHC distribution approximates the 1σ prediction of the FHC distribution. 116

5.31 Systematic covariance in units of ($\bar{\nu}_e$ CC events)^2 (left) and correlation (right) matrices describing how normalization changes in selected $\bar{\nu}_e$ CC events from the RHC sample are related to changes in the FHC sample. Bins are arranged as a linear representation of the 2-dimensional electron kinematic phase space, and matrix blocks correspond to beam mode. 116

5.32 Template normalization parameters extracted from a template fit to statistically-varied fake data sample. Conditioning samples are indicated below each figure. 118

5.33 A collection of template bins showing post-fit agreement between renormalized simulation and statistically-varied fake data. 119

5.34 Renormalized event rates extracted from a template fit to statistically-varied fake data. The bottom panels each show the ratio between fake data and post-fit MC. Hashed red regions indicate shape-only uncertainties estimated from systematically modified simulation. Solid red regions indicate total uncertainty on the number of selected events constrained by data via template fit procedure. 120

5.35 Ensemble of selected events in fake data divided by simulation before (top) and after (bottom) template fit. Gray histograms indicate relative event statistics (arbitrary units). A bias of at most 5% is observed in the post-fit event distributions when compared to fake data. 121

5.36 Ensemble of true $\bar{\nu}_e$-CC signal purity divided by purity estimated from performing a template fit. The ensemble of fake data is generated by statistically varying the nominal prediction. Gray histograms indicate relative event statistics (arbitrary units). 122

5.37 Unfolding matrices relating true and reconstructed quantities of selected signal events for the electron energy and cosine of the scattering angle (A), neutrino energy (B), and Q^2 (C). 125

5.38 Average MSE as a function of unfolding iterations for the electron energy and cosine of the scattering angle (A), neutrino energy (B), and Q^2 (C). 127

5.39 Overall fiducial $\bar{\nu}_e$-CC selection efficiency as a function of electron kinematics in RHC beam mode. 129

5.40 Fractional uncertainties on overall fiducial $\bar{\nu}_e$-CC selection efficiency as a function of electron kinematics in RHC beam mode. Bins with more than 20% total uncertainty are removed from the analysis signal phase space. 130

5.41 All simulated signal events (bin-width normalized) broken down by interaction mode, including Coherent Pion Production (COH), Deep Inelastic Scattering (DIS), Meson-Exchange Current (MEC), Quasi-Elastic (QE), and Resonant (RES), in electron kinematics and RHC beam mode. 131

5.42 Selected simulated signal events (bin-width normalized) broken down by interaction mode in electron kinematics and RHC beam mode. 132

5.43 Signal selection efficiency (bin-width normalized) broken down by interaction mode in electron kinematics and RHC beam mode. 133

5.44 Breakdown of signal selection efficiency (bin-width normalized) as a function of E_ν in RHC beam mode. 134

5.45 Breakdown of signal selection efficiency (bin-width normalized) as a function of Q^2 in RHC beam mode. 135

5.46 Template normalization parameters extracted from a template fit to the nominal simulation, demonstrating self-consistency of the fitting procedure. 138

5.47 Extracted double-differential $\bar{\nu}_e$-CC inclusive cross section from the nominal simulation (red). Results are compared to the NOvA (blue) and default (green) GENIE tunes. In this case, the fake data truth is the NOvA GENIE tune. 139

5.48 Extracted single-differential $\bar{\nu}_e$-CC inclusive cross sections from the nominal simulation (red). Results are shown as a function of electron energy (top) and scattering angle (bottom). Results are compared to the NOvA (blue) and default (green) GENIE tunes. In this case, the fake data truth is the NOvA GENIE tune. 140

5.49 Extracted total and single-differential $\bar{\nu}_e$-CC inclusive cross sections from the nominal simulation (red). Results are shown as a function of neutrino energy (top) and Q^2 (bottom). Results are compared to the NOvA (blue) and default (green) GENIE tunes. In this case, the fake data truth is the NOvA GENIE tune. 141

5.50 Extracted double-differential $\bar{\nu}_e$-CC inclusive cross section from fake data generated by statistically varying the nominal prediction (red). Results are compared to the NOvA (blue) and default (green) GENIE tunes. 142

5.51 Uncertainties on the double-differential $\bar{\nu}_e$-CC inclusive cross section extracted from fake data generated by statistically varying the nominal prediction. The largest effect is due to uncertainties on the template fit normalization parameters. The total uncertainty is a quadrature sum of the individual effects. 143

5.52 Top: Extracted single-differential $\bar{\nu}_e$-CC inclusive cross section as a function of electron energy from fake data generated by statistically varying the nominal prediction (red). Results are compared to the NOvA (blue) and default (green) GENIE tunes. Bottom:

Uncertainty breakdown on the single-differential cross section. The total uncertainty is a quadrature sum of the individual effects. 144

5.53 Top: Extracted single-differential $\bar{\nu}_e$-CC inclusive cross section as a function of electron scattering angle from fake data generated by statistically varying the nominal prediction (red). Results are compared to the NOvA (blue) and default (green) GENIE tunes. Bottom: Uncertainty breakdown on the single-differential cross section. The total uncertainty is a quadrature sum of the individual effects. 145

5.54 Top: Extracted single-differential $\bar{\nu}_e$-CC inclusive cross section as a function of Q^2 from fake data generated by statistically varying the nominal prediction (red). Results are compared to the NOvA (blue) and default (green) GENIE tunes. Bottom: Uncertainty breakdown on the single-differential cross section. The total uncertainty is a quadrature sum of the individual effects. 146

5.55 Top: Extracted total $\bar{\nu}_e$-CC inclusive cross sections as a function of neutrino energy from fake data generated by statistically varying the nominal prediction (red). Results are compared to the NOvA (blue) and default (green) GENIE tunes. Bottom: Uncertainty breakdown on the cross section. The total uncertainty is a quadrature sum of the individual effects. 147

5.56 Extracted double-differential $\bar{\nu}_e$-CC inclusive cross section from fake data generated with modified neutrino interaction and flux models (red). Results are compared to the NOvA (blue) and default (green) GENIE tunes. 148

5.57 Uncertainties on the double-differential $\bar{\nu}_e$-CC inclusive cross section extracted from fake data generated with modified neutrino interaction and flux models. The largest

effect is due to uncertainties on the template fit normalization parameters. The total uncertainty is a quadrature sum of the individual effects. 149

5.58 Top: Extracted single-differential $\bar{\nu}_e$-CC inclusive cross section as a function of electron energy from fake data generated with modified neutrino interaction and flux models (red). Results are compared to the NOvA (blue) and default (green) GENIE tunes. Bottom: Uncertainty breakdown on the single-differential cross section. The total uncertainty is a quadrature sum of the individual effects. 150

5.59 Top: Extracted single-differential $\bar{\nu}_e$-CC inclusive cross section as a function of electron scattering angle from fake data generated with modified neutrino interaction and flux models (red). Results are compared to the NOvA (blue) and default (green) GENIE tunes. Bottom: Uncertainty breakdown on the single-differential cross section. The total uncertainty is a quadrature sum of the individual effects. 151

5.60 Top: Extracted single-differential $\bar{\nu}_e$-CC inclusive cross section as a function of Q^2 from fake data generated with modified neutrino interaction and flux models (red). Results are compared to the NOvA (blue) and default (green) GENIE tunes. Bottom: Uncertainty breakdown on the single-differential cross section. The total uncertainty is a quadrature sum of the individual effects. 152

5.61 Top: Extracted total $\bar{\nu}_e$-CC inclusive cross sections as a function of neutrino energy from fake data generated with modified neutrino interaction and flux models (red). Results are compared to the NOvA (blue) and default (green) GENIE tunes. Bottom: Uncertainty breakdown on the cross section. The total uncertainty is a quadrature sum of the individual effects. 153

6.1 Selected data RHC (left) and FHC (right) NuMI exposure corresponding to 11.38×10^{20} POT and 13.85×10^{20} POT, respectively, compared to simulation. Data and simulation are shown in bins of reconstructed electron energy, electron scattering angle, and NueID score. Red regions indicate systematic uncertainty bands. Data are well-constrained within systematic error within the phase space of the analysis. An overall excess of data measured in the RHC sample is observed. 157

6.2 Template normalization parameters extracted from a template fit to data selected from NuMI exposure. Conditioning samples are indicated below each figure. 158

6.3 Renormalized event rates extracted from a template fit to NuMI data. The bottom panels each show the ratio between data and post-fit MC. Hashed red regions indicate shape-only uncertainties estimated from systematically modified simulation. Solid red regions indicate total uncertainty on the number of selected events constrained by data via template fit procedure. 159

6.4 Sample purity estimated by template fit to NuMI data in bins of reconstructed electron energy and cosine of the scattering angle. Errors are derived from correlated uncertainties in the template fit normalization parameters. 160

6.5 Measured double-differential $\bar{\nu}_e$-CC inclusive cross section using selected data from NuMI corresponding to 11.38×10^{20} POT (13.85×10^{20} POT) RHC (FHC) exposure. Results are compared to the NOvA (blue) and default (green) GENIE tunes. 161

6.6 Measured double-differential ν_e-CC inclusive cross section using selected data from NuMI corresponding to 11.38×10^{20} POT (13.85×10^{20} POT) RHC (FHC) exposure. Results are compared to [5] (red squares) and the NOvA (blue line) and default (green line) GENIE tunes. 162

6.7 Measured single-differential $\bar{\nu}_e$-CC inclusive cross section as a function of electron angle using selected data from NuMI corresponding to 11.38×10^{20} POT (13.85×10^{20} POT) RHC (FHC) exposure. Results are compared to the NOvA (blue) and default (green) GENIE tunes. 163

6.8 Measured single-differential $\bar{\nu}_e$-CC inclusive cross section as a function of the cosine of the electron scattering angle using selected data from NuMI corresponding to 11.38×10^{20} POT (13.85×10^{20} POT) RHC (FHC) exposure. Results are compared to the NOvA (blue) and default (green) GENIE tunes. 163

6.9 Measured single-differential $\bar{\nu}_e$-CC inclusive cross section as a function of Q^2 using selected data from NuMI corresponding to 11.38×10^{20} POT (13.85×10^{20} POT) RHC (FHC) exposure. Results are compared to the NOvA (blue) and default (green) GENIE tunes. 164

6.10 Measured total $\bar{\nu}_e$-CC inclusive cross section as a function of neutrino energy using selected data from NuMI corresponding to 11.38×10^{20} POT (13.85×10^{20} POT) RHC (FHC) exposure. Results are compared to the NOvA (blue) and default (green) GENIE tunes. 164

7.1 Event selection timing measurements as a function of the number of Message Passing Interface (MPI) ranks executing a PANDANA event selection program and the number of files among which $3\,\mathrm{TB}$ of uncompressed NOvA data is distributed. Measurements are performed using National Energy Research Scientific Computing Center (NERSC) Cori system. A consistent 10x speedup is achieved when data is contained in one Hierarchical Data Format, version 5 (HDF5) file when compared to 256. 168

7.2 Diagram of LLAMA `Histogram` addition and automatic aggregation during parallel execution of a LLAMA program. Each rank posses a copy of two histograms, which are added together. Each rank then holds partial, but not complete, results of the addition operation. MPI `Reduce` is invoked automatically when the user attempts to save the resulting `Histogram` to a file. 169

7.3 Demonstration of the HPC neutrino analysis workflow. Left: Distribution of selected events as a function of neutrino energy. Right: Predicted cross section as a function of neutrino energy with error bars. Error bars estimate uncertainties from detector calibration. 171

7.4 Runtime of the HPC analysis workflow as a function of the number of MPI processes (*i.e.* ranks) using the NERSC Perlmutter system. Results are compared to the theoretically most efficient (strong) scaling predicted by Amdahl's law [23]. 172

CHAPTER 1

Introduction

The discovery of neutrinos in 1956 spurred a flurry of scientific exploration into the fundamental workings of our universe. The discovery itself, made by Frederick Reines and Clyde Cowan, prompted the 1995 Nobel Prize in Physics to be awarded to Reines (Cowan had by that time passed away). A second Nobel Prize was awarded in 1988 to Leon Lederman, Melvin Schwartz, and Jack Steinberger for their method for developing a human-made neutrino beam using a high energy particle accelerator to fuel future neutrino experiments. In 2002, Raymon Davis Jr. and Masatoshi Koshiba were awarded the Nobel Prize for the detection of cosmic neutrinos proving that the sun's energy comes from neutrino-producing reactions. Finally, Takaaki Kajita and Arthur McDonald were awarded the 2015 Nobel Prize for proving the existence of neutrino mass by measuring oscillation.

Today, physicists stand on the shoulders of Giants to gaze at a universe illuminated by neutrinos. They continue to probe fundamental parameters of the Standard Model of particle physics using neutrinos, develop applications in nuclear antiproliferation by measuring the neutrino byproduct of Uranium enrichment, and look toward the sky for neutrino signals from collapsing stars with multi-messenger astronomy. As they continue studying neutrinos through the coming decades, they will be looking for clues to help explain the observed matter/antimatter asymmetry in the universe – a necessary condition for our existence.

At the heart of past and future discoveries are the physical processes neutrinos undergo to interact with the surrounding matter. Complicated structure within the nucleus clouds the physical theory to a point that is unsolvable even by today's largest computers. Instead, we must rely on approximations grounded in experimental observations to make progress. As we explore higher

and higher energy regimes of neutrino physics, we must continue to supplement these approximate models with experimental data in order to make reliable conclusions about the universe.

Today's neutrino oscillation experiments probe a unique energy range where different physical processes contribute equally to the ways in which they interact. From roughly 1 to 10 $\mathrm{GeV}$of neutrino energy, interactions produce different final-state particles due to effects within the target nucleus, and are modeled independently. These models are glued together post hoc with methods tuned to be empirically consistent with measured data, but the exact physics that governs these transition regions is not well understood. Moreover, important regions of the model phase space are not well constrained, particularly those involving the neutrino's antimatter counterpart, the antineutrino. This results in large uncertainties on model parameters and subsequent oscillation measurements where determination of the incoming neutrino energy is imperative.

One experiment aimed at studying the physics of neutrino and antineutrino oscillation is the NuMI Off-axis ν_e Appearance (NOvA) experiment. The neutrinos studied with this experiment come from the Neutrinos at the Main Injector (NuMI) beam at Fermilab based on Lederman, Schwartz, and Steinberger's Nobel-winning technology. Since 2012, NOvA has been used to set competitive limits on the parameters of the Pontecorvo-Maki-Nakagawa-Sakata (PMNS) oscillation formalism, which rests heavily on the interaction modeling and energy determination of both neutrino and antineutrinos with energies between 1 and 10 GeV. Additionally, the NOvA experiment has collected the largest sample of neutrino and antineutrino interactions ever assembled, which has enabled high-statistics measurements of both the neutrino and antineutrino cross sections on which it relies. As of today, the near detector has been used to measure the cross sections of interactions producing neutral pions, interactions of muon-flavor neutrinos, and, most recently, interactions of the electron-flavor neutrino.

This thesis aims to describe the analysis technique and measurement of the first double-differential electron antineutrino charged-current inclusive cross section ever made. In Chapter 2, an overview of neutrino physics including neutrino oscillations and our current understanding of neutrino interactions is presented. In Chapters 3 and 4, the NOvA experiment and the software and simulation used for the analysis are described. Chapter 5 describes the analysis sample and technique for measuring the double-differential electron antineutrino charged-current inclusive cross section with novel background constraint using neutrino data and tests of the analysis framework using mock data. Chapter 6 presents the cross section measurement. Chapter 7 presents additional contributions made by the author to the NOvA and Scientific Discovery through Advanced Computing: High Energy Physics Data Analytics on High Performance Computing (SciDAC-4) collaborations. Finally, concluding remarks are left for Chapter 8.

CHAPTER 2

Motivation and Neutrino Physics

An experiment [3] performed in 1927 by Charles Ellis and William Wooster seemed to suggest that a nuclear decay process, called β-decay, violated the universal law of conservation of energy. At the time, β-decay was thought to be a process by which a neutron would decay into a proton and electron ($n \rightarrow p + e$). The electron, β-particle, produced by this two-body decay would be emitted mono-energetically from the perspective of the proton, and this energy could be measured in the lab. With their experiment, they studied the β-decay of radium and measured a continuum of electron energies (Figure 2.1). With no other particles to receive the leftover mass energy of the neutron, it seemed that energy had not been conserved. Various theories were proposed to explain this observation, including one from Niels Bohr who argued that β-decay is allowed to violate energy conservation [24].

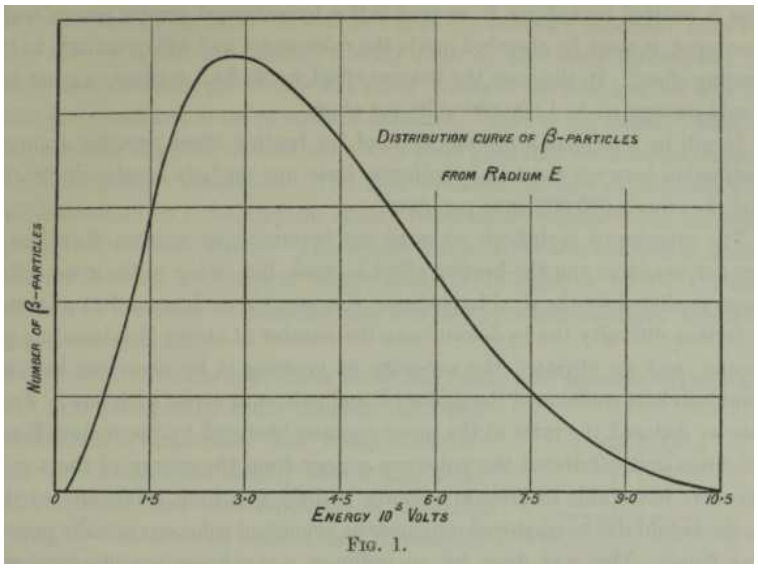

Figure 2.1. Average electron energy distribution measured by Ellis and Wooster [3] from radium β-decay.

In 1930, Wolfgang Pauli proposed a solution that would both rescue energy conservation and spur a rich area of study for centuries to come. In an open letter to renown nuclear physicists [25], he suggested a third particle could be produced in β-decay to share the energy that was thought to go into the electron, in this way conserving the overall energy of the reaction and explaining the observed energy distribution. The particle would have to be electrically neutral because it had been undetected by apparatus sensitive to electrical charge and possess a very small mass because the tail of the observed energy spectrum was very close to the energy the electron would have under the two-body assumption. The particle he imagined has since been named the neutrino, and in 1956 Clyde Cowan and Frederick Reines confirmed [26] that β-decay produces neutrinos ($n \rightarrow p + e + \bar{\nu}_e$). Reines won the Nobel Prize for this work in 1995.

In this chapter, the neutrino as it is described in the Standard Model (SM) of particle physics will be introduced and the importance of understanding neutrino-matter interactions will be motivated. Next, a brief overview of neutrino oscillations and their role in our understanding of the universe will be given. Finally, the interactions that allow experiments to measure oscillation, with emphasis on long-baseline oscillation experiments, will be summarized.

2.1. Neutrinos and the Standard Model of Particle Physics

Our current understanding of the fundamental particles and forces that make up the universe is described by the SM [27]. The SM formulates the universe as abstract, quantum mechanical fields: particles are excitations of the associated fields and forces emerge as interactions between the various fields. The fields and possible interactions within the SM can be summarized as in Figure 2.2. Three of the four known fundamental forces are carried by particles within the SM. For example, the photon carries the electromagnetic force; energy is transferred between electrons in copper wire by photons, which drives an electrical current. Similarly, the strong force is carried

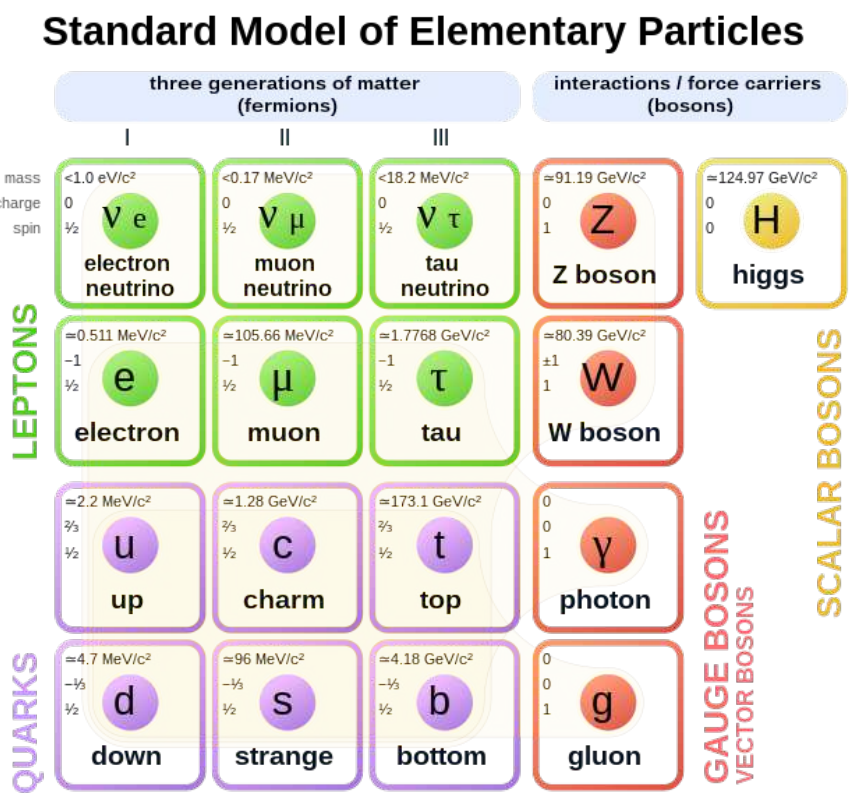

FIGURE 2.2. The Standard Model of particle physics.

by gluons, and the weak force is carried by the Z and W bosons. Gravity, the fourth and final fundamental force, is not yet included in the SM. Unifying the three SM forces together with gravity is perhaps the most sought-out theoretical achievement of our time.

Today, we know neutrinos (ν) to belong to a class of particles called leptons. Leptons have an intrinsic spin angular momentum of unit 1/2* and interact via the weak and electromagnetic forces. Leptons come in three varieties: electron-, muon-, and tau-type, each corresponding to a different generation of matter. In each generation, there are two quarks, a charged lepton and a neutral lepton called a neutrino. Neutrinos within each generation are tied to their charged cousins by a quantum mechanical degree of freedom called lepton number, L_l, where l is e, μ, or τ for the electron, muon, or tau generations, respectively.

*Natural units ($c = \hbar = 1$) will be used throughout this thesis.

One key difference between neutrinos and antineutrinos is their helicity. The helicity of a spin-1/2 particle, like the (anti)neutrino, is +1 (right-handed) if its spin angular momentum is aligned along its direction of motion, and -1 (left-handed) if its spin is anti-aligned. Up until the mid-1950's, physicists had assumed that there would be no preferred helicity of neutrinos based on previous experiments, but there had been no confirmation of this assumption. The following decade brought experimental evidence that neutrinos are left-handed [28] and antineutrinos are right-handed [29], challenging the long-held "mirror" symmetry, or parity, conservation. In fact, parity violation is a defining trait of the weak force.

Quarks and antiquarks make up most of the matter we experience every day. Molecules are made of elements, elements are made of protons and neutrons, and protons and neutrons are made of quarks. Specifically, protons are a bound triplet of three quarks: up, up, and down (uud). Neutrons are a bound triplet of up, down, and down quarks (udd). Quarks are bound together by gluons (g), and described by Quantum Chromo-Dynamic (QCD) theory. Quarks interact with the leptons by exchanging a W or Z boson by so-called Charged-Current (CC) or Neutral-Current (NC) interactions, respectively.

In the SM, antiparticle fields ($\bar{\psi}$) and particle fields (ψ) are related through the subsequent applications of the parity operator (P) and charge-conjugation operator (C) such that $CP\psi(x) = \bar{\psi}(x)$. The application of the CP operator to a reaction gives the same reaction involving antiparticles. For example β-decay under CP transformation is the decay of an anti-neutron: $\bar{n} \rightarrow \bar{p} + \bar{e} + \nu_e$.

The invariance of physical laws under CP transformation (CP invariance) would state that matter and antimatter are equal throughout the universe. In reality, we observe there to be a stark asymmetry in the matter and antimatter content of the universe. The violation of CP

invariance has been observed in the quark sector involving decays of neutral mesons [30–36], but is not enough to account for the observed asymmetry alone [37]. One contending theory, called leptogenesis [38], aims to explain the remaining asymmetry with CP violation in the lepton sector. One way to measure this leptonic CP violation is by measuring neutrino oscillation.

2.2. Neutrino Oscillation

Ideas about neutrinos "oscillating" or changing from one lepton generation, or flavor state, started with Bruno Pontecorvo in 1957 [39, 40]. Inspired by the ideas of Gell-Mann and Pais on the possibility of particle-antiparticle oscillation in the quark sector [41], Pontecorvo considered the possibility of neutrino-antineutrino oscillations since, at the time, the three flavor states of the neutrino had not been discovered. After the discovery of the muon neutrino, Ziro Maki, Masami Nakagawa, and Shoichi Sakata theorized [42] oscillation between muon and electron neutrinos ($\nu_\mu \leftrightarrow \nu_e$) that eventually lead to the modern three-flavor formalism named after the major contributors, Pontecorvo, Maki, Nakagawa, and Sakata (PMNS). This formalism includes a mechanism for leptonic CP violation required by leptogenesis.

Oscillations arise because neutrinos interact with the weak force, W and Z bosons, in states that are superpositions of mass states, i.e.

$$|\nu_\alpha\rangle = U^*_{\alpha 1}\,|\nu_1\rangle + U^*_{\alpha 2}\,|\nu_2\rangle + U^*_{\alpha 3}\,|\nu_3\rangle \tag{2.1}$$

where $|\nu_\alpha\rangle$ is the flavor eigenstate for lepton flavor α, $U^*_{\alpha i}$ are complex amplitudes and elements of the inverse of the unitary transformation matrix U, and $|\nu_i\rangle$ are neutrino mass eigenstates. These mass eigenstates propagate through space and time at different rates leading to a time-changing evolution of $|\nu_\alpha\rangle$.

The matrix U describes how much of each mass eigenstate makes up each flavor eigenstate. Since U represents a change in basis, it is unitary and can be represented as a rotation in three dimensions with up to 6 imaginary phases. The standard parameterization, often referred to as the PMNS matrix, is

$$
\begin{aligned}
U &= \begin{bmatrix} 1 & 0 & 0 \\ 0 & c_{23} & s_{23} \\ 0 & -s_{23} & c_{23} \end{bmatrix} \begin{bmatrix} c_{13} & 0 & s_{13}e^{-i\delta_{CP}} \\ 0 & 1 & 0 \\ -s_{13}e^{-i\delta_{CP}} & 0 & c_{13} \end{bmatrix} \begin{bmatrix} c_{12} & s_{12} & 0 \\ -s_{12} & c_{12} & 0 \\ 0 & 0 & 1 \end{bmatrix} P \\
&= \begin{bmatrix} c_{12}c_{13} & s_{12}c_{13} & s_{13}e^{-i\delta_{CP}} \\ -s_{12}c_{23} - c_{12}s_{13}s_{23}e^{i\delta_{CP}} & c_{12}c_{23} - s_{12}s_{13}s_{23}e^{i\delta_{CP}} & c_{13}s_{23} \\ s_{12}c_{23} - c_{12}s_{13}s_{23}e^{i\delta_{CP}} & -c_{12}c_{23} - s_{12}s_{13}s_{23}e^{i\delta_{CP}} & c_{13}c_{23} \end{bmatrix} P
\end{aligned} \tag{2.2}
$$

where $s_{ij} = \sin\theta_{ij}$ and $c_{ij} = \cos\theta_{ij}$, θ_{ij} are three-dimensional rotation angles, δ_{CP} is a phase factor, and P is a matrix containing additional phase factors. It is these phase factors, if found to be non-zero, that lead to CP violation in the lepton sector [43]. If neutrinos are found to be their own antiparticles, so-called Majorana particles, then the matrix P is a diagonal matrix containing two phase factors, otherwise, neutrinos are Dirac particles and P is the identity matrix [43].

As a neutrino travels through the vacuum of space, each mass eigenstate evolves at a different rate, assuming the states are nondegenerate. Solving the Schrödinger equation,

$$
|\nu_i(t)\rangle = e^{-iE_it}\,|\nu_i(t=0)\rangle = e^{-iE_it}\,|\nu_i\rangle \tag{2.3}
$$

where $E_i = \sqrt{p^2 + m_i^2}$. It follows that the time-evolution of flavor state α is,

$$
\begin{aligned}
|\nu_\alpha(t)\rangle &= \sum_i U^*_{\alpha i} e^{-iE_i t} |\nu_i\rangle \\
&= \sum_i U^*_{\alpha i} e^{-iE_i t} \sum_\beta U_{\beta i} |\nu_\beta\rangle
\end{aligned}
\tag{2.4}
$$

where the inverse of (2.1) has been substituted for $|\nu_i\rangle$. The probability of oscillating from flavor state α to β at a later time, t, is

$$
P(\nu_\alpha \to \nu_\beta) = |\langle \nu_\beta(t) | \nu_\alpha \rangle|^2. \tag{2.5}
$$

Assuming neutrinos are very light, i.e. ultra-relativistic, this equation can be written as

$$
\begin{aligned}
P(\nu_\alpha \to \nu_\beta) = \delta_{\alpha\beta} &- 4 \sum_{i<j} \mathrm{Re}[U_{\alpha i} U^*_{\beta i} U^*_{\alpha j} U_{\beta j}] \sin^2\left(\frac{\Delta m^2_{ij} L}{4E}\right) \\
&+ 2 \sum_{i<j} \mathrm{Im}[U_{\alpha i} U^*_{\beta i} U^*_{\alpha j} U_{\beta j}] \sin\left(\frac{\Delta m^2_{ij} L}{4E}\right)
\end{aligned}
\tag{2.6}
$$

where L is the distance of travel, E is neutrino energy, and $\Delta m^2_{ji} = m^2_j - m^2_i$. For antineutrino oscillation, the matrix U is exchanged for U^*, leading to a change of sign on the final term driven by δ_{CP}. Note that elements of the PMNS matrix enter into (2.6) through the real and imaginary parts of $U_{\alpha i} U^*_{\beta i} U^*_{\alpha j} U_{\beta j}$ and that it is independent of the complex Majorana phases, the third term vanishes for $\nu_\alpha \to \nu_\alpha$, or disappearance, oscillation, and that $P(\nu_\alpha \to \nu_\beta)$ is dependent on the phase δ_{CP} only when $\alpha \neq \beta$. Also note that if neutrinos are massless, or have the same mass, $\Delta m^2_{ij} = 0$ and neutrinos will not oscillate. Strong evidence of oscillation [44] was reported by the Super-Kamiokande collaboration in 1998 and later confirmed [45] in 2002 by the Sudbury Neutrino Observatory. Together, these experiments definitely proved the existence of massive neutrinos, which led to a Nobel Prize in 2015.

In developing Equation 2.6, the neutrinos were assumed to be traveling in the vacuum of space, however, today's experiments leveraging the intensity and control of terrestrial, human-made neutrino sources must consider the impact of matter on the propagation of neutrinos, or the Mikheev-Smirnov-Wolfenstein (MSW) effect [46, 47]. As neutrinos propagate through matter, oscillation amplitudes are affected by coherent forward-scattering of neutrinos off of electrons, which impact the propagation of electron neutrinos more than the muon or tau flavors. Long-baseline oscillation experiments use this effect using the earth's crust to determine the neutrino mass ordering [43]: the imbalance of matter-antimatter content in the crust leads to an enhancement in ν_e or $\bar{\nu}_e$ appearance probability depending on the sign of Δm^2_{32}. Since this also mimics the effect of a non-zero δ_{CP}, it is important that these experiments measure both neutrino and antineutrino oscillations.

2.3. Neutrino-Matter Interactions

Initial and oscillated neutrino flavors are determined experimentally by observing the outgoing lepton that is produced interactions between neutrinos and detector material. Subsequent oscillation probabilities are extracted by comparing initial to oscillated flavors as a function of neutrino energy, which is estimated from the energy deposited into detectors by the lepton and hadrons produced by the interaction. Both of these inferences require precise models of electroweak neutrino interaction rates, or cross sections, as a function of neutrino energy and observable final state particle kinematics.

Electroweak theory, developed between 1959 and 1967 by S. Glashow, A. Salam, J. Ward, and S. Weinberg [48–51], unites electromagnetic and weak interactions of leptons mediated by massless photons and parity-violating massive bosons. Weak interactions are responsible for

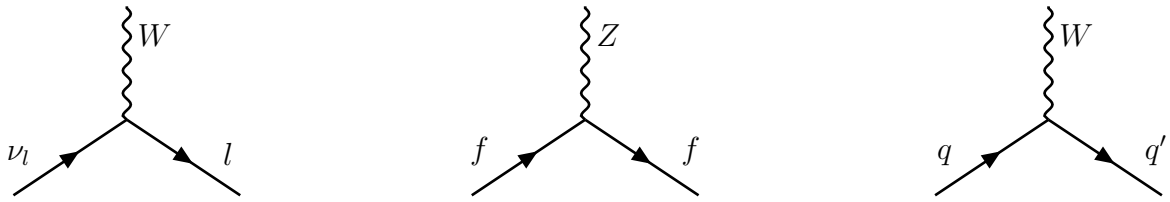

FIGURE 2.3. Fundamental vertices of the weak interaction involving fermions. The W bosons couple to leptons (left) and quarks (right), exchanging electric charge. The Z boson couples to all fermions (middle), exchanging no electric charge. Antifermion vertices are constructed by twisting the diagrams about the vertical axis.

parity violating decays [52] and the nuclear fusion that fuels the sun [53], and is the only process by which neutrinos interact with matter.

In the SM Lagrangian, the weak boson fields couple to all standard model fermions (spin-1/2), including quark and lepton fields, and are responsible for all neutrino-matter interactions. The W boson transfers electric charge between interacting particles in so-called Charged-Current (CC) interactions, while the Z mediates so-called Neutral Current (NC) interactions where electric charge is not exchanged. Feynman diagrams of the W and Z couplings with fermions are shown in Figure 2.3, which can be pieced together to form complete interactions. For example, the $\nu - e$ forward-scattering interactions that give rise to the MSW effect are

(2.7)
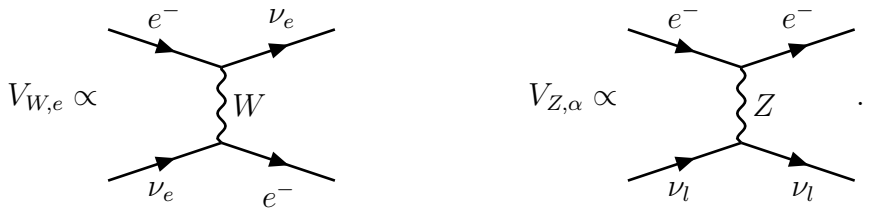

Notice at each interaction vertex, lepton number is conserved, prohibiting CC forward-scattering of $\nu_\mu - e$ and $\nu_\tau - e$.

The coupling of weak bosons with the lepton fields is weak compared to the strength of the electromagnetic (γ) and strong (g) forces. The W and Z bosons manifest in the electroweak Lagrangian as massive Yukawa propagators, implying an interaction potential energy of the form

$U(\boldsymbol{r}) \propto e^{-M|\boldsymbol{r}|}$, where $\boldsymbol{r}$ is the distance from the particles whose interaction is being mediated by the electroweak boson, and M is the mass of the boson. Their masses have been measured with great accuracy and are tabulated by the Particle Data Group (PDG) [54]. The mass of the Z boson is $M_Z = (91.1876 \pm 0.0021)\,\mathrm{GeV}$ and the mass of the W boson is $M_W = (80.377 \pm 0.012)\,\mathrm{GeV}$[†]. Such large masses result in a quickly-decaying potential energy and short interaction length, which make neutrino interactions exceptionally rare.

A defining feature of the weak force is its tendency to maximally violate parity conservation. Due to the "vector minus axial" (V-A) structure of the weak current, the W and Z bosons only couple to left-handed neutrinos and right-handed antineutrinos [27] leading to experimental observations that are asymmetrical with respect to (anti)neutrino helicity [28, 29, 52]. This also leads to an imbalance of interaction probabilities such that neutrino interactions are three-times more likely to occur than antineutrinos due to restrictions on the angular momentum phase space of the interaction [4].

2.3.1. Neutrino-Nucleus Interactions. There are many modes by which neutrinos can interact with baryonic matter, which all stem from the coupling of the quark fields with weak bosons. As energy increases, the neutrino is affected by different parts of the nuclear target: at low energies, the neutrino interacts with the nuclear system as a whole, and at high energies, it interacts with the individual quarks that make up the system [4]. Theoretical models spanning these two extremes must make judicious approximation due to the inherent complexities of a many-body quantum-mechanical system and rely on experimental constraints.

Oscillation experiments operate in an energy range that allows for three main categorical processes to occur: Quasi-Elastic (QE), Resonant (RES), Deep Inelastic Scattering (DIS). Figure

[†]For reference, the proton mass is $M_p = (0.93827000000 \pm 0.00000000029)\,\mathrm{GeV}$ [54].

2.4 shows theoretically-predicted cross sections of each category and their contributions to the total, or inclusive, cross section [4] for both neutrinos and antineutrinos. Note that measurements of the inclusive antineutrino cross section is comparatively sparse, demonstrating the need for such data for oscillation results.

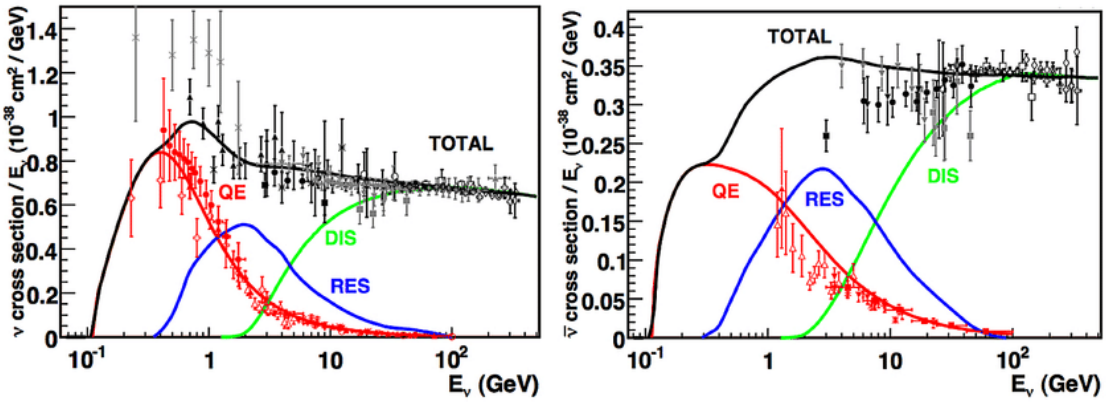

FIGURE 2.4. Neutrino cross section divided by neutrino energy as a function of neutrino energy [4]. For energies relevant to oscillation experiments, typically $1\,\mathrm{GeV}$ to $10\,\mathrm{GeV}$, QE, RES, and DIS occur at comparable rates for both neutrinos (left) and antineutrinos (right).

In addition to the outgoing lepton, RES and DIS interactions produce final state pions, which can complicate interaction topology and particle identification. Understanding these interactions is important for determining the neutrino energy in oscillation experiments [55]. As pions travel through detectors, they can be absorbed by the nuclear medium and/or elastically scatter leading to energy deposits that are invisible to detectors. This missing energy is impossible to account for without heavy reliance on neutrino interaction generators, leading to biased measurements and large errors from model uncertainties. Neutral pions produced by NC interactions ($\nu_l + N \rightarrow \nu_l + N + \pi^0$) contribute a significant and irreducible background to oscillation searches since photons produced from the decay of the π^0 can perfectly mimic the signature lepton of ν_e CC interactions.

2.3.1.1. *Quasi-Elastic Scattering.* QE interactions dominate the low energy region up to 2 GeV and is a process by which the neutrino interacts with a nucleon as a whole. Possible CC interaction channels are

$$\nu_l + n \rightarrow l^- + p \qquad\qquad \bar{\nu}_l + p \rightarrow l^+ + n$$

represented by Feynman diagrams,

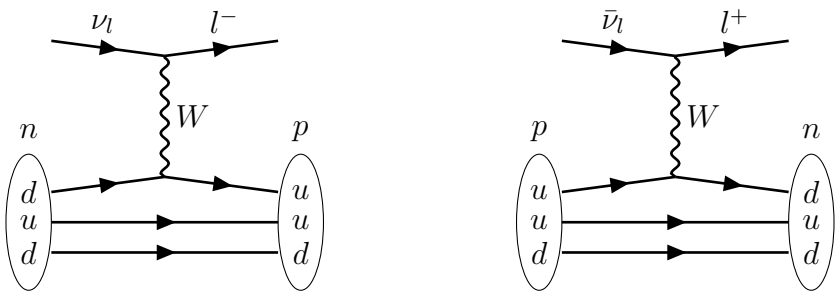

where l is e, μ, or τ and p and n are protons and neutrons, respectively. CCQE scattering interactions are characteristic two-body interactions, which allows experiments [56] to estimate the energy of the incoming neutrino by the energy and scattering angle of the outgoing charged lepton alone.

A theoretical treatment of QE interactions with free nucleon was developed by Llewelyn Smith [57] in 1972. Assuming unbound nucleons and neglecting higher order electromagnetic corrections, the differential cross section as a function of the squared four-momentum transfer to the nuclear system (Q^2) is [57]

$$\frac{d\sigma}{dQ^2} = \frac{G_F^2 M^2 |V_{ud}|^2}{8\pi E_\nu^2}\left[A \pm \frac{(s-u)}{M^2}B + \frac{(s-u)^2}{M^4}C\right] \tag{2.8}$$

where A, B, and C are

$$A = \frac{(m^2+Q^2)}{M^2}\Big[(1+\eta)F_A^2 - (1-\eta)F_1^2 + \eta(1-\eta)F_2^2 + 4\eta F_1 F_2 - \frac{m^2}{4M^2}\Big((F_1+F_2)^2 + (F_A+2F_P)^2 - \Big(\frac{Q^2}{M^2}+4\Big)F_P^2\Big)\Big], \tag{2.9}$$

$$B = \frac{Q^2}{M^2}F_A(F_1+F_2), \tag{2.10}$$

and

$$C = \frac{1}{4}(F_A^2 + F_1^2 + \eta F_2^2). \tag{2.11}$$

Here, M and m are the mass of the nuclear target and out-going lepton, respectively, G_F is the Fermi coupling constant, $(s-u) = 4ME_\nu - Q^2 - m^2$, V is the CKM matrix[‡], and $\eta = Q^2/4M^2$. The positive sign (+) is chosen for neutrinos and negative sign (-) is chosen for antineutrinos.

The various F functions, called form factors, are dependent on Q^2 and parameterize interactions with the many-body nuclear system in terms of a general tensor coupling. F_1 and F_2, known as the Dirac and Pauli form factors, can be measured with electron scattering experiments under the Conserved Vector Current (CVC) hypothesis [60, 4]. For NCQE scattering, the Dirac and Pauli vector form factors include additional terms from strange coupling. The pseudo-scalar form factor, F_P, appears multiplied by $m^2/M^2 \approx 1.2 \times 10^{-2}$ (3×10^{-7}) for ν_μ (ν_e) CCQE interactions and is typically ignored [4]. The remaining axial form factor, F_A, is assumed to be of dipole form

$$F_A(Q^2) = \frac{g_A}{\left(1+\frac{Q^2}{M_A^2}\right)^2} \tag{2.12}$$

[‡]Analogous to the PMNS matrix for leptons, the Cabibbo-Kobayashi-Maskawa (CKM) matrix describes the rotation between mass and weak-interacting quark eigenstates [58, 59]

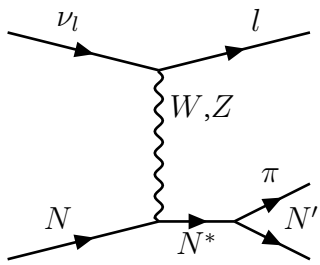

FIGURE 2.5. Feynman diagram of resonant single-pion production.

The empirical parameter g_A has been measured with precision, $g_A = 1.2694 \pm 0.0028$ [61]. The parameter M_A is likened to the mass of the QCD axial current [62] and has been measured by global fit to neutrino deuterium scattering experiments to be $M_A = (1.014 \pm 0.014)\,\mathrm{GeV}$ [63].

2.3.1.2. *Resonant Pion Production.* Resonant interactions occur when the neutrino imparts enough energy into the target nucleon to excite it to a higher energy state, which then decays to produce a charged ($\pi^{\pm}$) or neutral (π^0) pion (Figure 2.5). The possible CC reaction channels are [4]:

$$\nu_l + p \to l^- + p + \pi^+ \qquad \bar{\nu}_l + p \to l^+ + p + \pi^-$$

$$\nu_l + n \to l^- + p + \pi^0 \qquad \bar{\nu}_l + p \to l^+ + n + \pi^0$$

$$\nu_l + n \to l^- + n + \pi^+ \qquad \bar{\nu}_l + n \to l^+ + n + \pi^-,$$

and NC:

$$\nu_l + p \to \nu_l + p + \pi^0 \qquad \bar{\nu}_l + p \to \bar{\nu}_l + p + \pi^0$$

$$\nu_l + p \to \nu_l + n + \pi^+ \qquad \bar{\nu}_l + p \to \bar{\nu}_l + n + \pi^+$$

$$\nu_l + n \to \nu_l + n + \pi^0 \qquad \bar{\nu}_l + n \to \bar{\nu}_l + n + \pi^0$$

$$\nu_l + n \to \nu_l + p + \pi^- \qquad \bar{\nu}_l + n \to \bar{\nu}_l + p + \pi^-.$$

Predictions of the interaction cross sections and final state kinematics are owed to the Rein-Sehgal [64] and the Berger-Sehgal [65] models, the latter including contributions from lepton masses.

It is also possible for the neutrino to scatter coherently off of the nucleus wherein it transfers a negligible amount of energy ($Q^2 \approx 0$) to the nucleon leaving it unchanged and producing a single $\pi^{\pm}$ (CC) or π^0 (NC). The probability of Coherent Pion Production (COH) is comparatively small but non-negligible for oscillation searches [4]. Theoretical models predicting the cross section of this reaction have been developed again by Berger and Sehgal [66], which invokes the Partially Conserved Axial Current (PCAC) [67] hypothesis to relate it to pion-nucleon reactions.

2.3.1.3. *Deep-Inelastic Scattering.* Finally, DIS interactions occur at high energies where the neutrino interacts directly with the constituent quarks, which breaks apart the nucleus and produces a shower of hadronic activity. These interactions are particularly sensitive to the initial momentum of the nuclear target since that momentum is carried by the constituent quarks. Models of DIS interactions encode quark momentum in so-called parton functions, and differ the in QCD, nuclear, electromagnetic, and lepton mass effects they include. One such model commonly used by oscillation experiments was developed by A. Bodek and U. K. Yang [68]. It includes parameters whose values come from fits to DIS e^-/μ^- scattering data on hydrogen and deuterium. The Bodek-Yang model show good agreement to nuclear form factor measurements as a function of Q^2 from $1\,\mathrm{GeV}^2$ to $100\,\mathrm{GeV}^2$.

These processes, QE, RES, and DIS are separately predicted by models that describe the internal structure of the nucleus with varying degrees of granularity, which makes them incompatible with each other. Any attempt to unify these models must rely on experimental measurements in the regions where the models overlap, emphasizing the importance of inclusive measurements. One approach used by the GENIE generator to unify these models is described in Section 4.2.

2.3.1.4. *Nuclear Effects.* Many of the earlier models produced over the last 70 years assume neutrinos interact with individual free nucleons and are constrained to data that closely matches

that assumption, namely hydrogen and deuterium scattering data. Today's oscillation experiments utilize detectors constructed from heavy elements like Carbon, Argon, and Oxygen, which increase interaction probability and reduce statistical uncertainties at the cost of introducing effects from correlated nucleon.

A simple approach to scale these free nucleon models to heavy elements is to approximate the target nucleon as "quasi-free" by method of impulse-approximation [69] and treat the nuclear system as an ideal Fermi gas of non-interacting fermions [70]. In this model, referred to in literature as the Relativistic Fermi Gas (RFG) model, the nucleons exist in a well of potential energy occupying the lowest energy levels based on Pauli exclusion principle. This Pauli blocking suppresses interactions for incoming neutrino energies below the energy required to excite a nucleon within the well above the highest occupied energy level, or Fermi energy.

Corrections to this model have since been introduced that include correlated nucleon momenta distributions (spectral functions) [71], long-range correlations (Random Phase Approximation (RPA)) [72], and second-order correlations where the neutrino scatters off of a pair of strongly correlated nucleons (Meson-Exchange Current (MEC)) [73], and are commonly employed by today's neutrino interaction generators.

An additional complexity that is not accounted for by "quasi-free" nucleon models is that of interactions between final state particles, particularly pions, and the nuclear target as they travel through the nuclear medium, so-called Final State Interactions (FSI). FSI can lead to significant changes in outgoing kinematics of protons from CCQE interactions as well as pions from RES interactions [74]. The GENIE and NEUT neutrino event generators implement FSI as a cascade of hadron-nucleon (hN) interactions based on nuclear density and measured hN cross sections

[75, 76]. The GENIE hN model, which accounts for intranuclear pion production, agrees well with inclusive cross section measurements on ^{12}C and ^{56}Fe [74].

2.4. Importance of Electron Antineutrino Cross-section Measurements

The primary contribution of this thesis is a measurement of the double-differential electron antineutrino charged-current inclusive cross section in the NOvA Near Detector (ND). It is the first measurement of its kind thanks to the world's most intense accelerator-based neutrino beam, NuMI. The measurement provides an important constraint on neutrino generators used for oscillation measurements, which rely on lepton universality to derive models of $\bar{\nu}_e$-CC (ν_e-CC) interactions from $\bar{\nu}_\mu$-CC (ν_μ-CC) [77]. A measurement in the CCQE region is also important for constraining backgrounds in solar neutrino searches [78], which search for single electron final states.

2.4.1. Relevant Measurements.

Relatively few measurements of the electron antineutrino cross section have been made to date, largely due to low statistics and difficulty in removing photonic and ν_e-CC backgrounds [4]. The first measurement of the $\bar{\nu}_e$-CC inclusive cross section [79] in the $1\,\mathrm{GeV}$ to $10\,\mathrm{GeV}$ range made by the Gargamelle collaboration confirmed theoretical predictions of linear scaling of the cross section as a function of neutrino energy and a ratio to the ν_e-CC cross section of about 1/3 with only 61 measured interactions. Since then, as accelerator-based neutrino sources have increased in intensity, experiments have collected larger samples of electron antineutrino interactions enabling single-differential measurements of the $\bar{\nu}_e$-CC and ν_e-CC +$\bar{\nu}_e$-CC cross sections.

In 2016, the MINERvA collaboration [80] published single-differential measurements of the combined electron neutrino and antineutrino QE-like (0π) cross section in electron energy, angle, and momentum transfer. Using a tracking calorimeter composed of 95% CH, an exposure from

the NuMI beam of 3.49×10^{20} Protons on Target (POT)[§], and $\langle E_\nu \rangle = 3.6\,\mathrm{GeV}$, 2105 ν_e CCQE-like candidates were selected with an estimated 52% purity. The extracted cross sections agree well with GENIE models.

In 2021, the MicroBooNE collaboration [82] measured electron neutrino and antineutrino single-differential cross sections with respect to lepton energy and scattering angle on Argon. This measurement marks the first such measurement on Argon using Liquid-Argon Time Projection Chamber (LArTPC) detector technology. The analysis is carried out on a sample of data from NuMI, an exposure of 2.0×10^{20} POT, and average ν_e ($\bar{\nu}_e$) energy of $768\,\mathrm{MeV}$ ($961\,\mathrm{MeV}$). In total, 243 data events were recorded with estimated $\nu_e + \bar{\nu}_e$ selection efficiency and purity of 21% and 72%, respectively. MicroBooNE report single differential measurements in electron energy over a range of $0.12\,\mathrm{GeV}$ to $6\,\mathrm{GeV}$ that agrees well with predicted cross sections from the GENIE, NuWro [83], and GiBUU [84] generators.

In 2020, the T2K collaboration [85] reported the first $\bar{\nu}_e$-CC inclusive cross section since Gargamelle. Data from 11.92×10^{20} POT (6.29×10^{20} POT) of J-PARC's FHC (RHC) exposure were analyzed to select ν_e and $\bar{\nu}_e$ candidates with roughly 30-40% efficiency. Signal ν_e and $\bar{\nu}_e$ events were estimated using a likelihood-based template fitting approach that simultaneously fits signal and background models to multiple orthogonal samples. They extract single-differential cross sections in lepton momentum and scattering angle. They verify their results agree with NEUT, GENIE, and NuWro predictions.

Most recently, the first double-differential electron neutrino CC inclusive cross section was [5] measured with the NOvA ND, where $\langle E_\nu \rangle = 2.4\,\mathrm{GeV}$. The total uncertainty averaged over the reported bins is 18.2%. The measurement is systematically limited driven by hadron production

[§]POT is a measure of integrated power often used by accelerator-based neutrino sources and is a proxy for neutrino luminosity [81].

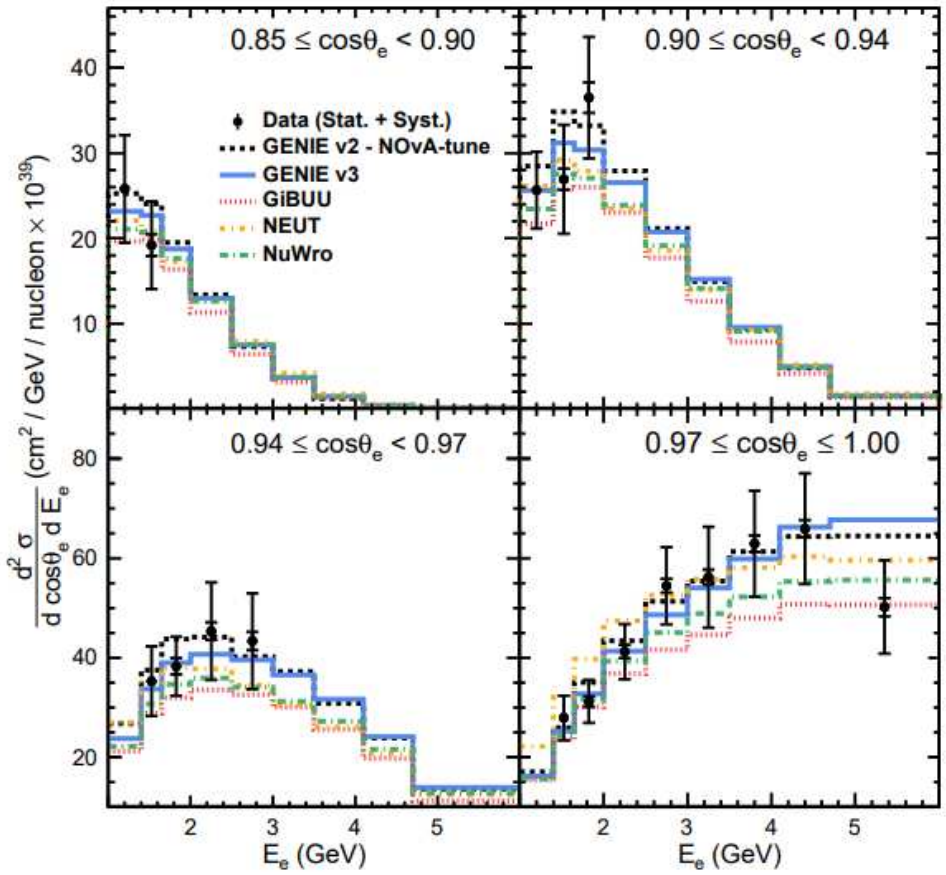

FIGURE 2.6. Double-differential ν_e-CC inclusive cross section measured with the NOvA experiment [5] and compared to neutrino generator predictions.

(10.3%) and neutrino-nucleus interaction (9.8%) model uncertainties. Candidate ν_e-CC interactions are selected with 35% efficiency. The sample, estimated to contain $9{,}200 \pm 1{,}000$ signal candidates, is 13.0 ± 1.3% pure with contributing interaction modes from QE (28%), MEC (20%), RES (31%), DIS (20%), and COH (1%). Overall, the measurement agrees well with a variety of interaction models, but tension is observed in the low Q^2 region with the NEUT generator.

CHAPTER 3

The NOvA Experiment

The NOvA experiment [9] is a long-baseline neutrino oscillation experiment built to determine the unknown parameter δ_{CP} and neutrino mass ordering. Since 2012, NOvA has been used to set competitive limits on parameters $|\Delta m^2_{32}|$, δ_{CP}, and $\sin^2\theta_{23}$, as well as mass ordering determination [86]. Additionally, the NOvA near detector enables high statistics measurements neutrino cross sections on hydrocarbon (CH_4), which is the topic of this thesis.

This chapter provides a description of the NuMI beam complex and NOvA detector technologies. Briefly, the NOvA experiment leverages the high intensity of the NuMI beam and a two-detector design to achieve its oscillation goals. Neutrinos are produced by the NuMI beam composed of mostly muon-type neutrinos. A Near Detector (ND) is used to sample the flavor composition of the beam before oscillations occur and enables extrapolation to the Far Detector (FD). The FD is positioned $810\,\mathrm{km}$ from the ND to maximize matter effects and hence sensitivity to mass ordering. The sizes of the near and far detectors are roughly $200\,\mathrm{ton}$ and $14\,\mathrm{kT}$, respectively. The detectors are identical in composition and functionality, which reduces systematic uncertainties that arise from the extrapolation. By comparing initial (ND) and final (FD) flavor composition, the NOvA collaboration is able to constrain oscillation parameters.

3.1. The NuMI Beam

The Fermilab accelerator complex produces the NuMI beam, the world's most intense source of muon neutrinos. Figure 3.1 shows the components of the complex responsible for producing NuMI. Protons are accelerated to $8\,\mathrm{GeV}$ by a linear ion-accelerator (Linac) and a charge-stripping Booster [8]. These protons are delivered in twelve batches at a rate of $15\,\mathrm{Hz}$ and held in the

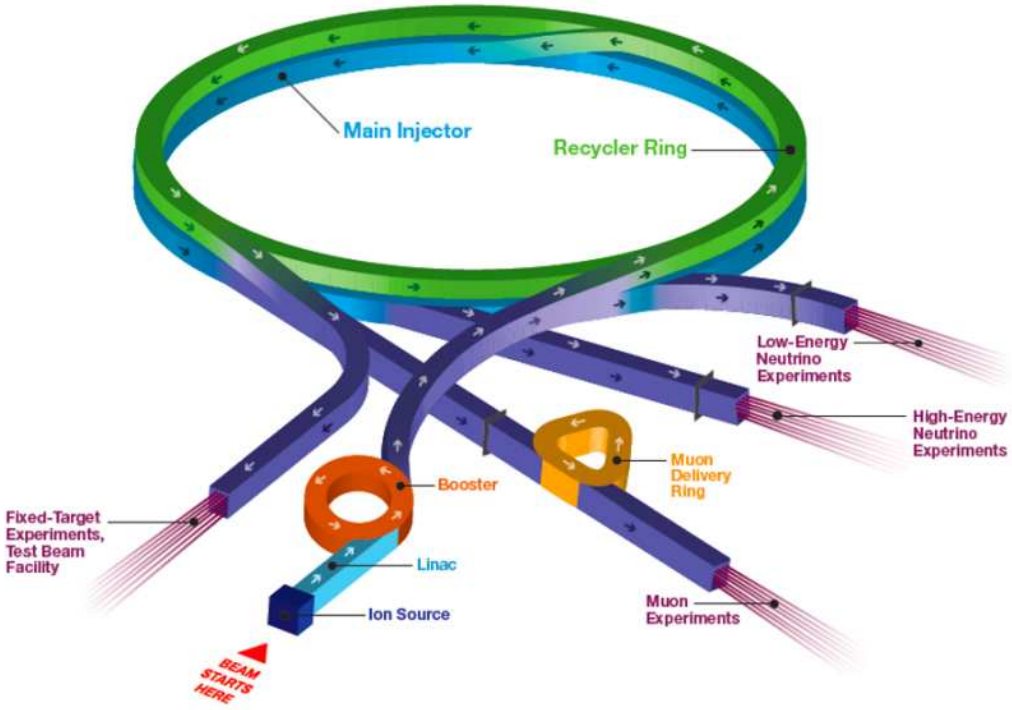

FIGURE 3.1. Diagram of the Fermilab accelerator complex [6].

Recycler Ring to perform "slip-stacking" [87, 88], which double-stacks batches resulting in six batches of twice the original intensity. The six batches are sent to the Main Injector (MI) [89] and accelerated to $120\,\mathrm{GeV}$. This process is repeated every $1.3\,\mathrm{s}$, from which they are extracted and directed through the NuMI beamline components (Figure 3.3). The result is a structured "spill" of protons to the NuMI target every $1.3\,\mathrm{s}$, where each spill contains six batches, enabling out-of-time detector calibration and no-beam physics studies with NOvA.

At the time of writing, the peak power of the NuMI beam stands at over $900\,\mathrm{kW}$ [90], with plans to ramp up to $1\,\mathrm{MW}$ [6]. Figure 3.2 shows the daily and integrated exposure in POT since the NOvA FD was commissioned [7]. Since then, the NOvA experiment has collected roughly 13.6×10^{20} POT and 12×10^{20} POT worth of neutrino-mode and antineutrino-mode data, respectively.

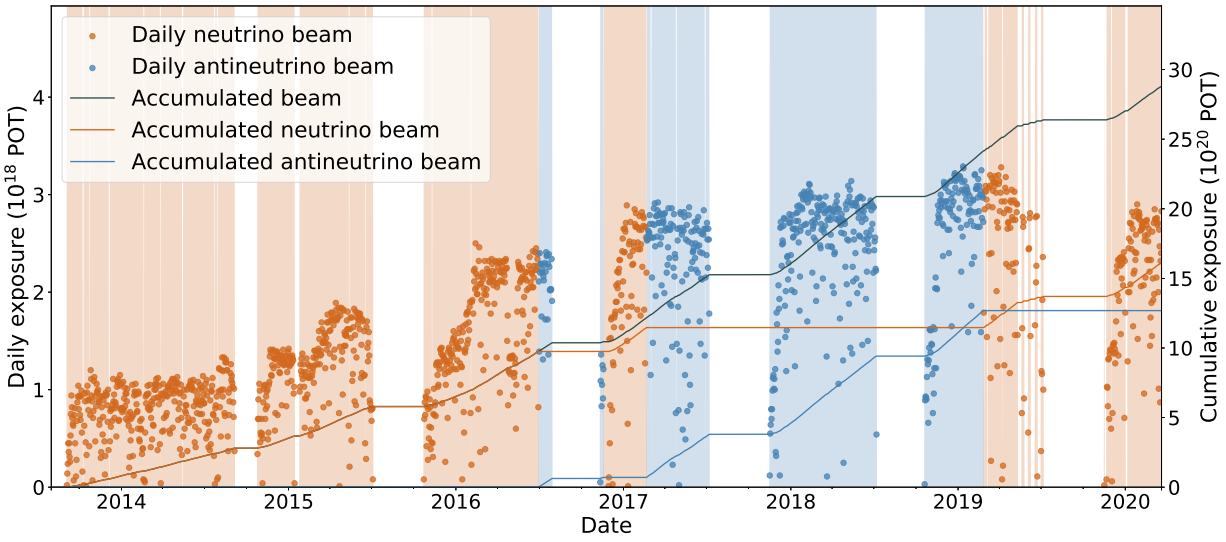

FIGURE 3.2. Daily exposure of the NuMI neutrino beam (orange) and antineutrino beam (blue) from the start of commissioning to March 2020. Lines indicate cumulative exposure for neutrino-mode (dark blue), antineutrino-mode (dark orange), and the total (dark gray) [7].

The target hall contains the NuMI target and magnetic horns to focus the outgoing charged mesons. The target is a carbon graphite structure surrounded with a stainless steel water coolant system designed to withstand the intense flux of high-energy protons while maximizing meson production yield. Collisions between the high-energy protons and target produce charged pions ($\pi^{\pm}$) and kaons ($K^{\pm}$). Modeling the production of these hadrons leads to a significant source of uncertainty for oscillation experiments (Section 5.4).

The charged mesons are focused by two electromagnetic horns to produce a collimated beam. Outgoing mesons from the $p - C$ collisions are focused to be approximately parallel to the azimuthal axis of the horn system. Horn 2 improves the efficiency of the focusing system by 50% by providing the mesons that were under- or over-focused an additional transverse momentum "kick", while having minimal effect on those that were well focused by Horn 1 [8]. Additionally, the current through the horns can be controlled to sign-select the desired mesons and produce

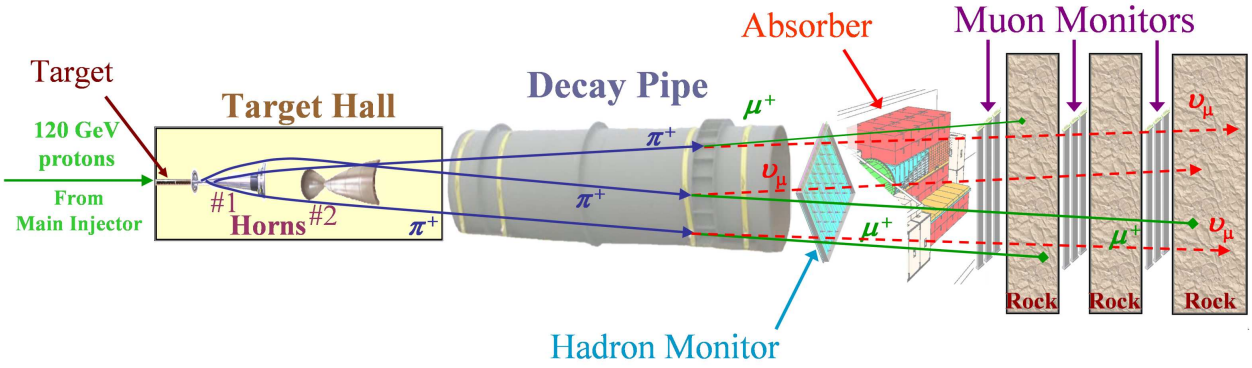

FIGURE 3.3. The NuMI beamline [8].

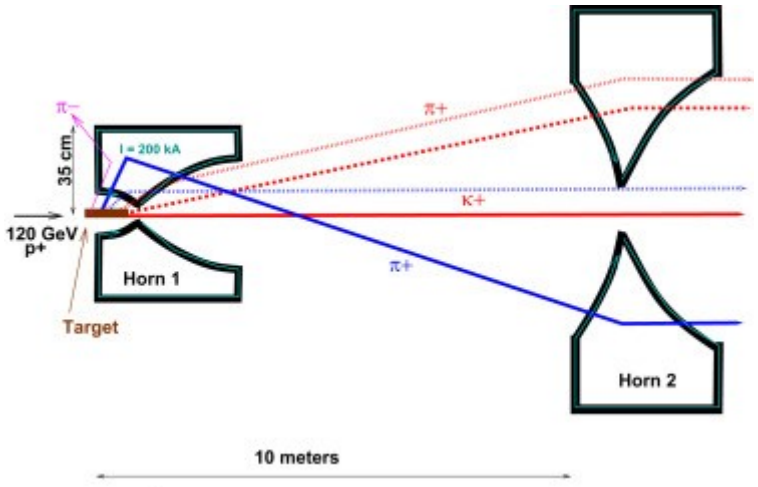

FIGURE 3.4. Schematic of the NuMI magnetic focusing horn system [8].

a beam enriched with neutrinos or antineutrinos. The neutrino-mode is referred to as Forward Horn Current (FHC) and the antineutrino mode is referred to as Reverse Horn Current (RHC) in reference to the direction of the electrical current that drives the horns' magnetic field.

The resulting mesons decay to produce a mostly pure (99%) beam of ν_μ ($\bar{\nu}_\mu$) [80]. The primary decay modes and relative decay rates [54], or Branching Ratios (BRs) are

$$\begin{aligned} \pi^+ &\to \mu^+\nu_\mu \quad (\mathrm{BR} = 99.9\%) & \pi^- &\to \mu^-\bar{\nu}_\mu \quad (\mathrm{BR} = 99.9\%) \\ K^+ &\to \mu^+\nu_\mu \quad (\mathrm{BR} = 63.6\%) & K^- &\to \mu^-\bar{\nu}_\mu \quad (\mathrm{BR} = 63.6\%). \end{aligned} \tag{3.1}$$

An intrinsic ν_e ($\bar{\nu}_e$) component (1%) comes from secondary muon decays and comparatively rare kaon decay modes [80]

$$\begin{aligned} \mu^- &\to e^- \bar{\nu}_e \nu_\mu \quad (\text{BR} \approx 100\%) & \mu^+ &\to e^+ \nu_e \bar{\nu}_\mu \quad (\text{BR} \approx 100\%) \\ K^+ &\to \pi^0 e^+ \nu_e \quad (\text{BR} = 5.1\%) & K^- &\to \pi^0 e^- \bar{\nu}_e \quad (\text{BR} = 5.1\%). \end{aligned} \tag{3.2}$$

The focused mesons are left to decay in flight through a $675\,\mathrm{m}$ helium-filled pipe. The length of the decay volume is based on the average time-of-flight of a $10\,\mathrm{GeV}$ pion.

Instrumentation downstream from the decay pipe is used to monitor beam quality and estimate outgoing neutrino flux. A hadron monitor is placed immediately downstream of the decay pipe and measures non-interacting protons from the MI to monitor the proton spot and target integrity. The hadron absorber, made of steel, aluminum, and concrete, acts as shielding for personnel areas downstream and prevents irradiation of groundwater. Finally, muon monitors are placed at $12\,\mathrm{m}$, $18\,\mathrm{m}$, and $210\,\mathrm{m}$ from the downstream end of the hadron absorber to measure the energy profile of the muons produced from pion-decay. Since muons and neutrinos are produced during the same decays, the muon flux can be used to infer characteristics of the neutrino flux.

3.2. Off-axis Design

The NOvA detectors are placed $14.6\,\mathrm{mrad}$ off of the axis of the NuMI beam to shape the energy distribution of the neutrino flux and reduce backgrounds. Outgoing neutrino energy is a function of parent pion energy (E_π) and off-axis angle (θ). It is given by [9]

$$E_\nu = \frac{0.43 E_\pi}{1 + \gamma^2 \theta^2} \tag{3.3}$$

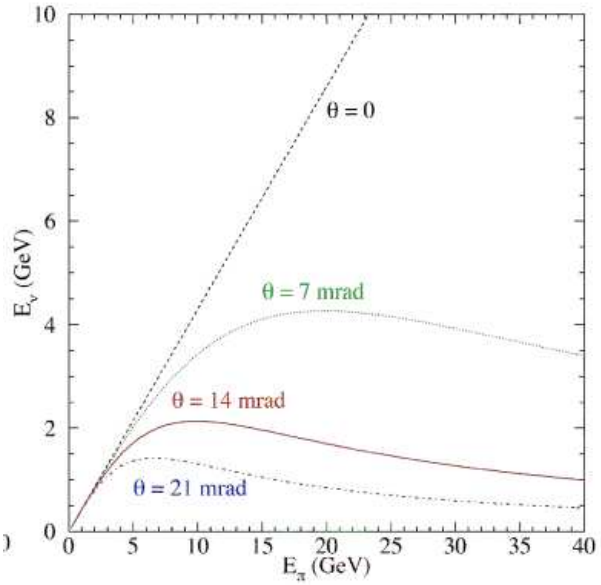

FIGURE 3.5. Neutrino energy as a function of parent-pion energy and off-axis angle [9]. The NOvA detectors are placed $14\,\mathrm{mrad}$ off-axis resulting in $\langle E_\nu \rangle = 2\,\mathrm{GeV}$.

where $\gamma = E_\pi / m_\pi$. Figure 3.5 shows the energy of the daughter neutrinos as a function of pion energy at various off-axis positions. At values $\theta \neq 0$, the neutrino energy reaches a maximum before slowly decaying as a function of E_π, leading to a sharp peak in the neutrino flux (Figure 3.6). Although this results in a decrease in neutrino intensity, the narrowband beam reduces measurement uncertainties due to neutrino energy resolution. Given the maximum achievable baseline of the NOvA experiment ($L = 810\,\mathrm{km}$), the off-axis angle of the detectors is chosen to be $\theta = 14\,\mathrm{mrad}$ to yield an average neutrino energy of $\langle E_\nu \rangle = 2\,\mathrm{GeV}$ and thereby maximizing ν_e appearance probability assuming $\Delta m^2_{32} = 2.4 \times 10^{-3}\,\mathrm{eV}^2$.

Off-axis positioning also increases the rejection of one of the most significant backgrounds to oscillation searches: NC interactions, particularly those producing π^0 (NCπ^0). Since the outgoing neutrino is not observed in the detector, NCπ^0 interactions can mimic the ν_e oscillation signal based on the visible energy deposited by the outgoing hadronic system ($\pi^0 \to 2\gamma$). Since most of

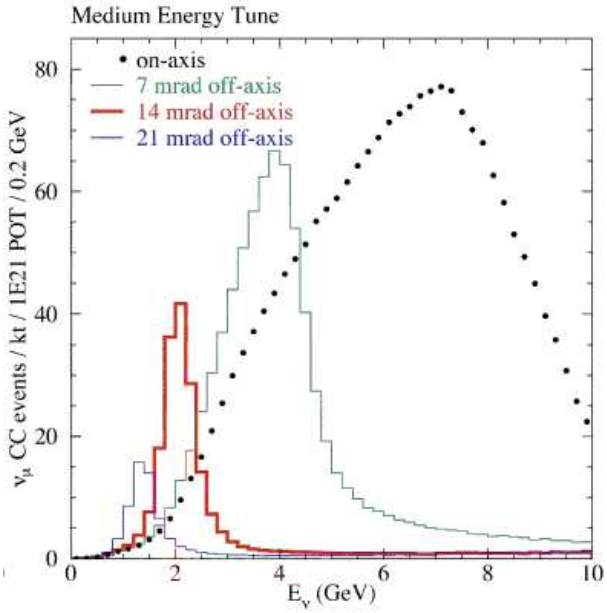

FIGURE 3.6. Energy distribution of pion-decay neutrinos at various off-axis positions (area normalized) [9]. The NOvA detectors are placed $14\,\mathrm{mrad}$ off-axis resulting in $\langle E_\nu \rangle = 2\,\mathrm{GeV}$.

the energy is carried away by the neutrino, the visible energy of NCπ^0 events tends to be lower than visible energy deposited by ν_e CC interactions as shown in Figure 3.7. Shaping a narrowband neutrino energy distribution by off-axis angle pushes background NC events further outside the signal region than a wideband on-axis beam.

3.3. NEUTRINO FLUX AT THE NOvA ND

The overall flux impinging upon the NOvA ND broken down by neutrino flavor is shown in Figure 3.8. As mentioned in Section 3.2, the off-axis positioning of the ND produces a strongly-peaked distribution of neutrino energy around $2\,\mathrm{GeV}$. Heavier charged ($K^\pm$) and neutral ($K^0_{L,S}$) kaons are responsible for the higher energy tail as shown in Figure 3.9.

Although they make up a very small contribution to the total neutrino flux, NuMI provides enough intrinsic $\bar{\nu}_e$ for high-statistics measurements of the $\bar{\nu}_e$ CC cross section, which is the topic of this thesis. The direct lineage of the antineutrinos produced by NuMI in RHC configuration is

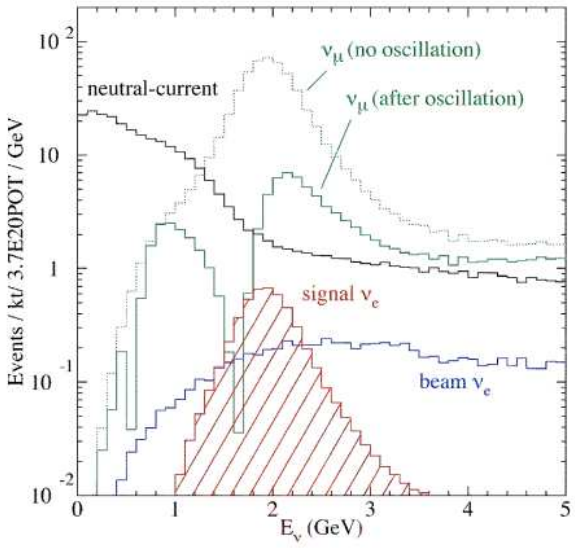

FIGURE 3.7. The affect of off-axis positioning on background NC interactions [9]. Although NCπ^0 interactions can mimic the topological signal of ν_e CC interactions, the visible energy deposited by these interactions is significantly lower.

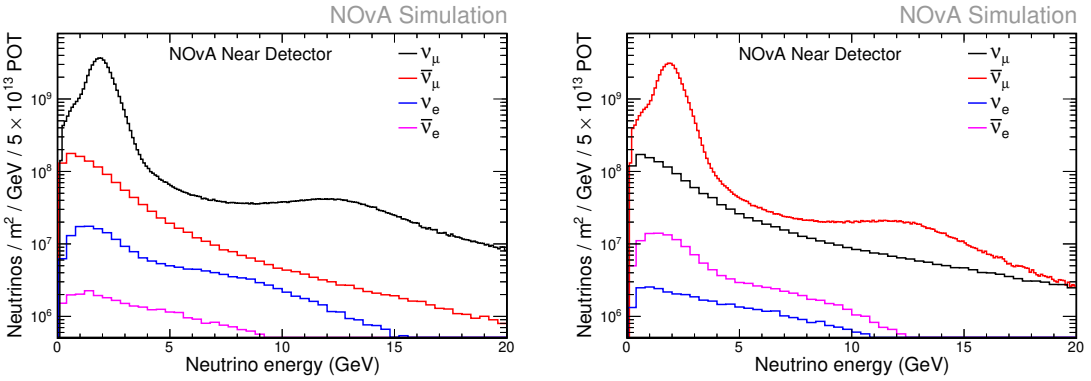

(A) Forward Horn Current (B) Reverse Horn Current

FIGURE 3.8. Neutrino flux from NuMI at the NOvA ND broken down by neutrino flavor for forward (A) and reverse (B) NuMI horn configurations [10].

shown in Figure 3.9b. These antineutrinos originate mostly from the decay of primary μ^- from $\pi^- \to \mu^- \bar{\nu}_\mu$ and are likewise peaked at 2 GeV. The next leading contribution is from the decay of K^-, whose leading electronic decay mode is $K^- \to \pi^0 e^- \bar{\nu}_e$ with BR $= (5.07 \pm 0.04)\,\%$. Finally, there is a contribution from the unfocused neutral kaons: $K_L \to \pi^- e^+ \bar{\nu}_e$ (BR$= (40.55 \pm 0.11)\,\%$) and $K_S \to \pi^- e^+ \bar{\nu}_e$ (BR$= (7.04 \pm 0.08) \times 10^{-2}\,\%$) [61]. The average energy of $\bar{\nu}_e$ from kaon

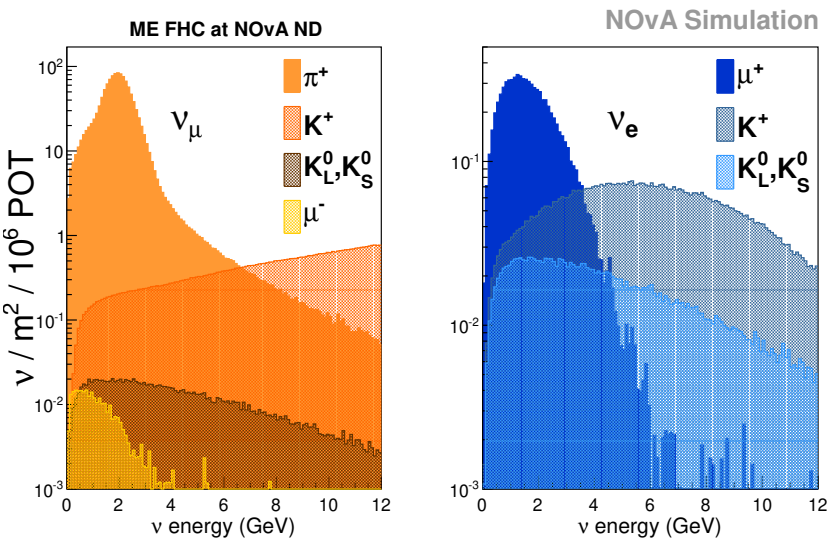

(A) Forward Horn Current

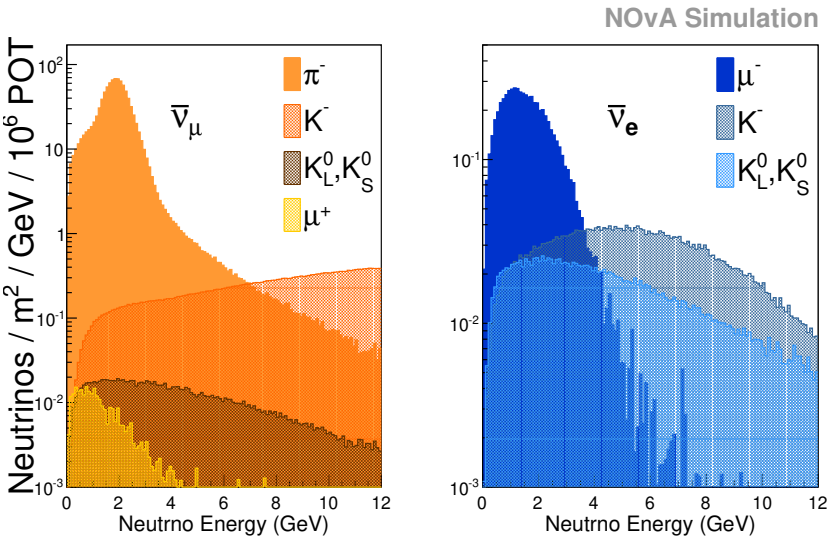

(B) Reverse Horn Current

FIGURE 3.9. Direct lineage of the neutrinos incident on the NOvA ND from collisions between MI protons and the NuMI target for NuMI forward (A) and reverse (B) horn configurations [10].

decays higher than those from μ^- (and hence π^-) driven by the comparatively large mass of the kaons ($M_{K^\pm} \approx 493\,\mathrm{MeV}$ and $M_{K^0} \approx 497\,\mathrm{MeV}$).

3.4. The NOvA Detectors

NOvA consists of two detectors: one Near Detector (ND) placed $1\,\mathrm{km}$ from the NuMI target, and one Far Detector (FD) placed $810\,\mathrm{km}$ from the beam source. The detectors have calorimetric and tracking capabilities that enable the identification of particles and estimation of particle kinematics. The detectors are functionally identical in that the most basic unit (cell) that composes both detectors is identically constructed and signals from both detectors are processed in the same way, which reduces overall systematic uncertainties on oscillation measurements by leveraging correlated sources of error. The detector granularity and composition are optimized for identification of muon tracks and electromagnetic showers. The result is a Molière radius* of 3 cells and radiation length of 6 planes [91], providing distinction from minimum-ionizing muon tracks. Photographs of the detectors are shown in Figures 3.10 and 3.11. Following [9], the discussion in this section will focus on the ND as it is the only detector used for the analysis presented in this thesis.

The most basic unit of the NOvA ND is a cell (Figure 3.12). Cells are rectangular PVC extrusions filled with liquid scintillator and wavelength-shifting fiber. The cell walls are $2\,\mathrm{mm}$ to $4.5\,\mathrm{mm}$ thick with an interior width of $3.8\,\mathrm{cm}$ and depth of $5.9\,\mathrm{cm}$. Cells are produced in 16-cell extrusion where cells are stacked side-by-side on the wide ($5.9\,\mathrm{cm}$) face.

Cell extrusions modules are glued together to form planes, and planes are layered in alternating horizontal and vertical orientations spanning the beam axis of the detector (Figure 3.13). In the ND, horizontal and vertical planes are composed of 96 and 64 cells, respectively. One-hundred and eighty (180) planes make up the primary volume of the detector. Ten (10) additional planes on the downstream end of the detector are interlaced with steel plates to provide additional stopping

*The Molière radius is defined as the radius of the cylinder with z-axis centered along the forward momentum of an electromagnetic shower such that 90% of energy deposition is contained within the cylinder.

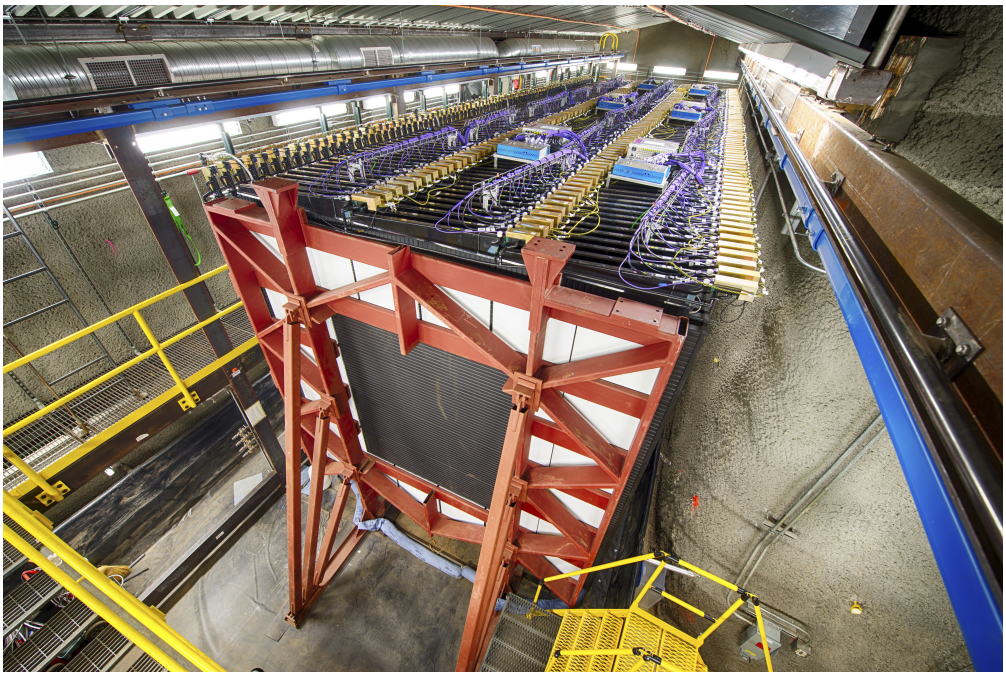

FIGURE 3.10. Photograph of the ND at Fermilab. The detector dimensions are $4.2\,\mathrm{m} \times 4.2\,\mathrm{m} \times 15.8\,\mathrm{m}$. The camera is pointed toward the beam direction.

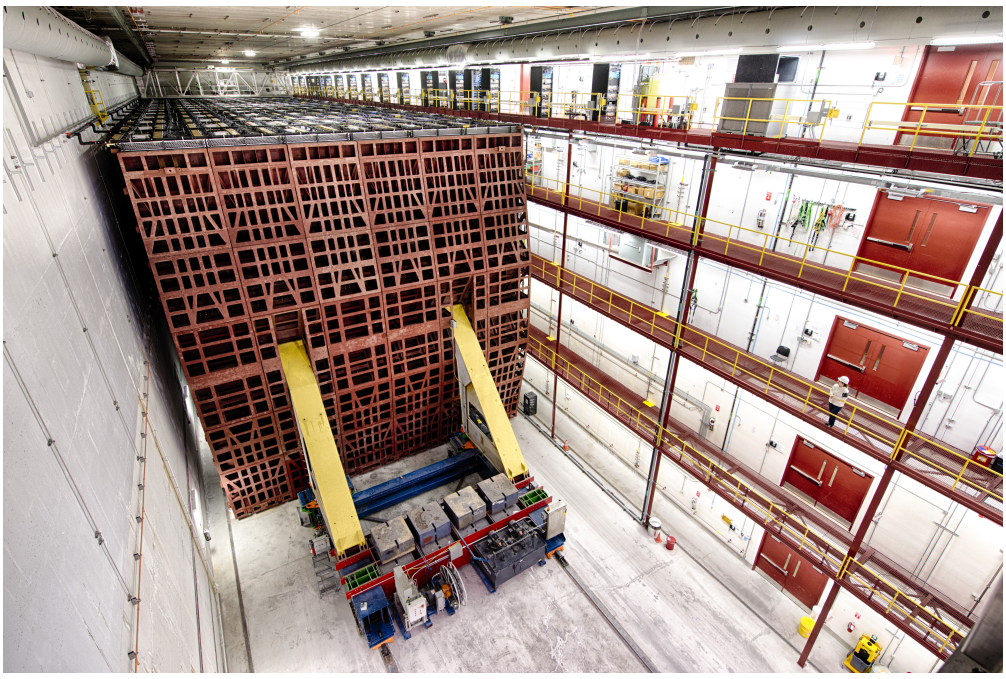

FIGURE 3.11. Photograph of the FD in Ash River, Minnesota. The detector dimensions are $15.6\,\mathrm{m} \times 15.6\,\mathrm{m} \times 63.0\,\mathrm{m}$. The camera is pointed toward the beam direction.

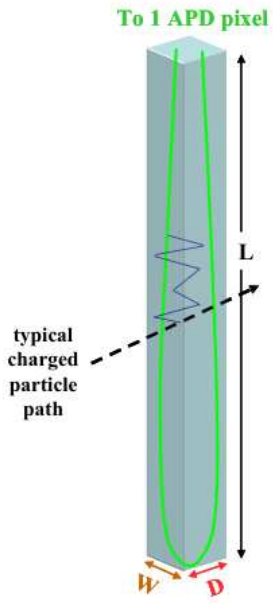

FIGURE 3.12. A cell of the NOvA detectors. Cells are filled with liquid scintillator that emits light when charged particles propagate through. The scintillation light is carried to Avalanche Photo Diodes (APDs) by wavelength-shifting fiber, which is looped to maximize collection efficiency [9].

power for high energy muons. This "muon catcher" is composed of recycled steel from the NOvA prototype detector, Near Detector On the Surface (NDOS) [92], and is shorter than ND modules. The muon catcher is not used for the analysis described in this thesis due to an electron's inability to penetrate the steel plates.

As charged particles pass through the cell wall, the scintillator produces light that is collected by the fiber. The scintillator makes up roughly 70% of the mass of the detector. It is mineral oil doped with 1,2,4-Trimethybenzene, 2,5-diphenyloxazole, and 1,4-di(methylstyryl)benzene, which produces light peaked at $400\,\mathrm{nm}$ to $450\,\mathrm{nm}$ to match the absorption spectrum of the fiber.

The fiber is composed of polystyrene doped with R27 dye to shift the wavelength of the light within $490\,\mathrm{nm}$ to $550\,\mathrm{nm}$ to match the response of the APDs. It is looped to increase the collection efficiency of scintillation photons.

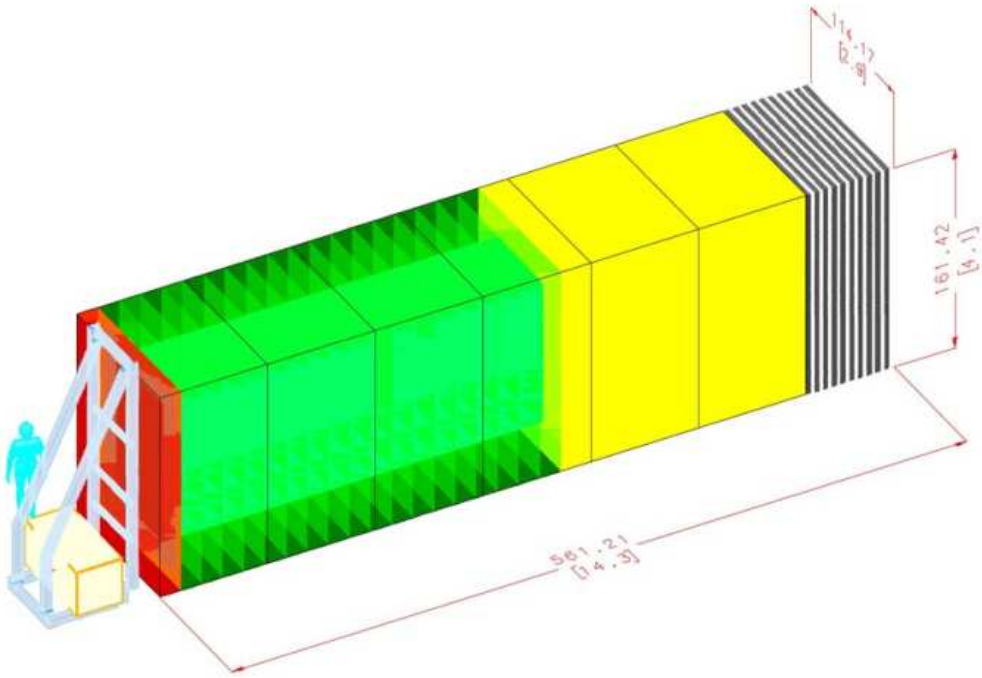

FIGURE 3.13. A schematic of the NOvA ND showing logical segmentation along the beam axis. Alternating planes span the length of the detector. Colors indicate veto (red), fiducial (green), shower containment (yellow), and muon catcher (black) regions of the detector [9]. The real muon catcher is two-thirds the height of the standard modules.

Photon signals from the fiber are converted to electrical signals using APDs. Each APD has a quantum efficiency of 85% for light within $520\,\mathrm{nm}$ to $550\,\mathrm{nm}$. The APDs are cooled below $-15\,^{\circ}\mathrm{C}$ to reduce thermal noise. Signals from the APDs are digitized by Analog-to-Digital Converters (ADCs). The digitized signal is processed by a Data Acquisition (DAQ) system, which aggregates the data and holds it in a 20-minute buffer for trigger processing. A software-based trigger system processes data in the buffer and records spills in which triggered data occur.

The proximity of the ND to the beam source results in a high rate of neutrino interactions. Within each $10\,\mu\mathrm{s}$ beam spill, an average of 1 to 6 neutrinos interact in the detector [93] and each interaction must be resolved. As such, the electronics continuously sample the APDs every

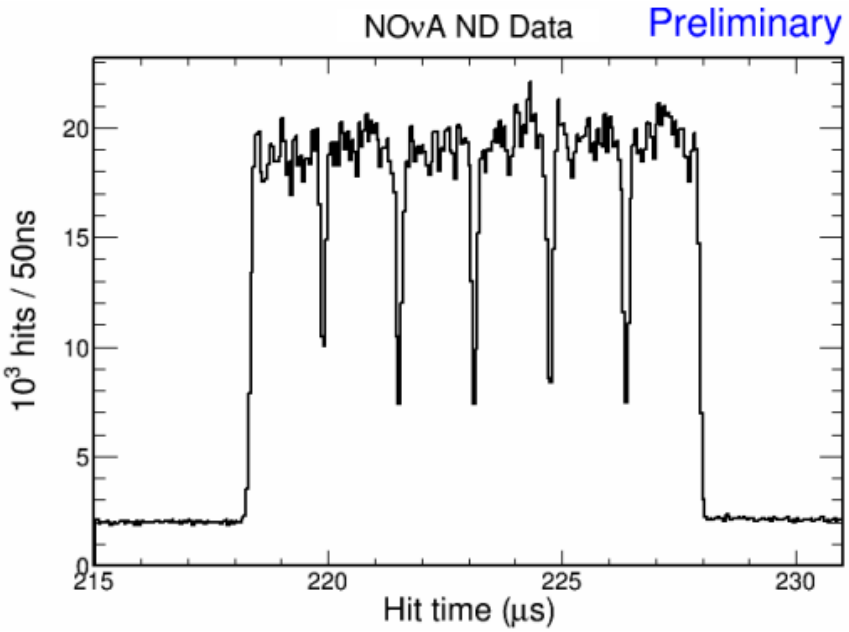

FIGURE 3.14. Time of hits relative to the start of the NuMI beam spill window illustrating ND timing resolution capabilities and NuMI beam structure.

125 ns. Figure 3.14 illustrates the timing resolution capabilities of the ND and the NuMI beam structure.

Three-dimensional tracking and calorimetry is made possible by the alternating planes and scintillator photon collection described above. Figure 3.15 shows an event display of a real neutrino interaction observed in the NOvA ND. Each pixel in the top (XZ) view represents a cell standing vertically, and each pixel in the bottom (YZ) view represents a cell lying horizontally. The muon catcher can be seen on the right side of each view. The cells are colored to indicate the time of photon detection relative to the beginning of the readout window. Charge deposition in each cell is measured and related to charged-particle energy deposition by a process called calibration.

3.4.1. DETECTOR CALIBRATION. As charged particles pass through the detector, scintillation photons are captured by wavelength-shifting fibers and directed toward APDs. The response of the scintillator, and thus the APD, is dependent on the energy that is deposited into the detector

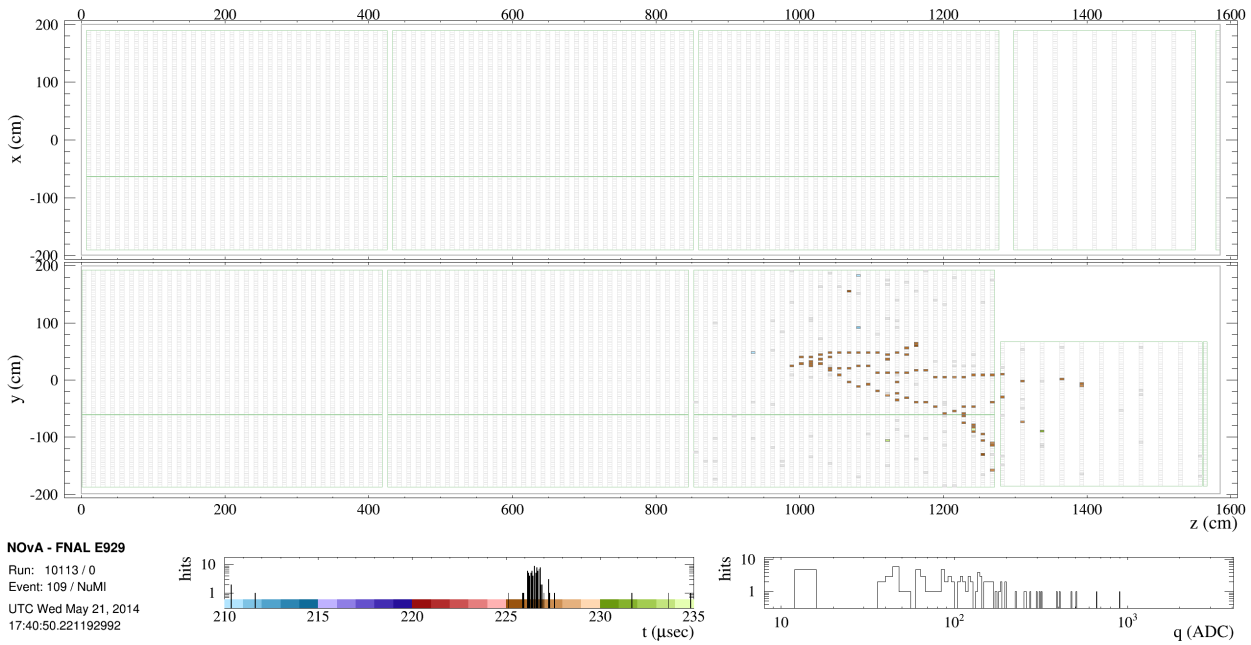

FIGURE 3.15. An event display of neutrino event occurring in the NOvA ND [11]. Color represents relative timing of detector hits.

by charged particles. This allows for the estimation of particle energy deposition based on APD response. The translation between detector response to deposited energy is called calibration.

In order to calibrate the detectors, a well-known source of energy deposition is required. The primary standard-candle used for calibration is energy deposition from cosmic-ray muons. According to the Bethe-Bloch equation†, cosmic-ray muons lose energy as they pass through the detectors primarily by ionization and at a rate that is slowly varying as a function of muon energy [61]. Since this occurs near the minimum of Bethe-Bloch equation, these muons are referred to as Minimum Ionizing Particles (MIPs).

Calibration is carried out in two steps. The first corrects for attenuation of light as it travels up the wavelength-shifting fiber and is dependent on the position of the incident particle interaction along the length of a cell. The second is an overall scaling that translates the corrected photoelectrons (PE) to energy (GeV).

†The Bethe-Bloch equation relates the average unit of energy deposited by a charged particle per unit length (dE/dx) traveled through a material to the speed of the particle.

Attenuation effects include both inefficiencies in the fiber's photon transport and APD response (or lack thereof) to the attenuated light [94]. Since attenuation depends on the length of fiber in which the photons travel, these effects are dependent on the position of the traversing particle along the length of the cell. Simulation is used to account for below threshold photons caused by fiber attenuation, and cosmic-muon data are used to estimate the average attenuation-corrected PE per unit length traversed through the scintillator.

Stopping cosmic muons are used to estimate the overall energy scale of the detector, translating attenuation-corrected PE to GeV. A track window technique is used [95], which measures the average detector response as a function of distance from the end of the muon track in a window between $100\,\mathrm{cm}$ to $200\,\mathrm{cm}$ (Figure 3.16). This window is chosen to minimize the impact to the average response due to uncertainty in the estimation of the muon stopping position. The mean detector response within the track window and the Bethe-Bloch prediction are used to apply a calibration scaling factor to attenuation-corrected PE measured uniformly throughout the detectors.

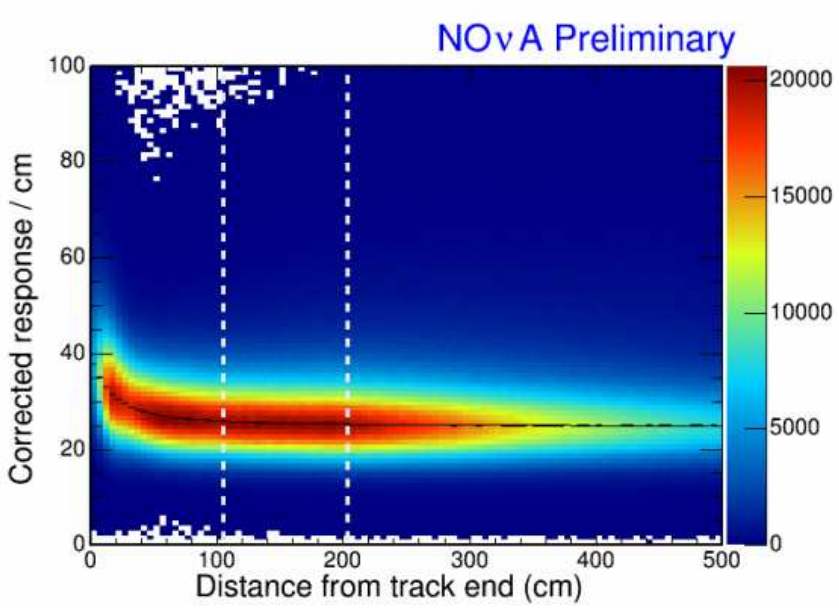

FIGURE 3.16. Average corrected detector response per unit length as a function of distance from the end of stopped muon tracks [12]

CHAPTER 4

NOvA Software and Simulation

In order to extract physics parameters from the raw signal in the NOvA detectors, all physical processes are first simulated to generate predictions. As in nature, simulation must include randomness when modeling quantum mechanical processes and processes too complex to describe exactly. This randomness is introduced by sampling pseudo-random numbers from probability distributions that describe the random physical processes. This class of algorithm is called Monte Carlo (MC) named after the famous gambling town of Monaco. As such, simulated "data" will be referred to as MC.

The NOvA experiment employs a number of software packages to carry out the MC simulation of physical phenomenon, as shown in Figure 4.1.

4.1. Simulation of the NuMI neutrino beam

The NuMI beamline is simulated in a self-contained software package called g4numi [96] based on the geant4 simulation toolkit [97]. g4numi simulates the propagation of particles

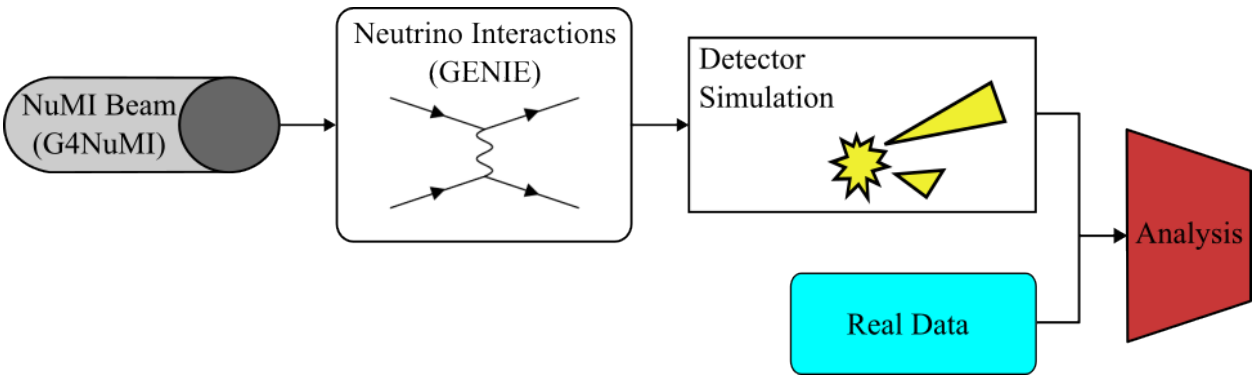

Figure 4.1. Flowchart of the NOvA simulation. The hadron production and transportation from the NuMI beam is simulated with g4numi. Neutrinos produced from g4numi interact with the detector material as simulated by the genie generator. Detector response is simulated with custom NOvA software and takes into account real detector running conditions, noise, and dead detector material.

through a detailed specification of the geometry and materials that primary protons and secondary particles encounter through the NuMI beamline using GEANT4.

The simulation of the NuMI neutrino flux is further tuned using hadron production data by a software package called Package to Predict the Flux (PPFX) [96]. Given neutrino kinematics and ancestry, PPFX calculates a weight for that interaction based on the difference between model predictions and measured data. PPFX corrects the predicted attenuation of the flux due to hadrons interacting with beamline materials and hadron production cross sections based on measurements [96]. The effect of these corrections on the NuMI flux components at the NOvA ND is shown in Figure 4.2. The overall impact of PPFX corrections is an increase in flux for all flavors of neutrino.

4.2. Simulation of Neutrino Interactions

Once neutrinos have been produced by G4NUMI, they are propagated through a detailed specification of the ND geometry and composition. The GENIE generator software [75, 98] (version 3.0.6) determines if the neutrinos interact, the type of interaction that occurs, and outgoing particles and their kinematics. It does this using a combination of models describing the inclusive interaction cross section, exclusive differential cross sections, initial nuclear state, and FSI.

CCQE interactions are modeled by the Valencia group [72]. This model improves upon the Llewellyn Smith formalism described in Section 2.3.1.1 by including long-range correlations (RPA) between bound nucleons and Coulombic interactions between the final-state charged leptons and the nuclear medium. The axial form factor is modeled as an expansion derived from QCD first principles rather than assuming a dipole form, and is fit to deuterium scattering data [99]. This model is extended to include $2p2h$ (2-particle, 2-hole) interactions in which a neutrino scatters off of a correlated nucleon pair [100]. Since these CCQE models interact on the nucleon level (as

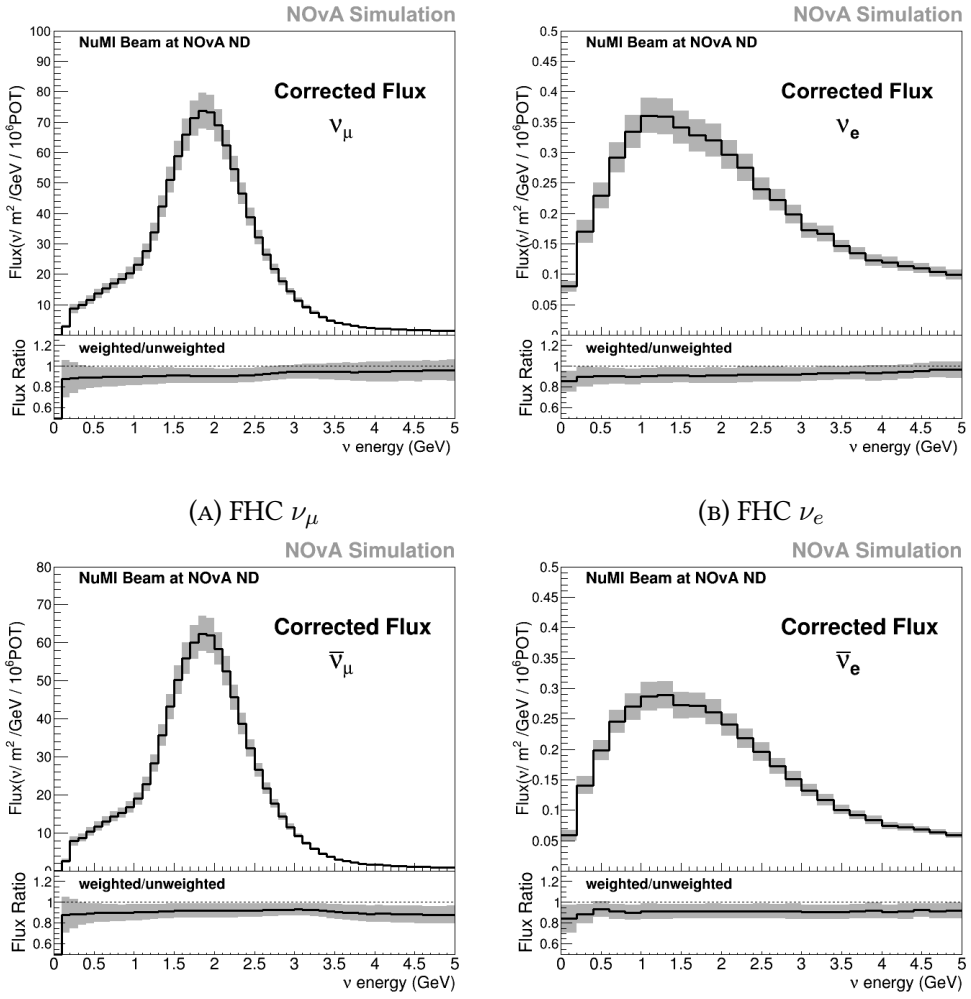

(A) FHC ν_μ (B) FHC ν_e

(C) RHC $\bar{\nu}_\mu$ (D) RHC $\bar{\nu}_e$

FIGURE 4.2. Corrected neutrino fluxes at the NOvA ND. Panels A and B show the ν_μ and ν_e flux in the FHC beam mode samples, respectively [13, 10]. Panels C and D show the $\bar{\nu}_\mu$ and $\bar{\nu}_e$ flux in the RHC beam mode samples, respectively. Error bands include data-constrained uncertainty on hadron production models. Flux ratio is the corrected flux divided by the uncorrected flux.

opposed to nucleus or quark), it is important to accurately describe the kinematics of the initial struck nucleon. The Velencia models do this by treating the nucleon statistics as a Local Fermi Gas (LFG), which modifies the nuclear density and hence the energy it takes to liberate nucleons from the nucleus. All other models in GENIE treat the initial nuclear state as a RFG.

NCQE interactions are implemented as an extension to the Llewellyn Smith formalism after reference [101]. An additional parameter is included in the axial form factor (2.12) given by

$$F_A(Q^2) = \frac{1}{2}\frac{g_A}{\left(1+\frac{Q^2}{M_A^2}\right)^2}(1+\eta) \tag{4.1}$$

to account for isoscalar contributions to the axial current [98]. In GENIE, $\eta = 0.12$.

As described in Sections 2.3.1.2 and 2.3.1.3, RES and COH pion production is modeled after Berger-Sehgal [65, 66]. It includes 16 possible baryon resonance states. The Berger-Sehgal model extends the Rein-Sehgal model [64] and includes effects from the mass of the outgoing lepton. Deep Inelastic Scattering is modeled after Bodek and Yang [68] with hadron production handled by PYTHIA [102] and tuned to data [103]. FSI is propagated through a nuclear-cascade model where pion cross sections are taken from data [104].

Each of the models described above is implemented in GENIE as independent and uncorrelated. To set the overall scale and energy dependence of the inclusive cross section,it is approximated as the sum of the dominant exclusive modes [75]

$$\sigma^{inc} = \sigma^{QE} \oplus \sigma^{RES} \oplus \sigma^{DIS}. \tag{4.2}$$

Care is taken in combining RES and DIS cross sections since RES interactions are an irreducible background to low pion-multiplicity DIS searches and vice versa. The transition region between RES and DIS is marked by a cut on invariant mass, W_{Cut}, which is tunable in the GENIE framework. Finally, the DIS contribution is adjusted to match data where the models overlap.

An additional source of background originates from neutrinos interacting with the rock that surrounds the ND, which produce muons that can penetrate through to the detector. These “rock

events" are accounted for by simulating the propagation of NuMI neutrinos through the larger volume of the detector hall, including the detector and surrounding rock. Interactions that originate outside the detector and deposit energy inside the detector are stored and used to overlay energy deposits within a beam spill of the standard simulation. These interactions are reused and overlaid at a rate corresponding to the simulated flux and rock event probability.

4.2.1. Model Tuning. The models implemented in GENIE contain a large set of parameters that are adjustable within the framework. The set of parameters, along with the specification of model set, is called a Comprehensive Model Configuration (CMC). The analysis presented in this thesis uses simulation derived from the CMC `N18_10j_00_000`*. The field `N18_10j` refers to the set of all models employed in the simulation. Rather than the CMC that is distributed with GENIE, `G18_10j`, the NOvA experiment has implemented a custom configuration, `N18_10j`, in which the dipole axial form factor involved in CCQE interactions is replaced with the Z-expansion described previously. Finally, `00_000` refers to the specific tune of the model set. The `00_000` marks the default tune of `N18_10j` where model parameters have been fit to inclusive neutrino scattering data [105, 106]

Additional corrections to the interaction model based on discrepancies observed between ND data and data from other experiments are applied [108]. A deficit of neutrino interactions in ND data compared to simulation is observed and attributed to the effect to the less-constrained Valencia MEC model. An empirical weight, modeled as a double-Gaussian as a function of $(|\vec{q}|, q_0)$, is fit to compensate for the discrepancy. A subsequent modification of hN-cascade FSI model

*After the simulation was produced, an inconsistency in the GENIE generator configuration was discovered. Two different CMCs were used: `N18_10j_02_11a` was used to set the integrated interaction rates and `N18_10j_00_000` was used to simulate the kinematics of the outgoing particles. A weight is applied to tune the existing simulation to a fully-consistent `N18_10j_00_000` configuration [107].

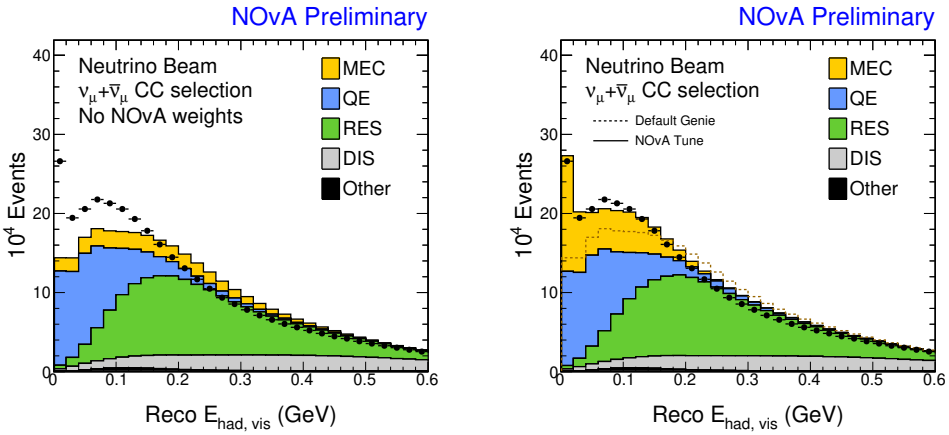

(A) Reconstructed visible hadronic energy before NOvA tune.

(B) Reconstructed visible hadronic energy after NOvA tune.

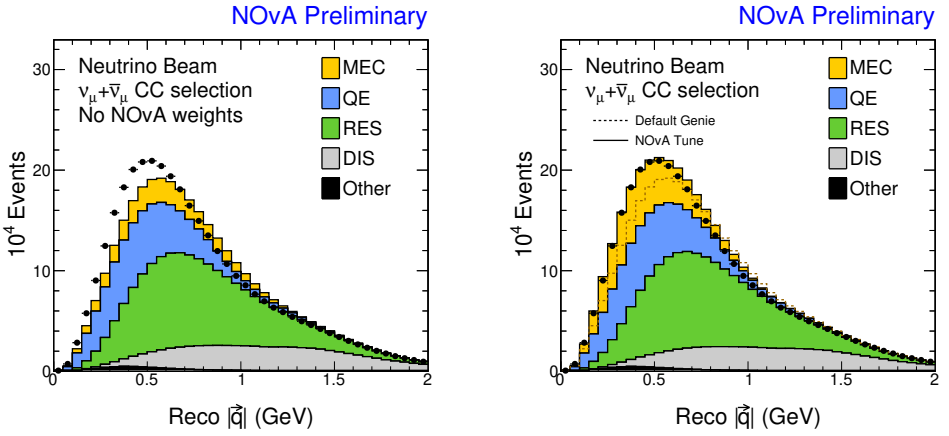

(C) Reconstructed 3-momentum transfer before NOvA tune.

(D) Reconstructed 3-momentum transfer after NOvA tune.

FIGURE 4.3. NOvA ND data compared to simulation before and after NOvA MEC and FSI tune [14].

improves agreement between external data and nominal GENIE predictions. Here, significant adjustments are made to pion re-interaction parameters, which improves agreement of the model with pion-scattering data, and weights are derived to reflect these changes in pion multiplicity and kinetic energy distributions [109]. Figure 4.3 shows the overall agreement of the interaction model with ND data before and after the application of both MEC and FSI weights.

4.3. Simulation of Particle Transport and Detector Response

Once GENIE has produced a set of outgoing particles that resulted from a neutrino interaction, the particles are transported through the material of the ND using GEANT4. GEANT4 accounts for the rescattering of all particles as they propagate through the detector beyond the initial neutrino interaction and produces scintillation photons.

A custom simulation [110] of the scintillation photon transport to electronic readout chain is employed to save computation time compared to a full GEANT4 propagation. Standard candles are used to constrain a transport model through a cell with parameters describing photon collection by the wavelength-shifting fibers, transport through the fiber, and response of the APD, including noise. Finally, all downstream electronic components that transform the APD signal into a digital signal are modeled independently.

4.4. Reconstruction of Neutrino Interactions

The ability to estimate the energy of interacting neutrinos rests entirely on the translation of raw charge to particle energies and trajectories. This process, called "reconstruction", involves inferring when and where a neutrino interaction occurs, what particles are produced by the interaction, and the energy and momentum of each particle. NOvA has implemented a chain of reconstruction algorithms that carry out subsequent steps arriving at particle-level clustering [16]. All reconstruction algorithms treat real detector activity and MC identically.

Given a readout window of $550\,\mu$s centered on the $10\,\mu$s beam spill, activity from neutrino interactions, rock muons, or cosmic ray muons, are formed into "slices". Slices are collections of hits that represent a physics interaction. They are formed using a time-density clustering algorithm that first approximates the center-point of each interaction, and then clusters nearby hits in space-time [15]. These clusters are formed in each view, then paired with a cluster in the

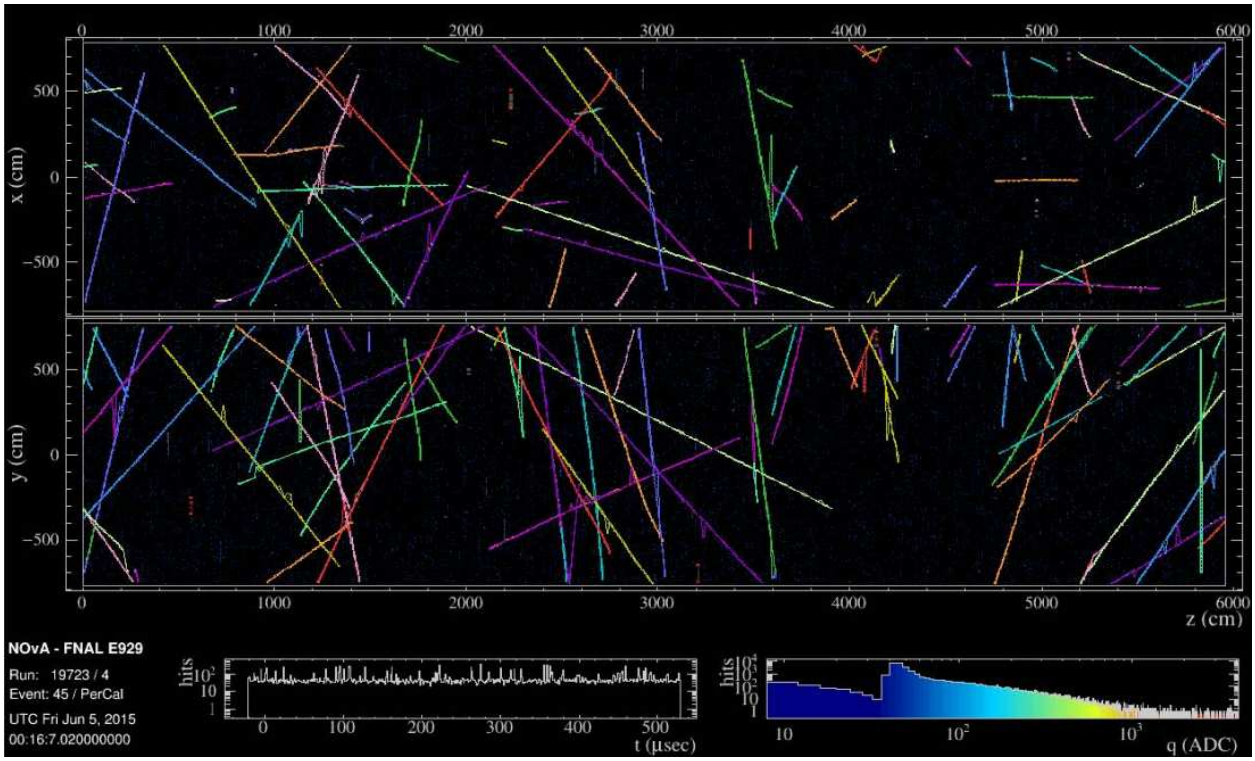

FIGURE 4.4. Slicing is performed on a $550\,\mu$s readout window of the NOvA FD. Colors represent different slices [15].

opposite view based on average $z-$ and $t-$coordinates of the clustered hits. Figure 4.4 shows the result of the slicing algorithm on a readout window of the FD, where hits belonging to slices are traced and represented by different colors. Multiple slices can be produced in each beam spill.

The performance of slicing is evaluated based on the algorithm's ability to cluster all of the energy deposited by a particular interaction into a single slice (completeness), and the (lack of) contamination energy from other interactions included in the clustering (purity). Good completeness and purity[†] metrics are important for the accurate assignment of energy to a particular interaction. The algorithm is tuned on ND MC to optimize slice purity and completeness and results in slices that are 99% pure and 92% complete, on average.

[†]Completeness and purity are measured on a scale from 0 to 1. A completeness measure of 1 means that all visible energy was clustered into a slice. A purity measure of 1 means that there was no energy clustered originating from a different interaction.

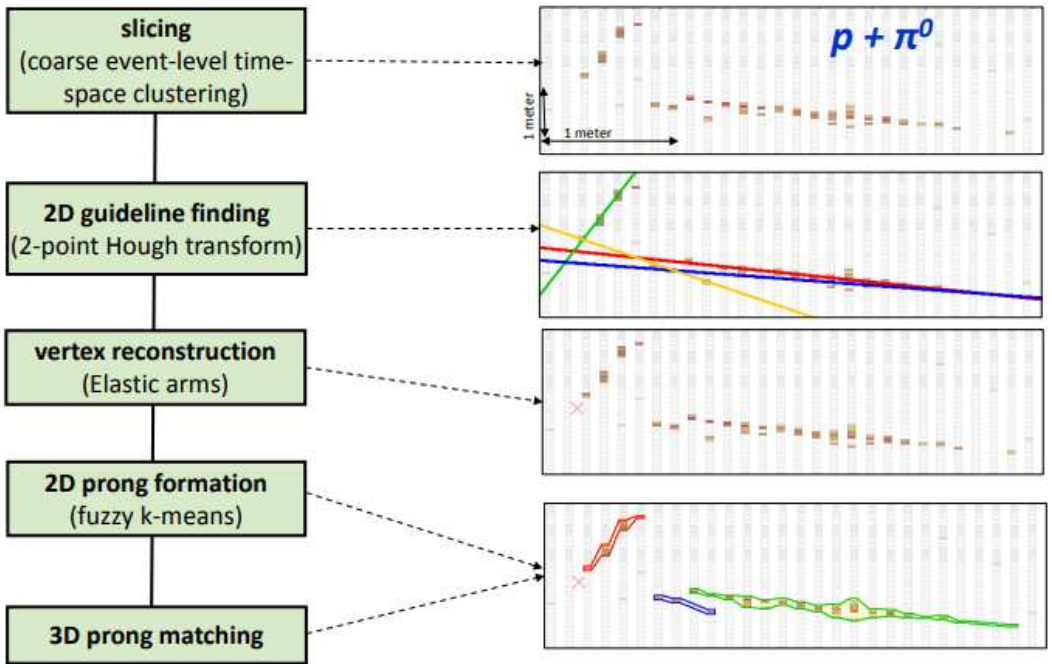

FIGURE 4.5. Reconstruction chain after slicing. An interaction vertex is found via a Hough Transform algorithm and prongs are formed to represent particle trajectories by a fuzzy k-means algorithm [16].

Figure 4.5 shows the chain of reconstruction algorithms subsequently performed on each slice, beginning with the identification of interaction vertex. Every pair of hits in a slice defines a line that is used to identify prominent flows of energy via Hough transform [111]. The prominent flows representing particle trajectories are used to seed a vertex-finding algorithm based on a modified elastic arms [112] (also known as deformable templates). The result is a three-dimensional point in the detector coordinates that represents the initial interaction point from which all energy in the slice originates.

Vertices are then used to seed a fuzzy k-means algorithm [113, 16] for clustering hits originating from individual particles. These clusters are called "prongs" and are described by an energy (sum of calibrated hits) and a direction. Two-dimensional prongs in each view are formed, which

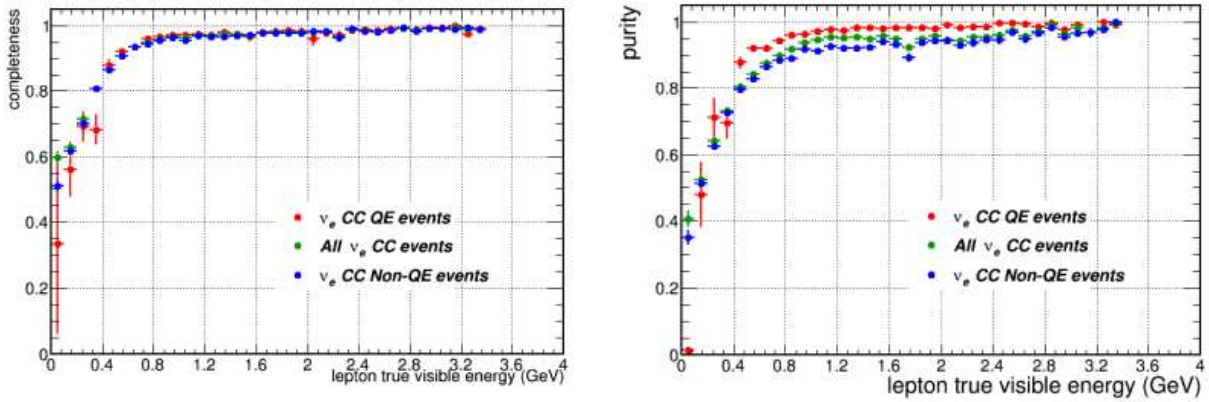

(A) Prong completeness

(B) Prong purity

FIGURE 4.6. Completeness (A) and purity (B) of prong clustering of visible lepton energy [16].

are then matched with prongs in the opposite view based on energy deposition profile (via [114]) to produce three-dimensional prongs.

Figure 4.6 shows completeness and purity of electron prongs from simulated ν_e-CC events in the FD taken from [16]. All electrons above $0.5\,\mathrm{GeV}$ are clustered with over 90% completeness and purity. Electrons from ν_e-CC QE interactions are typically clustered with higher purity than those from non-QE where more particles appear in the final state.

A second clustering algorithm is employed in parallel to prong formation that is better suited for tracking the long line of energy deposition from muons traveling in the detector. Starting from the downstream end of a slice, a Kalman filtering [115] algorithm produces a line by iterating over hits in the upstream direction. As hits are added, the line is updated. Once the algorithm reaches the end of a track, a cleanup process is started traversing the track in reverse. Two-dimensional Kalman tracks are first produced in each view of the detector. Finally, a view-matching algorithm based on track start and stop positions produces 3-dimensional Kalman tracks [116].

4.5. Estimation of Electron Kinematics

Accurate estimation of electron kinematics is important for reducing systematic uncertainties on the measurement of the electron antineutrino cross section. The electron from ν_e-CC and $\bar{\nu}_e$-CC interactions is most often (98.5%) associated with the most energetic prong within a slice, therefore the most energetic prong is used to estimate both the electron's energy and cosine of the scattering angle with respect to the NuMI beam. Bias and resolution are used to evaluate the quality of kinematic estimators, and are defined as

$$\text{Bias} = \frac{1}{N}\sum_{i}^{N}\frac{x_i^{\text{true}} - x_i^{\text{reco}}}{x_i^{\text{true}}} \tag{4.3}$$

$$\text{Resolution} = \sqrt{\frac{1}{N}\sum_{i}^{N}\left(\frac{x_i^{\text{true}} - x_i^{\text{reco}}}{x_i^{\text{true}}} - \text{Bias}\right)^2} \tag{4.4}$$

where x_i^{true} and x_i^{reco} are true and reconstructed quantities for reconstructed electron i and the sum is taken over N reconstructed electrons.

The cosine of the electron scattering angle with respect to the NuMI beam is estimated directly from the prong direction. Figure 4.7 shows approximately a 1:1 relationship between true and reconstructed $\cos\theta$ from $0.8 \leq \cos\theta \leq 1$, where most events occur. Overall, $\cos\theta$ is unbiased with a resolution of 2%.

An electron energy estimator is developed for the measurement of the $\bar{\nu}_e$-CC inclusive cross section to reduce a bias observed in the calorimetric energy estimation. Figure 4.8 shows the relationship between true electron energy and the calorimetric energy clustered within the electron prong. A clear bias is observed such that the calorimetric energy of the prong generally underestimates the true energy of the electron by 10% with a resolution of 16%. A correction to

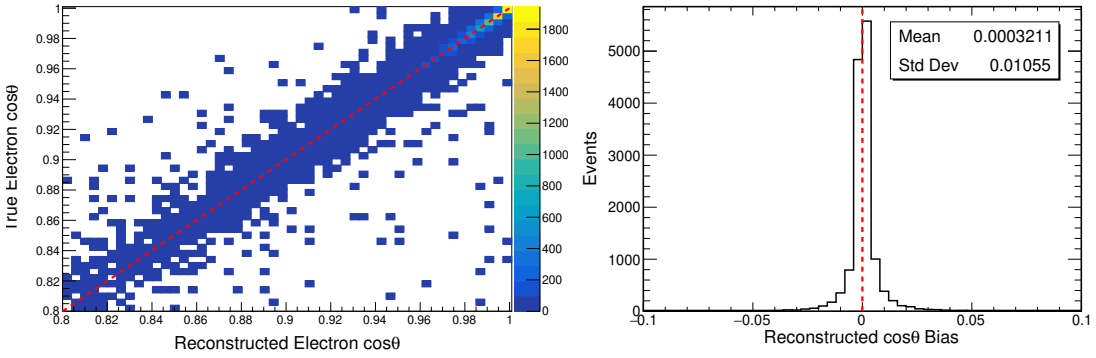

(A) (B)

FIGURE 4.7. Electron $\cos\theta$ bias of the reconstructed prong angle. A plot of true versus reconstructed electron angle (A) shows that the relationship closely follows a line with slope of 1 (dashed red line). Overall fractional bias (B) is shown to be essential 0% with 2% resolution.

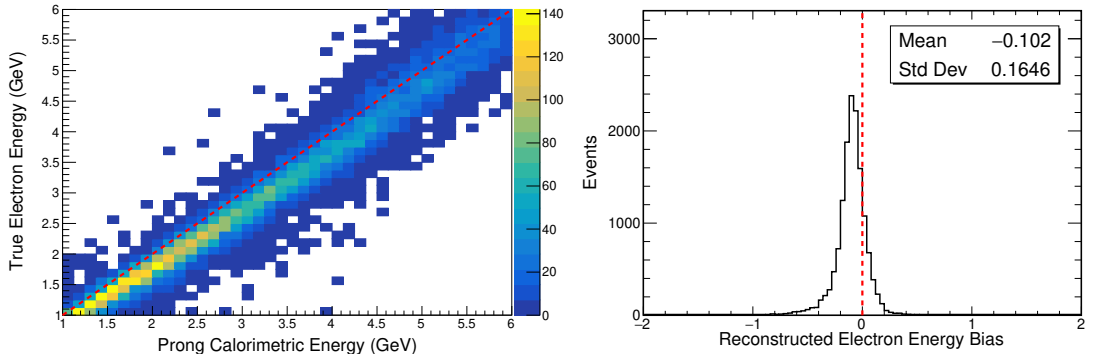

(A) (B)

FIGURE 4.8. Bias of the calorimetric energy estimation from the clustered electron prong. True electron energy versus calorimetric energy (A) shows the slope clearly deviating from 1 (dotted red line). Overall fractional bias (B) is shown to underestimate true electron energy by 10% with a resolution of 16%.

the calorimetric energy estimation is applied to reduce the bias and resolution of reconstructed electron energies. Estimated absolute bias[‡] is subtracted from prong calorimetric energy as a function of calorimetric energy such that

$$E_{\text{reco}}(E_{\text{cal}}; n) = E_{\text{cal}} - p(E_{\text{cal}}; n) \tag{4.5}$$

[‡]Absolute Bias $= \frac{1}{N}\sum_i^N (x_i^{\text{true}} - x_i^{\text{reco}})$; Absolute Resolution $= \sqrt{\frac{1}{N}\sum_i^N \left((x_i^{\text{true}} - x^{\text{reco}}) - \text{Absolute Bias}\right)^2}$

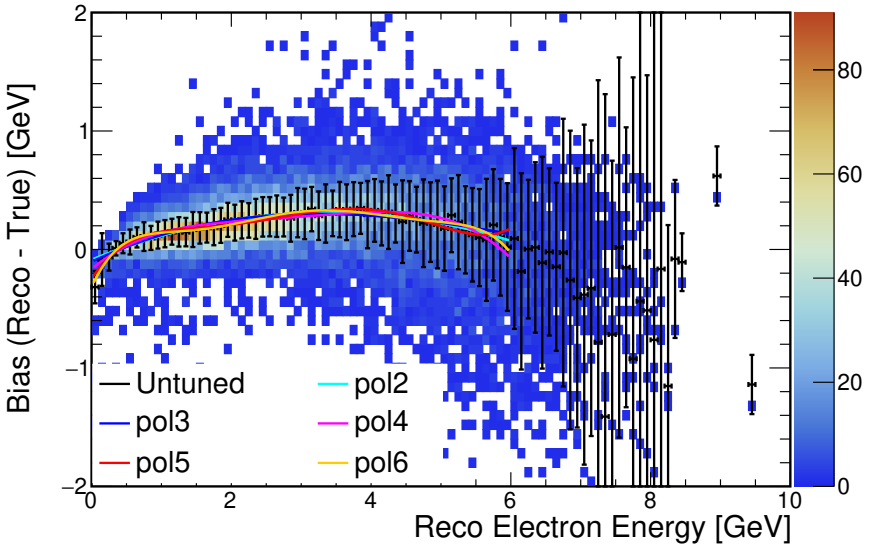

FIGURE 4.9. Polynomials are fit to calorimetric energy bias as a function of calorimetric energy within the range $0 \leq E_{\text{cal}}\,(\text{GeV}) \leq 6$.

where $p(E_{\text{cal}}; n)$ is an n^{th}-order polynomial fit to absolute bias in E_{cal}, the calorimetric energy of the most energetic prong in a slice.

Least-square regression is performed for a number of polynomial orders. The fits are constrained to the range $0 < E_{\text{cal}}\,(\text{GeV}) < 6$ due to limited MC statistics beyond $6\,\text{GeV}$. Figure 4.9 shows polynomials of orders two through six that are fit to average absolute bias as a function of calorimetric energy. Figure 4.10 shows absolute bias and resolution of polynomial-corrected energy estimators. Each estimator significantly reduces the absolute bias of electron energy estimation.

Given that all estimators perform similarly in terms of bias and resolution, the polynomial of order 2 is chosen because it is a smoother function of E_{cal} and therefore less sensitive to statistical fluctuations of the MC training sample. The following is used to estimate the energy of electrons

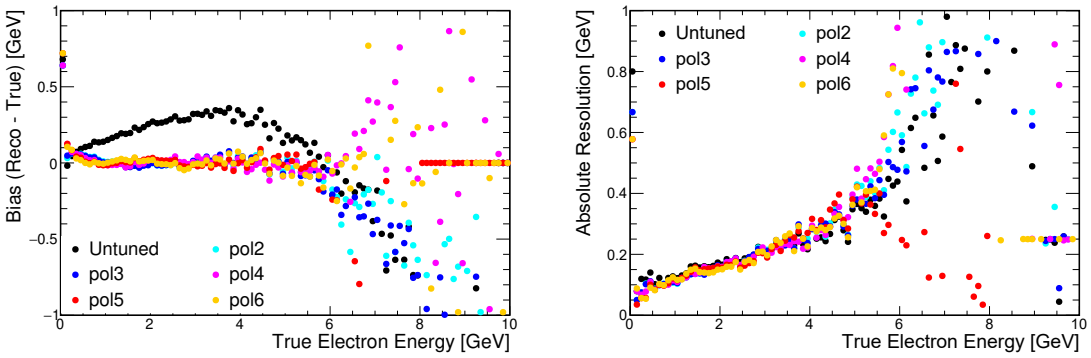

(A) (B)

FIGURE 4.10. Absolute bias (A) and resolution (B) of polynomial-corrected electron energy estimators as a function of true electron energy.

based on calorimetric energy clustered by prongs:

$$E_{\text{reco}} = \begin{cases} E_{\text{cal}} - (p_0 + p_1 E_{\text{cal}} + p_2 E_{\text{cal}}^2) & 0 \leq E_{\text{cal}}\,(\text{GeV}) \leq 6 \\ E_{\text{cal}} & 6 < E_{\text{cal}}\,(\text{GeV}). \end{cases} \tag{4.6}$$

Here, p_0, p_1, and p_2 are constants that result from the regression. The resulting constants and associated errors are

$$p_0 = -\,0.08 \pm 0.046$$

$$p_1 = +\,0.23 \pm 0.050$$

$$p_2 = -\,0.03 \pm 0.010.$$

Equation (4.6) reduces the average fractional bias and resolution of electron energy estimation to 1% and 14%, respectively. Results are shown in Figure 4.11.

4.6. Estimation of Neutrino Energy

The initial energy of electron antineutrinos interacting via charged current is estimated using a technique developed for the NOvA oscillation analysis [1]. Electromagnetic and hadronic

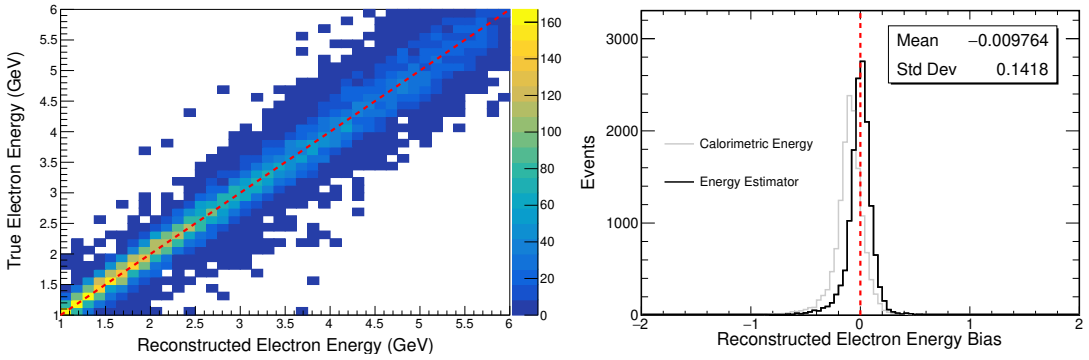

(A) (B)

FIGURE 4.11. Bias of the 2^{nd}-order polynomial electron energy estimator. A plot of true versus reconstructed electron energy (A) shows the relationship closely follows a line with slope of 1 (dashed red line). Overall fractional bias (B) is shown to be roughly 1% with 14% resolution, reduced from 16%.

energy depositions are weighted independently by a two-dimensional polynomial surface of degree two to arrive at a reconstructed neutrino energy. The functional form of the neutrino energy estimator is

$$\hat{E}_\nu = \frac{1}{1+\delta}(p_{00}E_{\text{EM}} + p_{10}E_{\text{Had}} + p_{01}E_{\text{EM}}^2 + p_{11}E_{\text{Had}}^2) \tag{4.7}$$

where the p_{ij} are constants that are determined by fitting procedure, E_{EM} and E_{Had} are calorimetric energy depositions associated with electromagnetic and hadronic prongs, respectively, and δ is a bias correction factor.

A Convolutional Neural Network (CNN) trained on simulated GENIE events [117] is used to identify prongs as electromagnetic or hadronic. Each prong in an event is classified based on the highest-scoring particle species. Energy from electron and photon prongs are summed to calculate E_{EM} and energy from muon, proton, and pion prongs are summed to calculate E_{Had}.

True ν_e-CC ($\bar{\nu}_e$-CC) interactions from FHC (RHC) simulation samples are used to calculate average true neutrino energy as a function of E_{EM} and E_{Had} as shown in Figure 4.12. The polynomial

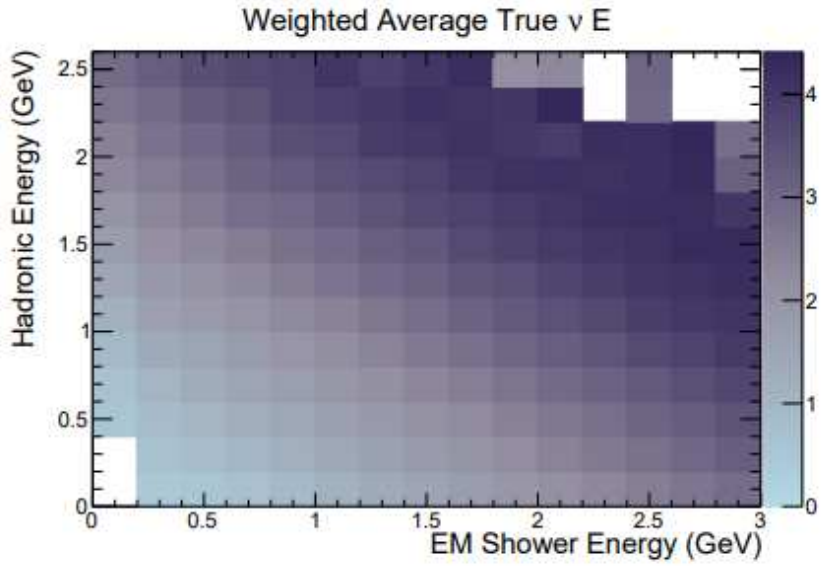

FIGURE 4.12. Average energy of true ν_e-CC interactions selected from FHC simulation as a function of E_{EM} and E_{Had} [1].

TABLE 4.1. Best fit parameters that define the second-order polynomial surface of the FHC and RHC neutrino energy estimators [1].

Parameter	FHC fit	RHC fit
p_{00}	1.01777	0.988258
p_{10}	1.10868	1.20084
p_{01}	1.43541×10^{-3}	1.92904×10^{-7}
p_{11}	1.09628×10^{-1}	1.20704×10^{-7}
δ	0.0355622	0.0111873

surface (4.7) is fit to this distribution (while $\delta = 0$). The bias correction factor (δ) is determined by average bias of the resulting energy estimation.

Table 4.1 shows the best fit parameters that define the FHC and RHC neutrino energy estimator second-order polynomial surfaces [1]. The resulting estimators are unbiased from $0.5\,\text{GeV} \leq E_\nu < 4.5\,\text{GeV}$ as shown in Figure 4.13. The overall electron (anti)neutrino energy resolution is 10.3% (9.1%).

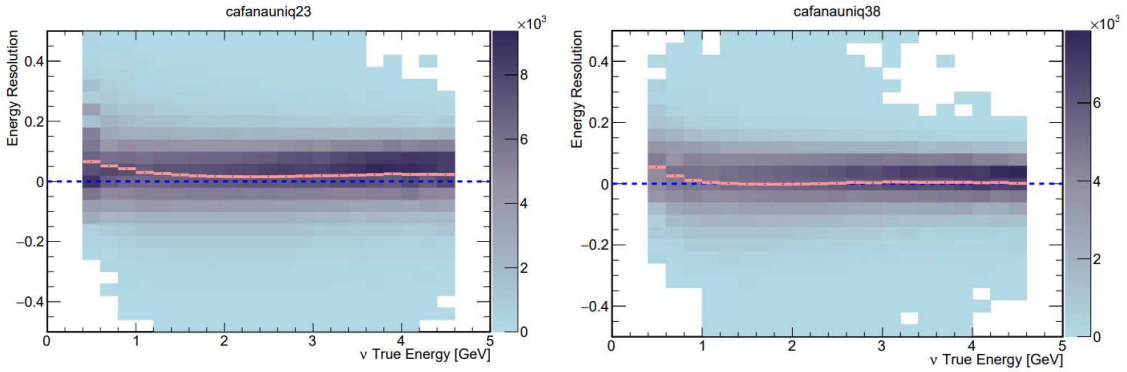

FIGURE 4.13. Reconstructed neutrino energy bias as a function of true neutrino energy for simulated ν_e-CC events in FHC (left) and $\bar{\nu}_e$-CC events in RHC (right) [1].

4.7. ANALYSIS SOFTWARE

The NOvA experiment supports many unrelated physics analyses that require different features to be extracted from the raw data. The algorithms that extract these features often depend on basic reconstruction (slicing and clustering) and might include simple geometric measures of the clustered topology, output from CNNs, or other forms of Particle Identification (PID). To avoid code-duplication and ensure consistency in the basic representation of neutrino interactions among all NOvA analyses, these features are stored in a Common Analysis File (CAF) format, while the fundamental objects (e.g. hits) are not.

CAFs are stored as a ROOT [118] file-format to support the analysis framework that ingests them. Data products are stored within the file as a tree structure in the ROOT framework called a `TTree`. Leaves of the tree contain the products of various data processing algorithms, which may be performed on the nested representations of the event. The tree contains C++ objects called Standard Records (SRs). The structure of the tree associated with each slice is defined by the `StandardRecord` type, which can contain nested trees of other SR types. Notably, the `SRNeutrino` type is a tree of values describing the true parameters of the simulated interaction. The `SRNeutrino` object describes interactions that were matched with slices, but an identical

structure is stored in a `TTree` parallel to `StandardRecord` `TTree` describing every neutrino interaction within the detector, which is important for estimating detector acceptance effects. Reconstructed data and MC are stored identically, but data files do not contain `SRNeutrino` trees.

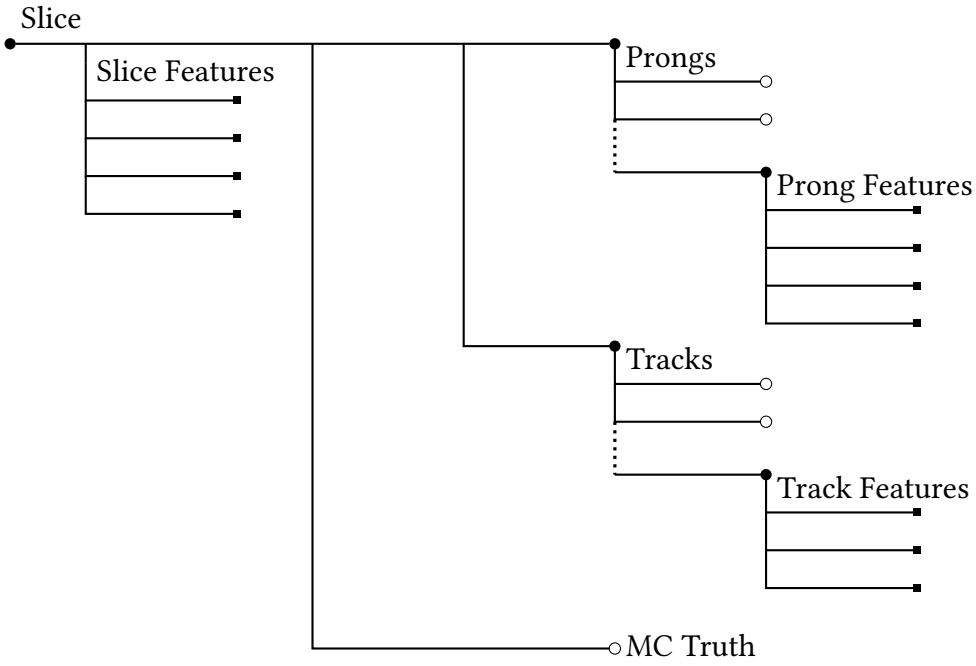

FIGURE 4.14. A simplified illustration of the nested-tree structure of slice in the CAF format. Every slice contains a collection of prongs, tracks, and a tree of MC truth information. Each slice can contain any number of prongs or tracks indicated by the dotted lines. Each prong contains features that describe the prong. Each track contains features that describe the track. Tree leaves are indicated by a square end point. A closed circle indicates a branching point. An open circle indicates a branching point that potentially contains many nested branches that are not shown in the diagram.

Data (MC) are categorized by NuMI and NOvA detector run conditions, where data (MC) from similar run conditions make up a NOvA dataset. During data analysis, analyzers will typically process data from specific datasets to ensure that the data are consistent and comparable. Datasets typically contain many thousands of individual ROOT files, where each file is roughly $50\,\mathrm{MB}$. The file size is kept small for efficient transfer to compute nodes on the FermiGrid [119] or the Open

TABLE 4.2. NOvA dataset statistics

Dataset	No. Files	Avg. File Size (MB)	Avg. Slices per File	Avg. Spills per File	Avg. ν per File
FHC Data	17,083	42.7	12,527	2,340	-
RHC Data	9,961	34.1	10,084	2,426	-
FHC MC	221,976	52.1	5,233	698	17,536
RHC MC	202,672	22.6	2,353	514	7,430

Science Grid [120]. Table 4.2 shows the average slice, spill, and simulated neutrino content for files in the standard NOvA datasets consisting of data and MC from FHC and RHC NuMI beam modes.

Analyzers extract physics information from CAFs with the CAFANA [121] library and the ROOT analysis framework. CAFANA provides tools for filtering and transforming neutrino data, a process called "event selection", as well as fitting oscillation parameters. Users declare `Spectrum` objects with data filtering criteria (`Cut`) and variables (`Var`) that are used to fill histograms. Users can also weigh events as they are added to histograms using a `Weight` object and modify the `StandardRecord` with `SystShifts` objects. These objects operate on the `StandardRecord` and return native C++ types. Data is read from file lazily, meaning only when needed, using a proxy mechanism to read only the data that requested in the user-defined CAFANA objects.

Analyzers use the FermiGrid to process entire NOvA datasets. The FermiGrid is an opportunistic grid-computing network shared among Fermilab experiments designed for data-parallel[§] processing. NOvA's current dedicated allocation of resources consists of $5{,}700$ concurrent cores available for jobs.

The average processing time of a CAFANA analysis using the FermiGrid can be anywhere from one hour to many days depending on the number of files processed per compute node and

[§]Data-parallel processing means data are processed independently and results are aggregated at a later step.

the number of unique histograms filled. Filled histograms are saved to disk and aggregated using the `hadd` utility, which stands for histogram add, provided by the ROOT analysis framework.

CHAPTER 5

The $\bar{\nu}_e$-CC Inclusive Cross Section Analysis

This chapter outlines the measurement of the double-differential electron antineutrino charged-current inclusive cross section of the events in the NOvA ND. The analysis signal will be defined and the methodology for extracting the cross section of the signal based on data collected in the NOvA ND from the NuMI neutrino and antineutrino beams will be described.

In general, the number of neutrino interactions observed in the detector is a function of neutrino flux (ϕ), cross section (σ), the number of scattering targets in the detector (T), detector efficiency (ϵ), and a matrix (U) that represents the effects of an imperfect detector by relating truth quantities (E_ν) to reconstructed quantities ($\hat{E}_\nu$)

$$N(\hat{E}_\nu) = \int_0^\infty U^{-1}(\hat{E}_\nu, E_\nu)\phi(E_\nu)\sigma(E_\nu)T\epsilon(E_\nu)\, dE_\nu \tag{5.1}$$

where E_ν and $\hat{E}_\nu$ are true and estimated neutrino energies. The cross section is extracted by inverting (5.1) such that

$$\sigma(E_\nu) = \frac{\int_0^\infty U(\hat{E}_\nu, E_\nu)N(\hat{E}_\nu)\, d\hat{E}_\nu}{\phi(E_\nu)T\epsilon(E_\nu)}. \tag{5.2}$$

In order to reduce bias toward the interaction models described in Section 4.2, introduced by reconstructing $\hat{E}_\nu$, the differential cross section as a function of observables is also measured.

$$\frac{\partial\sigma}{\partial\eta} = \frac{\int_0^{2\pi} U(\hat{\eta}, \eta)N(\hat{\eta})\, d\hat{\eta}}{\bar{\phi}T\epsilon(\eta)}\frac{1}{\partial\eta} \tag{5.3}$$

where η is an observable kinematic variable such as scattering angle or energy, $\bar{\phi}$ is the neutrino flux integrated over all neutrino energies. For binned analyses, the integrals and derivatives are

discretized,

$$\left(\frac{\partial\sigma}{\partial\eta}\right)_i = \frac{1}{\bar{\phi}T\epsilon_i\Delta_i}\sum_{i'} U_{ii'}N_{i'} \tag{5.4}$$

such that bins of η and $\hat{\eta}$ are labeled i and i', respectively, and Δ_i is the width of bin i. Taking the derivative once more with respect to some other kinematic variable, ρ,

$$\left(\frac{\partial^2\sigma}{\partial\eta\partial\rho}\right)_{ij} = \frac{1}{\bar{\phi}T\epsilon_{ij}\Delta_{ij}}\sum_{i'j'} U_{ii'jj'}N_{i'j'} \tag{5.5}$$

where i and j are bins of η vs. ρ, and primed indices are reconstructed bins.

This thesis presents a measurement of the double-differential $\bar{\nu}_e$-CC inclusive cross section as a function of the cosine of the electron scattering angle with respect to the NuMI beam direction ($\cos\theta$), and electron energy (E_e). Single-differential cross sections are also reported in $\cos\theta$, E_e, and four-momentum transfer squared (Q^2), in addition to the total cross section as a function of neutrino energy ($\sigma(E_\nu)$). The data selection criteria for this analysis are described in Section 5.2. A description of systematic sources of error is presented in Section 5.4. The estimation of $\bar{\nu}_e$-CC signal candidates is presented in Section 5.5. The compensation for detector smearing and acceptance effects is presented in Section 5.6. The estimation of integrated $\bar{\nu}_e$ flux from the NuMI beam is presented in Section 5.4.1. Finally, the estimation of scattering targets is presented in Section 5.7. The analysis is also described in [122].

5.1. Signal Definition

The signal for this analysis is any charged-current electron antineutrino interaction occurring within a fiducial volume of the NOvA ND and a restricted phase space of electron kinematics. The

signal interaction is defined as

$$\bar{\nu}_e + N \to e^+ + X \tag{5.6}$$

where N is a nucleon (p or n), e^+ is the outgoing positron, and X can be any other particle(s). The kinematic phase space of the positron is restricted to

$$\begin{aligned}
&(0.85 \leq \cos\theta < 0.90 \quad \cap \quad 1.0 \leq E_e\,(\mathrm{GeV}) < 2.0) \cup \\
&(0.90 \leq \cos\theta < 0.94 \quad \cap \quad 1.0 \leq E_e\,(\mathrm{GeV}) < 2.5) \cup \\
&(0.94 \leq \cos\theta < 0.97 \quad \cap \quad 1.0 \leq E_e\,(\mathrm{GeV}) < 3.5) \cup \\
&(0.97 \leq \cos\theta \leq 1.00 \quad \cap \quad 1.0 \leq E_e\,(\mathrm{GeV}) < 6.0)
\end{aligned}$$

due to detection and reconstruction inefficiencies of the detector (Sections 4.5 and 5.6).

5.2. Event Selection

Before signal estimation is performed, the data are filtered of obvious background, like ν_μ-CC events, poorly reconstructed events, interactions near the detector edges, and data from poor data-taking conditions. Where appropriate, selection criteria, referred to as "cuts", are determined by an optimization procedure to minimize the average uncertainty of the cross section measurement.

5.2.1. Data Quality. The first set of cuts ensures the data analyzed are collected during good-running conditions of both the NuMI beam and NOvA ND. The following conditions are met for all data considered in the analysis [123]:

- **Nominal Detector Conditions:** The full detector is required to be operational and noise-levels within tolerance [123].
- **NuMI-ND Time Synchronization:** The time reported by NuMI for each spill must be closely synchronized ($\Delta t < 5 \times 10^{-10}\,\mathrm{s}$) with the time of the recorded spill window.
- **Nominal NuMI Beam Conditions:** The NuMI horn current, beam position and width are checked to be within typical ranges [124].

The selected data meet the following requirements to ensure that the reconstruction algorithms performed as expected and were are not heavily influenced by detector noise:

- **Hits per plane < 8:** Events with many hits per plane are likely due to noise.
- **Reconstructed Vertex:** An interaction vertex is required for subsequent reconstruction algorithms. The interaction vertex is found by the elastic-arms algorithm described in Section 4.4. This results in a bias in the case of 1-prong events where the interaction vertex can be reconstructed 1-2 planes downstream the true interaction vertex [16].
- **Reconstructed Prongs:** At least one prong must be reconstructed in order to estimate lepton kinematics.
- **More than 5 hits in the primary shower:** This requirement is enforced for both the XZ and YZ views of the detector to ensure there is enough energy deposited to reliably reconstruct the particle's energy.
- **Primary shower gap from the vertex is less than 100 cm:** A shower that is reconstructed far from the vertex is indicative of a poorly constrained vertex or a cluster of stray hits.
- **Showers must not be anti-linear:** Bad channels in the detector can result in sparse energy deposition from a single particle that can result in the creation of two antilinear

prongs. This criteria ensures the two most energetic prongs are likely from two different particles, or at worst, a hard-scatter of one particle. The requirement is that the cosine of the angle between the two leading showers be less than -0.95.

- **More than 70% of hits in a slice are associated with 3D prongs:** This criteria guards against slices where a large fraction of the hits could not be associated with a 3D prong due to either bad matching or noise.
- **Symmetric showers:** Shower symmetry is required to ensure good 3D matching of 2D showers. The asymmetry between views is defined as

$$\text{View Asymmetry} = \frac{|N_x - N_y|}{N_x + N_y} \tag{5.7}$$

where N_x and N_y are the number of hits in the XZ and YZ views of the shower, respectively. The requirement is that the shower View Asymmetry be less than 0.4.

5.2.2. Number of Planes from the Front of the Detector. Data are required to be sliced further than six (6) planes from the front of the ND. This criteria is intended to remove sliced activity from interactions occurring in the rock surrounding the detector.

5.2.3. Number of Hits in Slice. An additional requirement on the number of hits in a slice is included to reject slices that are difficult to properly characterize. Slices are required to have at least 20 and at most 200 hits. Slices with below 20 hits, less than $0.4\,\mathrm{GeV}$ of deposited energy, are likely from noise or NC events with small nuclear recoil. Slices with hits above 200 contain a high particle multiplicity, which impacts the clustering purity and energy estimation.

5.2.4. Containment Volume. Hits from an individual interaction must be fully contained within the detector to accurately reconstruct the energy of final-state particles and thus parent neutrino. Signal events are required to have all associated hits be no less than

- $55\,\mathrm{cm}$ from the East wall,
- $30\,\mathrm{cm}$ from the West wall,
- $50\,\mathrm{cm}$ from the top wall,
- $30\,\mathrm{cm}$ from the bottom wall,
- $150\,\mathrm{cm}$ from the front wall,

and no activity is allowed in the muon catcher (Section 3.4). These bounds were determined in [17] to be optimal in reducing uncertainty on a measurement of total ν_e-CC inclusive cross section (Section 5.2.5). The agreement between RHC data and MC in variables of distance from the detector walls to the nearest hits is shown in Figure 5.1. This containment volume is determined to be optimal for the $\bar{\nu}_e$-CC inclusive analysis based on good agreement between data and MC.

The remaining criteria are determined by optimization procedure [125] designed to reduce the uncertainty on the total extracted cross section.

5.2.5. Selection Optimization Procedure. Cut thresholds of continuous or discrete variables are optimized to reduce the uncertainty on the measured cross section. For this procedure, the total cross section is defined as

$$\sigma = \frac{1}{T\phi\epsilon}\left(N_{\text{Sel,Data}} - s \cdot N_{\text{Bkgd, MC}}\right) \tag{5.8}$$

where T, ϕ, and ϵ are the number of nucleon scattering targets, neutrino flux, and detector efficiency, respectively. $N_{\text{Sel,Data}}$ is the total number of events selected from data*, $N_{\text{Bkgd,MC}}$ is the MC

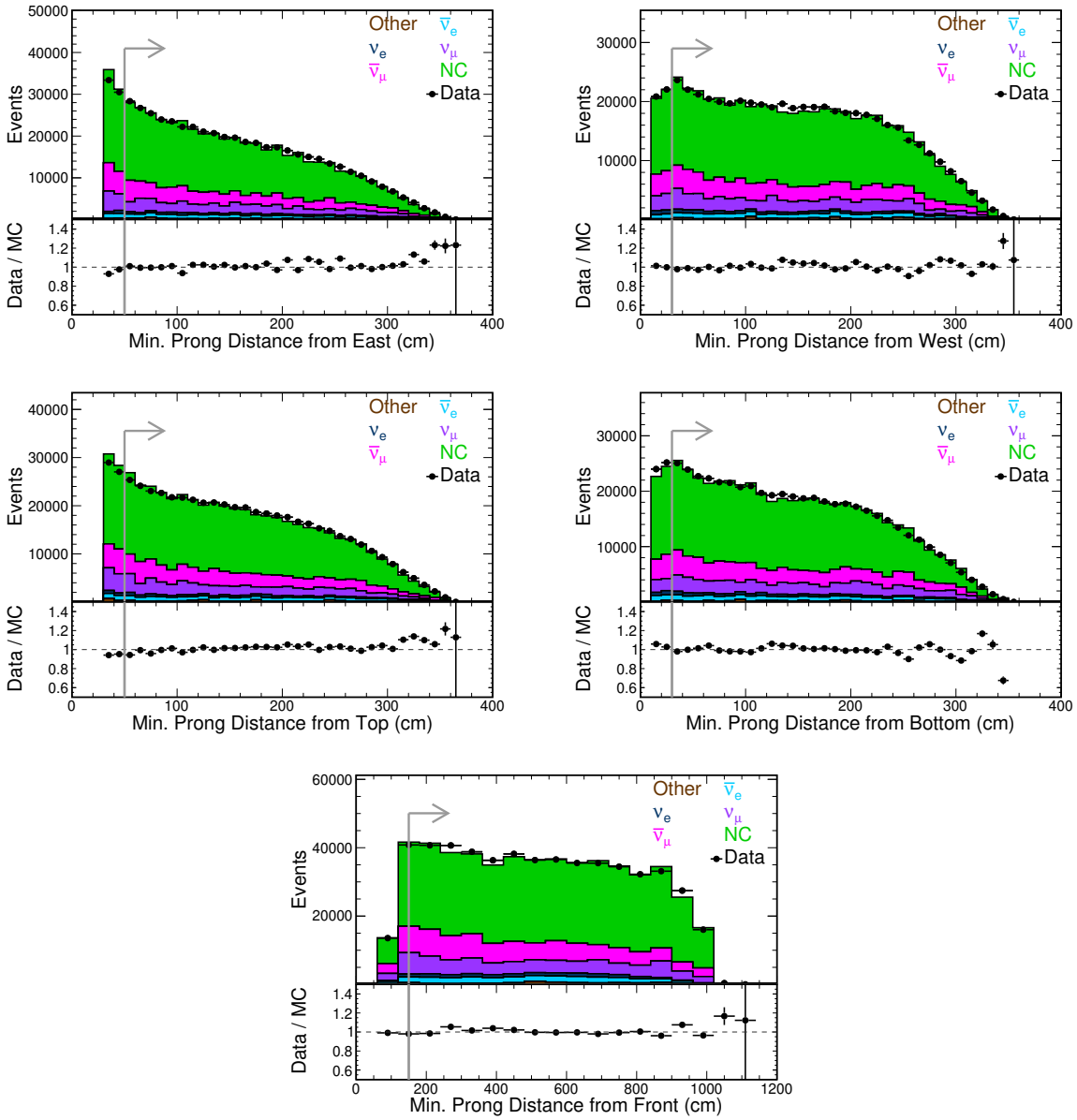

FIGURE 5.1. Distance from the closest clustered energy deposition to the walls of the detector for RHC data and MC events. Arrows indicate containment cuts optimized for the ν_e-CC analysis [17]. Good agreement is shown between data and MC beyond the optimized containment cut values.

prediction for the background contained in the selected sample, and s is the POT scaling factor applied to the MC ($s = \frac{\text{POT}_{\text{Data}}}{\text{POT}_{\text{MC}}}$).

*Simulation normalized to the expected POT is used in place of real data for this optimization procedure.

For a function (f) of independent variables ($\vec{x}$), the squared-error is

$$(\delta f)^2 = \sum_i \left(\frac{\partial f}{\partial x_i} \cdot \partial x_i\right)^2 \tag{5.9}$$

where the sum is taken over the vector components of $\vec{x}$. Applying this to (5.8),

$$\begin{aligned}(\delta\sigma)^2 = &\left(\frac{\partial\sigma}{\partial N_{\text{Sel,Data}}} \cdot \partial N_{\text{Sel,Data}}\right)^2 + \left(\frac{\partial\sigma}{\partial N_{\text{Bkgd,MC}}} \cdot \partial N_{\text{Bkgd,MC}}\right)^2 + \left(\frac{\partial\sigma}{\partial\epsilon} \cdot \partial\epsilon\right)^2 \\ &+ \left(\frac{\partial\sigma}{\partial(T\phi)} \cdot \partial(T\phi)\right)^2.\end{aligned} \tag{5.10}$$

Flux and target uncertainties for the NOvA experiment are constant (Section 5.4) so the final term is omitted. Uncertainties for each individual term are given as a quadrature sum of statistical and systematic errors,

$$(\partial g)^2 = (\partial g_{\text{stat}})^2 + \sum_{\text{syst}} (\delta g_{\text{syst}})^2 \tag{5.11}$$

where the sum is taken over all sources of systematic error. Statistical errors are assumed to be Poisson distributed ($\partial g_{\text{stat}} = \sqrt{g}$). Efficiency of selecting signal events is given by:

$$\epsilon = \frac{N_{\text{Signal,Selected}}}{N_{\text{Signal, All}}}. \tag{5.12}$$

After simplification, the fractional uncertainty on total cross section is

$$\begin{aligned}\left(\frac{\partial\sigma}{\sigma}\right)^2 = &\frac{N_{\text{Sel, Data}}}{(N_{\text{Sel, Data}} - s \cdot N_{\text{Bkgd,MC}})^2} + \frac{s^2 N_{\text{Bkgd,MC}}}{(N_{\text{Sel, Data}} - s \cdot N_{\text{Bkgd,MC}})^2} \\ &+ \frac{s^2 \cdot \sum_{\text{syst}} (\partial N_{\text{Bkgd,syst}})^2}{(N_{\text{Sel,Data}} - s \cdot N_{\text{Bkgd,MC}})^2} + \frac{\sum_{\text{syst}} (\partial\epsilon_{\text{syst}})^2}{\epsilon^2}\end{aligned} \tag{5.13}$$

where the $\partial\epsilon_{\text{stat}}$ has been ignored based on large MC statistics.

Equation (5.13) is used to optimize a selection threshold over a range of possible values. For every point over a regular grid spanning the threshold range, (5.13) is calculated to find the minimum uncertainty on the total cross section. This method is used to optimize the bounds of the fiducial volume (Section 5.2.6) and muon rejection (Section 5.2.8) threshold.

5.2.6. Fiducial Volume. Data are required to be reconstructed with a vertex within a smaller internal volume of the detector. The purpose of an internal fiducial volume is to mitigate the effects of rock interactions and neutral particles leaving the detector before depositing visible energy, which lead to an underestimation of particle kinematics. This fiducial volume partly defines the signal of the analysis because it determines the number of nucleon targets in (5.5).

An optimized fiducial volume was obtained in [17] for the ν_e-CC inclusive measurement, the signal of which produces a similar final-state topology in the NOvA ND. These bounds are verified to be optimal for this analysis by independent optimization and agreement between data and simulation. The fiducial volume is defined in terms of detector coordinates as

$$\begin{aligned} -130.0 < X\,(\mathrm{cm}) < 150.0 \\ -140.0 < Y\,(\mathrm{cm}) < 140.0 \\ 150.0 < Z\,(\mathrm{cm}) < 800.0. \end{aligned} \tag{5.14}$$

The $X < 0$ outer wall of the detector is exposed to the NuMI flux due to the off-axis positioning of the detector. By defining a fiducial volume asymmetric in X, uncertainties due to background rock interactions is reduced [17]. Similarly, the first $150\,\mathrm{cm}$ of the detector is not included in the fiducial volume.

An independent optimization is performed to cross-check the results of the ν_e-CC inclusive analysis. A basic selection, which includes the detector, beam, and reconstruction quality criteria

defined in Sections 5.2.1 to 5.2.3, is applied to isolate the effect of varying the fiducial bounds. Relaxed fiducial, containment (Section 5.2.4), and muon rejection (Section 5.2.8) requirements have also been applied, in addition to a cut on reconstructed electron phase space (Section 4.5). The uncertainty on the combined ν_e-CC and $\bar{\nu}_e$-CC cross section is optimized using RHC MC. Systematic uncertainties from neutrino interaction models and detector calibration are included. Figure 5.2 shows surfaces of fractional uncertainty on the total cross section as a function of fiducial volume bounds. These surfaces are minimal and smooth near the bounds of (5.14) indicating a robustness to systematic uncertainties in the reconstruction of the vertex position.

Agreement between data and MC is also assessed when optimizing the fiducial bounds in (5.14). Figure 5.3 shows good agreement between the bounds of (5.14). We consider the bounds of (5.14) to be optimal for the $\bar{\nu}_e$-CC inclusive analysis due to these results and the total cross-section uncertainty surface of Figure 5.2.

5.2.7. Electron Phase Space. A cut is placed on the reconstructed energy and angle (Section 4.5) of the most energetic prong in a slice. This cut mimics the true lepton phase space of the analysis signal and removes a significant amount of background NC and $\bar{\nu}_\mu$-CC interactions. The number of signal events that do not pass this cut is estimated using simulation and included in the double-differential measurement via the unfolding procedure (Section 5.6).

5.2.8. Muon Rejection. Finally, obvious muon candidate events are removed using Boosted Decision Tree (BDT) classification algorithm. A BDT is trained to classify Kalman tracks as muon-like based on track topology [126]. The output of the BDT is a score, referred to as MuonID, between -1 and 1 corresponding to the likelihood of an individual track being associated with a muon. The more likely the track is to have been produced by a muon, the higher the assigned MuonID score. Figure 5.4 shows the maximum MuonID score per slice in a sample of RHC MC.

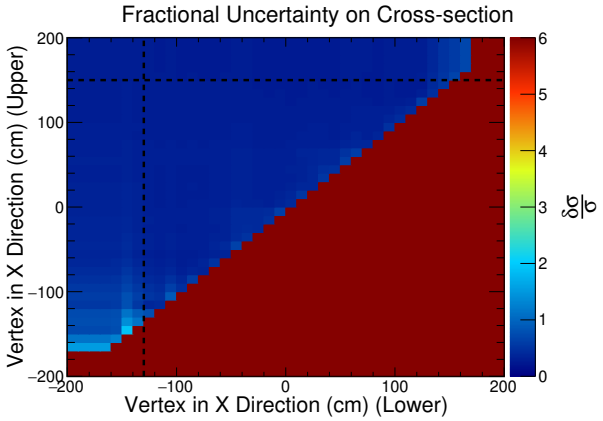

(A) x-coordinate of the reconstructed vertex.

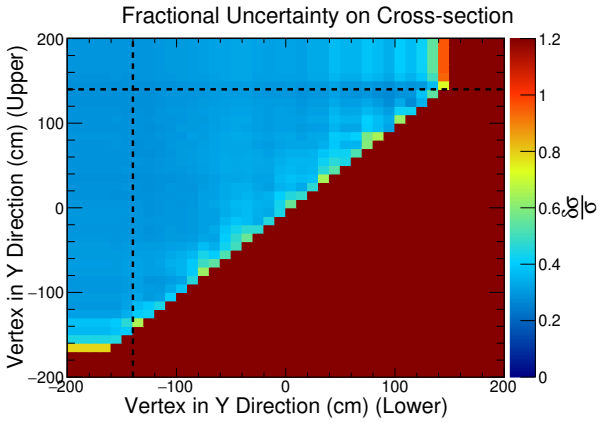

(B) y-coordinate of the reconstructed vertex.

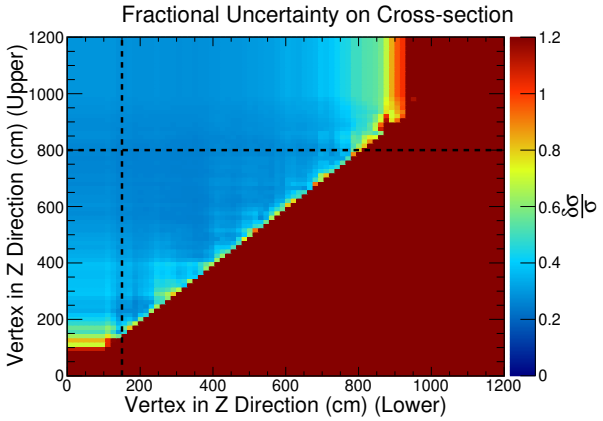

(C) z-coordinate of the reconstructed vertex.

FIGURE 5.2. Fractional uncertainty on the total cross section as a function of upper and lower bounds of the x- (A), y- (B), and z-coordinates (C) defining the fiducial volume. Dashed lines indicate the optimal bounds of the ν_e-CC inclusive analysis [17] defined in (5.14). The surface of fractional uncertainty is smooth near the optimal bounds.

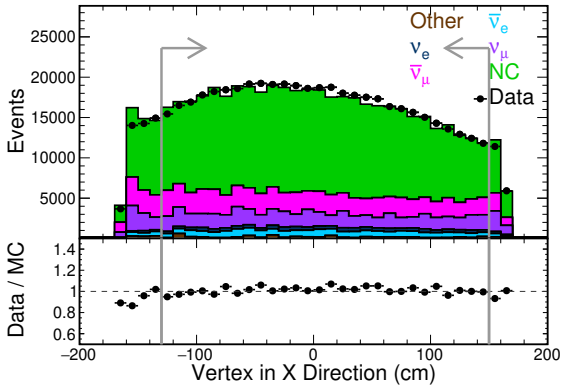

(A) Vertex x-coordinate.

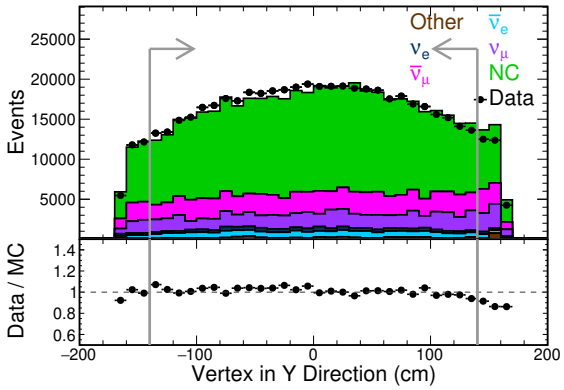

(B) Vertex y-coordinate.

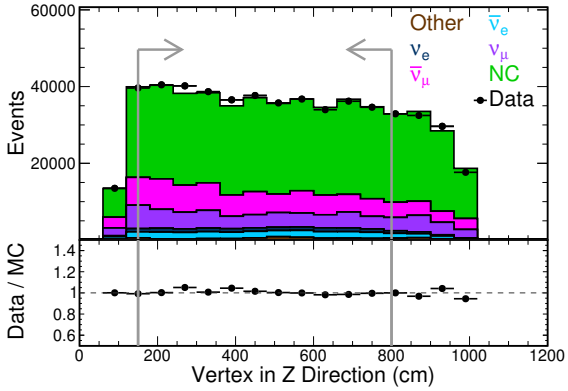

(C) Vertex z-coordinate.

FIGURE 5.3. Reconstructed vertex x- (A), y- (B), and z-coordinates (C) from RHC data and MC. Agreement is observed between the optimal fiducial bounds (5.14).

Clear separation is observed between interactions with and without a true muon in the final state.

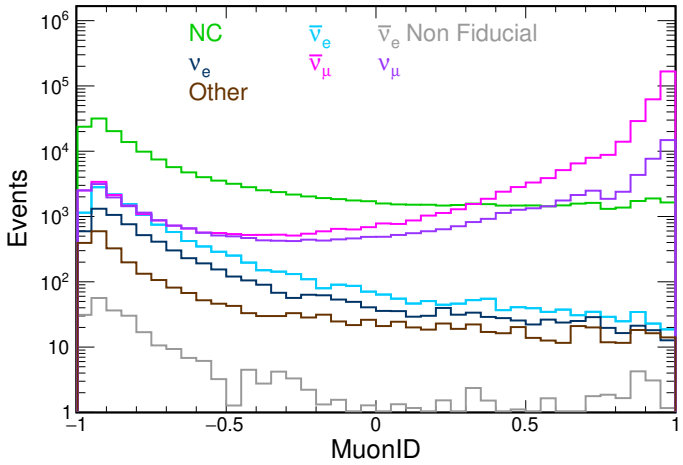

FIGURE 5.4. Maximum MuonID classification score per slice of simulated RHC events, broken down by CC flavor and NC. Clear separation is observed between interactions with and without a true muon in the final state.

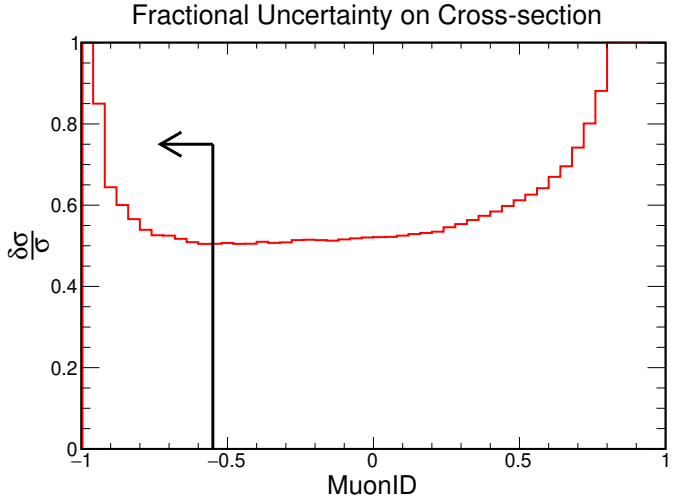

FIGURE 5.5. Fractional uncertainty on total cross section as a function of MuonID cut value. The optimal cut is found to be MuonID < -0.55.

The optimization procedure described in Section 5.2.5 results in an optimal cut on MuonID score requiring a score of less than -0.55 (Figure 5.5).

5.3. Cut Flow and Composition of Analysis Sample

The overall signal selection efficiency and purity as individual selection criteria are progressively applied are shown in Table 5.1. The largest impact comes from the cut on reconstructed

electron kinematics. In total, almost $9{,}000$ signal events are expected to be selected with 30% efficiency, resulting in a sample with 17% signal purity.

Figure 5.6 shows the predicted distribution of events in bins of reconstructed electron kinematics for both RHC and FHC samples of nominal MC. The ν_μ-CC and $\bar{\nu}_\mu$-CC backgrounds diminish at high electron energy and significant NC backgrounds are predicted throughout the phase space especially in low energy bins.

Figures 5.42, 5.44 and 5.45 show the selected signal events in RHC beam mode broken down by interaction mode. All modes contribute significantly to the final sample, particularly QE and MEC interactions at lower energies and DIS at higher energies.

TABLE 5.1. Overall efficiency and signal purity as stages of the selection criteria are applied to an RHC MC sample normalized to 12.6×10^{20} POT.

Cut	Signal	Bkgd.	Total	Signal Efficiency	Efficiency Relative to Previous	Signal Purity
Data Quality	18,094	3.2×10^6	3.2×10^6	0.619	(1)	0.006
NHits	15,535	3.0×10^6	3.0×10^6	0.531	(0.859)	0.005
Front Planes	15,483	2.9×10^6	2.9×10^6	0.529	(0.997)	0.005
Fiducial	15,163	1.2×10^6	1.2×10^6	0.518	(0.979)	0.012
Contain	10,939	6.4×10^5	6.5×10^5	0.374	(0.721)	0.017
Kinematic	10,567	3.0×10^5	3.1×10^5	0.361	(0.966)	0.034
MuonID	8,705	42,741	51,446	0.298	(0.824)	0.169

5.4. SYSTEMATIC UNCERTAINTIES

Systematic uncertainties are quantified using additional samples of simulation with adjusted detector properties, or event weights that result in shifted distributions. Complete re-simulation is necessary when the source of the uncertainty, like detector threshold levels, affects basic reconstruction. Weights are used to adjust interaction yields, as is the case of flux and cross-section

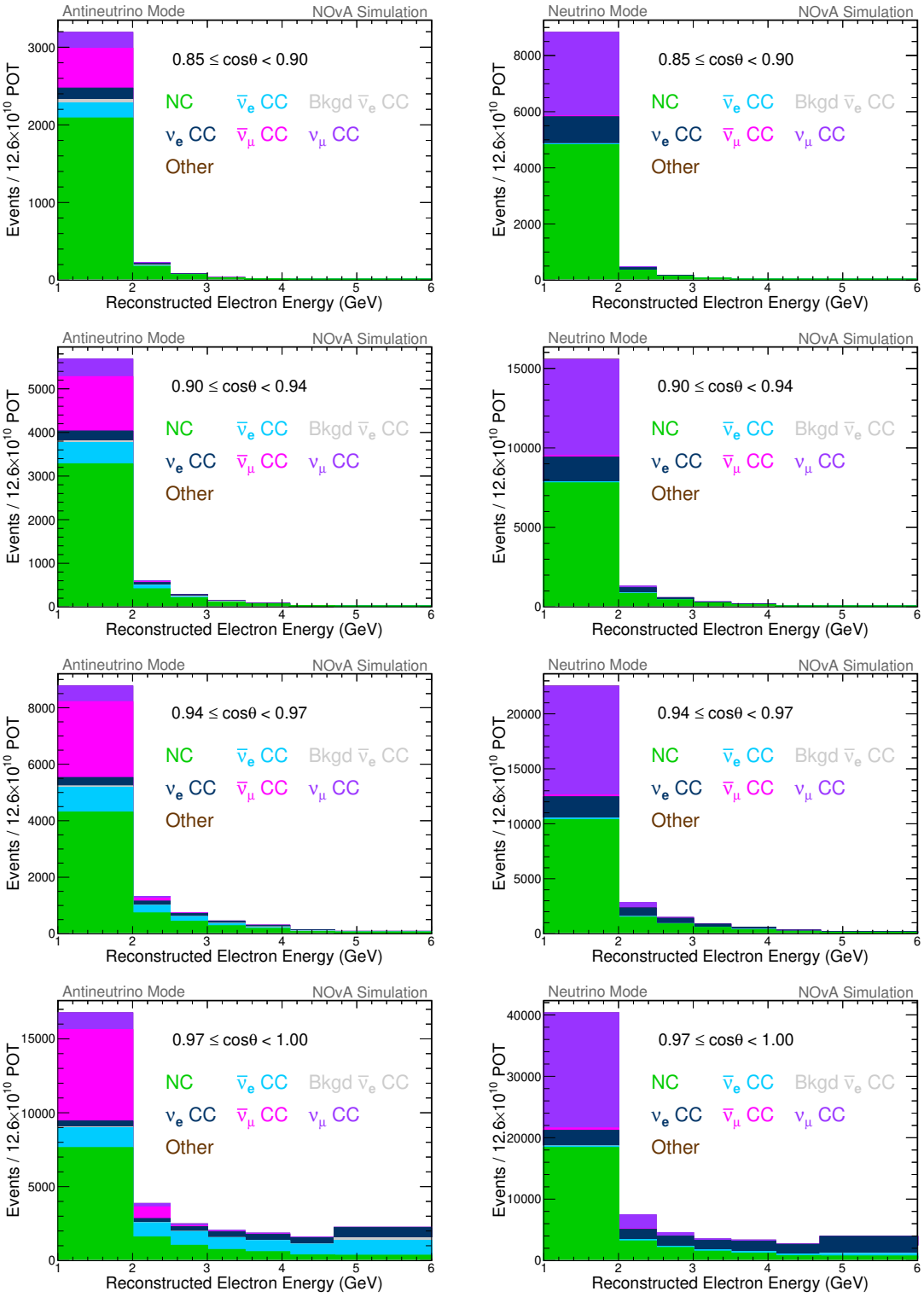

FIGURE 5.6. Selected events from the nominal RHC (left) and FHC (right) MC samples broken down by CC flavor and NC interactions.

model uncertainties. A "multiverse" approach is used to correlate uncertainties among the many parameters of the flux and cross-section models.

5.4.1. Flux Uncertainties. As described in Section 4.1, the neutrino flux at the NOvA ND is simulated using the g4numi package. g4numi predicts the production of hadrons from collisions between MI protons and the NuMI target using the FTFP_BERT [127] hadron production model implemented in geant4. Hadrons are subsequently propagated through a detailed specification of the NuMI beam line. The simulation is corrected to better match external hadron-production data using ppfx and event-by-event weights,

$$w_i = \frac{N_i^{\text{data}}}{N_i^{\text{MC}}} \tag{5.15}$$

where i represents the initial and final state of the interaction, N_i^{data} is data from hadron production experiments, and N_i^{MC} is the MC prediction of the process [96]. Where data are unavailable, ppfx uses isospin symmetry and material scaling arguments to extrapolate to these processes.

Flux uncertainties are estimated using a multiverse method that uses reported uncertainties on hadron production measurements. For each hadron production dataset, the reported covariance matrix is used together with the measurement to randomly sample from the multivariate Gaussian distribution they define. The sampled data, $N_i^{\text{data'}}$, are then used to calculate a new weight:

$$w_i' = \frac{N_i^{\text{data'}}}{N_i^{\text{MC}}}. \tag{5.16}$$

This sampling is repeated 100 times to produce 100 weights[†] for every neutrino. Applying the weights to the neutrino events as they are filled into histograms creates an ensemble of distributions that have been varied within the uncertainties of the hadron production data. The spread of the universes is measured as the overall hadron production uncertainty.

Figure 5.7 shows hadron production uncertainties derived by PPFX for FHC ν_μ and RHC $\bar{\nu}_\mu$ fluxes from [13]. The driving contributor to the total uncertainty is from nucleon interactions with targets that are not contained in the hadron production data. Figure 5.8 shows the spread of PPFX universes predicting RHC $\bar{\nu}_e$ flux. The total hadron production uncertainty on the average flux used for the double-differential $\bar{\nu}_e$-CC measurement is roughly 13%.

Neutrino flux is also affected by uncertainty in the configurations of the components that focus the NuMI beam. Table 5.2 lists the parameters and associated uncertainties of the various beam components used to simulate the flux [2]. Figure 5.9 shows the effect of the beam focusing uncertainties on the analysis. The most significant impact comes from uncertainty in the water cooling layer surrounding the target.

5.4.2. Cross-section Modeling Uncertainties. The simulation of neutrino interactions with nuclei, including final-state kinematics, is done with a reweighting technique using weights provided by the GENIE software package [128] and implemented with the NOvARwgt software package [129]. GENIE allows for model parameters, or knobs, to be independently adjusted resulting in changes to exclusive interaction yields. Event weights are developed to capture the effects from varying the knobs so that when applied the nominal MC, the event distributions change as if the simulation had been reproduced with the given knob configuration.

[†]The number of PPFX universes available was limited by the computational resources available at the time the simulation files were produced.

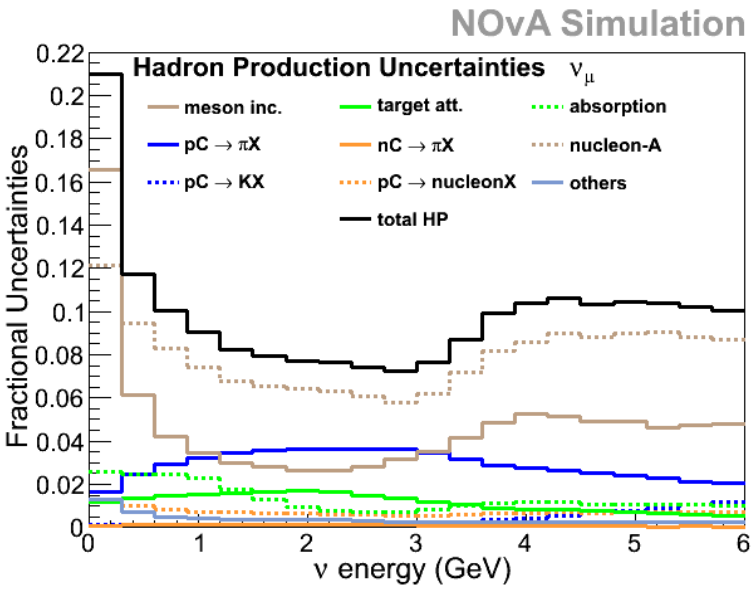

(A) FHC ν_μ

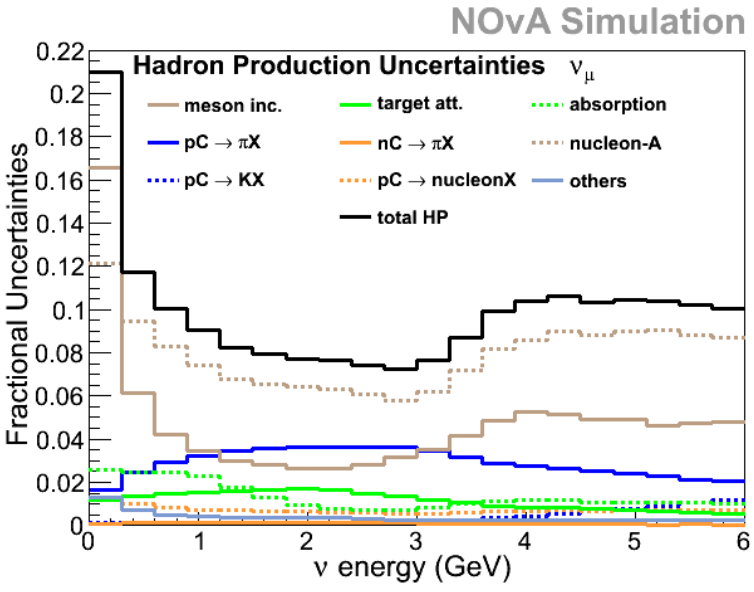

(B) RHC $\bar{\nu}_\mu$

FIGURE 5.7. Hadron production uncertainties on FHC ν_μ (A) and RHC $\bar{\nu}_\mu$ (B) from [13]. The dominant source (nucleon-A) is from nucleon interactions with targets not covered by data.

Figure 5.10 shows the effect of each knob on the rate of signal interactions and on the number of selected signal events in the ND. The 40 most-impactful knobs out of 72 total are shown. Knobs of the RES and DIS models generally have the largest impact, especially before high-multiplicity

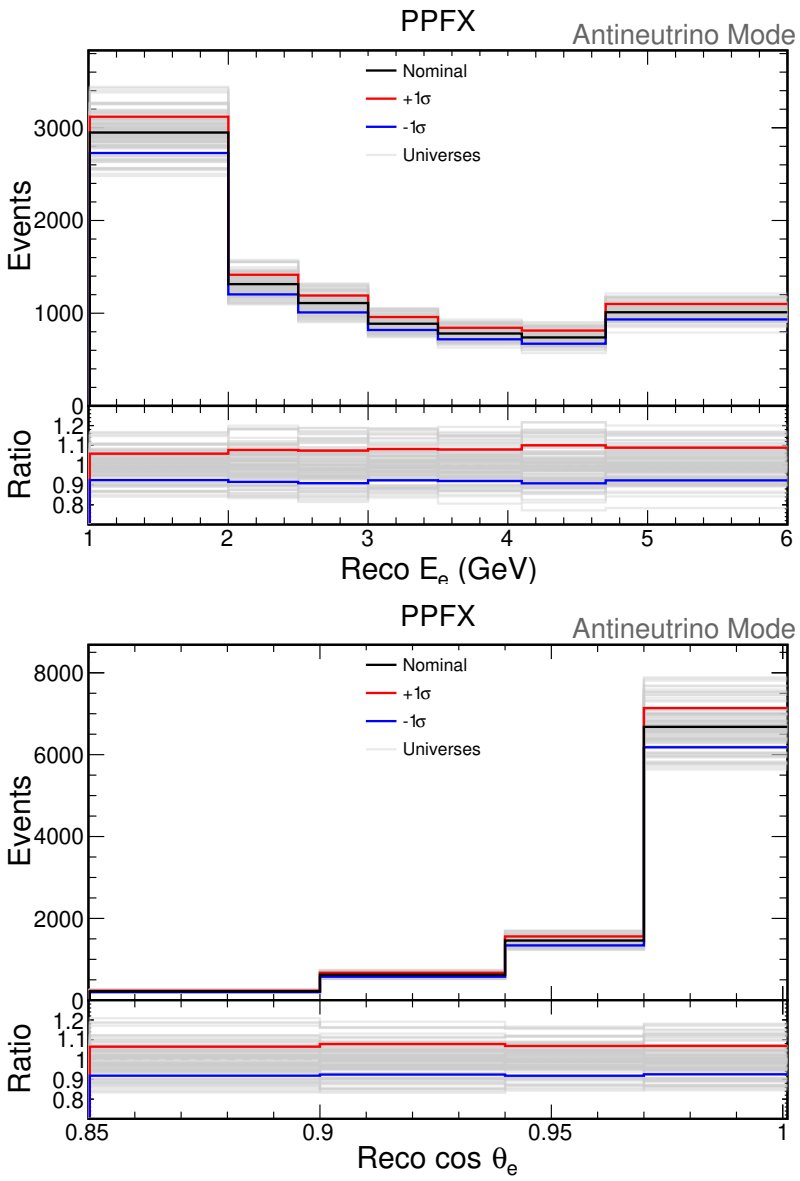

FIGURE 5.8. Ensemble of PPFX universes of selected events in bins of reconstructed electron energy (top) and scattering angle (bottom).

events are removed by selection. After selection, zero-meson events make up most of the sample, and the knobs of zero-meson models have the largest impact.

Since there are numerous adjustable model parameters, many of which are correlated, the multiverse method described in Section 5.4.1 is used to derive an uncertainty. For each universe,

TABLE 5.2. Parameters of the NuMI beam simulation and associated uncertainties from [2]. Decay Pipe B_i is the magnetic field along the i axis of the decay pipe

Beam Component	Nominal Value	Uncertainty
Horn Current	$\pm 200\,\mathrm{kA}$	$\pm 2\,\mathrm{kA}$
Horn1 Pos. X	$0\,\mathrm{mm}$	$\pm 3\,\mathrm{mm}$
Horn1 Pos. Y	$0\,\mathrm{mm}$	$\pm 3\,\mathrm{mm}$
Horn2 Pos. X	$0\,\mathrm{mm}$	$\pm 3\,\mathrm{mm}$
Horn2 Pos. Y	$0\,\mathrm{mm}$	$\pm 3\,\mathrm{mm}$
Beam Pos. X	$0\,\mathrm{mm}$	$\pm 0.2\,\mathrm{mm}$
Beam Pos. Y	$0\,\mathrm{mm}$	$\pm 0.2\,\mathrm{mm}$
Beam Spot Size X	$1.3\,\mathrm{mm}$	$\pm 0.2\,\mathrm{mm}$
Beam Spot Size Y	$1.3\,\mathrm{mm}$	$\pm 0.2\,\mathrm{mm}$
Horn Water Layer	$1\,\mathrm{mm}$	$\pm 1\,\mathrm{mm}$
Target Pos. Z	$-143.3\,\mathrm{cm}$	$\pm 7\,\mathrm{cm}$
Decay Pipe B_x	$0\,\mathrm{G}$	$0.1\,\mathrm{G}$
Decay Pipe B_y	$0\,\mathrm{G}$	$-0.3\,\mathrm{G}$
Decay Pipe B_z	$0\,\mathrm{G}$	$-0.07\,\mathrm{G}$

all parameter values are sampled simultaneously from Gaussian distributions describing parameter uncertainties. Each deviate is associated with a weight, and the product of all the deviate weights is used to weigh the neutrino event. Four-hundred (400) random knob configurations are used to produce an ensemble of event distributions and the spread of the ensemble defines the overall cross-section modeling uncertainty.

5.4.3. Detector Uncertainties.

5.4.3.1. *Detector Light Model Uncertainties.* As charged particles traverse the scintillator, photons are emitted by excitation and subsequent de-excitation of the scintillating material and Cherenkov radiation[‡]. The total number of photons emitted by the passage of charged particles through the NOvA detector that are subsequently collected by the fiber is

$$N_\gamma = F_{\text{view}}(Y_s E_{\text{Birks}} + \epsilon_C C_\gamma) \tag{5.17}$$

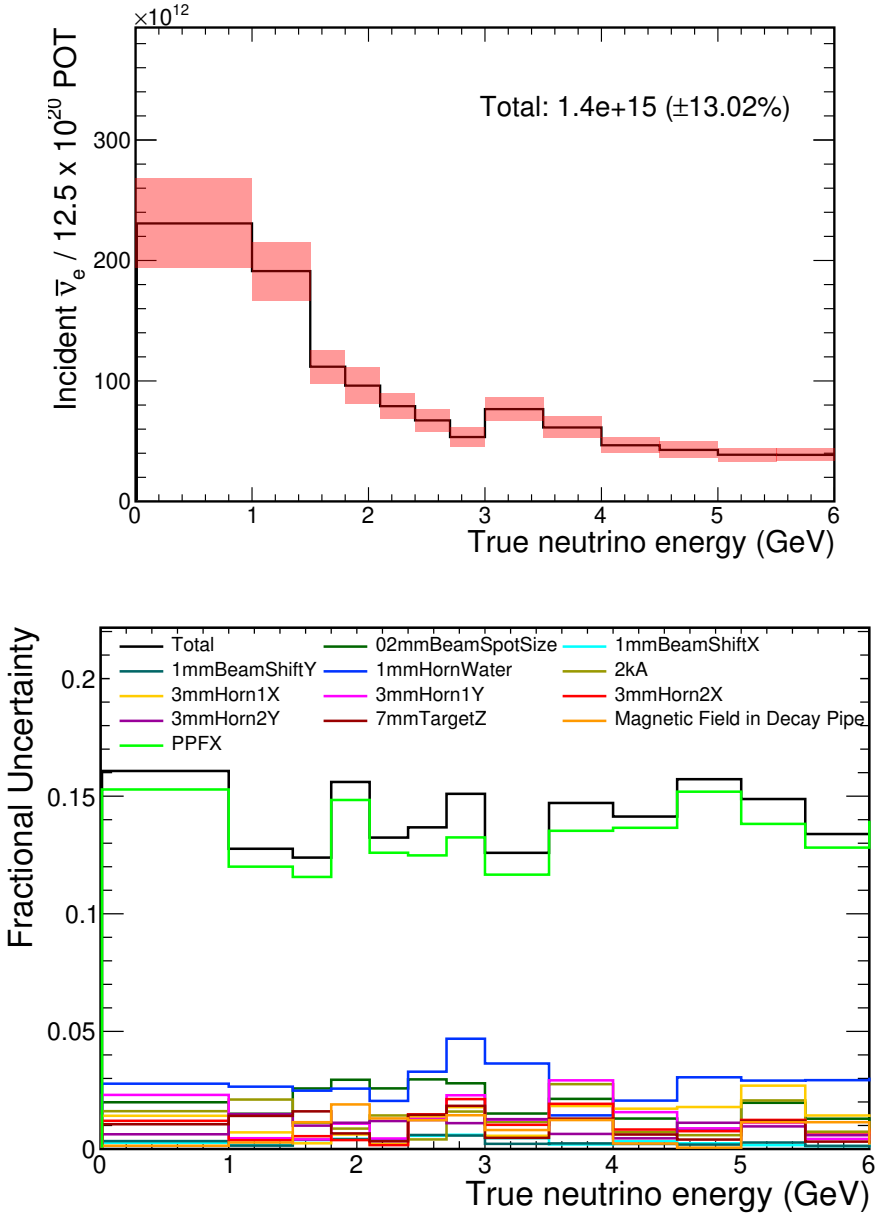

FIGURE 5.9. Top: Electron antineutrino flux at the NOvA ND. Bottom: Flux uncertainties from beam focusing and hadron production.

where E_{Birks} and C_γ are the number of photons emitted by scintillation and Cherenkov emission, respectively. Y_s and ϵ_C are scaling factors on scintillation and Cherenkov emission, and F_{view} is an overall scaling factor for each view of each detector. Attenuation of light by the wavelength-shifting fiber is also accounted for [18]. Four F_{view} parameters, Y_s, and ϵ_C are fit to cosmic muons and beam muons and protons [130]. The best-fit parameter values define the nominal light model

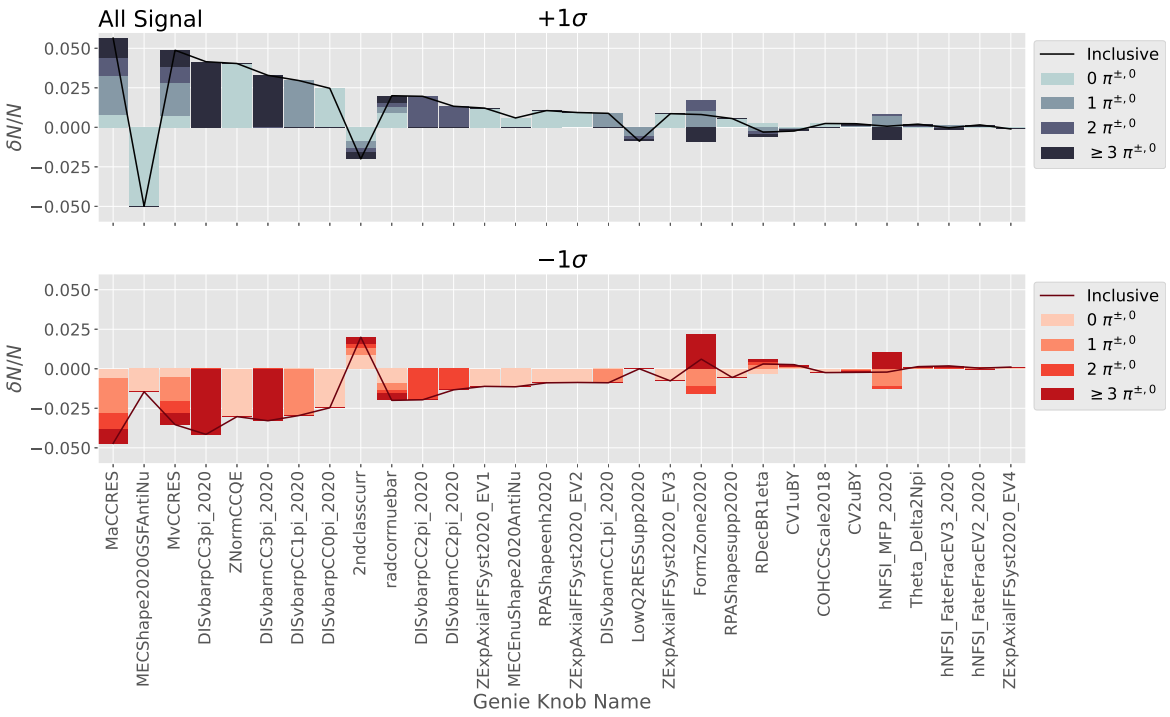

(A) All signal events.

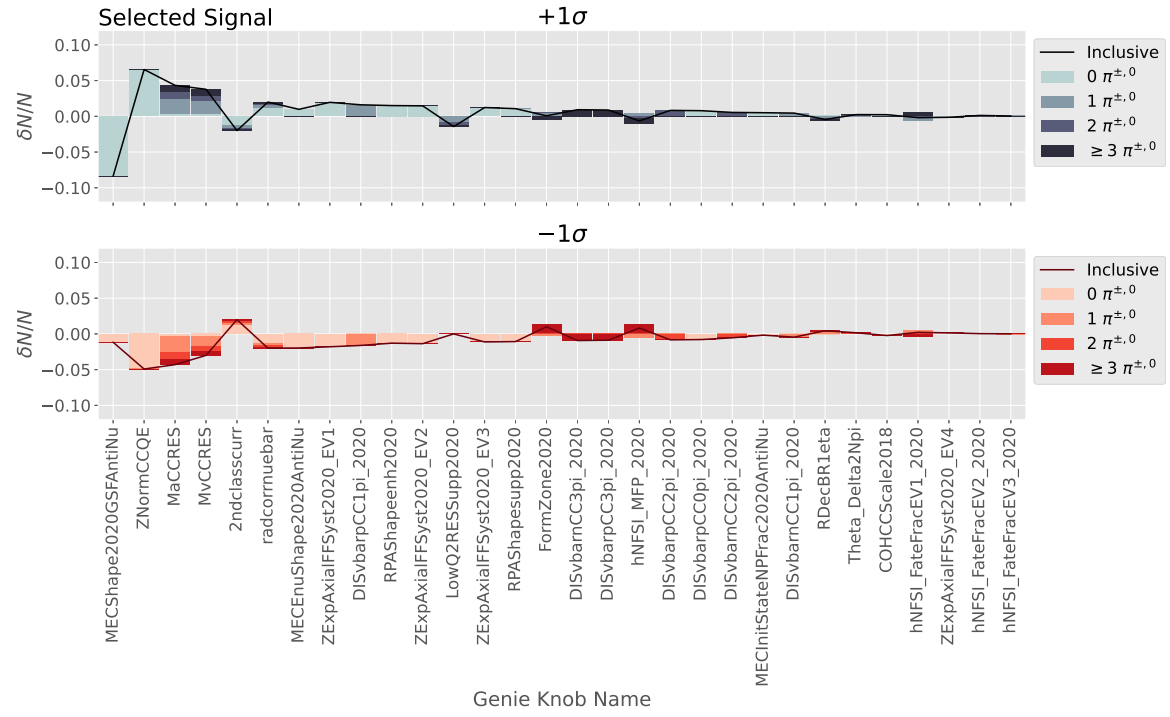

(B) Selected signal events.

FIGURE 5.10. Fractional change in all signal (A) and selected signal (B) event rate due to varying individual GENIE parameters $\pm 1\sigma$, broken down by final-state pion multiplicity. The 40 knobs with the largest impact on signal rate are shown.

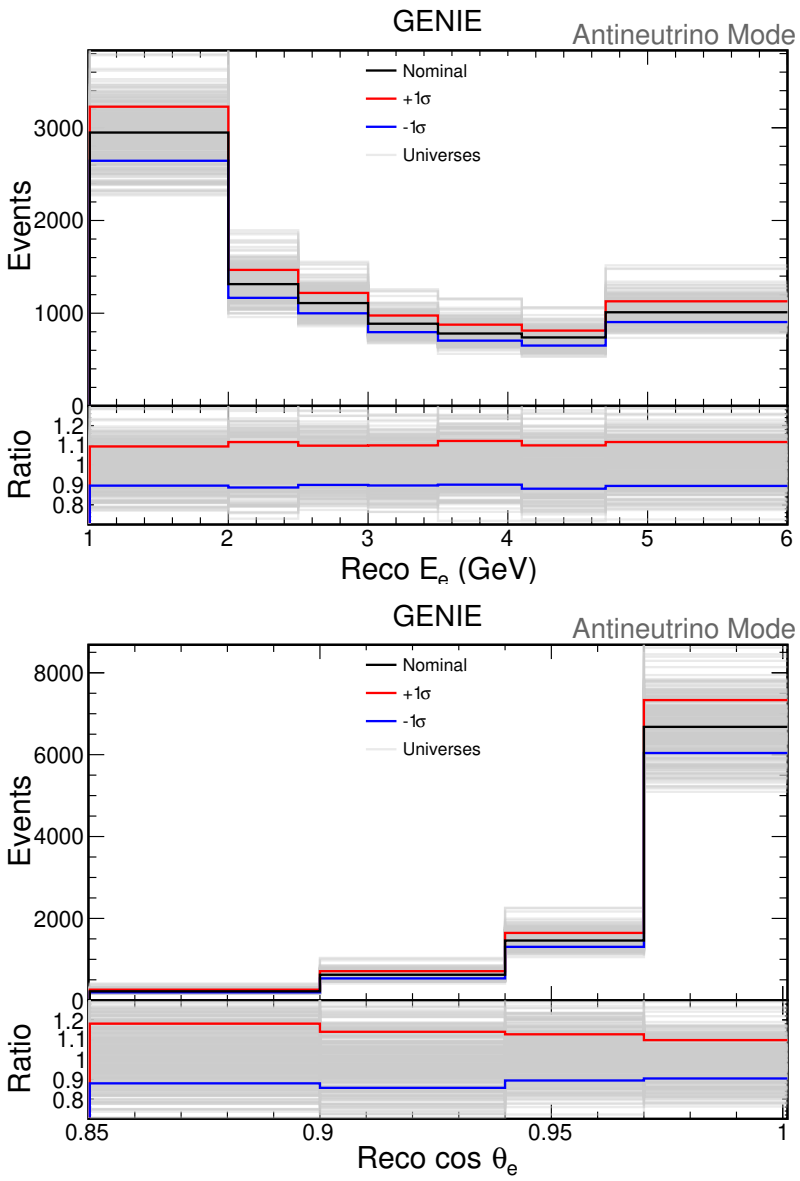

FIGURE 5.11. GENIE multiverse of selected signal events in bins of reconstructed electron energy (top) and scattering angle (bottom).

used to simulate photon emission due to the passage of charged particles through the NOvA detectors.

An uncertainty on the Cherenkov scaling factor (ϵ_C) is included to cover discrepancies between proton dE/dx measured in data and simulation [130]. The scale of the uncertainty is

‡Cherenkov radiation is the emission of photons by charged particles propagating through a dielectric medium at speeds greater than the speed of light in the dielectric.

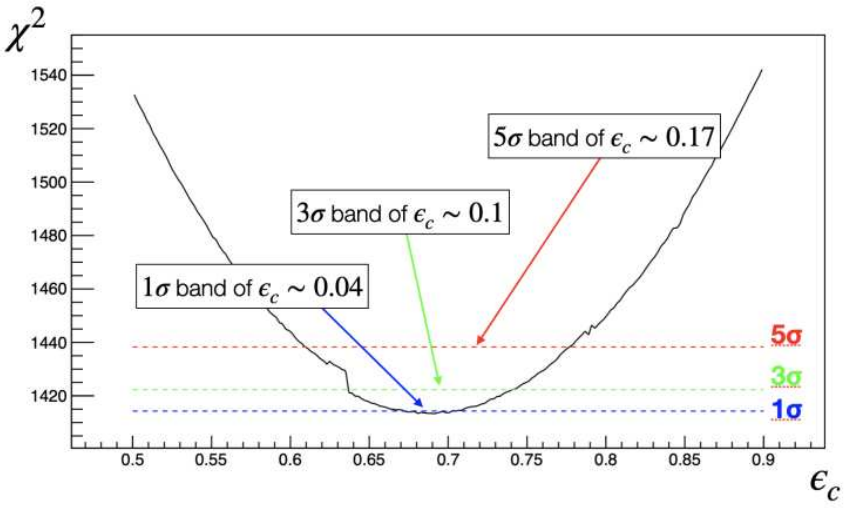

FIGURE 5.12. Profile of the Cherenkov scaling factor of the NOvA light model [18]. The 3σ interval is conservatively chosen to represent the uncertainty in Cherenkov photon production.

determined by χ^2-profile as a function of ϵ_C in a fit to the light model tuning data. Figure 5.12 shows the result of the profiling. The 3σ interval is conservatively chosen to represent the uncertainty in Cherenkov photon production.

Similarly, uncertainty in the scaling factors F_{view} is evaluated. A 2-dimensional χ^2-profile is produced as a function of F_{XZ} and F_{YZ} as shown in Figure 5.13. The 3σ region is conservatively chosen to represent the uncertainty in the overall scaling of photon production, resulting in a $\pm 5\%$ uncertainty on both F_{XZ} and F_{YZ}.

5.4.3.2. *Detector Calibration Uncertainties.* The procedures described in Section 3.4.1 enable a reliable calibration of detector response that is used universally for all types of particles. However, uncertainties in the models used to perform the calibration will lead to uncertainties in the calibration itself. To evaluate these uncertainties, calibrated simulation and data are compared.

An uncertainty is evaluated on the attenuation correction calibration by comparing the corrected number of photoelectrons between data and simulation. Figure 5.14 shows measured PE corrected for attenuation effects in data simulation from [19]. A piece-wise linear function is fit to

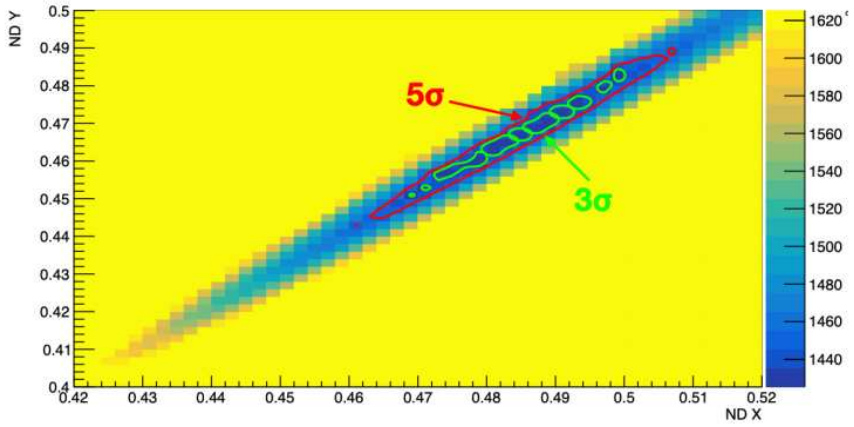

FIGURE 5.13. Profile of the F_{XZ} (ND X) and F_{YZ} (ND Y) scaling factors of the NOvA light yield model [18]. The 3σ region is conservatively chosen to represent the uncertainty in the overall scaling of photon production.

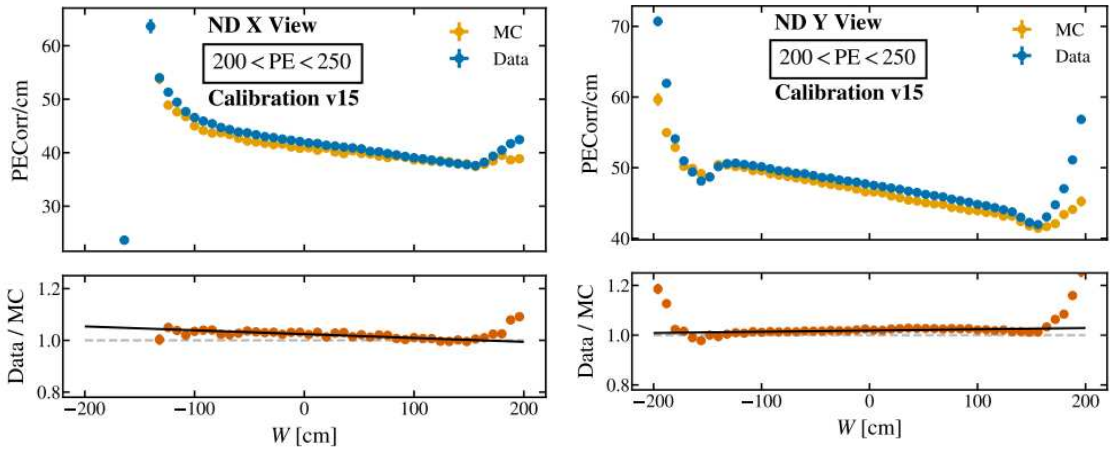

FIGURE 5.14. Corrected photoelectrons deposited per particle path length as a function of distance from center of the cell length is measured in data and simulation [19]. A line is fit to the Data/MC ratio between $-160 < W < 160$, which is used to derive a systematic uncertainty on the calibration procedure. Lines are also fit near the edges (not shown).

the ratio between data and simulation. This function is used to modify the attenuation calibration of an independently generated sample of simulation. This simulated sample of events represents an estimate of NOvA data under a 1σ-level modification of the cell-by-cell shape calibration.

An uncertainty on light yield due to detector ageing is assigned by comparing the measured number of hits in a slice as a function of time to simulation [130, 18]. The difference motivates

a 4.5% change to light yield every year with respect to the mid-point of data-taking, January 1, 2017.

An additional uncertainty is developed on the absolute energy scaling. In addition to the dE/dx of stopping muons, other standard candles are measured and compared to simulation [18]. The dE/dx of protons and muons from ν_μ-CC QE interactions and rock muons are measured to be within 2% of simulated predictions. The energy deposited by electrons that are produced by muon decays is measured to be with 1% of simulation, and the mass of the π^0 is measured to be within 1% of the global fit value [61]. These differences measured using standard candles of different particle species motivates an overall energy scaling uncertainty of $\pm 5\%$. This uncertainty is propagated through the analysis using independent simulation samples generated at shifted energy scales.

5.4.4. Neutron Uncertainties. Neutrons pass through the ND undetected because they have no electrical charge to activate the liquid scintillator. Instead, their presence is inferred based entirely on charged particles produced by secondary elastic and quasi-elastic interactions, making the energy of the neutron as it is leaving the nucleus difficult to determine. Since CC antineutrino interactions produce final state neutrons, the estimation of antineutrino energy from these interactions is susceptible to uncertainties in the modeling of neutron propagation.

Once neutrons from antineutrino interactions are ejected from the target, their propagation is handled by GEANT4. These neutrons elastically or inelastically scatter with the nuclear medium, most often producing protons or photons [131]. Figure 5.15 shows the visible energy distributions produced by neutron secondaries within a sample designed to isolate neutron prong candidates [20]. A significant over-estimation in low energy prongs is observed coinciding with

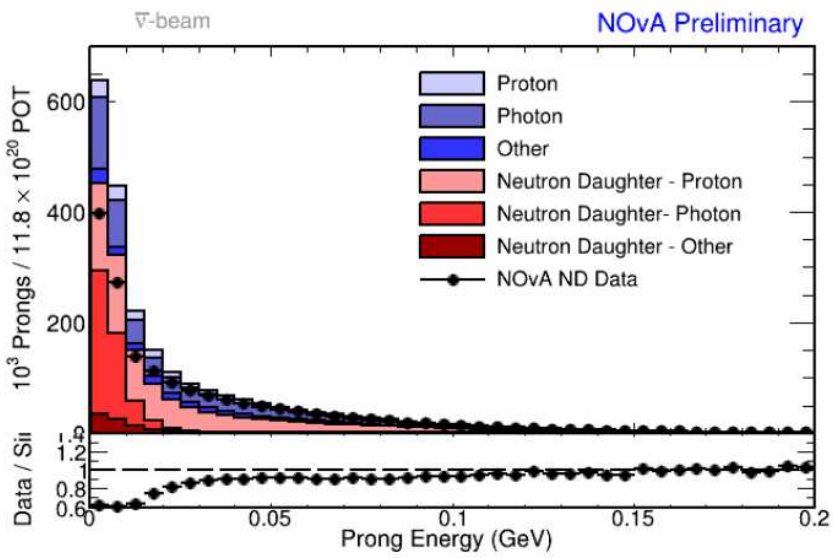

FIGURE 5.15. Prong energy distributions from a sample of neutron prong candidates in RHC beam mode [20]. The MC is broken down by the type of particle the parent neutron interacted with that is clustered into a prong. Comparisons to data show that the simulation significantly over-estimates the number of low-energy neutron prong candidates.

the distribution of photon daughter prongs, implying that GEANT4 is producing too many photons. Work is ongoing within the NOvA collaboration to understand this discrepancy with hints pointing at mismodeling of intranuclear neutron transport [131].

For this analysis, a systematic uncertainty is developed to account for the discrepancies observed between data and MC in Figure 5.15. Since visible energy deposits from neutron-daughter prongs below $40\,\mathrm{MeV}$ are likely responsible for the discrepancy, energy from these prongs is scaled with some probability. The amount of energy scaling, S, and probability of modification, P, are determined by grid search to find the parameters that result in the best χ^2 agreement between data and MC. The grid search finds $S = 3.6$ and $P = 0.33$ to produce the best match, which is shown in Figure 5.16. This neutron-daughter prong energy modification is implemented as a systematic uncertainty in the analysis. It is highly unlikely to impact the double-differential measurement since neutron-daughter prongs are rarely misidentified as the electron shower (most

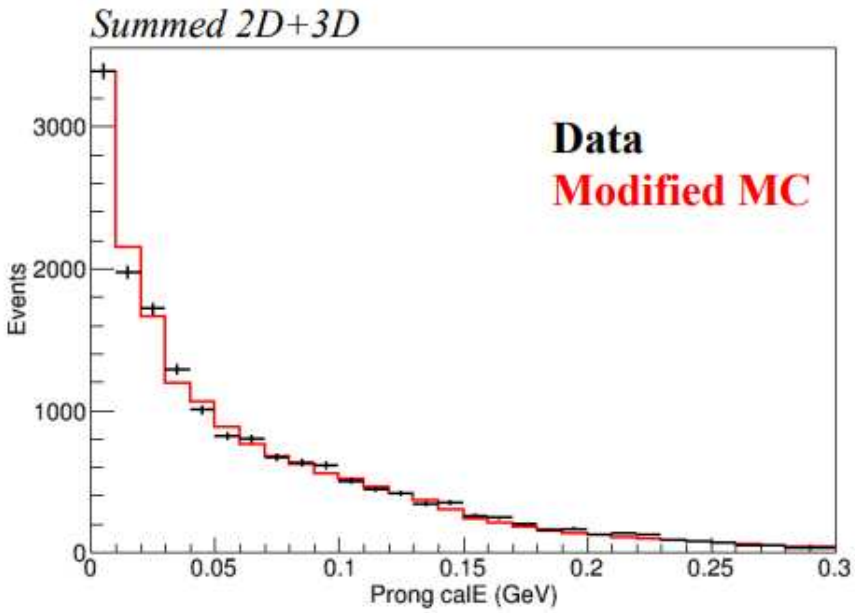

FIGURE 5.16. Calorimetric energy of 2- and 3-dimensional prongs (Summed 2D+3D) after modification by neutron-daughter prong energy scaling factor of $S = 3.6$ and probability of $P = 0.33$ [21].

energetic prong) and the implementation modifies only neutron-daughter prongs. It will, however affect the extracted $\sigma(E_\nu)$ and $\frac{\partial\sigma}{\partial Q^2}$.

5.5. SIGNAL ESTIMATION

5.5.1. PARTICLE IDENTIFICATION WITH A CONVOLUTIONAL NEURAL NETWORK. CNNs algorithms have proven to be valuable tools for particle identification in the context of High Energy Physics (HEP). The NOvA collaboration has developed CNNs for the classification tasks of determining neutrino interaction flavor [132] and individual particle identification [133], which have shown improvement over previous techniques. One advantage comes from the network's ability to discover features within simple inputs that are important to classification, rather than requiring algorithms that can introduce biases or impact efficiency. This makes the classification task insensitive to compounding errors in human-designed feature extraction and limitations of the user's

imagination. However, CNNs are difficult to interpret due to the inherent abstract representation of the classification model and lack of built-in quantification of classification uncertainty.

When employing CNNs for analysis tasks, one must consider the relative trade-offs between Deep Learning (DL) and traditional Machine Learning (ML) approaches. With traditional ML algorithms, like BDTs, features used for classification are manually designed. This benefits the analyzer by providing transparency as to what the algorithm is using to perform the classification. A disadvantage is that these features are susceptible to selection and representation inefficiencies. Conversely, DL algorithms are able to operate with very basic representations of data that are less susceptible to this type of inefficiency. However, the complexity of DL algorithms makes it difficult to determine the feature(s) the algorithm uses for classification. This is important in the context of neutrino cross section measurements because DL algorithms can result in classification bias toward the interaction models they are meant to constrain. On the other hand, it is often the case that statistical uncertainties are a significant contribution to the overall uncertainty of the measurement, which can be exasperated by classification inefficiencies of traditional ML algorithms.

This analysis uses a CNN, and its ability to automatically discover species-dependent characteristics of particle propagation, while controlling for biases toward neutrino interaction models. The network, called Prong Convolutional Vision Network (CVN) aids in the identification of signal $\bar{\nu}_e$-CC events by classifying charged particles in the NOvA ND. It was trained using a large sample of particles that were simulated without the use of a neutrino interaction model to avoid biasing the cross section measurement toward the models it is meant to constrain. The performance of the network is evaluated based on the classification accuracy of particles produced from neutrino interactions simulated with GENIE.

5.5.1.1. *Network Design.* The CNN is designed to process images of prongs produced in the NOvA ND. These images, or Pixel Maps (PMs), encode the propagation characteristics of the particle to be classified. These PMs are simple 2-dimensional arrays where each entry is the calibrated energy deposited into a cell in the prong cluster, and one PM is produced for each view. The PMs are assembled from a window of detector activity that is just 100 planes wide by 80 cells tall and preserves the local information of the interaction. The PM is anchored to the most upstream plane that contains hits[§] and centered vertically in each view independently. For example, Figure 5.17 shows PMs in the XZ view of simulated charged particles propagating in the NOvA ND.

The network is based on MobileNetV2 [134] and modified to process the independent PMs. Because there is expected to be no correlation in the propagation of energy between the X and Y directions, the network consists of two towers that independently processes PMs corresponding to the XZ or YZ views of the prong. Similar networks were developed for the NOvA oscillation analysis to identify neutrino interaction flavor [132, 117]. Each tower extracts the features in one prong PM, which are later combined and eventually processed by a 1024 node[¶] fully-connected neural network. This final layer is connected to five nodes corresponding to the five most common charged-particle species observed in the ND: electrons, photons, pions, protons, and muons. The output of each node is a value between 0 and 1, and is interpreted as the probability of the given particle to belong to the corresponding species. Together, the 5 output values must sum to 1.

[§]Eight additional planes downstream from the anchor must contain at least 4 hits to avoid including extraneous noise.

[¶]A neural network node is the basic unit of a neural network. In general, it is a function that takes a number of input variables, $\vec{x}$, and ouputs a single value, y. Each node has a number of weights, $\vec{w}$, equal to the number of input variables. The weight values are determined by the training procedure.

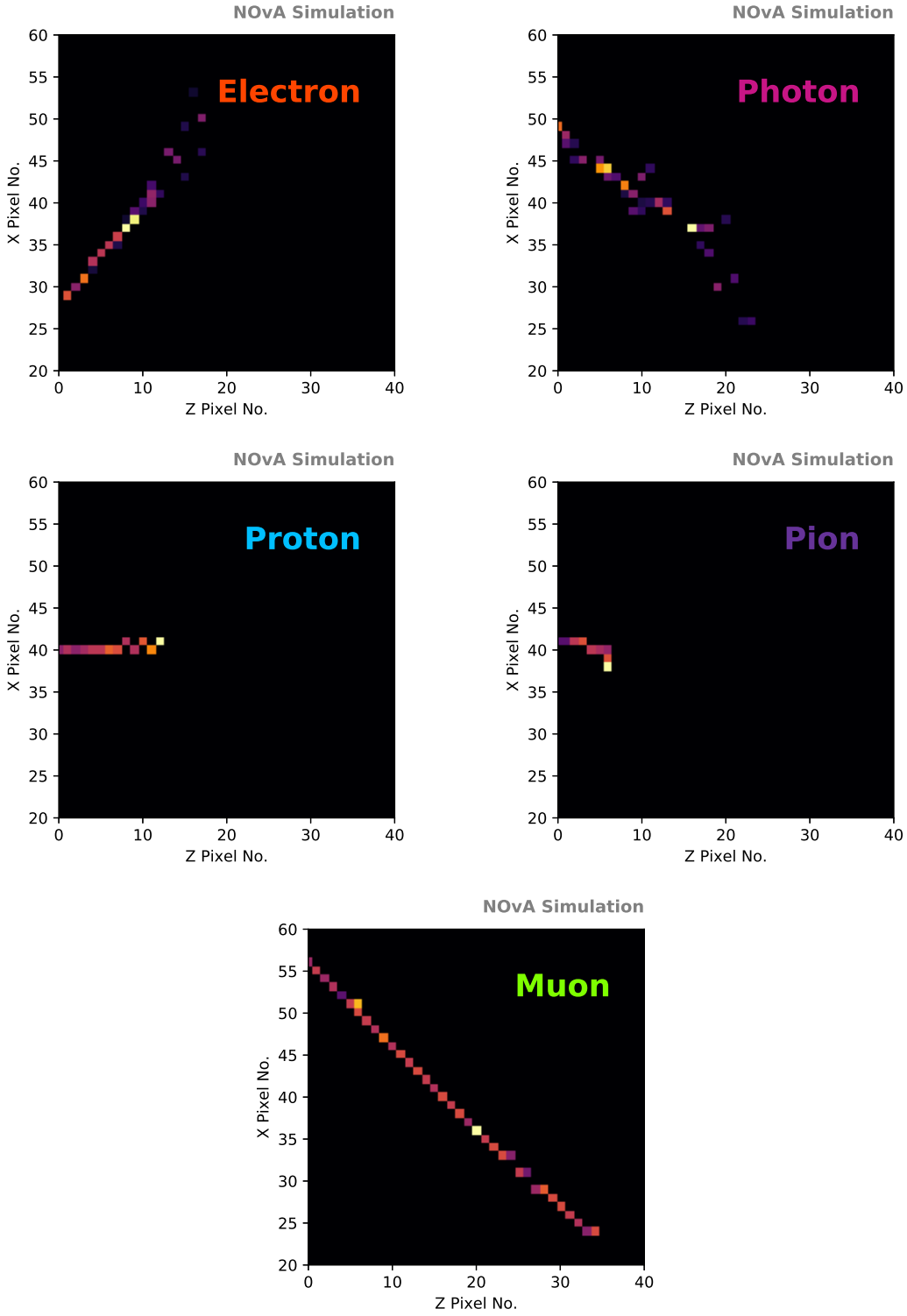

FIGURE 5.17. Pixel maps of simulated charged particles propagating in the NOvA ND.

TABLE 5.3. Upper-bound momenta used to simulate freely propagating particles.

Particle type	$\lvert\vec{p}\rvert_{\text{max}}$ (GeV)
Electron	5.0
Photon	5.0
Charged Pion	1.5
Proton	2.5
Muon	4.0

TABLE 5.4. Percent of surviving muons, pions, and protons after the containment filter.

Particle type	Pass Containment
Charged Pion	68%
Proton	73.7%
Muon	17.6%

5.5.1.2. *Training Sample.* Neutrino interaction models impact the simulation by influencing the neutrino interaction type, energy dependence, and final state particle kinematics and multiplicities. To avoid introducing a bias toward these population characteristics, and therefore the interaction model, a training sample is produced that does not rely on any interaction model. Instead, freely propagating particles are simulated in the ND in equal proportions and with kinematics distributed uniformly and isotropically in momenta.

Particle momenta are sampled uniformly from $0\,\text{GeV}$, to capture detection threshold effects, to an upper-bound momentum. The upper-bound, $|\vec{p}|_{\text{max}}$, is determined for each particle type based on GENIE simulation such that the full range of observed momenta is covered [135]. Table 5.3 shows $|\vec{p}|_{\text{max}}$ for each particle type included in the training sample[‖]. Particle trajectories are sampled uniformly to achieve 4π coverage to avoid biasing classification toward any preferred scattering angle.

[‖]Originally, the $|\vec{p}|_{\text{max}}$ of photons was determined to be $1.5\,\text{GeV}$ based on GENIE predictions. This was extended to $5.0\,\text{GeV}$ to be consistent with the $|\vec{p}|_{\text{max}}$ of electrons.

To save computation, muons, pions, and protons exiting the detector with more than $100\,\mathrm{MeV}$ kinetic energy are removed from further processing [136]. Table 5.4 shows the percent of surviving pions, protons, and muons after the containment filter is applied. Additionally, prongs with length greater than $5\,\mathrm{m}$ are removed from training because they are most often (95%) from muons and are easily identified with classical algorithms.

Imperfect reconstruction and secondary interactions can cause some particles to produce multiple prongs. This can happen when hadrons elastically scatter in the detector at angles too extreme for the prong-forming algorithm to contain or when secondary particles are produced during propagation that complicate the interaction topology. To avoid training the network on multiple representations of the particle initially simulated, one prong from every interaction was chosen based on a quality metric defined as the product of prong completeness and prong purity.

Figure 5.18 shows kinematic distributions of particles that pass the containment filter and are selected as the highest quality prong formed. Notably, the containment filter removes high-energy muons and hadrons that exit the detector, and all particles that start near the edges. Also note that these distributions only include photons generated from $0\,\mathrm{GeV}$ to $1.5\,\mathrm{GeV}$ momentum based on GENIE predictions, but that the upper bound on photon momentum was extended to $5.0\,\mathrm{GeV}$ for the final training sample in order to match the upper-bound momentum of simulated electrons.

The training sample is composed of particles with equal proportions to avoid introducing a preference in particle type to the classification task. Since π^+ and π^- particles are indistinguishable to the detector, these are included such that the sum of π^+ and π^- particles are equal to all

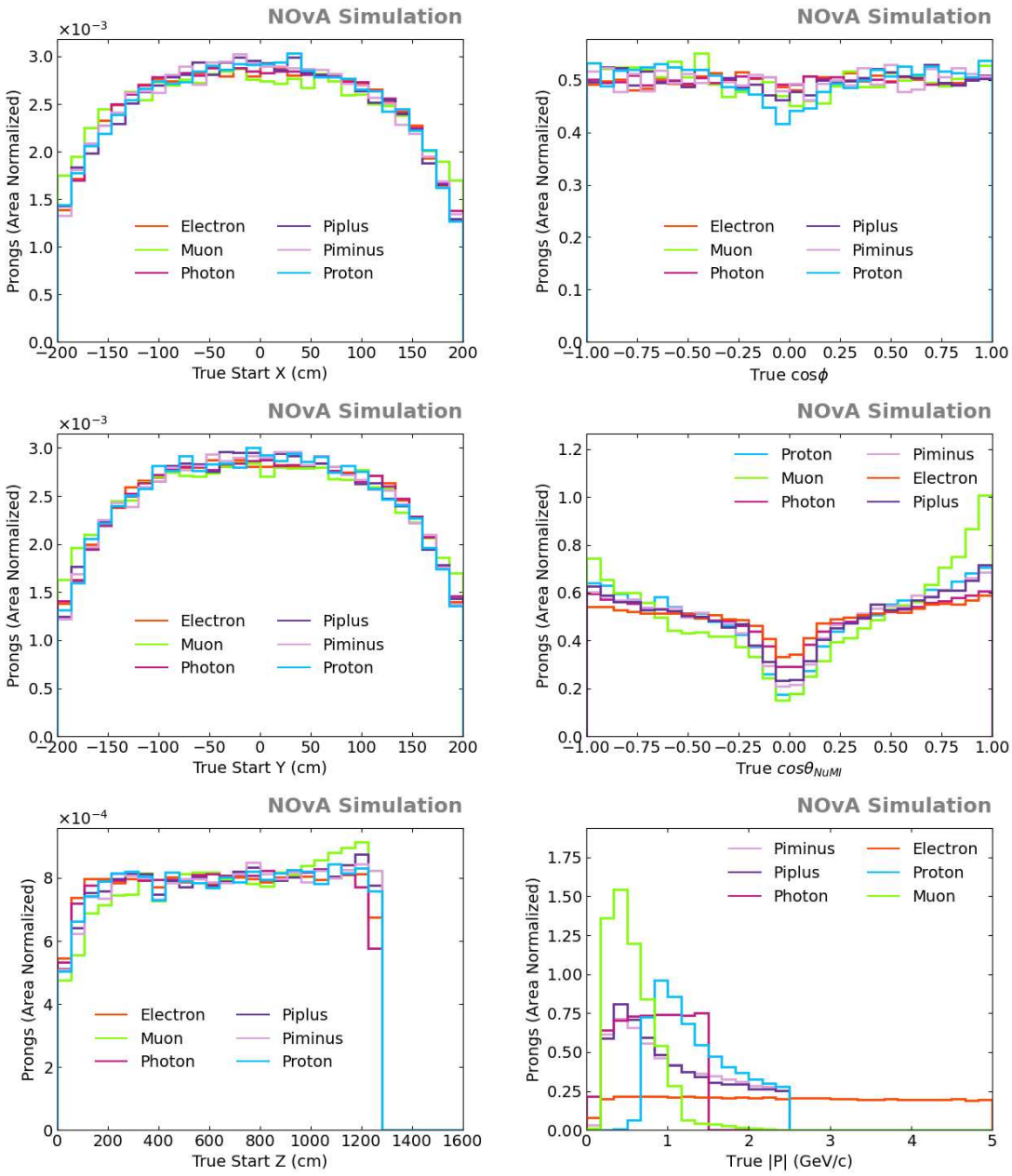

FIGURE 5.18. Particle kinematics of Prong CVN training sample.

other particles. Figure 5.19 shows the number of each particle type making up the training sample. In total, over 1.75-million particles were used to train the Prong CVN network, corresponding to 350,000 of each species.

[‖]These convolution blocks are made of separable convolutions, which are a defining feature of the MobileNetV2 architecture [134]. These two-stage convolutions are shown to be more computationally efficiency than standard convolutions and perform empirically comparable.

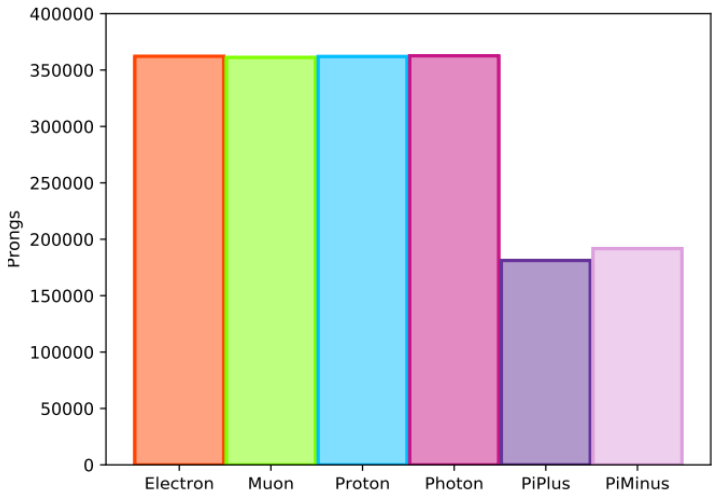

FIGURE 5.19. Particles in the Prong CVN training sample

TABLE 5.5. Prong CVN training hyperparameters optimized by grid search.

Hyperparameter	Optimized Value
batch size	64
training iterations	1000
testing iterations	100
learning rate	0.05
SGD Nesterov momentum	0.68
learning rate reduction factor	0.75
learning rate patience	10 epochs
early stopping patience	50 epochs

5.5.1.3. *Training.* Training was performed with a KERAS [137] implementation of Stochastic Gradient Descent (SGD) on the Fermilab Wilson Cluster [138] with NVIDIA Tesla Pascal P100 GPUs and optimized using a categorical cross-entropy loss function. Ten-percent (10%) of the training sample was used to test the network for overfitting during training. Hyperparameters** were chosen by grid-search optimization based on classification accuracy. Figure 5.21 shows classification accuracy and cross-entropy loss as a function of training epoch. Similarities between the solid and dashed lines indicate a lack of overfitting.

**Hyperparameters are parameters of the training process and are different from the model parameters that are optimized by the training.

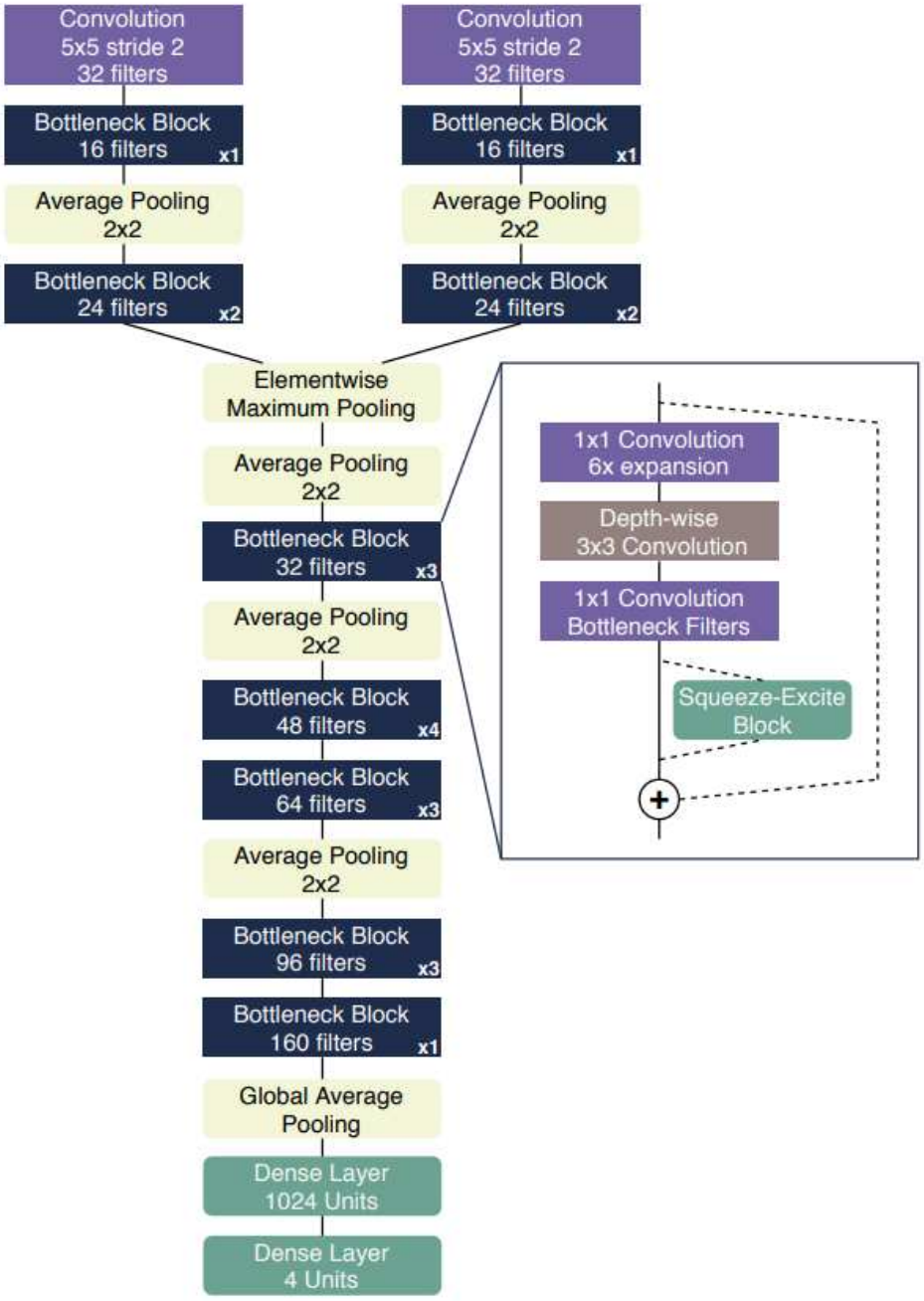

FIGURE 5.20. Diagram of the Prong CVN architecture [22] based on MobileNetV2.

5.5.1.4. *Performance.* The network evaluated is based on the accuracy of correctly classifying prongs from GENIE interactions to estimate performance on real data. One metric that evaluates binary classification is the Receiver Operating Characteristic (ROC) curve [139], which is a plot of the true positive rate versus the false positive rate of a classifier. Figure 5.22 shows ROC curves

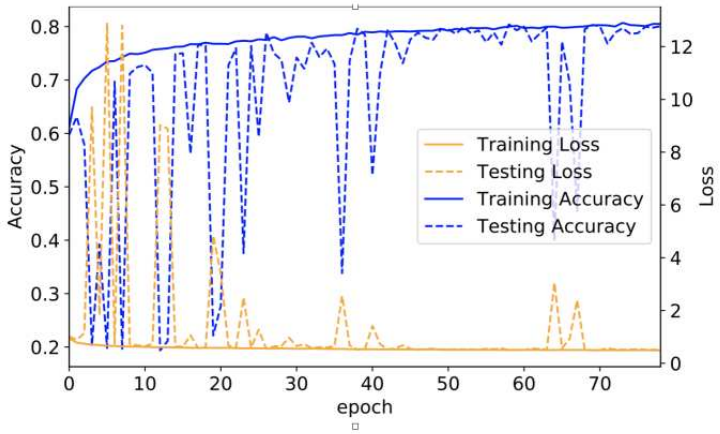

FIGURE 5.21. Training accuracy and loss as a function of epoch. Solid lines indicate the data sample used to minimize the loss and dashed lines indicate the statistically-independent data sample used evaluate over-fitting.

for each particle species under binary classification by the Prong CVN. A dashed line in drawn to indicate the classification performance level of a coin-flip. As these curves extend toward a false positive rate of 0 and a true positive rate of 1 (upper left corner), classification is considered more accurate. The Area Under the Curve (AUC) is a measure of probability of ranking one random positive occurrence higher than one random negative occurrence. This means that for each species label, S, the AUC is the probability of ranking one random prong of true species S_{true} as higher than a random prong as a different species S'_{true}. An AUC of 1 means that label S will always rank prongs of species S_{true} higher than species S'_{true}.

Signal and background efficiencies and purities are arranged in a matrix to illustrate how the network confuses the different particle species. Prong categorization is done by taking the highest Prong CVN score from the available species labels. Elements of an Efficiency Confusion Matrix (ECM) are defined as

$$\text{ECM}_{\hat{S},S} = \frac{\text{Number of prongs labeled } \hat{S}}{\text{Number of prongs of true species } S} \tag{5.18}$$

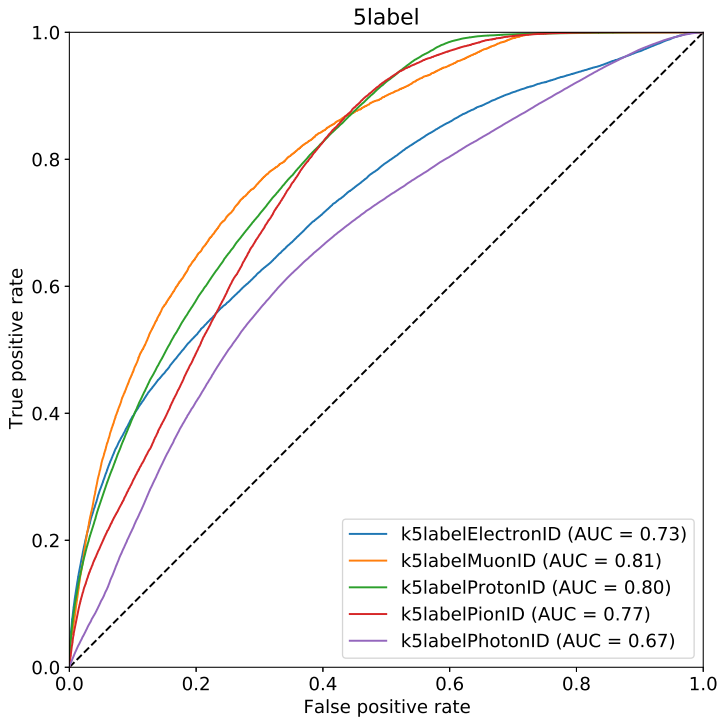

FIGURE 5.22. ROC curves for the Prong CVN classification of GENIE prongs.

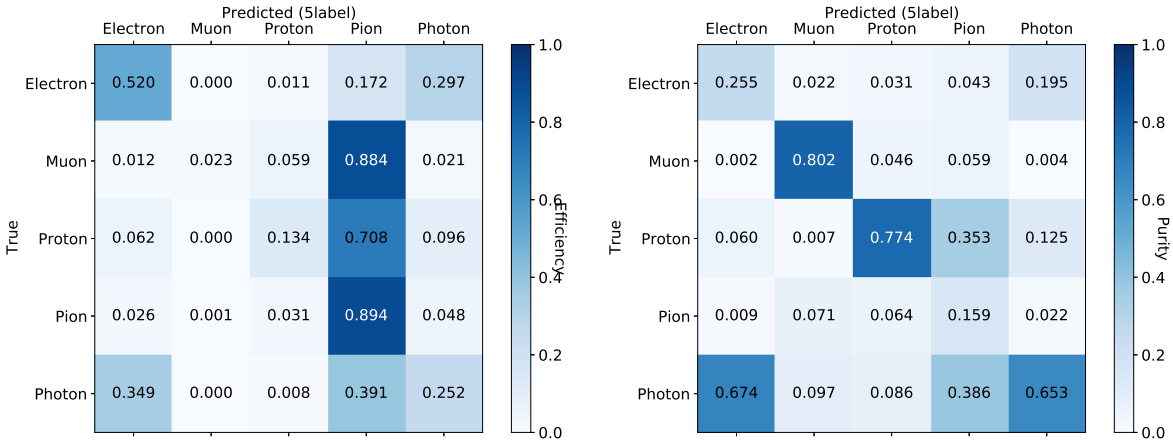

FIGURE 5.23. Confusion matrices for the Prong CVN evaluated on GENIE prongs.

where $\hat{S}$ is the predicted species label and S is the true species of the prong. Similarly, elements of a Purity Confusion Matrix (PCM) are defined as

$$\text{PCM}_{\hat{S},S} = \frac{\text{Number of } S \text{ prongs labeled } \hat{S}}{\text{Number of prongs labeled } \hat{S}}. \tag{5.19}$$

Figure 5.23 shows ECM and PCM for the Prong CVN. The ECM shows that the network tends to incorrectly classify true muon and protons as pions and, as expected, electrons and photons are indistinguishable. The PCM again shows confusion between electrons and photons and particularly poor performance in pion classification.

These metrics are reflected in score distributions when decomposed into true particle species. Figure 5.24 (Figure 5.25) shows electron and photon (muon and hadron) scores decomposed into true particle species. Pion confusion is shown in the PionID distribution where all particle species contribute throughout the score range including the high-scoring (high pion probability) tail. Electron and photon confusion is shown in the PhotonID and ElectronID distributions, where the high-scoring regions of each distribution are dominated by both true electrons and photons.

As shown in Figure 5.24, a strength of Prong CVN is in the identification of electromagnetic showers. However, additional information is required to determine whether the shower is caused by a positron produced by a signal $\bar{\nu}_e$-CC interaction or a photon produced by a NCπ^0 interaction, the largest background of the analysis.

5.5.2. Identification of $\bar{\nu}_e$-CC Interactions. A BDT is used in this analysis to selectively introduce event-level context into the signal selection procedure. Unlike a CNN, a BDT gives fine control over the information the algorithm uses to classify interactions. Relevant topological information is chosen to optimize separation between signal and NC events.

Resonant NC interactions are the largest background in the analysis due to the production of a π^0 in the final state that decays to two photons. Like electrons and positrons, photons electromagnetically cascade in the detector, producing wide showers of activity that are difficult to distinguish from electrons or positrons. Moreover, π^0 decay can produce two overlapping photons or only one photon that is energetic enough to make a prong. Both of these possibilities

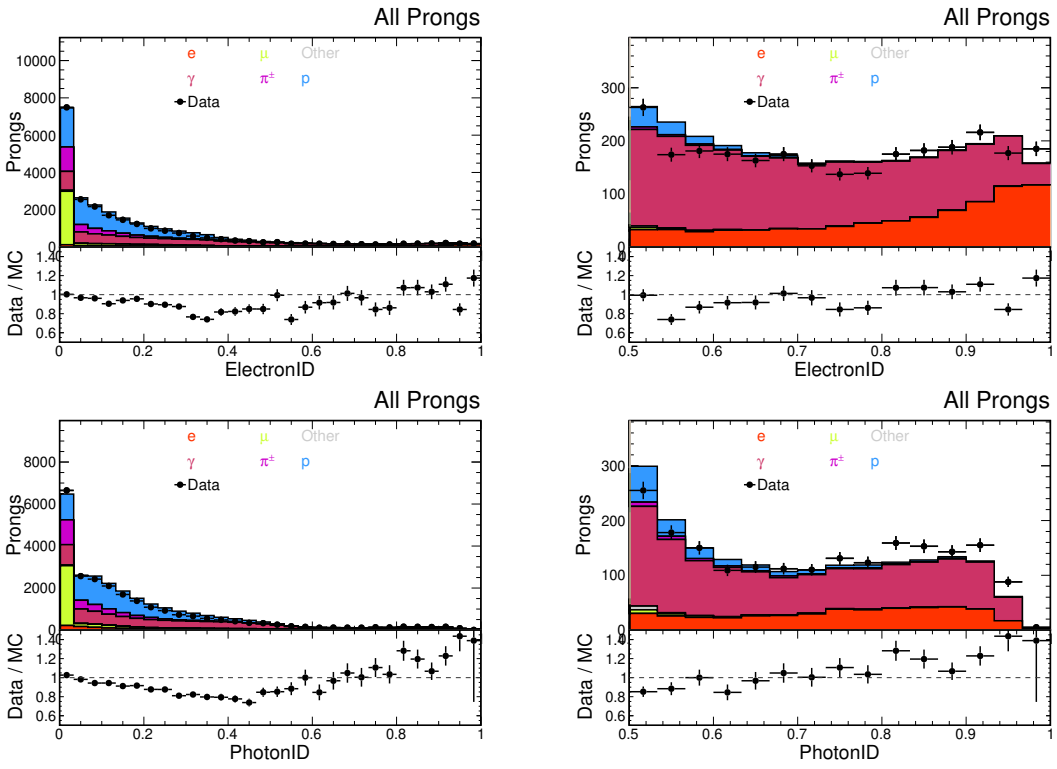

FIGURE 5.24. Prong CVN electron and photon scores decomposed into true particle species. The left column shows the full range of the scores ([0-1]) and the right column is zoomed in to [0.5-1].

perfectly mimic the topology of a CCQE $\bar{\nu}_e$ interaction. Reconstructed quantities that are sensitive to these effects are used in addition to the Prong CVN (Section 5.5.1) to train the BDT.

The input variables to the BDT are the following:

Electron Score: The largest value of the Prong CVN Electron score among all prongs in the event (the most electron-like prong).

Shower Width: The width of the most electron-like prong in the event. The Molière radius, which describes the evolution of electromagnetic shower radius as a function of propagation distance, is approximately constant with respect to electron energy. Prongs that cluster hadronic activity and semilinear photons from π^0 decay are typically wider and contribute to the high tail in the background distribution.

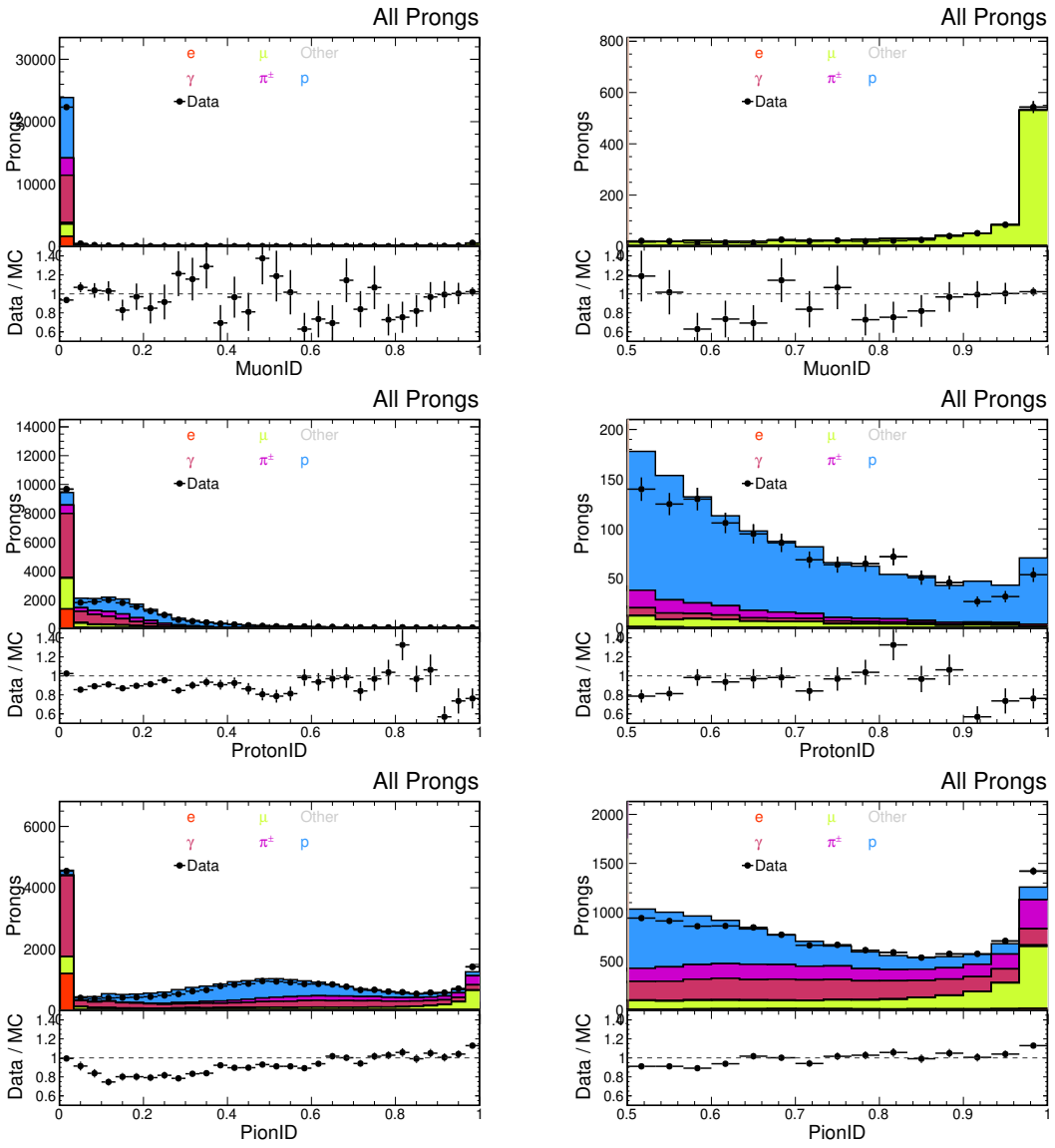

FIGURE 5.25. Prong CVN muon and hadron scores decomposed into true particle species. The left column shows the full range of the scores ([0-1]) and the right column is zoomed in to [0.5-1].

Shower Gap: The distance from the reconstructed interaction vertex to the start of the most electron-like prong. Positrons from true $\bar{\nu}_e$-CC interactions deposit visible energy immediately following the interaction vertex. A π^0 produced from a NC interaction will travel some time before decaying into photons, producing an observable gap between the start of the photon shower(s) and the reconstructed vertex.

***dE/dx* Log-likelihood ratio:** The difference between the logarithm of the likelihood function of the transverse electron and π^0 dE/dx. The transverse dE/dx profile of the most electron-like prong is compared to what is expected from electrons and overlapping photons from π^0 decay. The difference in log-likelihoods is a measure of which particle hypothesis the deposited energy profile is more consistent with.

The BDT outputs a score, called NueID, corresponding to the likelihood of a slice being either a ν_e-CC or $\bar{\nu}_e$-CC interaction. Figures 5.26 and 5.27 show the distributions and correlations of input variables. All variables show good separation between signal and background with little correlation.

The BDT was trained using the TMVA Toolkit [140]. Training hyperparameters are chosen by grid search optimization over a range of possible values [141]. The resulting network shows good separation between signal and background.

Figure 5.28 shows distributions of NueID classification scores in both FHC and RHC samples, broken down by neutrino interaction type. The network performs well at separating NC from ν_e-CC and $\bar{\nu}_e$-CC interactions, but cannot distinguish ν_e-CC from $\bar{\nu}_e$-CC interactions. Furthermore, figure 5.29 shows that the network is able to efficiently classify all modes of signal interaction, which is important for an inclusive measurement.

5.5.3. Template Fit Overview. A template fit is used to estimate sample purity by adjusting "templates" derived from simulation to agree with data. These templates are distributions of events belonging to specific categories that, when summed together, model the selected data. In a template fit, the normalization of the various templates are varied in search of the best fit to data. These templates must be significantly different from one another otherwise the model will be degenerate. Finally, the resulting normalization parameters are used to adjust the nominal purity

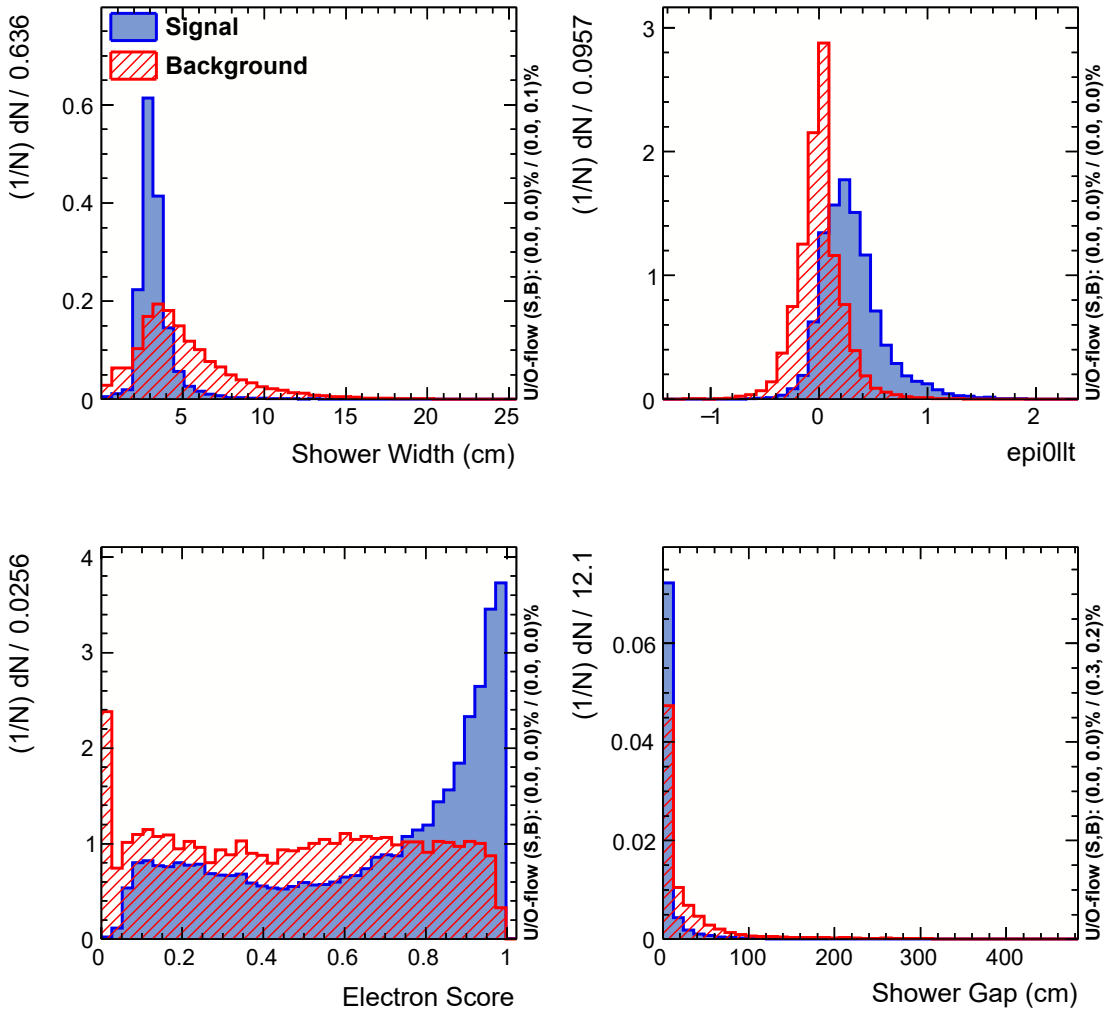

FIGURE 5.26. NueID training variables where "signal" is defined as true ν_e-CC or $\bar{\nu}_e$-CC interactions that pass the analysis preselection criteria.

prediction. Uncertainty on the estimated purity is derived from the normalization parameter uncertainties.

For this analysis, templates are produced from NueID distributions in each bin of electron energy and angle, and a global fit is performed. In each kinematic bin, the normalization of $\bar{\nu}_e$-CC, ν_e-CC, ν_μ- and $\bar{\nu}_\mu$-CC, and NC templates are varied to fit the measured NueID distribution. Purity is then estimated as a function of electron energy and angle and used to estimate the signal contained in the selected sample.

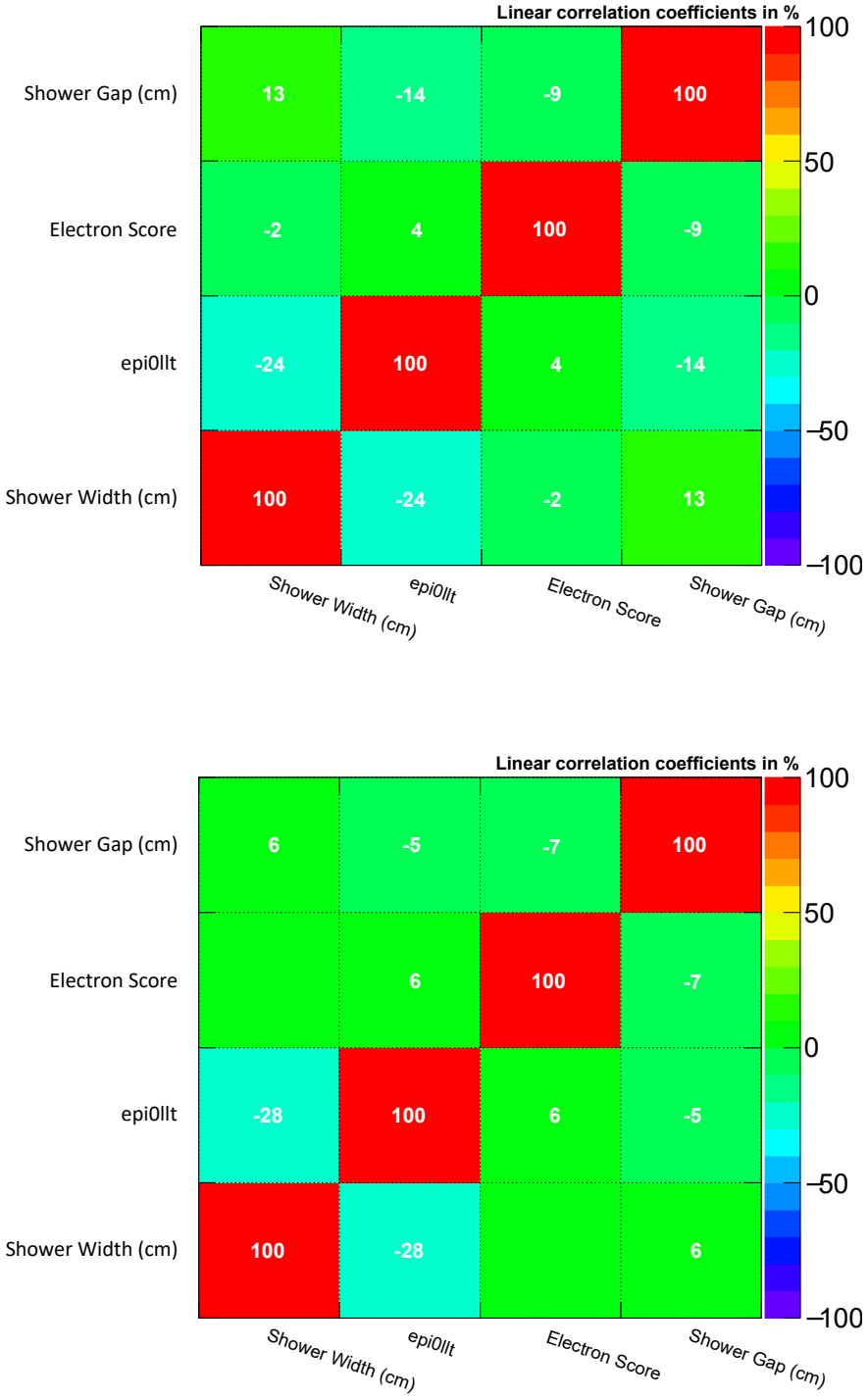

FIGURE 5.27. Correlation between NueID input variables showing only small correlations between shower width and dE/dx log-likelihood ratio. Correlations between these variables are shown for signal (top) and background (bottom) events.

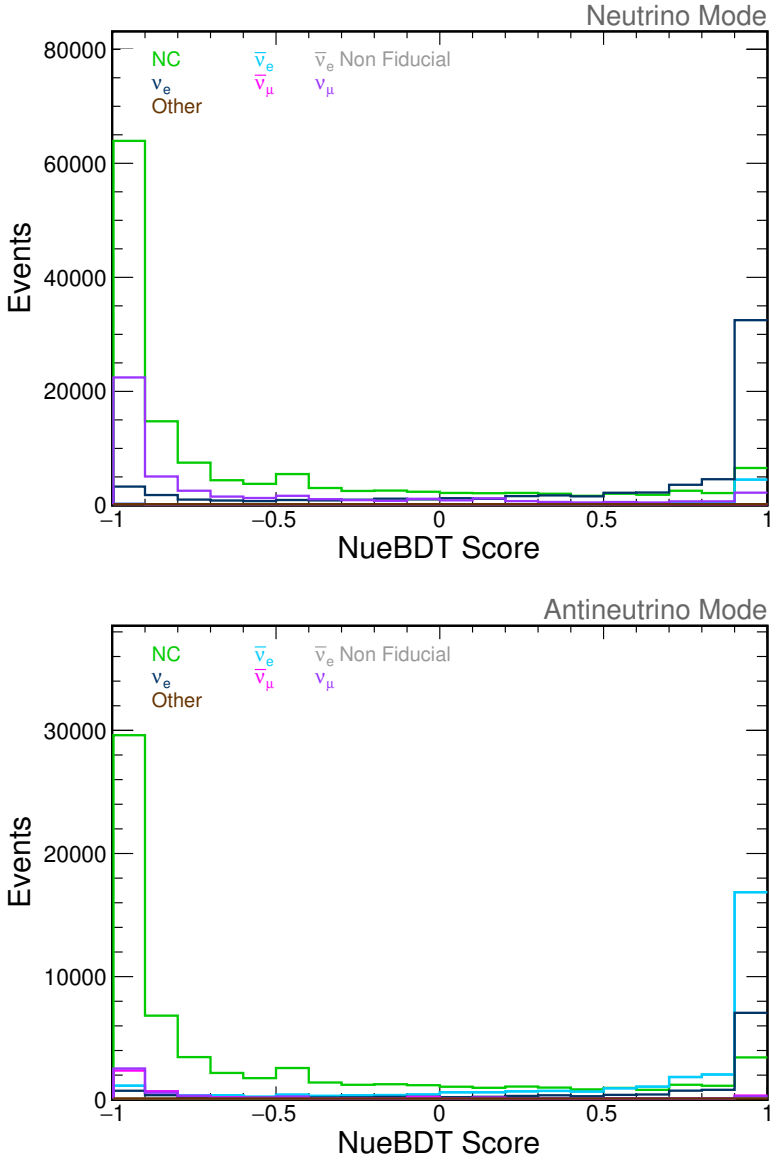

FIGURE 5.28. NueID distributions broken down by type of neutrino interaction for FHC (top) and RHC (bottom) samples showing good separation between signal and background in both beam-modes.

To illustrate a simple example, consider the FHC distributions shown in figure 5.28. To estimate the composition of a measured NueID distribution by neutrino interaction type, $\vec{x} = (x_0, x_1, x_2, ..., x_n)$ is first defined, where x_i is the total number of observed events in bin i and n is the total number of bins in the histogram. To model $\vec{x}$ using the distributions of the individual

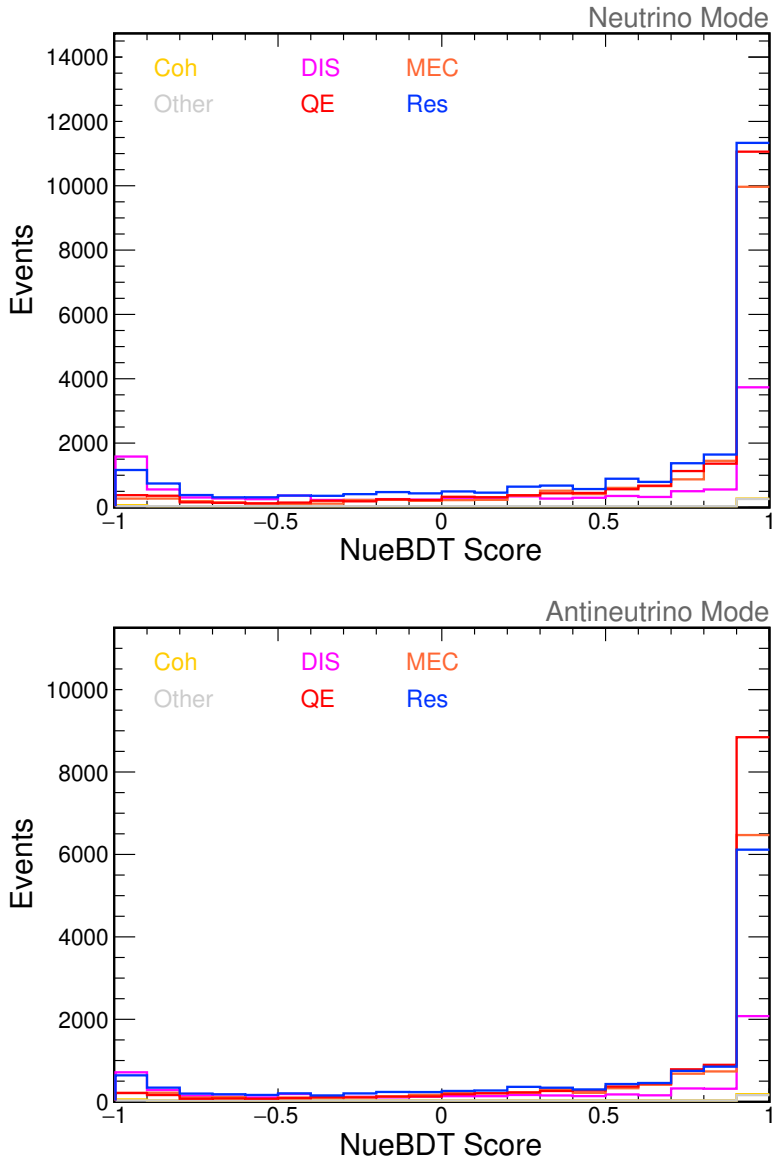

FIGURE 5.29. NueID distributions broken down by interaction mode of ν_e CC and $\bar{\nu}_e$ CC events for FHC (top) and RHC (bottom) samples.

components weighed by a yet-unknown normalization, the following are defined

$$\begin{aligned}\vec{x} = & \; a_{NC} \cdot \vec{n}_{NC} \\ & + a_{\nu_e CC} \cdot \vec{n}_{\nu_e CC} + a_{\bar{\nu}_e CC} \cdot \vec{n}_{\bar{\nu}_e CC} + a_{\bar{\nu}_e CC,\text{Bkgd.}} \cdot \vec{n}_{\bar{\nu}_e,\text{Bkgd.}} \\ & + a_{\nu_\mu CC} \cdot \vec{n}_{\nu_\mu CC} + a_{\bar{\nu}_\mu CC} \cdot \vec{n}_{\bar{\nu}_\mu CC} \\ & + a_{other} \cdot \vec{n}_{other}\end{aligned} \tag{5.20}$$

where $\vec{n}_\alpha$ is a vector of bin contents of events of category α distributed among bins of NueID, and a_α is a constant scaling factor for the α-component NueID distribution. Templates of similar shape must be combined, simplifying to,

$$\vec{n}_{\nu_e CC-like} = \vec{n}_{\nu_e} + \vec{n}_{\bar{\nu}_e} + \vec{n}_{\bar{\nu}_e,\text{Bkgd.}}$$

$$\vec{n}_{\nu_\mu CC-like} = \vec{n}_{\nu_\mu} + \vec{n}_{\bar{\nu}_\mu}.$$

The final model becomes,

$$\vec{x} = a_{NC} \cdot \vec{n}_{NC} + a_{\nu_e CC-like} \cdot \vec{n}_{\nu_e CC-like} + a_{\nu_\mu CC-like} \cdot \vec{n}_{\nu_\mu CC-like} + a_{other} \cdot \vec{n}_{other}. \tag{5.21}$$

The measured NueID distribution, $\vec{X}$, can be used to estimate all a_α normalization parameters as long as the number of data points exceeds the number of degrees of freedom of the model, or the number of normalization parameters. The set of Maximum Likelihood Estimators (MLEs) of the $\vec{a}$ is extracted to estimate the true normalizations. A Gaussian likelihood function ($\mathcal{L}$) is used, and the MLEs are found by minimizing

$$-2\log\mathcal{L} = \chi^2 = [X - x(\vec{\alpha})]^T V^{-1}(\vec{\alpha})[X - x(\vec{\alpha})]. \tag{5.22}$$

The covariance matrix, V, is the sum of a systematic, V_{syst}, and a statistical, V_{stat}, covariance matrix. The statistical component, V_{stat}, is diagonal and calculated as the sum of Poisson errors from each of the model templates. The systematic component, V_{syst}, is constructed using shifted samples of simulation representing systematic effects on the distribution of NueID, but normalized to the total nominal prediction to describe a shape-uncertainty on the model.

Systematic variations in the analysis are constructed in three different ways depending on the underlying uncertainty of the physical parameter(s): one-sided, two-sided, and multiverse ensemble variations. A one-sided variation corresponds to a change in physical parameter in only one direction. An example is the detector ageing systematic, which is taken to only reduce, and not increase, the overall light yield over time. A two-sided variation corresponds to a physical parameter that is uncertain in two directions, for example Cherenkov light yield (Figure 5.12). A multiverse ensemble is produced to evaluate the systematic effect of many correlated parameters such as GENIE or PPFX parameters. In each case, error bands are symmetrized to approximate Gaussian errors.

For one-sided variations, the bin-wise difference between the shifted distribution and the nominal prediction is taken to be the one-sigma error.

$$\begin{aligned} \sigma_i =& \mu'_i \cdot \frac{\sum_j \mu_j}{\sum_j \mu'_j} - \mu_i \\ =& \mu'_i \cdot \frac{s}{s'} - \mu_i \end{aligned} \tag{5.23}$$

where μ_i and μ'_i are the total number of events predicted in bin i by the nominal and systematically modified simulation, respectively, and $s = \sum_j \mu_j$ is the integrated number of predicted events. The factor s/s' is applied to μ'_j remove normalization effects from varying the physical parameter. Covariances are calculated as

$$V_{ij} = \sigma_i \sigma_j. \tag{5.24}$$

For two-sided variations, the average of the $+1\sigma$ and -1σ one-sided covariances is chosen as the total covariance. Each variation is first corrected to remove normalization effects,

$$\begin{aligned} \sigma^{+} =& \mu_i^{+} \cdot \frac{s}{s^{+}} - \mu_i \\ \sigma^{-} =& \mu_i^{-} \cdot \frac{s}{s^{-}} - \mu_i \end{aligned} \tag{5.25}$$

where σ^{+} and σ^{-} are the shape-only effects of varying some physical parameter by $+1\sigma$ and -1σ, respectively. The total covariance is calculated by averaging the individual variations,

$$V_{ij} = \frac{1}{2}(\sigma_i^{+}\sigma_j^{+} + \sigma_i^{-}\sigma_j^{-}). \tag{5.26}$$

For multiverse uncertainties, an average of individually-varied universes is taken to represent the total covariance. Each universe, indexed with k, is first corrected to remove normalization effects,

$$\sigma^{k} = \mu_i^{k} \cdot \frac{s}{s^{k}} - \mu_i. \tag{5.27}$$

The total covariance is calculated by averaging the individual variations,

$$V_{ij} = \frac{1}{N}(\sum_{n}^{N} \sigma_{n,i}\sigma_{n,j}) \tag{5.28}$$

where N is the number of universes.

Finally, covariance matrices representing individual sources of systematic uncertainties are combined by a linear sum to create the total covariance matrix in equation 5.22.

Minimizing (5.22) with respect to the normalization parameters results in an estimate of the normalization parameter, $\hat{a}_\alpha$ with covariance, W. The resulting covariance contains shape-only

systematic uncertainties propagated by (5.22) and normalization uncertainties constrained by the measured data. These are used to calculate a signal purity of the selected sample that has been adjusted to best match the measured distributions. In this simple example, the adjusted purity is a single value,

$$\hat{P} = \frac{\hat{a}_{\text{Signal}} \sum_i n_{\text{Signal},i}}{\sum_\alpha \hat{a}_\alpha \sum_i n_{\alpha,i}}. \tag{5.29}$$

The integrated number of signal events contained within the sample is estimated by multiplying the renormalized purity by the total number of measured events,

$$\hat{N}_{\text{Signal}} = \hat{P} \cdot \sum_i X_i. \tag{5.30}$$

A confidence interval on $\hat{N}_{\text{Signal}}$ is constructed by varying the estimated purity within the uncertainties of the fitted parameters, $\hat{a}_\alpha$. Random samples are drawn according to [142] to propagate the uncertainty on normalization parameters through to the purity estimation. The sampling is performed by first decomposing the fit parameter covariance (W) into upper (U) and lower (L) triangular matrices such that,

$$W = L \cdot L^T. \tag{5.31}$$

A set of normalization parameters is sampled according to

$$\vec{a}^k = \hat{\vec{a}} + \vec{R} \cdot L \tag{5.32}$$

where $\hat{\vec{a}}$ is the set of best-fit normalization parameters and $\vec{R}$ is a vector of values that are randomly sampled from a standard normal distribution, $\mathcal{N}(0,1)$. For each $\vec{a}^k$ universe, an adjusted

signal purity is calculated according to (5.29). The result is an ensemble of purity estimates that have been varied according to all of the systematic and statistical uncertainties of the analysis. The uncertainty on the estimated purity, and therefore the uncertainty on the estimated number of signal events is given by:

$$\frac{\delta N_{\text{Signal}}}{\hat{N}_{\text{Signal}}} = \pm\sqrt{\frac{1}{N}\sum_{k}(P^k - \hat{P})^2}. \tag{5.33}$$

5.5.4. Global Template Fit Overview. The template fit procedure can be extended to make simultaneous and correlated measurements of the number of signal events in two or more neighboring analysis bins. In this case, template distributions are contained in each analysis bin. The template model within each analysis bin is defined identically as described in the previous section. A global model is constructed that correlates systematic effects between all template bins within all analysis bins. This procedure was developed by the analysis of the ν_e-CC inclusive cross section in the NOvA ND [5].

First, a global model of m analysis bins is defined such that each analysis bin contains templates with n bins,

$$\vec{x}_g = \begin{pmatrix} \vec{x}^0 \\ \vec{x}^1 \\ \vdots \\ \vec{x}^m \end{pmatrix} = \begin{pmatrix} a^0_{NC}\cdot\vec{n}^0_{NC} + a^0_{\nu_e CC-like}\cdot\vec{n}^0_{\nu_e CC-like} + a^0_{\nu_\mu CC-like}\cdot\vec{n}^0_{\nu_\mu CC-like} + a^0_{other}\cdot\vec{n}^0_{other} \\ a^1_{NC}\cdot\vec{n}^1_{NC} + a^1_{\nu_e CC-like}\cdot\vec{n}^1_{\nu_e CC-like} + a^1_{\nu_\mu CC-like}\cdot\vec{n}^1_{\nu_\mu CC-like} + a^1_{other}\cdot\vec{n}^1_{other} \\ \vdots \\ a^m_{NC}\cdot\vec{n}^m_{NC} + a^m_{\nu_e CC-like}\cdot\vec{n}^m_{\nu_e CC-like} + a^m_{\nu_\mu CC-like}\cdot\vec{n}^m_{\nu_\mu CC-like} + a^m_{other}\cdot\vec{n}^m_{other} \end{pmatrix} \tag{5.34}$$

where all a^j_α are taken as independent. In practice, x_g is arranged as a 1-dimensional vector, making it trivial to construct the covariance matrix, V, as described above once the linearization is complete. Again, errors are assumed to be Gaussian and (5.22) is minimized to find $\hat{a}^j_\alpha$.

Signal purity is estimated in each analysis bin similar to of Equation (5.29), and the signal is extracted by multiplying the estimated purity to the total measured event rate in each analysis bin

$$\hat{N}_{\text{Signal},i} = \hat{P}_i \sum_j X_{ij} \tag{5.35}$$

where $\hat{P}_i$ is the estimated purity in the i^{th} analysis bin and the sum is taken over template bins j. The uncertainty on the extracted signal is estimated by a random sampling of the fit parameter covariance matrix to produce an ensemble of purity estimations that have been varied by the uncertainties of the analysis. Since this covariance matrix correlates of the all template component normalizations and all analysis bins, all correlations are accounted for in the resulting confidence interval.

5.5.5. A Simultaneous Two-sample Global Template Fit. The simple and global template fits presented in Sections 5.5.3 and 5.5.4 rely on differences in template shapes in order to reliably extract template normalization parameters. Electron neutrino and antineutrino CC interactions are clearly separated from NC, ν_μ-CC, and $\bar{\nu}_\mu$-CC interactions in the distribution of NueID BDT score (Figure 5.28). Because there is little difference between ν_e-CC and $\bar{\nu}_e$-CC templates, these components are added together in the simple and global fit examples. By doing so, it is assumed that normalization of ν_e-CC and $\bar{\nu}_e$-CC templates are fully correlated. This is not necessarily true since, for example, ν_e and $\bar{\nu}_e$ are produced in the NuMI beam by the decay of different hadrons and therefore have different uncertainties associated with their production. It may be possible to approximate full correlation if $N_{\nu_e CC} \gg N_{\bar{\nu}_e CC}$, as is the case in the analysis of FHC NOvA data for measuring the ν_e-CC inclusive cross section [5]. For this analysis, the ν_e-CC contamination in the antineutrino beam, referred to as "wrong-sign", is a significant background: the ν_e-CC

content in the RHC sample is 30% of the total ν_e-CC and $\bar{\nu}_e$-CC content. In order to constrain the wrong-sign component for this analysis, an additional set of data is required considering the similarities between ν_e-CC and $\bar{\nu}_e$-CC NueID templates.

A major contribution to this analysis is the development of a simultaneous template fit procedure for extracting signal in the presence of a significant irreducible background. Data taken during RHC and FHC run periods are used to constrain the normalization of template components predicted by the simulation of corresponding run periods. By using the NuMI flux model and the FHC sample to constrain the ν_e-CC cross section, $\bar{\nu}_e$-CC and ν_e-CC templates are varied independently and signal $\bar{\nu}_e$-CC interaction rate is extracted from the RHC data.

The RHC sample is used to constrain the RHC ν_e-CC component by an extrapolation procedure that correlates the systematic normalization effects between the two samples. Similarly, the RHC sample is used to extrapolate the normalization of all other template components to the FHC sample. For template component α, normalization uncertainties on the number of α events in each sample are correlated by treating the number of events predicted in each analysis bin as a vector of random variables,

$$\vec{N}_{\alpha}^{\phi} = \begin{pmatrix} N_{\alpha,0}^{\phi} \\ N_{\alpha,1}^{\phi} \\ \vdots \\ N_{\alpha,m}^{Mode} \end{pmatrix}. \tag{5.36}$$

Here, $\vec{N}_\alpha^\phi$ represents the number of predicted events of template component α in ϕ beam-mode for m bins of electron phase space. Vectors from each beam mode are combined to form

$$\vec{N}_\alpha = \begin{pmatrix} \vec{N}_\alpha^{RHC} \\ \vec{N}_\alpha^{FHC} \end{pmatrix}. \tag{5.37}$$

The covariances between elements of $\vec{N}_\alpha$ are estimated using systematically-shifted distributions for all systematic effects accounted for in the analysis. For each shifted sample, an $\vec{N}'_\alpha$ is formed to represent the number of simulated events of template component α under the effect of the particular systematic. The covariance due to each systematic effect is calculated similarly as described in Section 5.5.3, but without the normalization correction factors. The individual covariance matrices are combined to create a total covariance matrix as shown in Figure 5.31. The figures show that changes in the normalization of the RHC $\bar{\nu}_e$-CC component are strongly correlated to changes in the normalization of the FHC $\bar{\nu}_e$-CC component, but they are not perfectly correlated. This is expected since most of the systematic uncertainties are beam-mode agnostic; uncertainties due to detector effects and GENIE model parameter uncertainties should be the same regardless of the NuMI horn current. Flux uncertainties, however, can depend on the focusing of the charged hadrons by the NuMI focusing horns. Together, these uncertainties result in strong, but not perfect, correlations between the RHC and FHC samples. These arbitrary correlations are encoded by the covariance construction described above.

The normalization covariance together with the nominal predictions (5.37) define a multivariate normal distribution,

$$f_\alpha(\vec{N}_\alpha^{RHC}, \vec{N}_\alpha^{FHC}) \propto \exp\left[(\vec{N}_\alpha - \vec{\mu}_\alpha)V_\alpha^{-1}(\vec{N}_\alpha - \vec{\mu}_\alpha)\right] \tag{5.38}$$

where $\vec{\mu}_\alpha$ is the mean value of $\vec{N}_\alpha$, or number of events of category α observed in the analysis bins, predicted from the nominal simulation.

Given an arbitrary normalization of component α in sample ϕ_1, the most likely normalization of α in sample ϕ_2 can be determined using (5.38). Mathematically, this is equivalent to finding the mean of the conditional distribution $f(\vec{N}_\alpha^{\phi_2}|\vec{N}_\alpha^{\phi_1})$ [143]. Because of this, ϕ_1 and ϕ_2 are referred to as "conditioning" and "complementary" samples, respectively. A result from probability theory provides a convenient way of calculating the mean of a multivariate Gaussian distribution conditioned on a subset of its random variables [144]. Given the nominal prediction of (5.37), $\mu_\alpha^{\phi_1}$, and arbitrary normalization parameters, $\vec{a}_\alpha^{\phi_1}$ such that $N_\alpha^{\phi_1} = \vec{a}_\alpha^{\phi_1} \cdot \vec{\mu}_\alpha^{\phi_1}$, the i^{th} component of $\vec{a}_\alpha^{\phi_2}$ is

$$a_{\alpha,i}^{\phi_2} = \frac{1}{\mu_{\alpha,i}^{\phi_2}}\left[\mu_{\alpha,i}^{\phi_2} + \sum_j \sum_k V_{ik}^{21} V_{kj}^{11} \mu_{\alpha,j}^{\phi_1}(a_{\alpha,i}^{\phi_1} - 1)\right] \tag{5.39}$$

where V^{21} and V^{11} are the upper left and bottom left block matrices of the joint normalization covariance matrix (Figure 5.31).

Strong correlations between component normalization in RHC and FHC samples as shown in Figure 5.31, will lead to predictable results. Namely, if a 1σ enhancement of measured $\bar{\nu}_e$-CC events is observed in RHC, then approximately a 1σ enhancement of measured $\bar{\nu}_e$-CC events should be observed in the FHC sample. Figure 5.30 shows the nominal prediction for the number of selected $\bar{\nu}_e$ CC events weighed by FHC normalization parameters predicted by (5.39) given a 1σ enhancement observed in the RHC sample. The renormalized prediction roughly equates to a 1σ enhancement of $\bar{\nu}_e$ CC events in the FHC sample as expected.

Of course, ϕ_1 is the RHC sample for extrapolating signal $\bar{\nu}_e$-CC events, and ϕ_1 is FHC in the case of the wrong-sign component, as previously stated. For the remaining components, the ϕ_1

TABLE 5.6. Conditioning (ϕ_1) and complementary (ϕ_2) samples listed for each component of the simultaneous template fit. The "Other" component is held fixed at the nominal prediction during the fit.

α	ϕ_1	ϕ_2
$\bar{\nu}_e$ CC	RHC	FHC
ν_e CC	FHC	RHC
NC	RHC	FHC
ν_μ CC-like	RHC	FHC
Other	-	-

is chosen to be RHC in order to give most freedom the RHC normalization parameters since the RHC sample is most sensitive to the $\bar{\nu}_e$-CC cross section. One could easily choose a different configuration of ϕ_1 samples, which may lead to different results for the extracted signal rate. However, any choice is equally valid as long as the estimator is unbiased and consistent with the true parameter being measured, and the resulting confidence intervals possess the proper coverage. Since the estimator, $\hat{\vec{a}}_{\bar{\nu}_e CC}$ is a MLE, it is asymptotically unbiased [143]. It is assumed the resulting intervals possess proper coverage because conditions of normality[††] are met and any non-linearity between estimators are accounted for by likelihood profiling [143, 118]. Table 5.6 summarizes the choices of ϕ_1 and ϕ_2 for each α component of the simultaneous template fit.

The fit is performed against measured distributions of selected events binned according to reconstructed electron energy, the cosine of the reconstructed electron scattering angle, and NueID score. Templates are formed from simulation broken down by neutrino interaction type: $\bar{\nu}_e$-CC, ν_e-CC, ν_μ-CC or $\bar{\nu}_\mu$-CC, and NC interactions. The $\bar{\nu}_e$-CC template contains signal and background $\bar{\nu}_e$-CC events, which occur outside the fiducial volume or electron kinematic limits. An "Other" category is included to account for slices in simulation that could not be matched by truth to any of the other categories and may contain noise, cosmic, or rock muons. It is held fixed in the fit at the nominal prediction due to lack of statistics. All other components are allowed to vary.

[††]The measured event rate is large, parameters are far from physical boundaries, and errors are Gaussian.

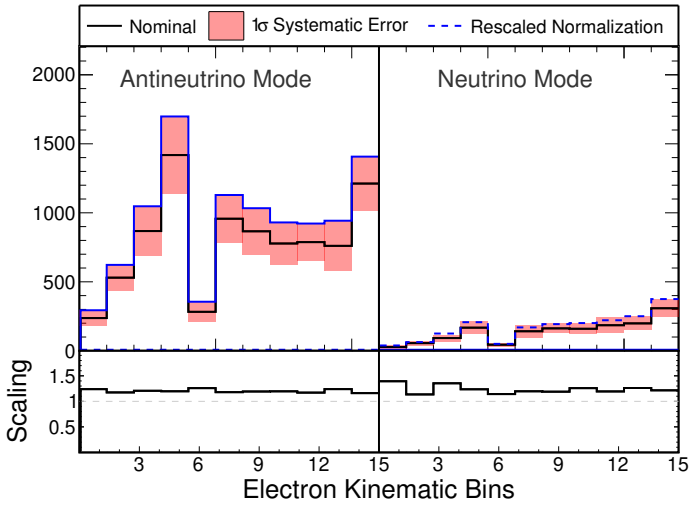

FIGURE 5.30. On the left, a 1σ enhancement of the RHC $\bar{\nu}_e$-CC component is shown by the solid blue line. Equation (5.39) is used to calculate the most likely FHC $\bar{\nu}_e$-CC distribution given the 1σ enhancement in the RHC sample. The result is shown on the right in the dashed blue line and compared to the 1σ error band on the FHC $\bar{\nu}_e$-CC component. Because normalization uncertainties are highly correlated between the RHC and FHC samples, the predicted FHC distribution approximates the 1σ prediction of the FHC distribution.

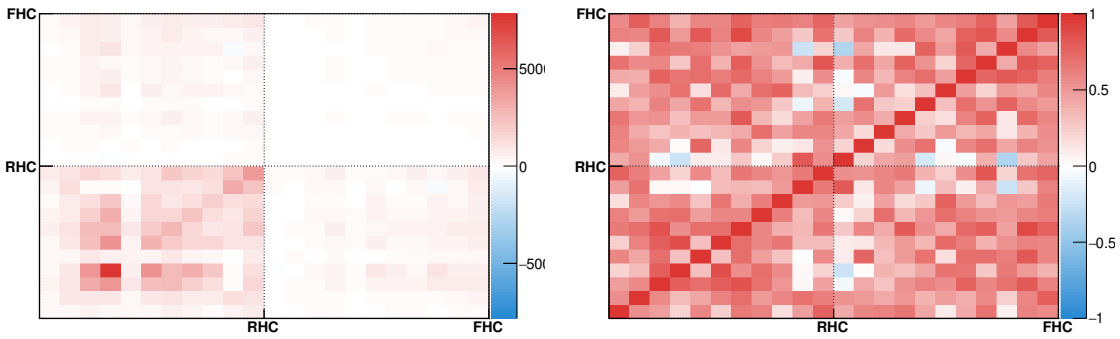

FIGURE 5.31. Systematic covariance in units of ($\bar{\nu}_e$ CC events)^2 (left) and correlation (right) matrices describing how normalization changes in selected $\bar{\nu}_e$ CC events from the RHC sample are related to changes in the FHC sample. Bins are arranged as a linear representation of the 2-dimensional electron kinematic phase space, and matrix blocks correspond to beam mode.

The MINUIT [145] library is used to perform the likelihood minimization. The free parameters of the fit are the normalization factors of template components measured in the conditioning samples (ϕ_1) as summarized in Table 5.6. Complementary sample (ϕ_2) template normalizations also vary throughout the fit, but are directly tied to the free parameters through (5.39).

The fit is restarted at many random configurations of the free parameters to avoid local minimum. These are generated by sampling random numbers from a Gaussian distribution, where $\mu = 1$ and $\sigma = 0.2$, to create a vector of random fit parameters. One hundred such vectors are used to evaluate the fit objective function. The fit is started at each of the ten configurations found to be most consistent with the data, and the best fit (lowest χ^2) is chosen to represent the estimated normalization parameters. Final uncertainties associated with each normalization parameter, including correlations, are evaluated using the likelihood profiling, or MINOS, method implemented within MINUIT [145].

5.5.6. Application of Two-sample Global Template Fit to Fake Data. To illustrate the two-sample global template fit procedure used for this analysis, results from a fit to statistically varied fake data are presented. Fake data distributions are generated by varying nominal predictions within Poisson uncertainties. Templates and covariance matrices are derived from simulation. The fit is performed in bins of electron energy, cosine of the electron scattering angle, and NueID. The electron kinematic bins are treated as the analysis bins and NueID bins as the template bins. Conditioning samples are defined in Table 5.6.

Figure 5.32 shows the best fit parameters for each of the components that are free to vary in the fit. These parameters are used to renormalize template distributions. For illustration, templates measured in the most forward-going region of electron kinematics ($0.97 \leq \cos\theta \leq 1.0$) are shown in Figure 5.33 and compared to renormalized templates derived from simulation. Good agreement is shown throughout the phase space, but particularly in the low energy region ($1.0 \leq E\,(\mathrm{GeV}) < 2.0$) where most events occur. Event rates are extracted as a function of electron kinematics by integrating over the NueID axis of the renormalized templates. Figure 5.34 shows the post-fit event rates compared to data in bins of electron kinematics. Uncertainty on

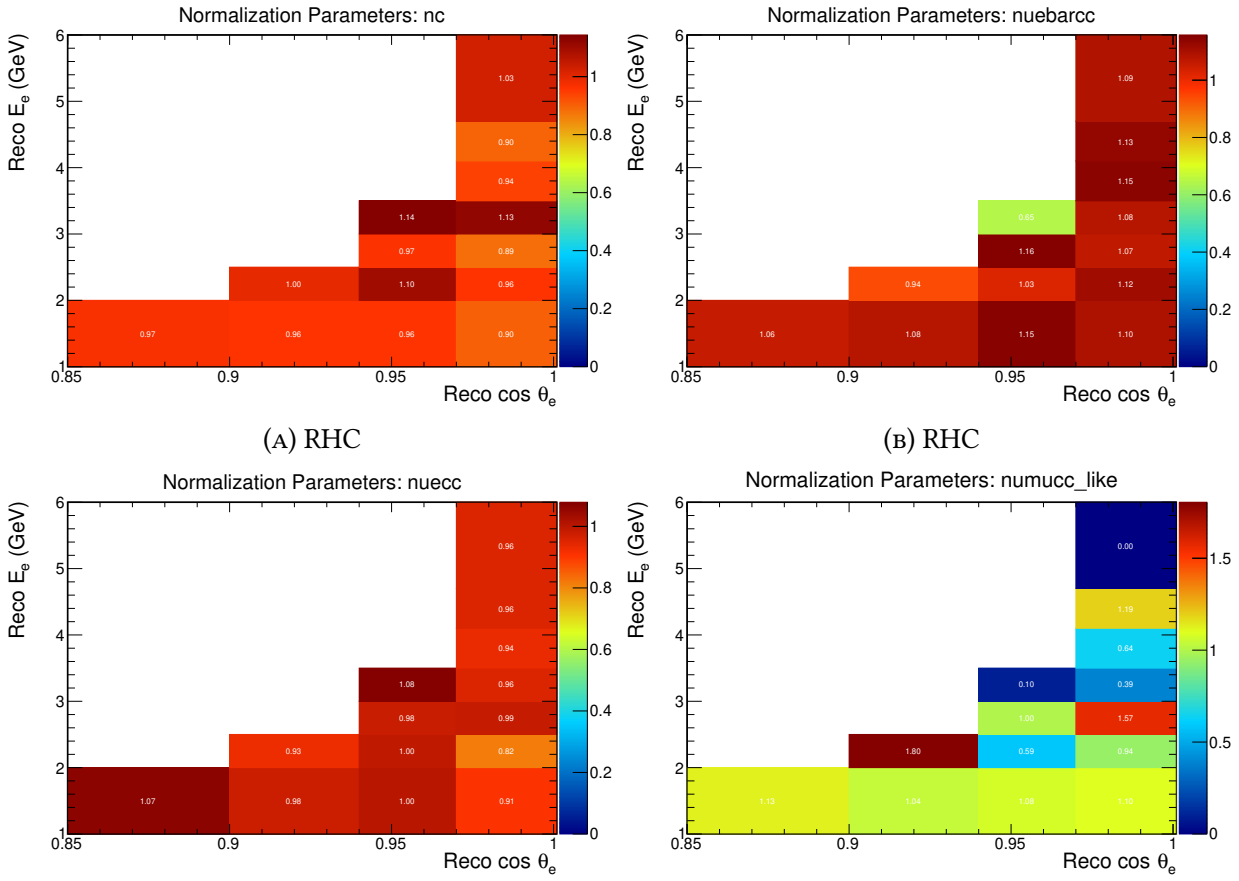

(A) RHC (B) RHC

(C) FHC (D) RHC

FIGURE 5.32. Template normalization parameters extracted from a template fit to statistically-varied fake data sample. Conditioning samples are indicated below each figure.

the number of selected events is shown to be greatly reduced by constraining the uncertainty model to the measured template distributions.

5.5.6.1. *Template Fit Bias.* A bias is observed in the estimation of the total number of selected events extracted from the template fit procedure. An ensemble of fake data template distributions is generated by statistically varying the nominal MC prediction of the total number of selected events in bins of electron energy, cosine of the electron scattering angle, and NueID. A fit is performed to each fake data universe and the ratio of selected events in fake data and the post-fit MC prediction is calculated. Figure 5.35 shows the ensemble of ratios before and after the template

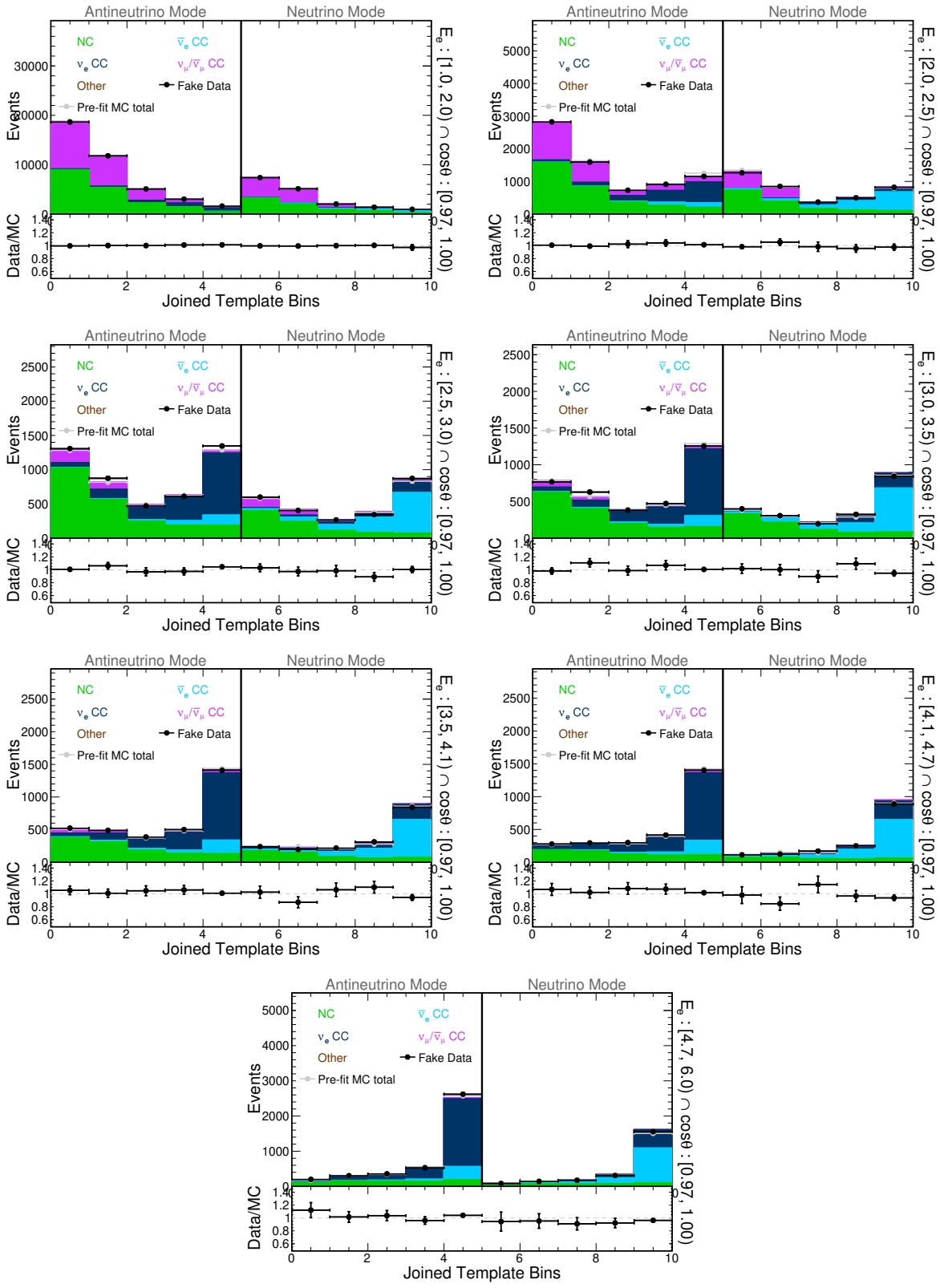

FIGURE 5.33. A collection of template bins showing post-fit agreement between renormalized simulation and statistically-varied fake data.

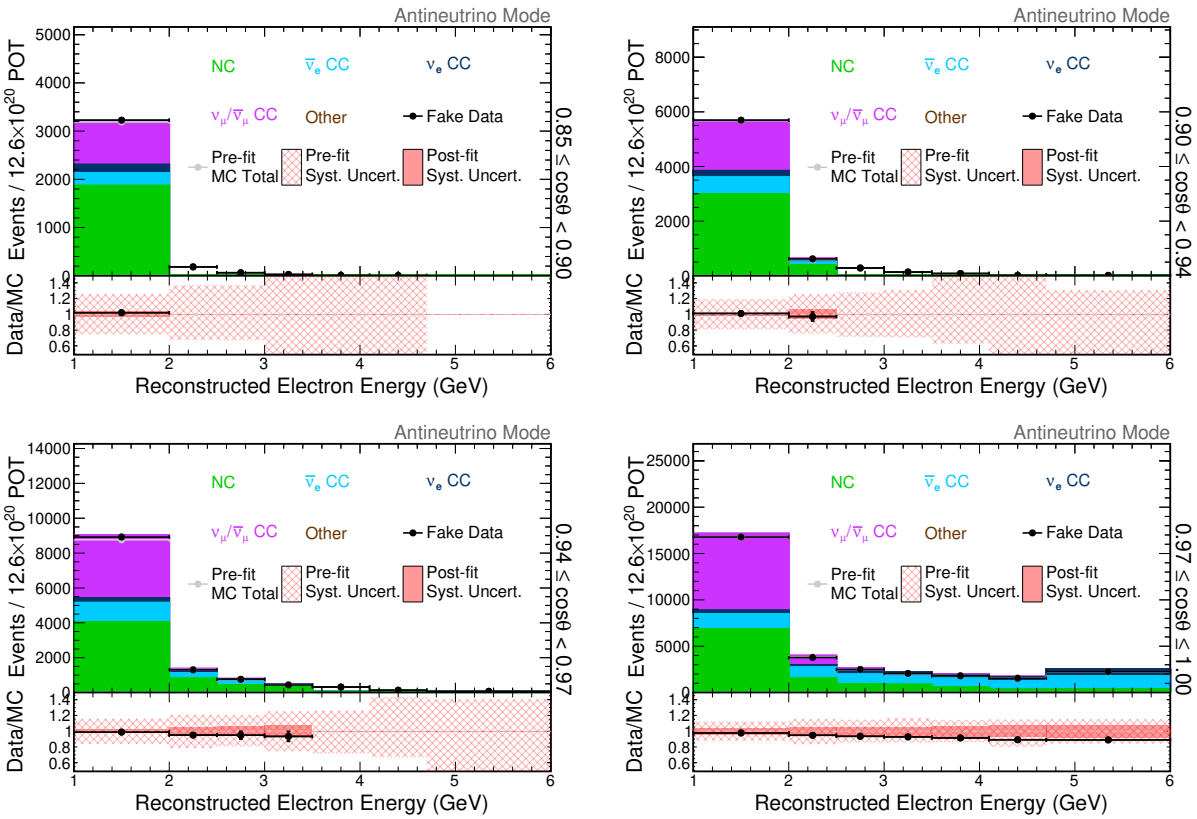

FIGURE 5.34. Renormalized event rates extracted from a template fit to statistically-varied fake data. The bottom panels each show the ratio between fake data and post-fit MC. Hashed red regions indicate shape-only uncertainties estimated from systematically modified simulation. Solid red regions indicate total uncertainty on the number of selected events constrained by data via template fit procedure.

fit. The ensemble statistics indicate a bias in the estimation of the total number of selected events of roughly 5% in the most forward-going region of electron kinematics ($0.97 \leq \cos\theta \leq 1.0$). Studies [146] suggest the bias is caused by systematic correlations between template bin event rates due to GENIE model uncertainties. These correlations are expected to exist because of the dependence of neutrino interaction cross section on lepton kinematics.

Although a bias is observed in the total number of selected events after the template fit is performed, $\bar{\nu}_e$-CC signal purity is shown to be unbiased. Figure 5.36 shows the ensemble of true signal purity divided by purity extracted from template fits to the fake data ensemble. Because

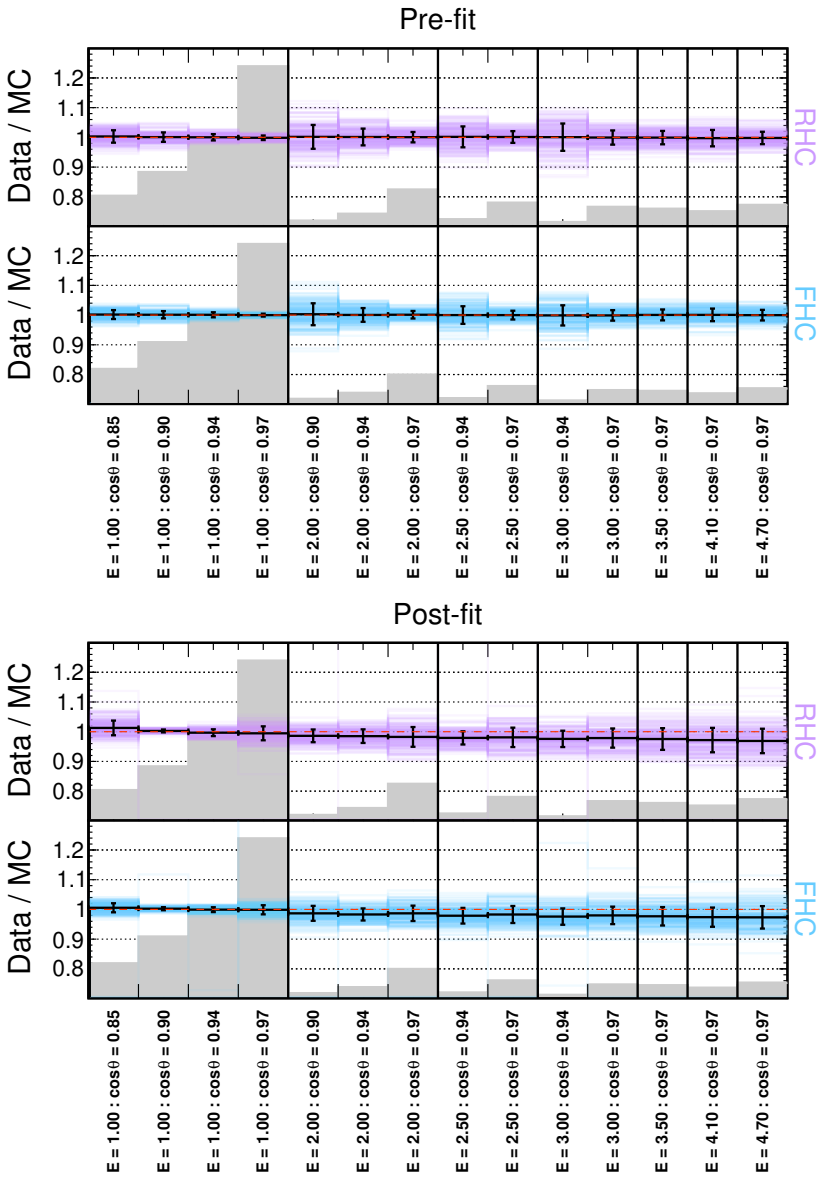

FIGURE 5.35. Ensemble of selected events in fake data divided by simulation before (top) and after (bottom) template fit. Gray histograms indicate relative event statistics (arbitrary units). A bias of at most 5% is observed in the post-fit event distributions when compared to fake data.

the estimated signal rate is derived from this unbiased purity, as will be discussed in Section 5.5.7, the bias will not propagate to the extracted cross section. However, a uniform 5% uncertainty on the cross section is included to cover the effect of the bias on the total event rate prediction.

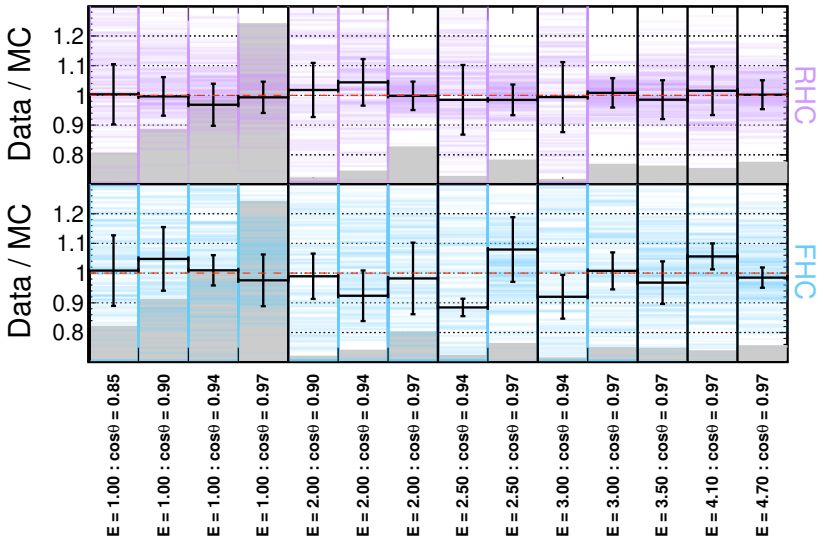

FIGURE 5.36. Ensemble of true $\bar{\nu}_e$-CC signal purity divided by purity estimated from performing a template fit. The ensemble of fake data is generated by statistically varying the nominal prediction. Gray histograms indicate relative event statistics (arbitrary units).

5.5.7. PURITY CORRECTION. The signal $\bar{\nu}_e$-CC event rate as a function of electron energy and scattering angle is estimated by multiplying the data measured in bins of electron energy and scattering angle with the renormalized purity resulting from the template fit. The uncertainty on the fit parameters is propagated to the signal estimation via the purity ensemble method described in Section 5.5.3.

The signal $\bar{\nu}_e$-CC event rates as a function of $E_{\bar{\nu}}$ and Q^2 are also estimated via a modified purity correction. Simulation is used to determine the relationship between reconstructed electron kinematics and these variables, and events are weighed according to template normalization parameters. The number of events of type α in bin i of $E_{\bar{\nu}}$ or Q^2 is

$$m_{\alpha,i} = \sum_{j,k} \hat{a}_{\alpha,j,k} n_{\alpha,i,j,k} \tag{5.40}$$

where $n_{\alpha,i,j,k}$ is the predicted number of events of type α in bin i of $E_{\bar{\nu}}$ or Q^2, j of the cosine of the electron scattering angle, and k of electron energy, and $\hat{a}_{\alpha,j,k}$ is the best fit template normalization parameter corresponding to template α and electron kinematic bins j and k. Modified purity as a function of $E_{\bar{\nu}}$ or Q^2 is

$$\hat{P}_i = \frac{m_{\text{Signal},i}}{\sum_\alpha m_{\alpha,i}}. \tag{5.41}$$

Finally, estimated signal rate is

$$\hat{N}_{\text{Signal},i} = \hat{P}_i X_i. \tag{5.42}$$

The uncertainties on $\hat{P}_i$ as a function of $E_{\bar{\nu}}$ and Q^2 are constrained entirely by the leptonic system. Since the $\hat{N}_{\text{Signal},i}$ are also sensitive to mismodeling of the hadronic system, these uncertainties are propagated through the unfolding procedure, which will be discussed in Section 5.6.1.

5.6. Correcting for Detector Effects

5.6.1. Unfolding. Experiments estimate physical quantities based on detector response. Ideally, these estimates would be perfect representations of the true quantities that caused the response, but physical detectors are limited in their ability to resolve the physics being measured. The NOvA detectors, for example, have granularity that is much larger than the scale of the nucleon on which a neutrino interacts. This often leads to a failure to resolve the propagation of two overlapping particles. Detector inefficiencies can also smear true quantities, as is the case when scintillator photons are not absorbed by fiber or fail to start the electromagnetic cascade of the APD. These smearing effects are compensated for in order to obtain a better estimate of true physics quantities by a process called “unfolding”.

In the most general sense, unfolding is the process by which true quantities are estimated from reconstructed quantities based on detector response. Many unfolding methods exist, including a simple approach using a transformation matrix relating event rates between true and reconstructed bins. Another approach simply uses weights derived from simulation to account for bin-by-bin differences between true and reconstructed quantities. The advantages and disadvantages of these are discussed in [147]. The method used here, and by other NOvA cross-section measurements, is often referred to as "iterative Bayesian" or D'Agostini unfolding [148]. It has the advantages that it will always estimate positive event rates and converge to the maximum likelihood estimate given infinite iterations. This analysis uses the iterative Bayesian unfolding method implemented by the RooUnfold [149] software package.

Iterative Bayesian unfolding estimates true quantities x_j based on measured quantities y_i and an unfolding matrix A_{ij}. The unfolding matrix contains selected signal event rates as a function of true and reconstructed quantities and is derived from simulation. Unfolding matrices for this analysis are shown in Figure 5.37. Unfolding to $\hat{x}_j$ is done iteratively such that

$$x_j^{(n+1)} = x_j^{(n)} \sum_i^N \frac{A_{ij} y_i}{\sum_k^N A_{ik} x_k^{(n)}} \tag{5.43}$$

where N is the number of bins of true and reconstructed quantities.

The true quantities estimated from (5.43), $\hat{x}_j$, are unbiased in the limit of large n, but the convergence rate is slow and comes at the cost of increasing variance [147]. Therefore, a trade-off between bias and variance has to be made when determining how many iterations to perform. This analysis uses a weighted average Mean-squared Error (MSE) to evaluate the trade-off in

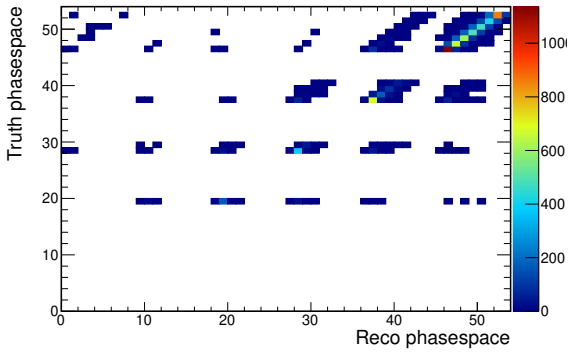

(A) E_e vs. $\cos\theta$

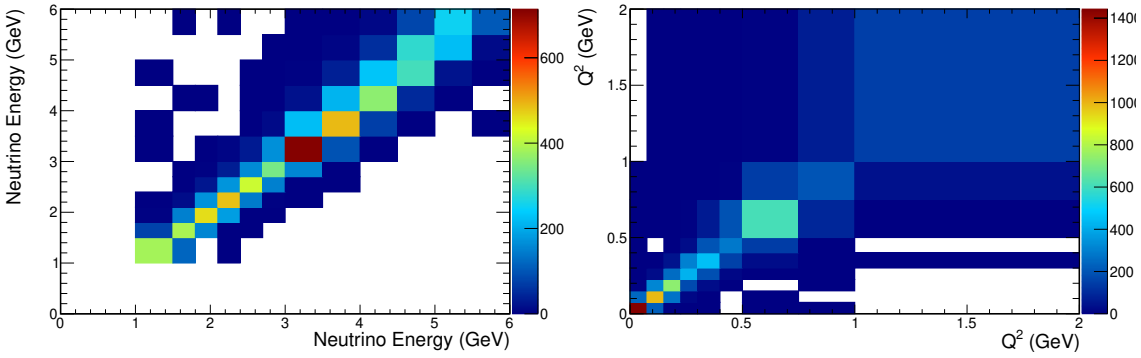

(B) E_ν (C) Q^2

FIGURE 5.37. Unfolding matrices relating true and reconstructed quantities of selected signal events for the electron energy and cosine of the scattering angle (A), neutrino energy (B), and Q^2 (C).

search for an optimal number of unfolding iterations. The weighted average MSE is defined as

$$\langle \text{MSE} \rangle = \frac{1}{U}\frac{1}{M}\sum_{k}^{U}\sum_{i}^{M}\frac{(\sigma_i^k)^2 + (\hat{b}_i^k)^2}{(x_i^k)^2} \tag{5.44}$$

where U and M are the number of samples in the ensemble of fake data and the number of bins, respectively, k is the fake-data sample index, σ_i^k is the variance of $\hat{x}_i^k$, and $\hat{b}_i^k = x_i - \hat{x}$. The variance term is calculated by RooUnfold. RooUnfold measures the variance of an ensemble of unfolded toy experiments. Toy samples are generated by applying Poisson fluctuations to the nominal distribution of events binned in the reconstructed quantity. Bins with less than 100 events are excluded from the calculation of the MSE.

The average MSE is calculated for an ensemble of fake data samples. Fake data samples are generated by applying Poisson fluctuations to the nominal truth distribution, then smeared using the unfolding matrix. For every sample, the truth distribution is drawn from a multivariate Poisson distribution centered at the nominal prediction. From the k^{th} sample, the corresponding reconstructed distribution is generated according to

$$y_i^k = \sum_j \Big(\frac{A_{ij}}{\sum_i A_{ij}} \Big) x_j^k. \tag{5.45}$$

The average MSE is calculated for the ensemble of fake data samples as a function of unfolding iterations. This is done independently for each phase space in which a cross section is measured: electron energy and cosine of the scattering angle (E_e vs. $\cos\theta$), E_ν, and Q^2. The results are shown in Figure 5.38 and optimal values reported in Table 5.7

The unfolding procedure is applied to the estimated signal rate from Section 5.5.5. Signal rate and uncertainty as a function of true electron kinematics is found by direct application of the procedure to the corresponding reconstructed quantities.

The true signal rates as functions of E_ν and Q^2 are sensitive to mismodeling of both the leptonic and hadronic parts of the interaction. The template fit procedure (Section 5.5.5) propagates uncertainties associated with the leptonic system. Uncertainties on the hadronic system are propagated to the true signal rate as a function of these variables by the unfolding procedure. Unfolding matrices that relate reconstructed to true quantities are produced by systematically modified simulation. The uncertainty on the signal rate as a function of these true quantities is

$$\Big(\frac{\delta N}{N} \Big)^2 = \Big(\frac{\delta \hat{P}}{\hat{P}} \Big)^2_{\text{Leptonic}} + \sum_{\text{syst}} \Big(\frac{\delta (U_{\text{syst}} \hat{P} X)}{U \hat{P} X} \Big)^2_{\text{Hadronic}}. \tag{5.46}$$

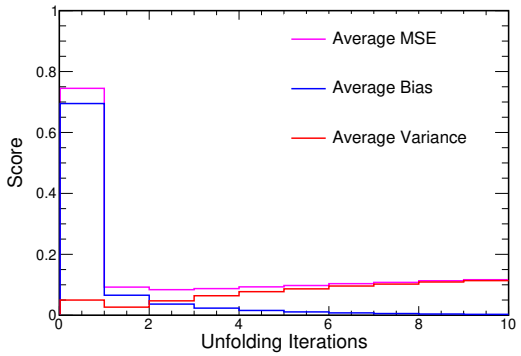

(A) E_e vs. $\cos\theta$

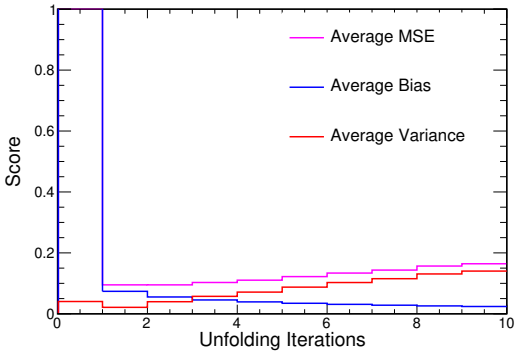

(B) E_ν

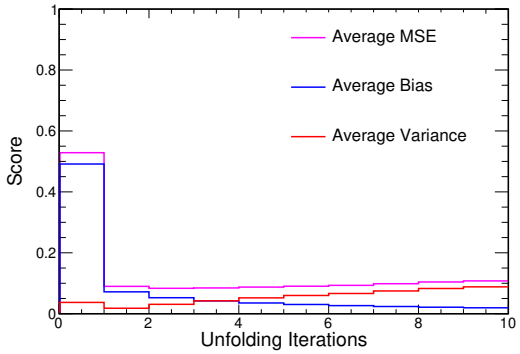

(C) Q^2

FIGURE 5.38. Average MSE as a function of unfolding iterations for the electron energy and cosine of the scattering angle (A), neutrino energy (B), and Q^2 (C).

TABLE 5.7. Optimal unfolding iterations found by minimization of $\langle \text{MSE} \rangle$.

Phase Space	Optimal Unfolding Iterations
E_e vs. $\cos\theta$	2
E_ν	2
Q^2	2

Here, U_{syst} represents an unfolding matrix derived from systematically modified simulation. These include uncertainties in detector calibration and light yield, neutron energy deposition, and GENIE interaction model parameters.

5.6.2. EFFICIENCY. Reconstruction failures, below-threshold energy deposition, and selection criteria can result in a failure to select true fiducially-interacting $\bar{\nu}_e$-CC signal events. For example, this can happen when a $\bar{\nu}_e$-CCQE interaction fails to produce a prong due to readout dead time.

To account for the signal interactions that are not selected in the analysis, selection efficiency is estimated by

$$\epsilon = \frac{\text{No. Selected Signal Interactions}}{\text{No. All Simulated Signal Interactions}} \tag{5.47}$$

where both numerator and denominator are derived from simulation. Efficiency is calculated bin-by-bin and separately for each variable in which a cross section is measured.

Figure 5.39 shows the overall selection efficiency of fiducially-interacting $\bar{\nu}_e$-CC events in RHC beam mode. Selection efficiency generally decreases as electron energy increases due to containment and an increasingly complicated final state topology. Additionally, lower statistics at larger scattering angles and higher electron energies (for $0.85 \leq \cos\theta < 0.97$) lead to large systematic uncertainties as shown in Figure 5.40. Bins with low selection efficiency ($< 10\%$) are not included in the analysis to reduce model dependence from large efficiency corrections, and neither are bins with uncertainties greater than 20%.

Figures 5.41 and 5.42 show event distributions of all simulated and selected signal $\bar{\nu}_e$-CC interactions, respectively, broken down by interaction mode, in electron kinematics and RHC beam mode. These figures show that all interaction modes contribute significantly to the inclusive cross section within the analysis phase space and that DIS dominates at electron energies greater than $3\,\mathrm{GeV}$. Figure 5.43 shows the signal selection efficiency. QE and MEC are selected with the greatest efficiency due to their clean interaction topology and DIS is selected with less than 20% efficiency throughout due to high final-state multiplicity. Figures 5.44 and 5.45 show these breakdowns as a function of $E_{\bar{\nu}}$ and Q^2.

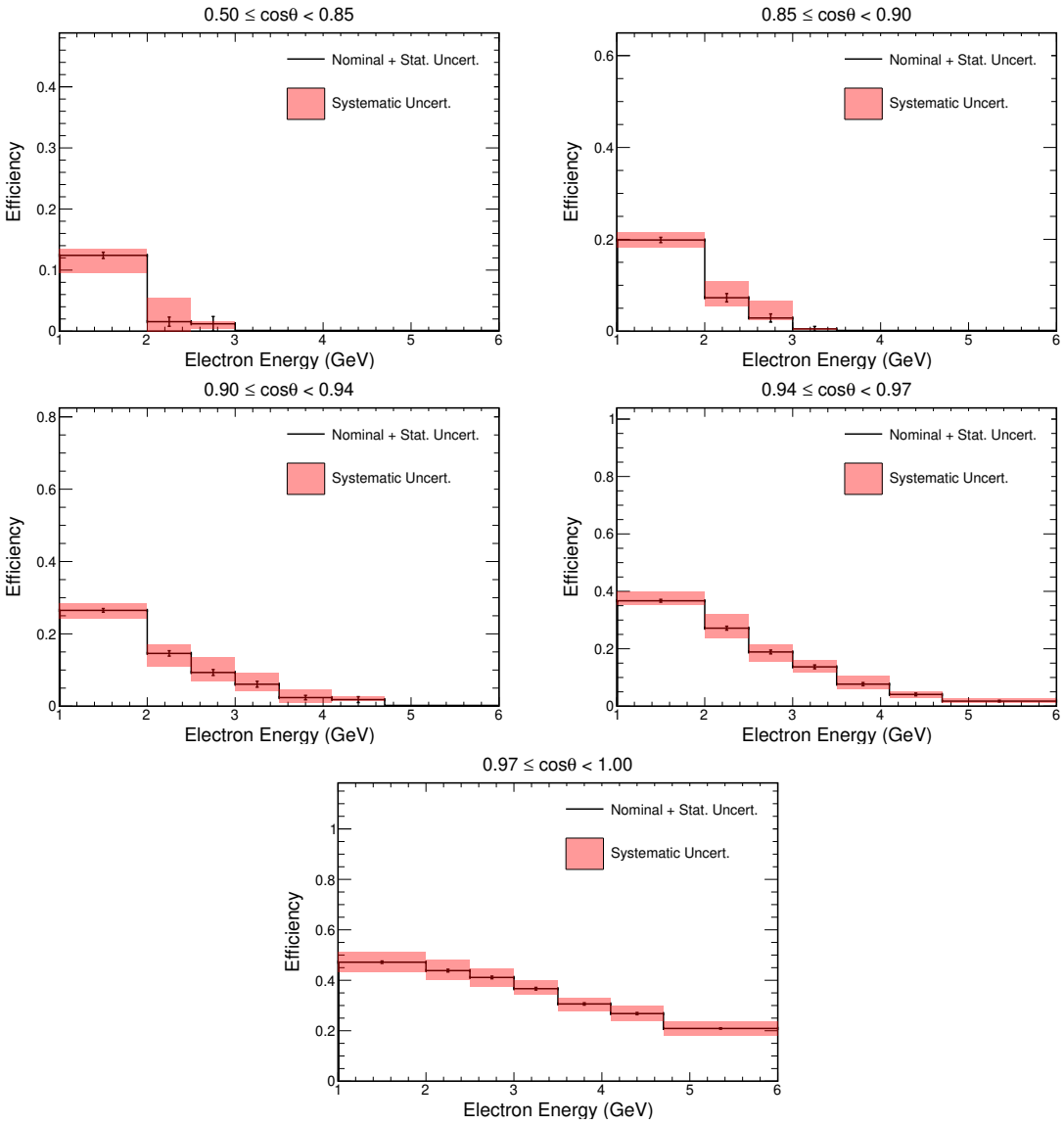

FIGURE 5.39. Overall fiducial $\bar{\nu}_e$-CC selection efficiency as a function of electron kinematics in RHC beam mode.

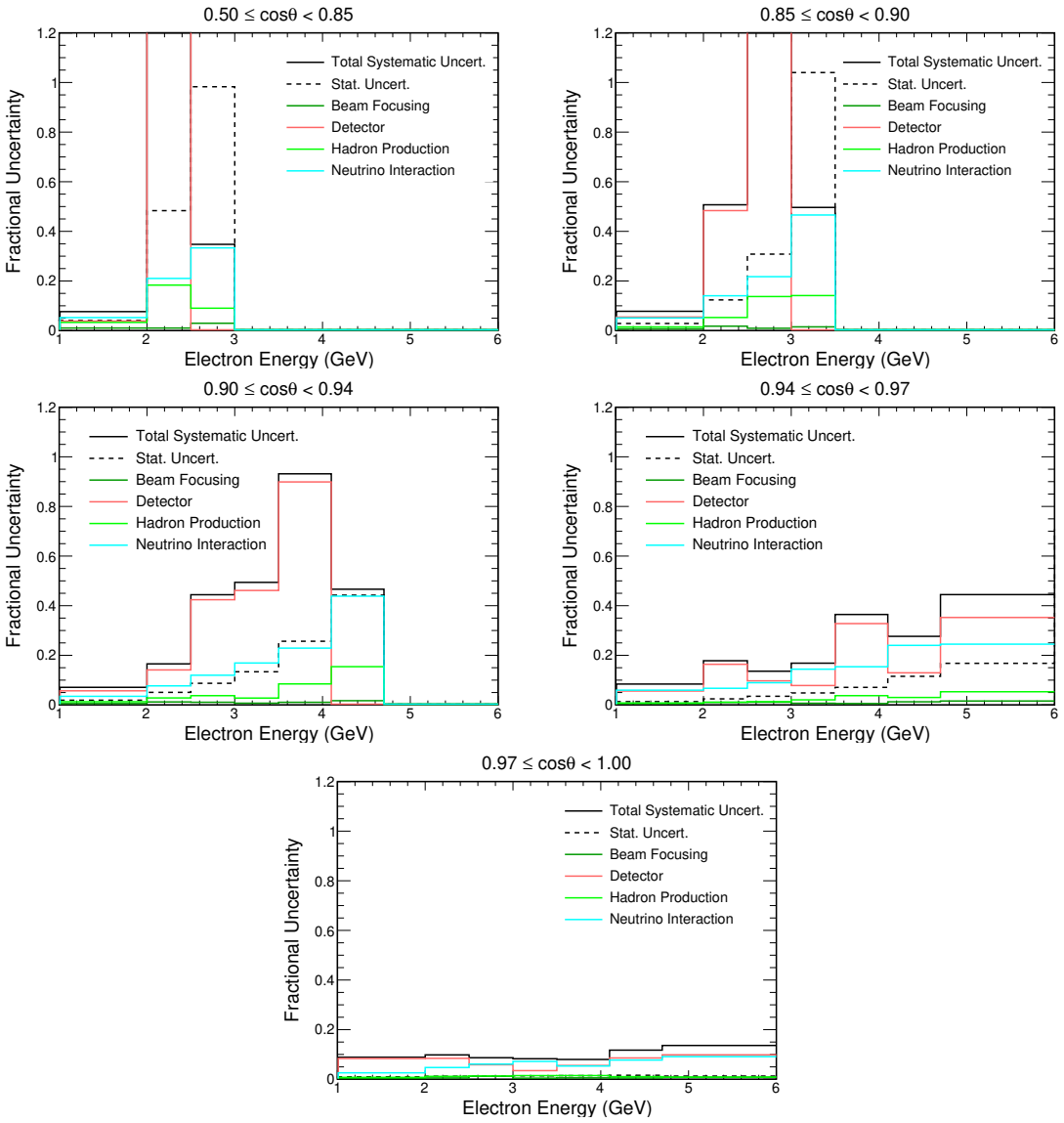

FIGURE 5.40. Fractional uncertainties on overall fiducial $\bar{\nu}_e$-CC selection efficiency as a function of electron kinematics in RHC beam mode. Bins with more than 20% total uncertainty are removed from the analysis signal phase space.

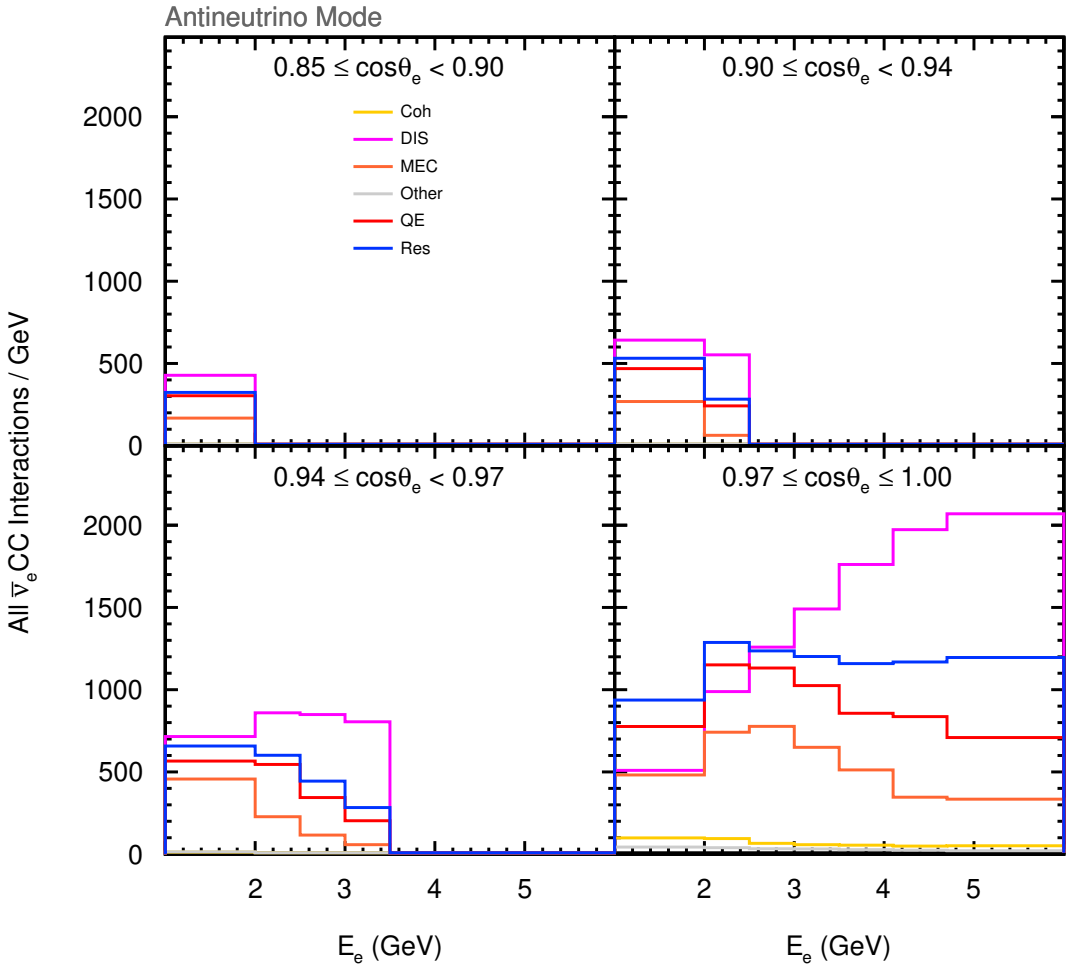

FIGURE 5.41. All simulated signal events (bin-width normalized) broken down by interaction mode, including Coherent Pion Production (COH), Deep Inelastic Scattering (DIS), Meson-Exchange Current (MEC), Quasi-Elastic (QE), and Resonant (RES), in electron kinematics and RHC beam mode.

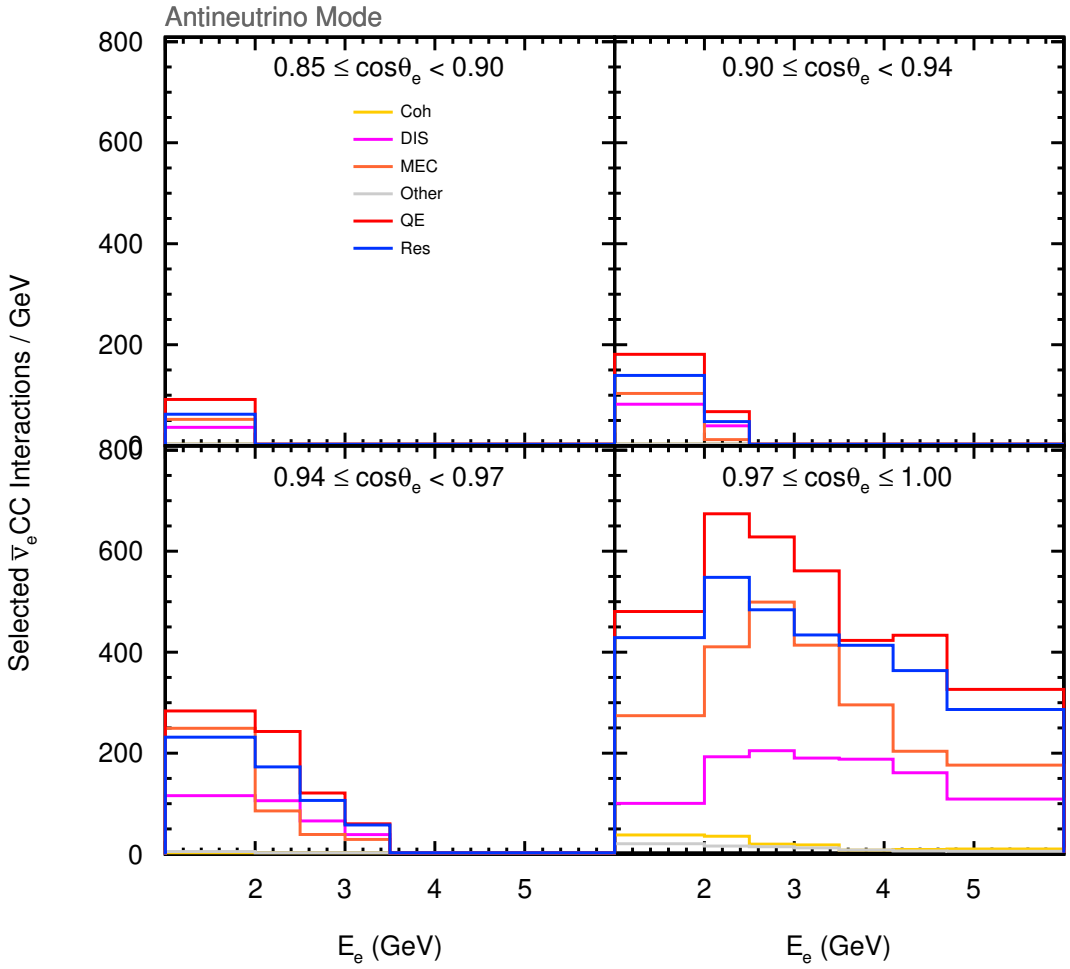

FIGURE 5.42. Selected simulated signal events (bin-width normalized) broken down by interaction mode in electron kinematics and RHC beam mode.

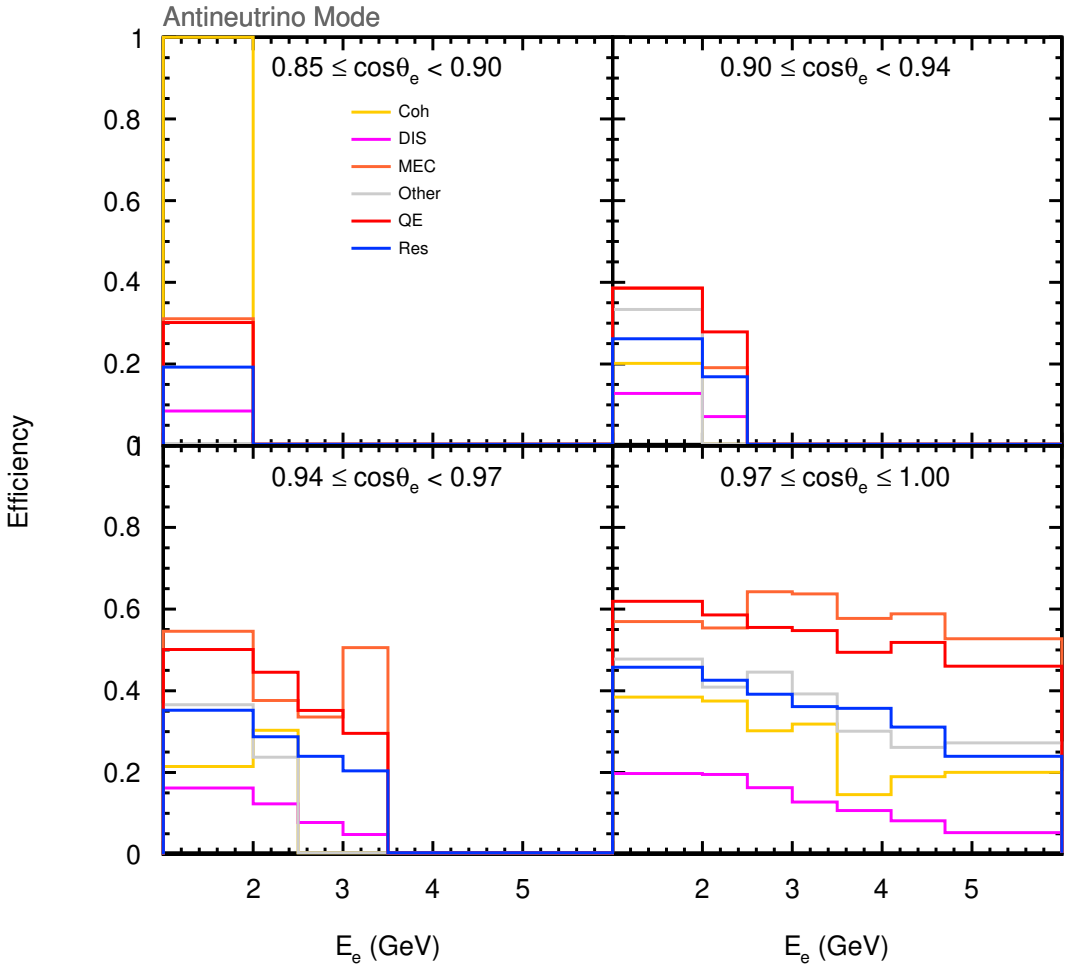

FIGURE 5.43. Signal selection efficiency (bin-width normalized) broken down by interaction mode in electron kinematics and RHC beam mode.

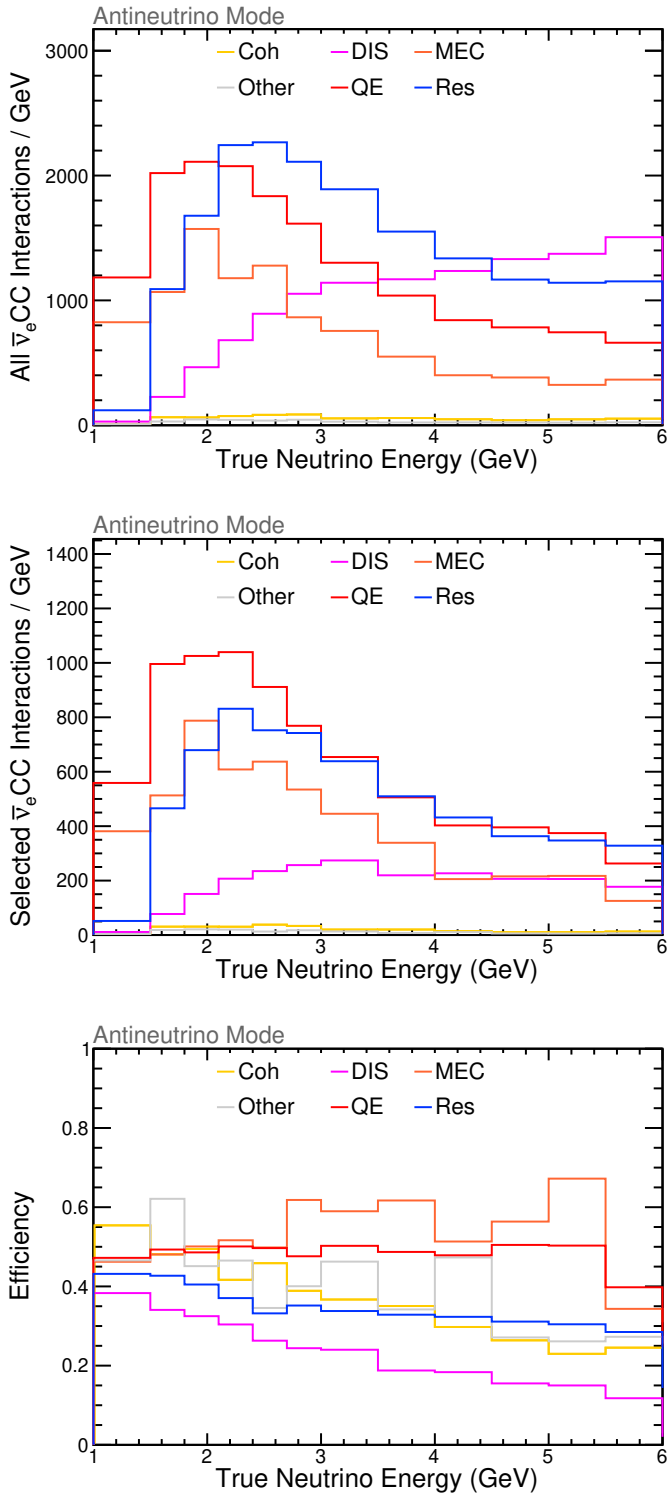

FIGURE 5.44. Breakdown of signal selection efficiency (bin-width normalized) as a function of E_ν in RHC beam mode.

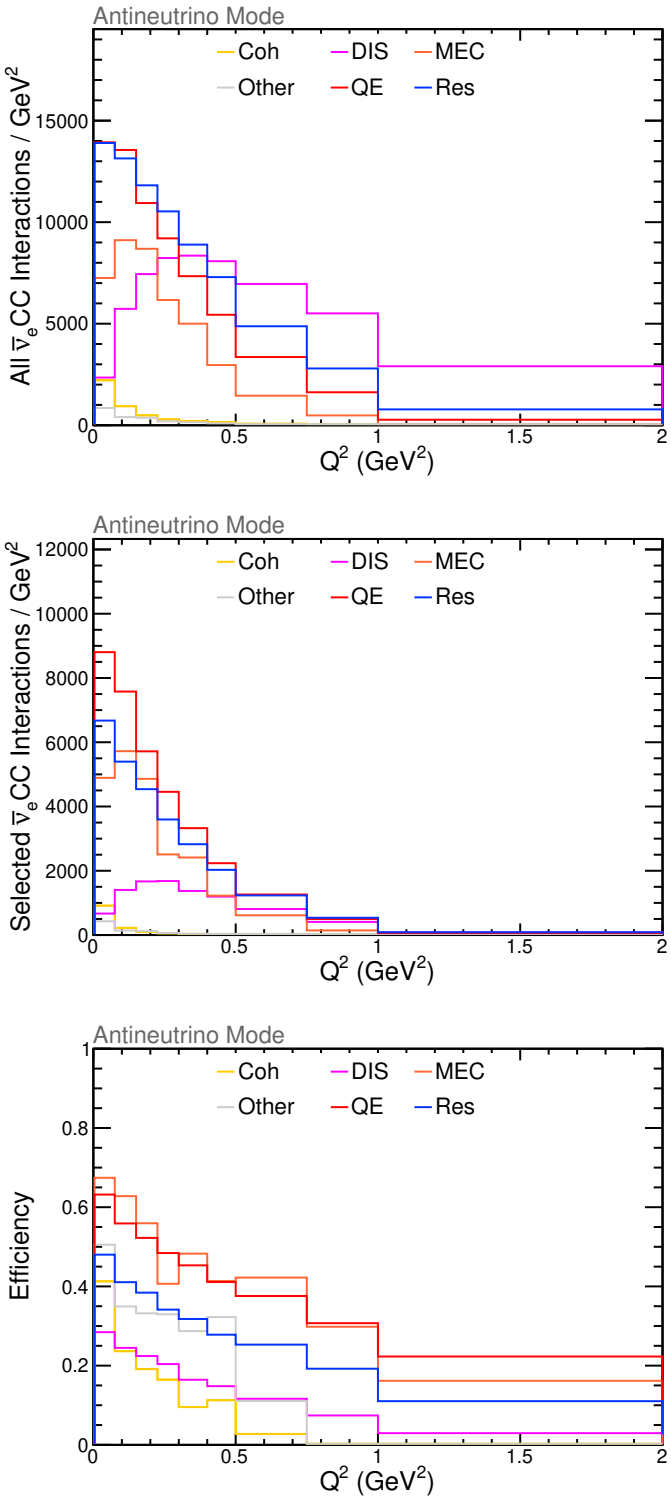

FIGURE 5.45. Breakdown of signal selection efficiency (bin-width normalized) as a function of Q^2 in RHC beam mode.

5.7. Target Count

The number of target nucleons within the fiducial volume of the detector is determined by a random sampling procedure [122] using a detailed specification of the detector geometry and composition [150, 151]. One-million (10^6) points are randomly sampled within the detector geometry. Each point is a small volume of material such that $v = \text{Fiducial Volume}/10^6$. The density of the material within each volume is used to accumulate mass contributions from each material, each element, and the total mass contained within the fiducial volume. The total number of nucleons is calculated by multiplying the $Z = N_{\text{neutron}} + N_{\text{proton}}$ of each material's mass contribution by Avogadro's number. Table 5.8 shows the materials sampled, contributions to the total detector mass, and uncertainties. Table 5.9 shows the sampled chemical elements, contributions to the total detector mass, and uncertainties. The total mass of the fiducial volume is found to be $(50{,}184.8 \pm 499.8)\,\text{kg}$. The total number of nucleons within the fiducial volume is found to be $(3.0219 \pm 0.0301) \times 10^{31}$. The error includes uncertainty in detector assembly [152] and a statistical error from the MC sampling of $\pm 16.3\,\text{kg}$.

5.8. Fake Data Studies

The final extraction of $\bar{\nu}_e$-CC inclusive cross section is performed by combining the unfolded signal estimation with flux and target estimation and efficiency correction. Equation (5.5) is used to calculate the double-differential cross section as a function of electron energy and cosine of the

Table 5.8. Materials and mass contributions of the fiducial volume of the NOvA ND.

Material	Mass (kg)	Mass contribution (%)	Uncertainty (kg)
Scintillator	31,564.6	62.90	189.4
PVC	18,260.8	36.39	292.2
Glue	357.6	0.71	17.9
Air	1.9	<0.01	<0.1

TABLE 5.9. Elements and mass contributions of the fiducial volume of the NOvA ND.

Element	Z	Mass (kg)	Mass contribution (%)	Uncertainty (kg)
C	6	33,488.9	66.74	273.5
Cl	17	8,053.1	16.05	129.4
H	1	5,400.9	10.76	41.8
Ti	22	1,613.2	3.21	25.8
O	8	1,493.8	2.98	26.8
Sn	50	59.6	0.12	1.0
S	16	48.0	0.10	0.8
Ca	20	13.2	0.03	0.2
N	7	13.0	0.03	0.1
Na	11	1.3	<0.01	<0.1

scattering angle. Single-differential cross sections as functions of electron energy, cosine of the electron scattering angle, and Q^2 are calculated using Equation (5.4). Finally, total cross section as a function of neutrino energy is calculated using Equation (5.2).

The analysis is performed on a number of fake data samples to validate the codes and test the robustness of the methodology. Section 5.8.1 demonstrates the template fit procedure and subsequent cross section extraction from the nominal simulated prediction of measured neutrino interactions, validating the calculation of each term in (5.5). Sections 5.8.2 and 5.8.3 test the robustness of the analysis against statistical fluctuations and changes to the underlying cross-section and flux models.

5.8.1. ANALYSIS SELF-CONSISTENCY. The implementation of the analysis methodology is validated by extracting the neutrino cross section from the nominal simulation sample. Since the nominal simulation is used to predict the analysis templates, efficiency correction, and neutrino flux, the extracted cross section should be equal to that which is calculated directly from the simulation.

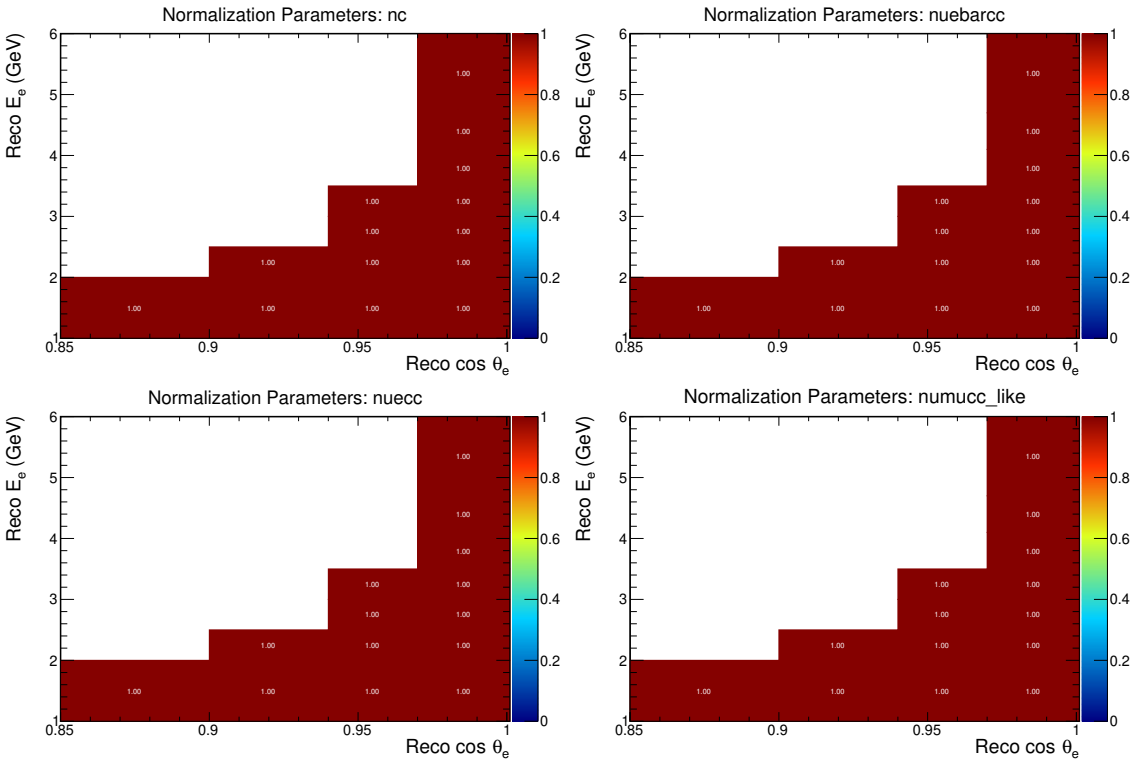

FIGURE 5.46. Template normalization parameters extracted from a template fit to the nominal simulation, demonstrating self-consistency of the fitting procedure.

Figure 5.46 shows the template fit normalization parameters resulting from a fit to the nominal simulation. As expected, all values are equal to unity since the fake data is composed of the sum of template distributions. Figures 5.47 to 5.49 show the cross sections subsequently extracted by unfolding the signal rate estimated from the template fit and dividing by flux, efficiency, and scattering targets. Since these cross sections are equal to that used to derive the nominal simulation (NOvA GENIE Tune N18_10j_000), analysis self-consistency is demonstrated.

5.8.2. STATISTICAL FLUCTUATIONS. A collection of cross section measurements using statistically varied fake data samples is presented. The double-differential $\bar{\nu}_e$-CC inclusive cross section is shown in Figures 5.50 and 5.51. Single-differential measurements as functions of electron energy and cosine of the scattering angle are shown in Figures 5.52 and 5.53. Total cross section as a function of neutrino angle and single-differential cross section as a function of Q^2 are shown

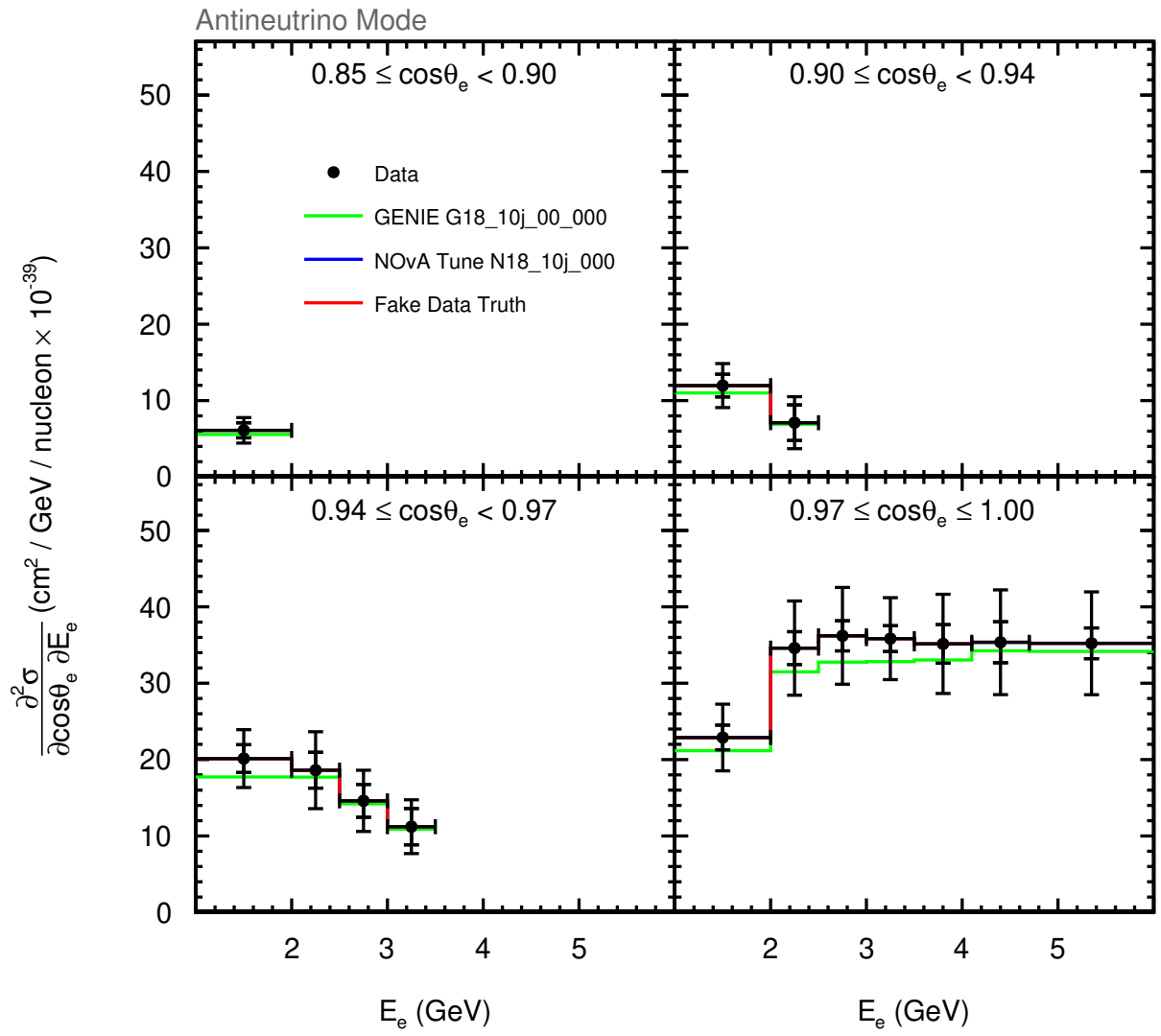

FIGURE 5.47. Extracted double-differential $\bar{\nu}_e$-CC inclusive cross section from the nominal simulation (red). Results are compared to the NOvA (blue) and default (green) GENIE tunes. In this case, the fake data truth is the NOvA GENIE tune.

in Figures 5.54 and 5.55. Results are compared to the fake data truth[‡‡], NOvA and default GENIE-tuned samples. The fake data truth is well-contained within uncertainties demonstrating the analysis is robust to statistical fluctuations.

[‡‡]Here, the fake data truth is identically the NOvA GENIE-tune sample.

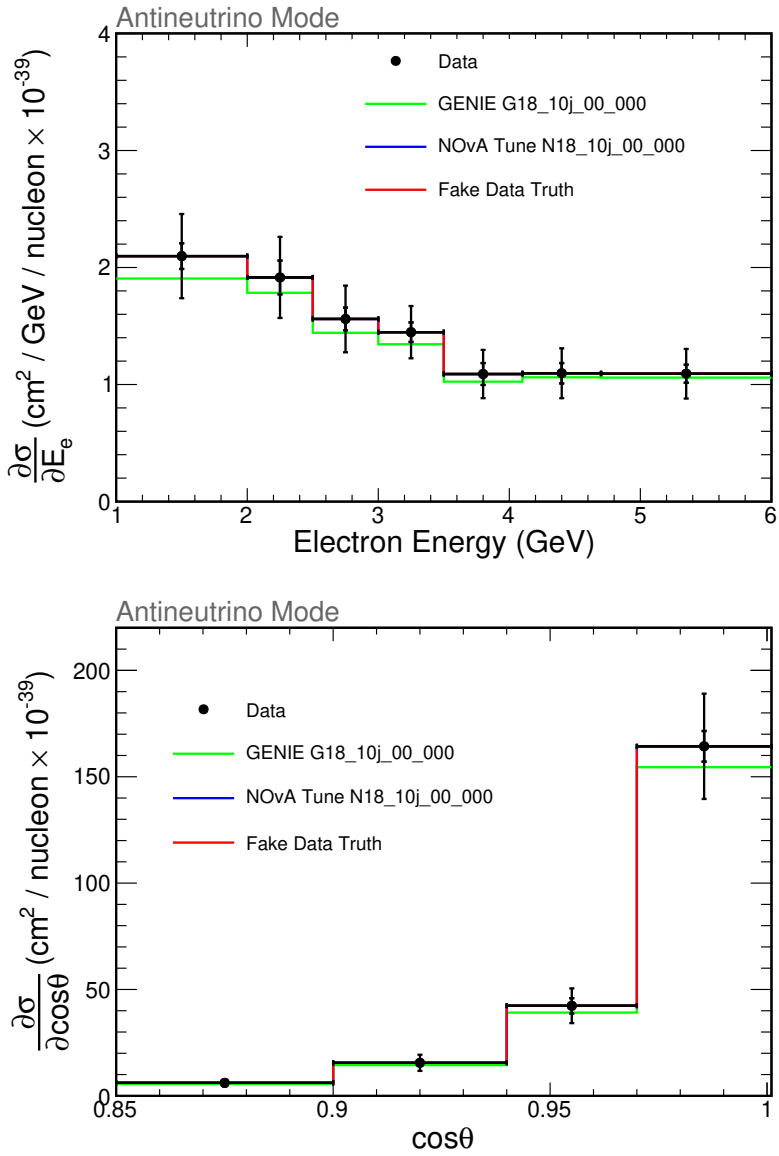

FIGURE 5.48. Extracted single-differential $\bar{\nu}_e$-CC inclusive cross sections from the nominal simulation (red). Results are shown as a function of electron energy (top) and scattering angle (bottom). Results are compared to the NOvA (blue) and default (green) GENIE tunes. In this case, the fake data truth is the NOvA GENIE tune.

5.8.3. MODIFIED NEUTRINO INTERACTION AND FLUX MODEL. Fake data are generated using alternative neutrino cross section and flux models. The neutrino cross-section model used is the default GENIE CMC, G18_10j_000. The flux model uses the FTFP_BERT hadronic model [127] and GEANT4 specification of the NuMI beamline without constraints to hadron data with PPFX.

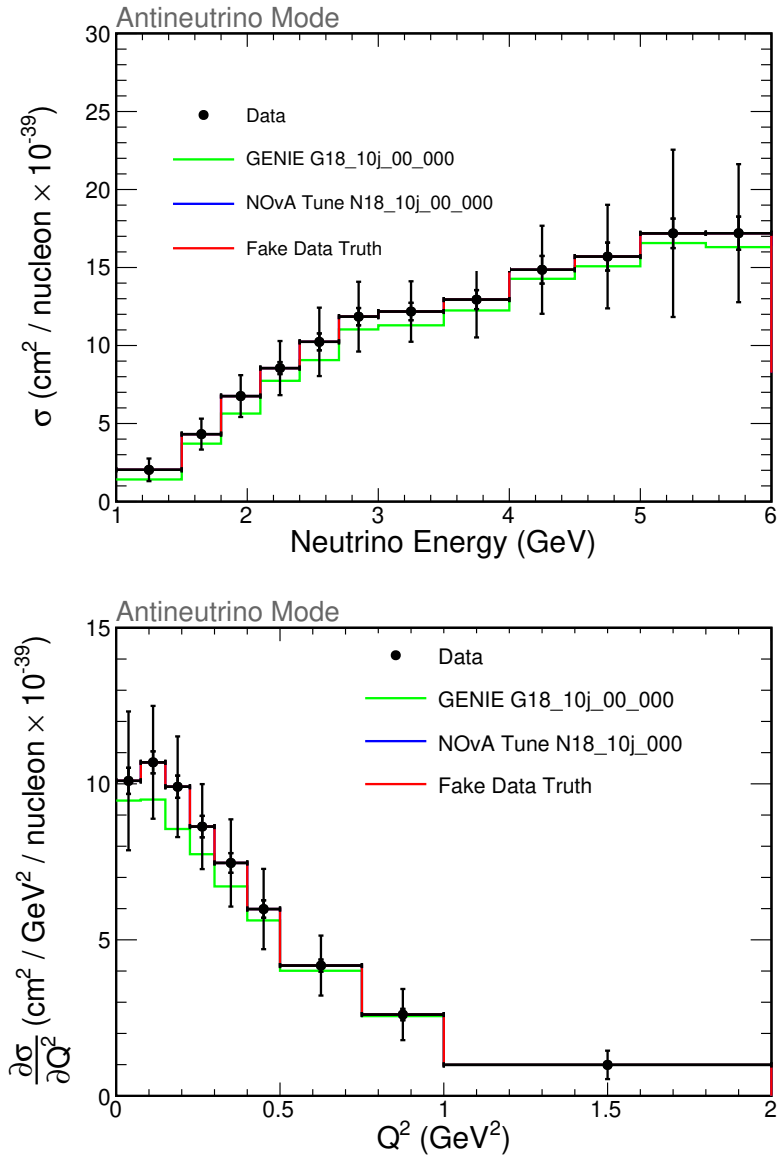

FIGURE 5.49. Extracted total and single-differential $\bar{\nu}_e$-CC inclusive cross sections from the nominal simulation (red). Results are shown as a function of neutrino energy (top) and Q^2 (bottom). Results are compared to the NOvA (blue) and default (green) GENIE tunes. In this case, the fake data truth is the NOvA GENIE tune.

These represent changes to the two models with the largest uncertainties, yet the analysis is able to estimate the true cross section within error. Figures 5.56 and 5.57 show the double-differential cross section results, Figures 5.58 and 5.59 show single-differential results as functions of electron

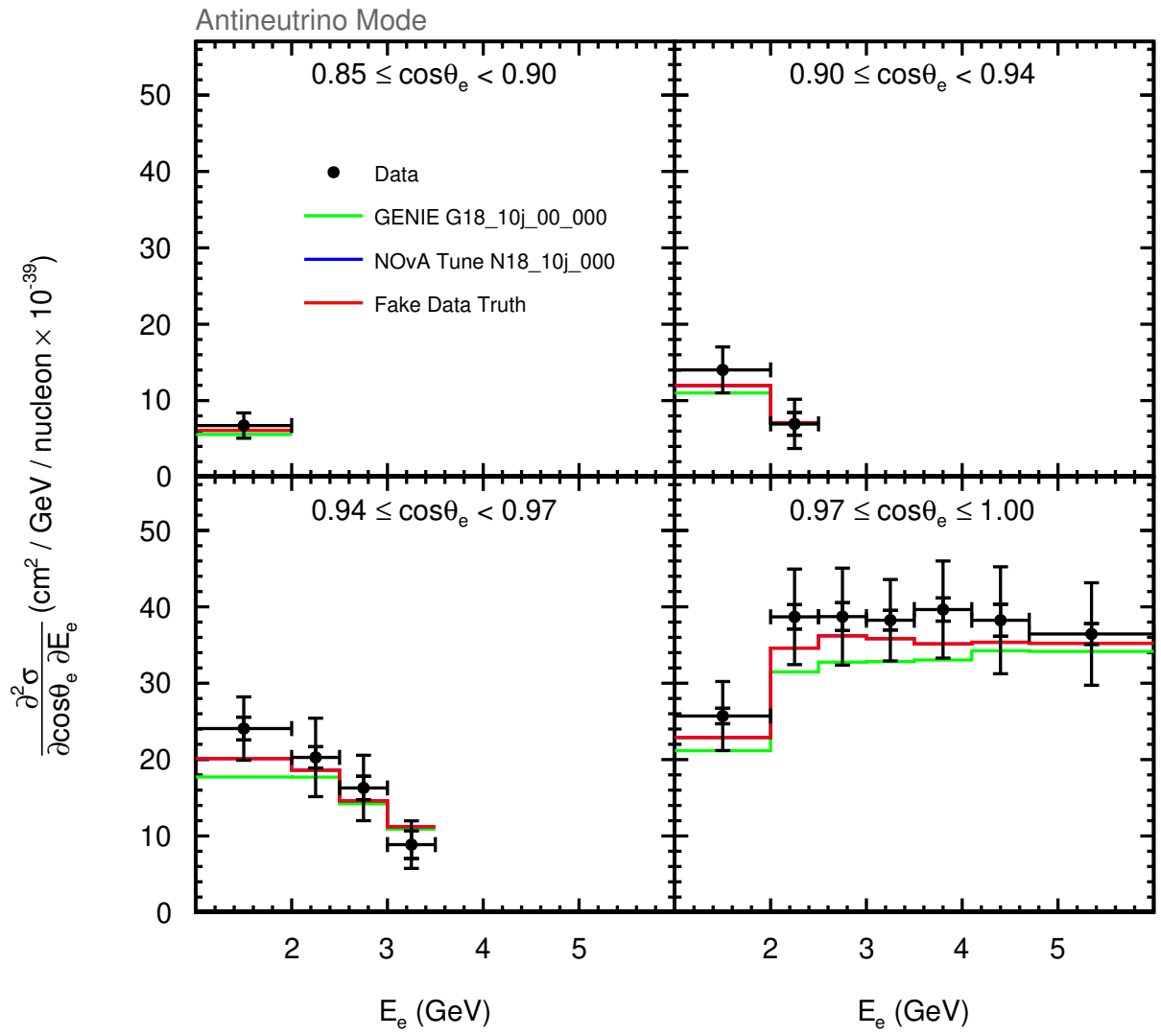

FIGURE 5.50. Extracted double-differential $\bar{\nu}_e$-CC inclusive cross section from fake data generated by statistically varying the nominal prediction (red). Results are compared to the NOvA (blue) and default (green) GENIE tunes.

energy and scattering angle, and Figures 5.60 and 5.61 shows the differential cross section as a function of Q^2 and total cross section as a function of neutrino energy.

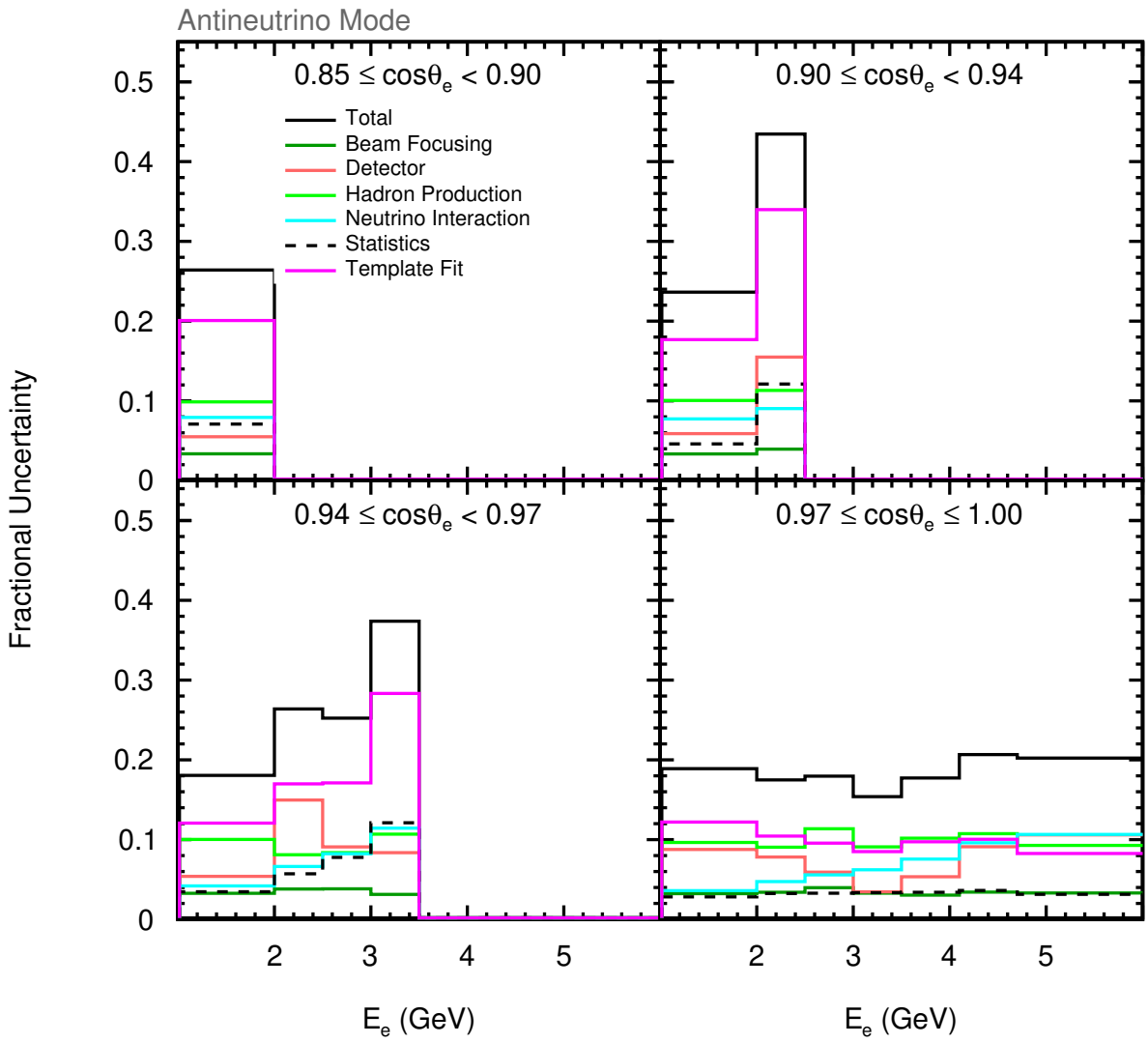

FIGURE 5.51. Uncertainties on the double-differential $\bar{\nu}_e$-CC inclusive cross section extracted from fake data generated by statistically varying the nominal prediction. The largest effect is due to uncertainties on the template fit normalization parameters. The total uncertainty is a quadrature sum of the individual effects.

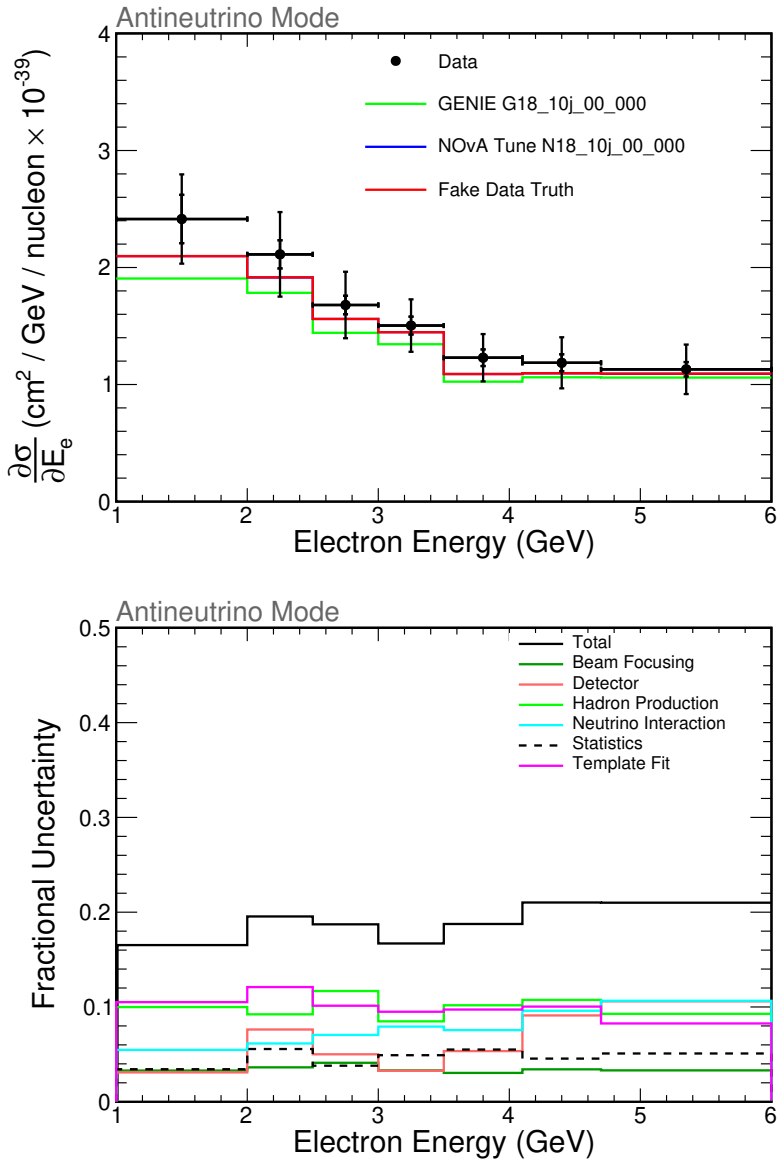

FIGURE 5.52. Top: Extracted single-differential $\bar{\nu}_e$-CC inclusive cross section as a function of electron energy from fake data generated by statistically varying the nominal prediction (red). Results are compared to the NOvA (blue) and default (green) GENIE tunes. Bottom: Uncertainty breakdown on the single-differential cross section. The total uncertainty is a quadrature sum of the individual effects.

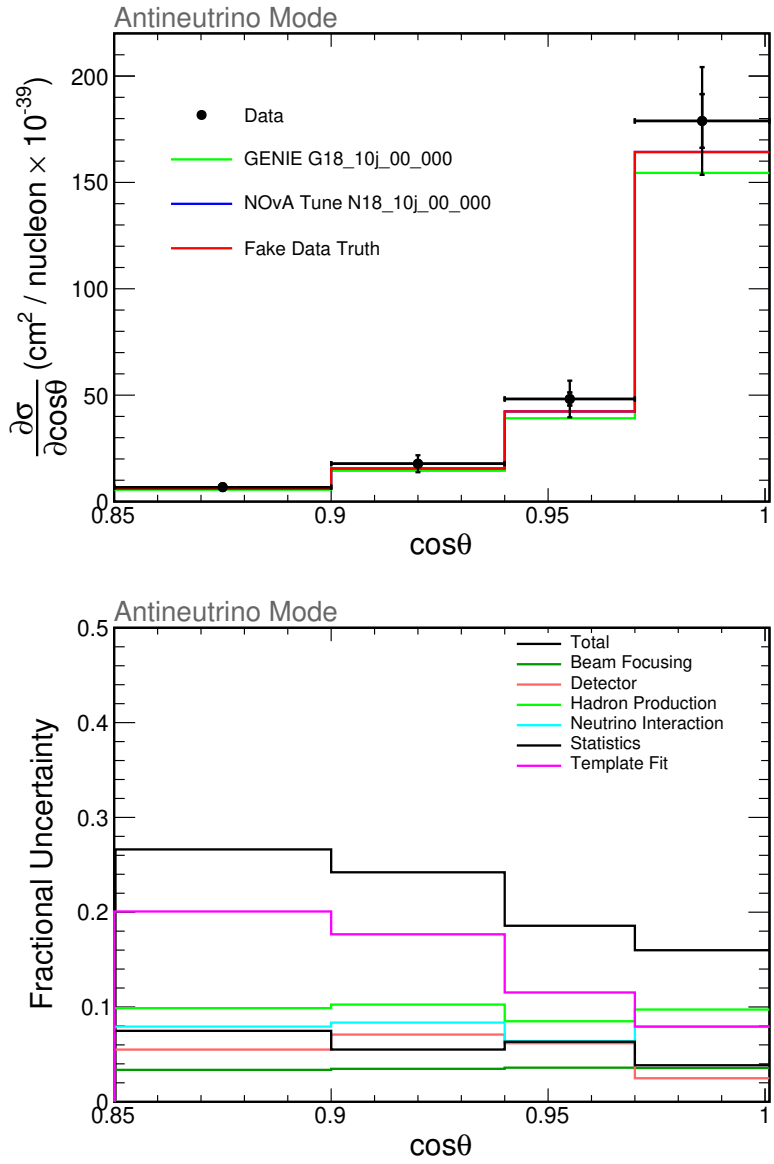

FIGURE 5.53. Top: Extracted single-differential $\bar{\nu}_e$-CC inclusive cross section as a function of electron scattering angle from fake data generated by statistically varying the nominal prediction (red). Results are compared to the NOvA (blue) and default (green) GENIE tunes. Bottom: Uncertainty breakdown on the single-differential cross section. The total uncertainty is a quadrature sum of the individual effects.

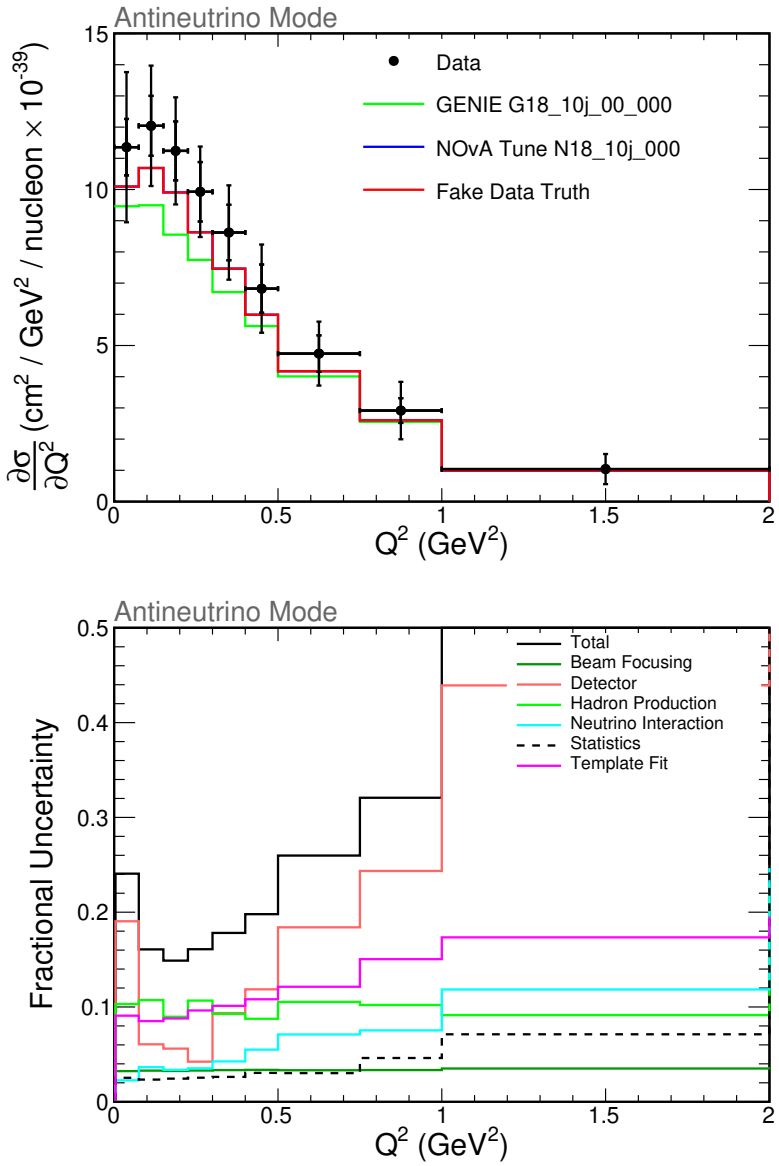

FIGURE 5.54. Top: Extracted single-differential $\bar{\nu}_e$-CC inclusive cross section as a function of Q^2 from fake data generated by statistically varying the nominal prediction (red). Results are compared to the NOvA (blue) and default (green) GENIE tunes. Bottom: Uncertainty breakdown on the single-differential cross section. The total uncertainty is a quadrature sum of the individual effects.

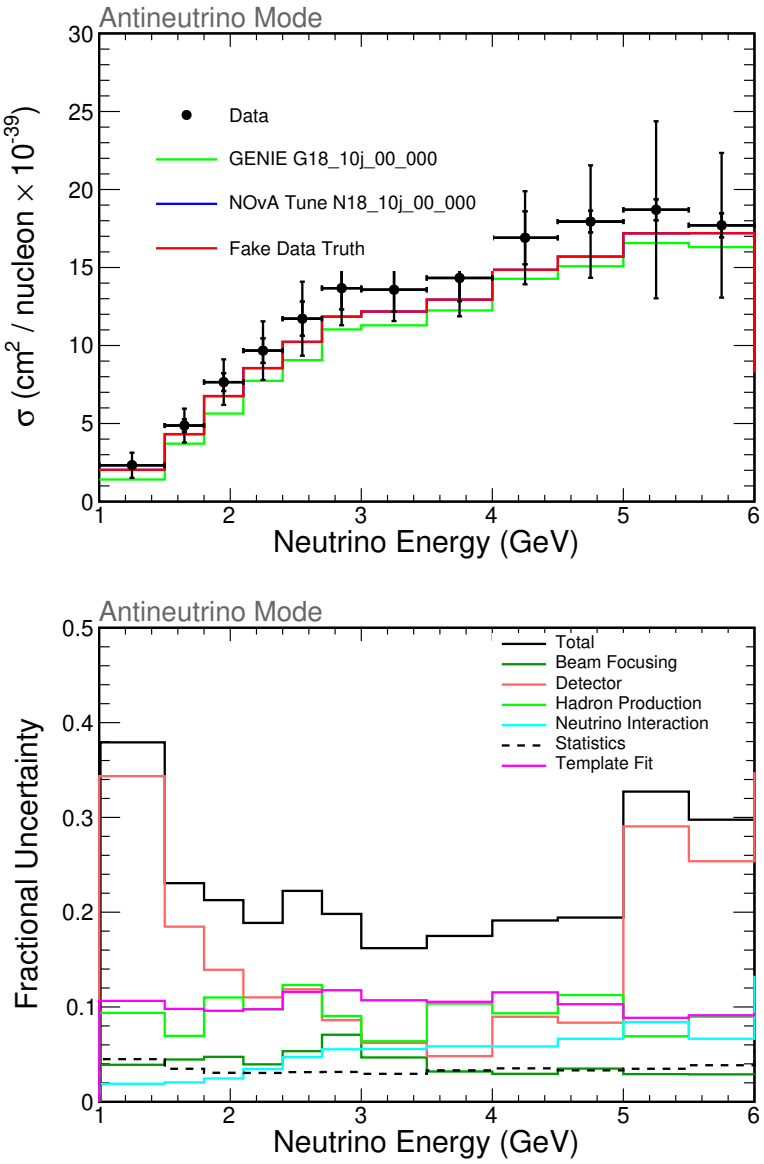

FIGURE 5.55. Top: Extracted total $\bar{\nu}_e$-CC inclusive cross sections as a function of neutrino energy from fake data generated by statistically varying the nominal prediction (red). Results are compared to the NOvA (blue) and default (green) GENIE tunes. Bottom: Uncertainty breakdown on the cross section. The total uncertainty is a quadrature sum of the individual effects.

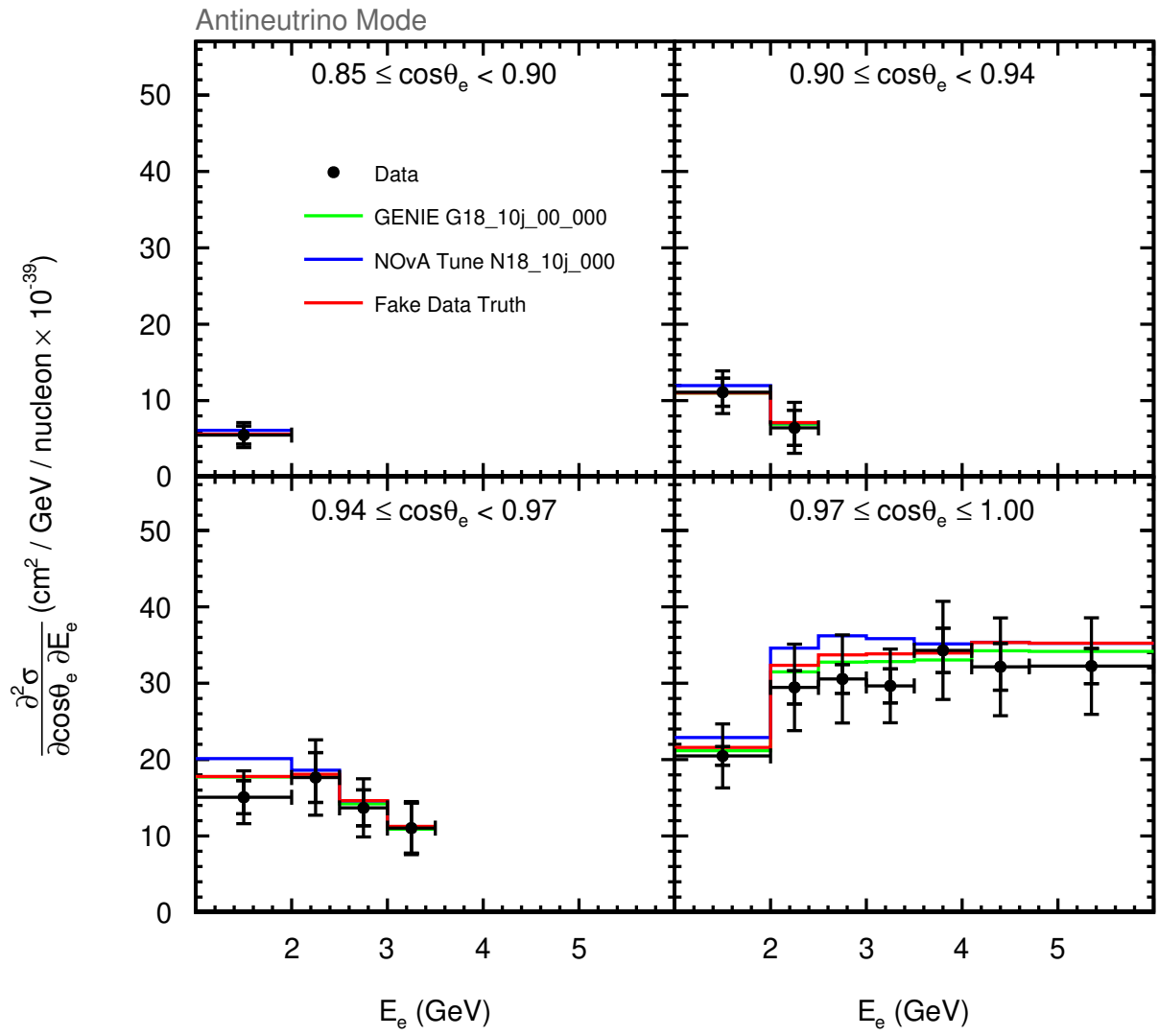

FIGURE 5.56. Extracted double-differential $\bar{\nu}_e$-CC inclusive cross section from fake data generated with modified neutrino interaction and flux models (red). Results are compared to the NOvA (blue) and default (green) GENIE tunes.

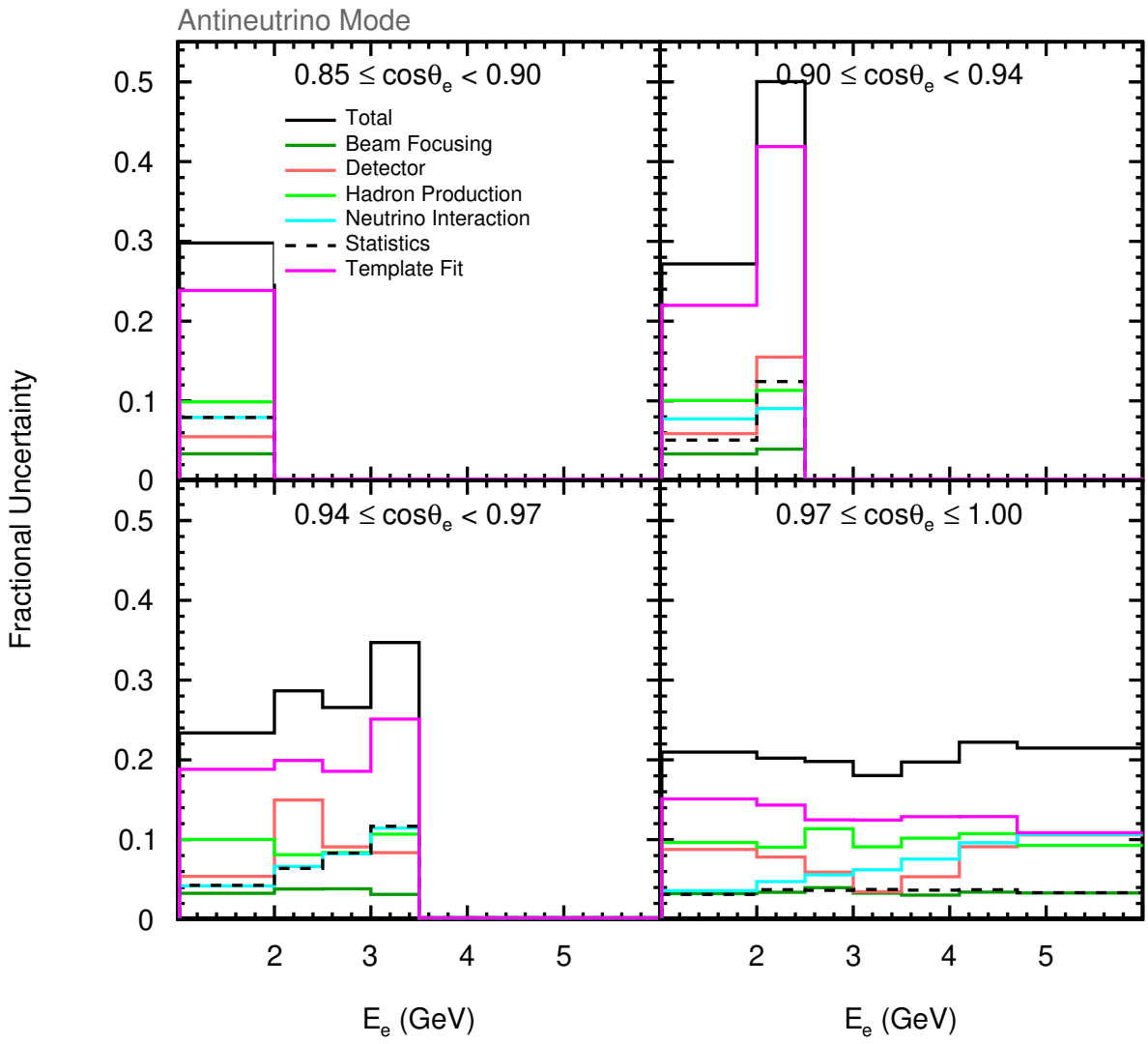

FIGURE 5.57. Uncertainties on the double-differential $\bar{\nu}_e$-CC inclusive cross section extracted from fake data generated with modified neutrino interaction and flux models. The largest effect is due to uncertainties on the template fit normalization parameters. The total uncertainty is a quadrature sum of the individual effects.

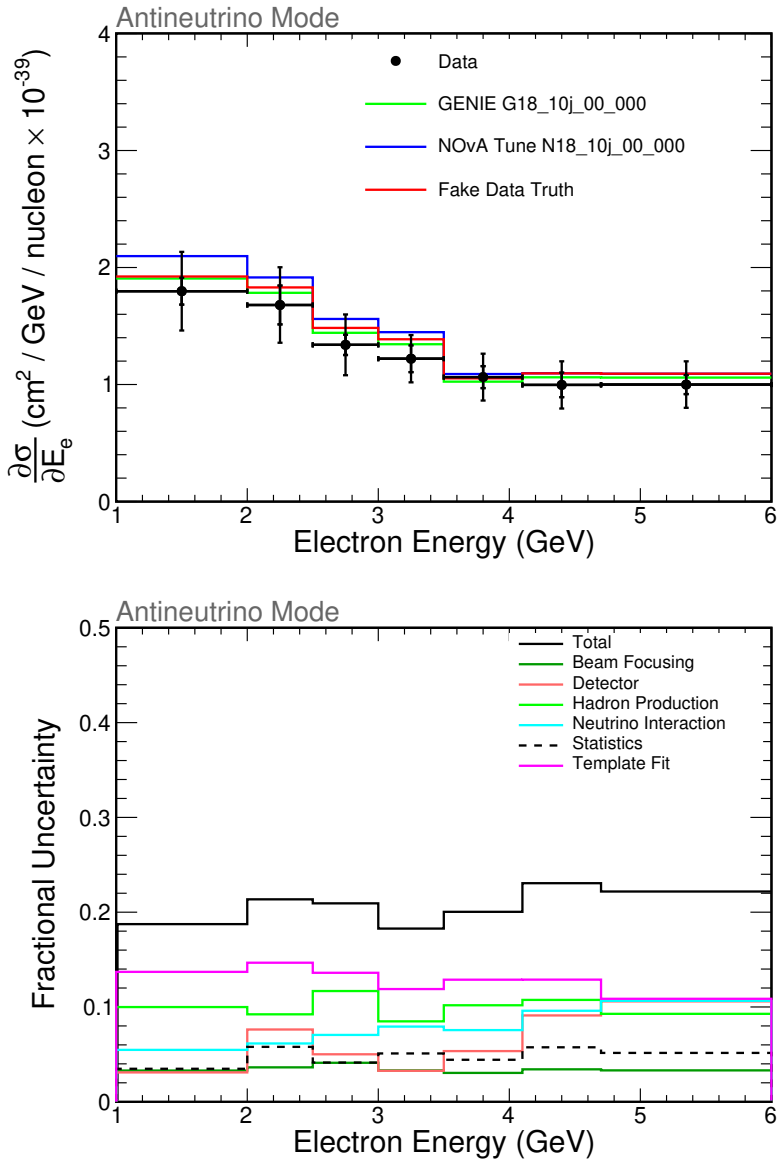

FIGURE 5.58. Top: Extracted single-differential $\bar{\nu}_e$-CC inclusive cross section as a function of electron energy from fake data generated with modified neutrino interaction and flux models (red). Results are compared to the NOvA (blue) and default (green) GENIE tunes. Bottom: Uncertainty breakdown on the single-differential cross section. The total uncertainty is a quadrature sum of the individual effects.

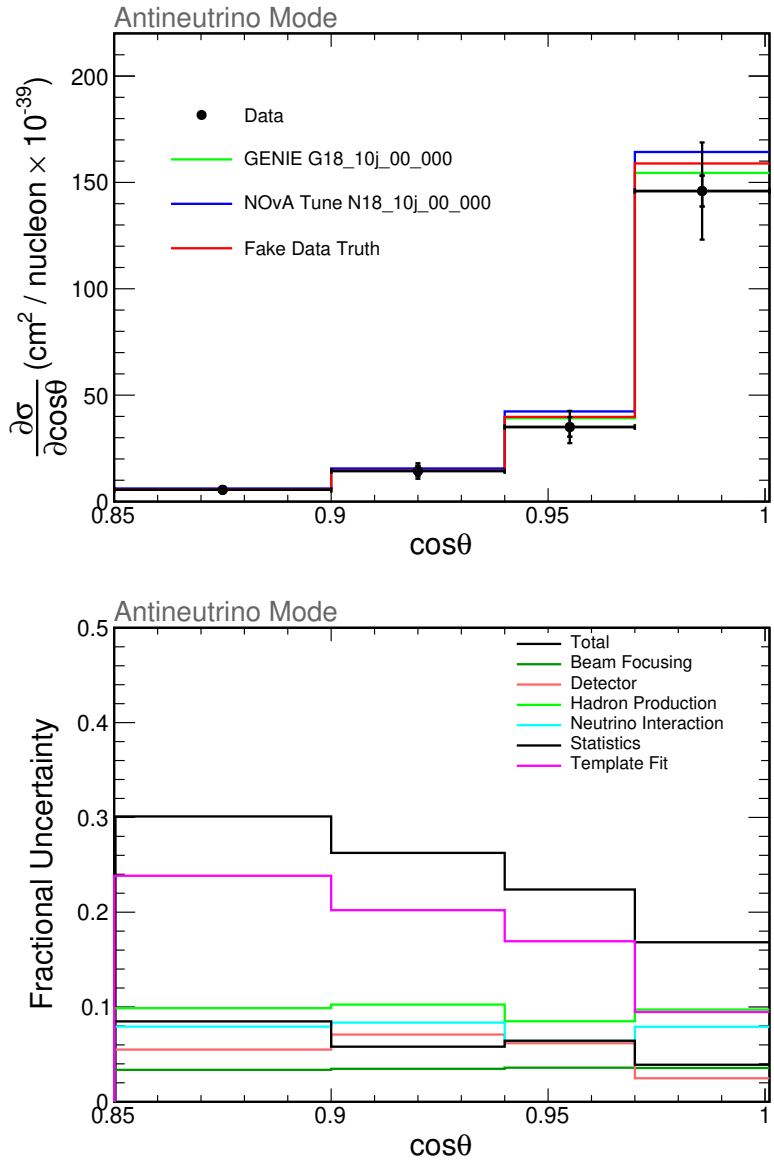

FIGURE 5.59. Top: Extracted single-differential $\bar{\nu}_e$-CC inclusive cross section as a function of electron scattering angle from fake data generated with modified neutrino interaction and flux models (red). Results are compared to the NOvA (blue) and default (green) GENIE tunes. Bottom: Uncertainty breakdown on the single-differential cross section. The total uncertainty is a quadrature sum of the individual effects.

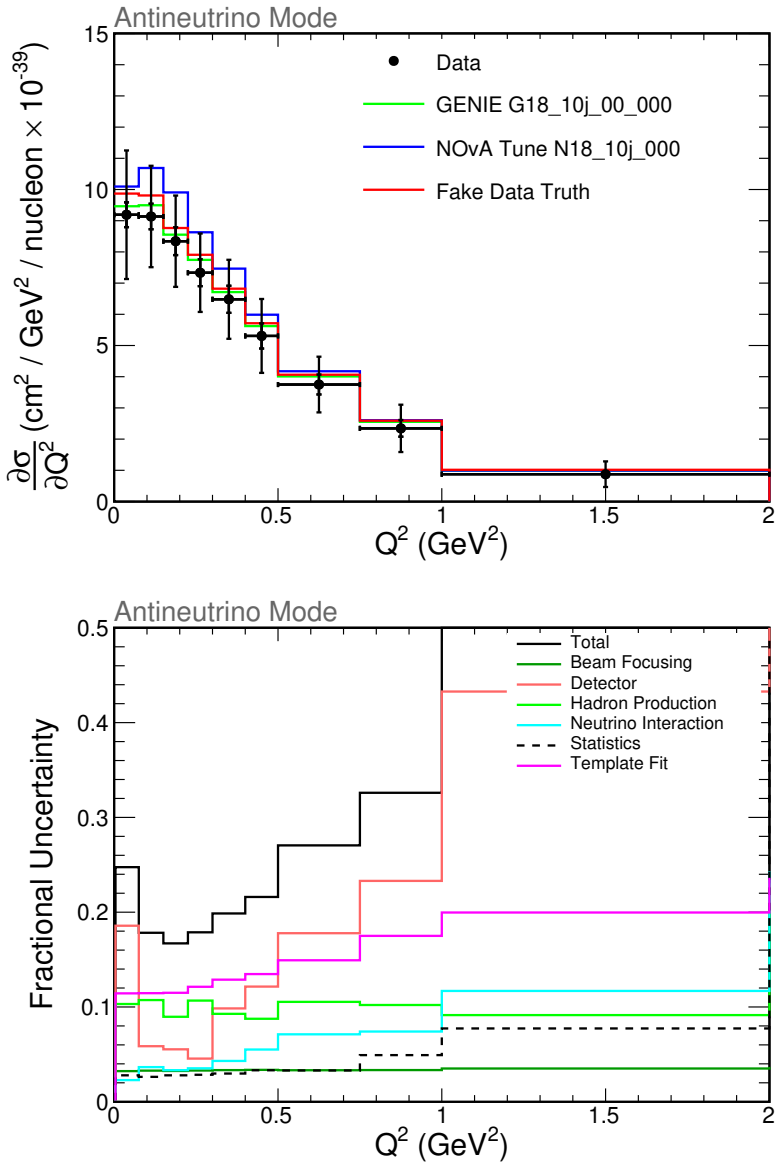

FIGURE 5.60. Top: Extracted single-differential $\bar{\nu}_e$-CC inclusive cross section as a function of Q^2 from fake data generated with modified neutrino interaction and flux models (red). Results are compared to the NOvA (blue) and default (green) GENIE tunes. Bottom: Uncertainty breakdown on the single-differential cross section. The total uncertainty is a quadrature sum of the individual effects.

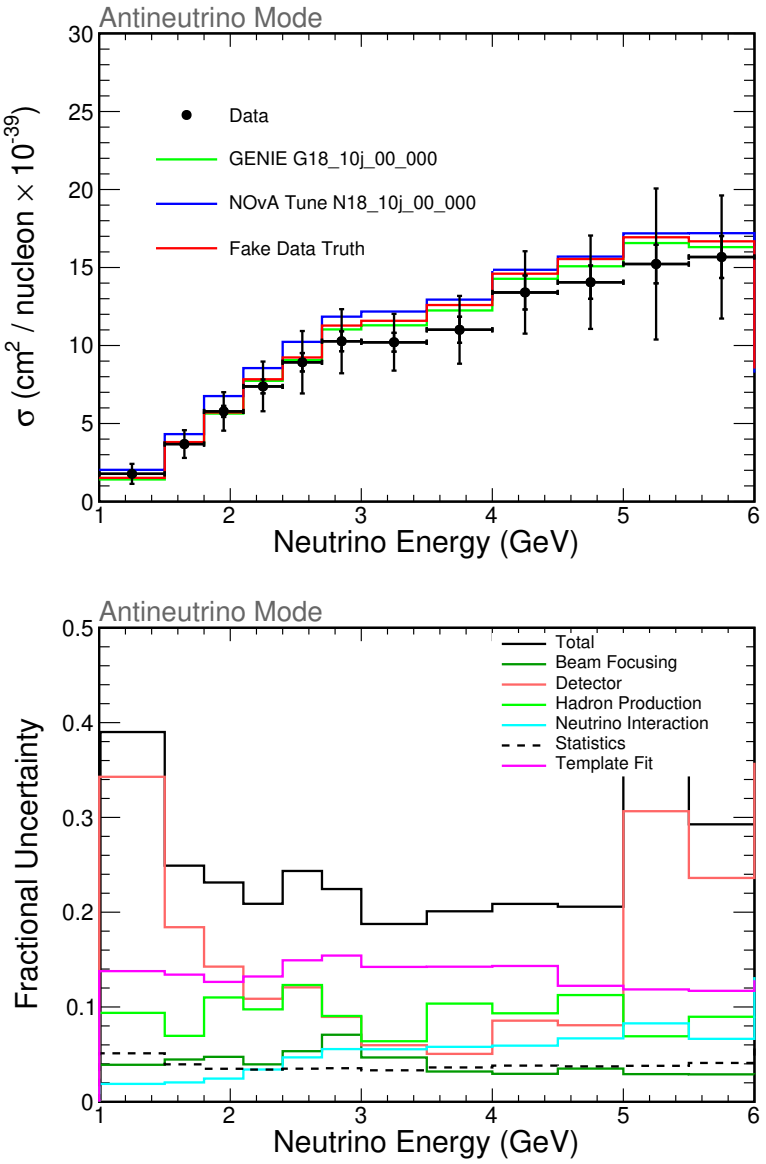

FIGURE 5.61. Top: Extracted total $\bar{\nu}_e$-CC inclusive cross sections as a function of neutrino energy from fake data generated with modified neutrino interaction and flux models (red). Results are compared to the NOvA (blue) and default (green) GENIE tunes. Bottom: Uncertainty breakdown on the cross section. The total uncertainty is a quadrature sum of the individual effects.

CHAPTER 6

Results of the $\bar{\nu}_e$-CC Inclusive Cross Section Measurement

The analysis methods described in Chapter 5 were employed to measure the electron antineutrino charged-current inclusive cross section using NuMI data. Data were selected from samples collected during RHC (FHC) NuMI exposure corresponding to 11.38×10^{20} POT (13.85×10^{20} POT). Efficiency of signal candidate selection was estimated to be $(28 \pm 3)\,\%$. Figure 6.1 shows a comparison between the selected data and simulation in bins of reconstructed electron energy, cosine of the scattering angle, and NueID score. Data are well-constrained within systematic errors throughout the phase space of the analysis. A 7% excess of data measured in the RHC sample is observed.

A template fit (Section 5.5.5) was performed in bins of reconstructed electron energy, scattering angle, and NueID score. Template normalization parameters were extracted for each component, NC, ν_e-CC, $\bar{\nu}_e$-CC, and ν_μ-CC or $\bar{\nu}_\mu$-CC, in bins of electron energy and scattering angle. Figure 6.2 shows the extracted normalization parameters for each component. Figure 6.3 shows the post-fit agreement of selected events between data and simulation in bins of electron energy and cosine of the scattering angle. The template fit procedure is shown to improve agreement between data and simulation.

The sample purity was estimated by adjusting the nominal MC prediction according to the template normalization parameters. Sample purity and associated uncertainty in bins of electron energy and cosine of the scattering angle are shown in Figure 6.4. The average purity was estimated to be $(25 \pm 4)\,\%$, increasing to $(41 \pm 5)\,\%$ for $0.97 \leq \cos\theta \leq 1$. It is estimated that $8{,}203.72 \pm 811.11$ signal events were selected in the RHC NuMI sample.

TABLE 6.1. Contributions to the average uncertainty on the measured double-differential cross section.

Source	Average Uncertainty (%)
Total	21.7
Template Fit	13.6
Hadron Production	11.1
Detector	8.7
Neutrino Interaction Model	8.0
Statistics	4.7
Beam Focusing	3.8

Finally, the double-differential $\bar{\nu}_e$-CC inclusive cross section was extracted and compared to the NOvA (N18_10j_00_000) and default (G18_10j_00_000) GENIE models in Figure 6.5. The measurement agrees well with the NOvA GENIE-tuned samples described in Section 4.2.1 with a χ^2 per degree of freedom ($d.f.$) of $\chi^2/d.f. = 5.02/14$. A measurement of the double-differential ν_e-CC inclusive cross section was also performed using the extracted ν_e-CC normalization parameters as a cross check of the template fitting procedure and shows good agreement with GENIE models and a measurement made by the NOvA collaboration [5] (Figure 6.6).

The average total uncertainty on the measured double-differential cross section is $21.6\,\%$. The dominant sources of uncertainty originate from the template fit, hadron production models, and detector calibration and light yield. Table 6.1 shows the contribution of each source of uncertainty.

Also reported are single-differential cross sections as functions of electron energy (Figure 6.7), cosine of the electron scattering angle (Figure 6.8), and Q^2 (Figure 6.9), and total cross section as a function of neutrino energy (Figure 6.10).

A χ^2 was calculated to quantify the agreement between measurements and GENIE models, which accounts for correlated uncertainties in the measurement. The χ^2 is defined as

$$\chi^2 = (\hat{x} - x)V^{-1}(\hat{x} - x) \tag{6.1}$$

TABLE 6.2. χ^2 values comparing model predictions to the measured cross sections and uncertainties. Degrees of freedom ($d.f.$) for each measurement are also shown.

Cross Section	$d.f.$	N18_10j_00_000	G18_10j_00_000
$\frac{\partial^2\sigma}{\partial E_e \partial \cos\theta}$	14	5.02	5.23
$\frac{\partial\sigma}{\partial \cos\theta}$	4	0.10	0.25
$\frac{\partial\sigma}{\partial E_e}$	7	3.24	3.69
$\frac{\partial\sigma}{\partial Q^2}$	9	3.26	4.80
$\sigma(E_\nu)$	12	3.08	5.91

where $\hat{x}$ and V are the measured cross section and covariance matrix and x is the model prediction. Table 6.2 shows χ^2 values and the numbers of degrees of freedom ($d.f.$) for each measurement. While a $\chi^2/d.f. < 1$ can be indicative of over fitting, the fake data study presented in Section 5.8.3 shows the analysis is able to extract an alternative cross-section model.

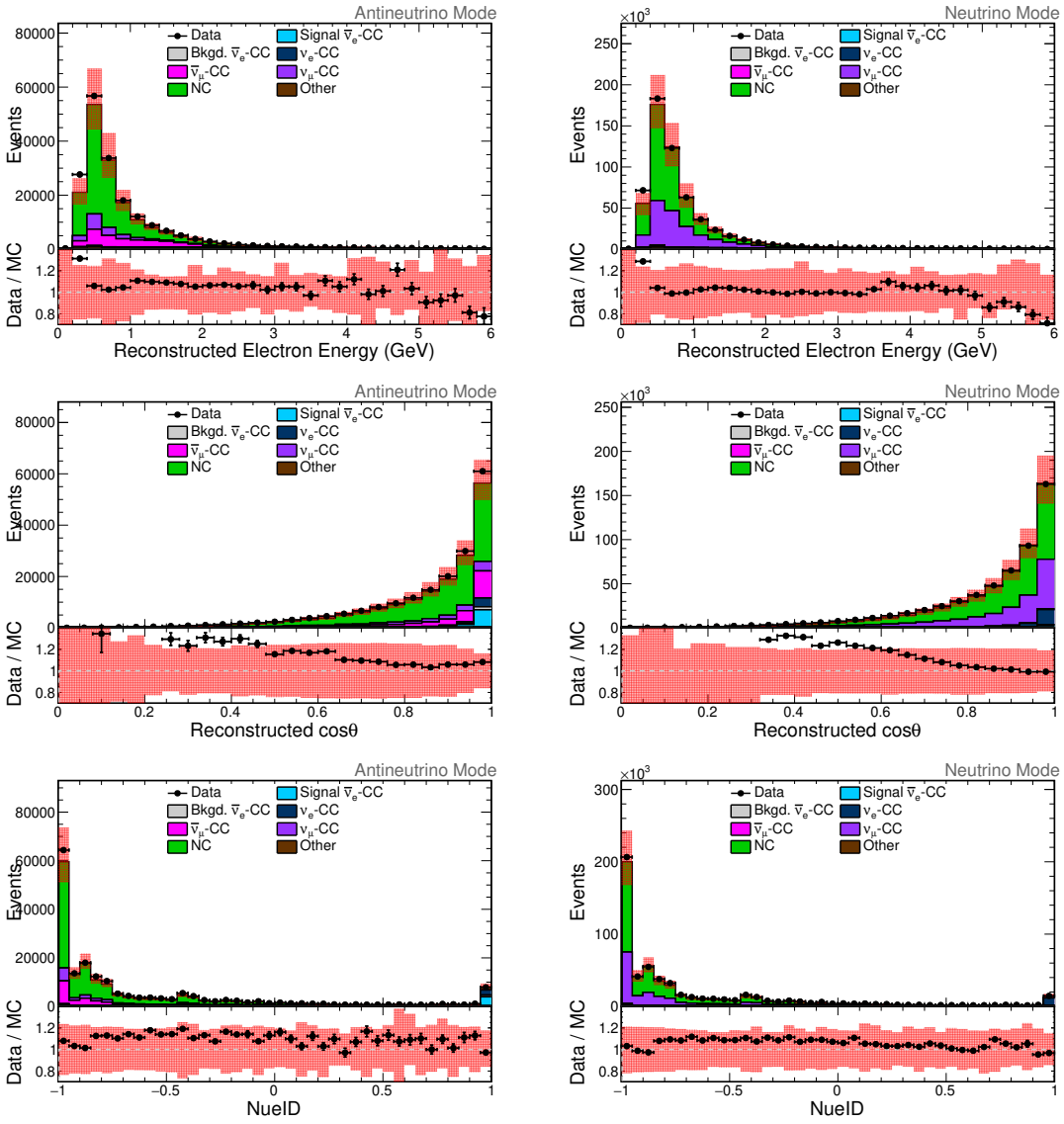

FIGURE 6.1. Selected data RHC (left) and FHC (right) NuMI exposure corresponding to 11.38×10^{20} POT and 13.85×10^{20} POT, respectively, compared to simulation. Data and simulation are shown in bins of reconstructed electron energy, electron scattering angle, and NueID score. Red regions indicate systematic uncertainty bands. Data are well-constrained within systematic error within the phase space of the analysis. An overall excess of data measured in the RHC sample is observed.

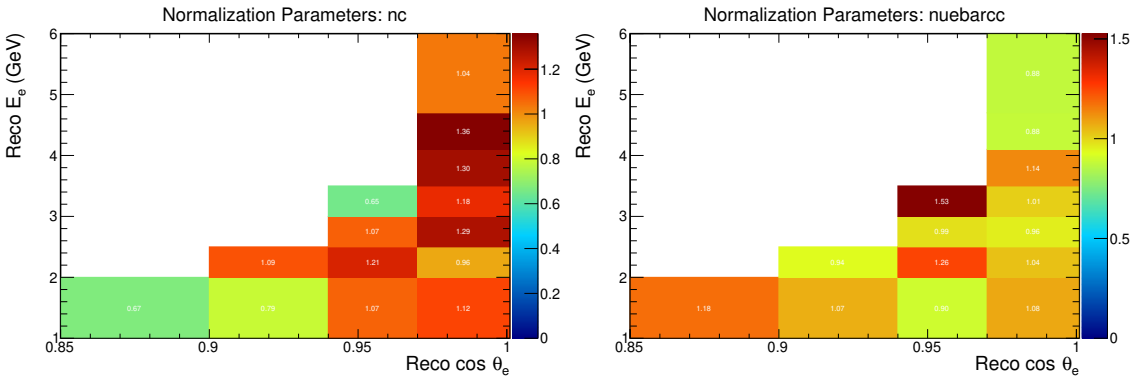

(A) RHC

(B) RHC

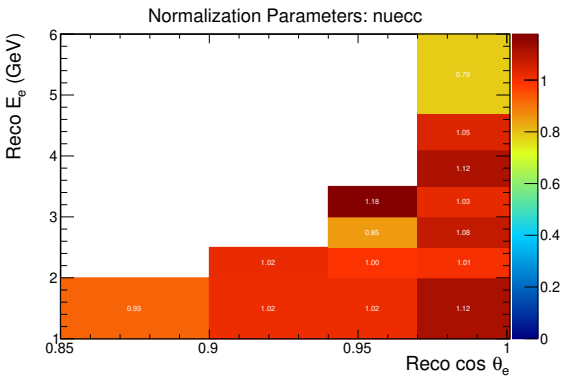

(C) FHC

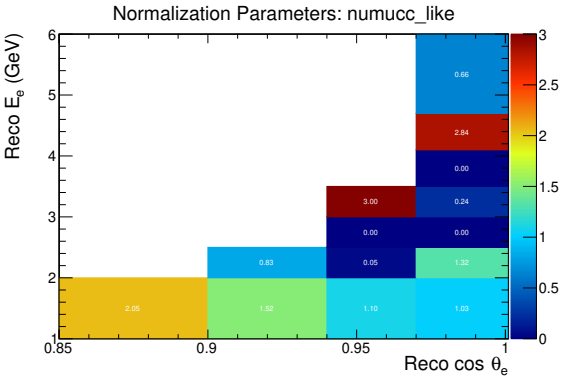

(D) FHC

FIGURE 6.2. Template normalization parameters extracted from a template fit to data selected from NuMI exposure. Conditioning samples are indicated below each figure.

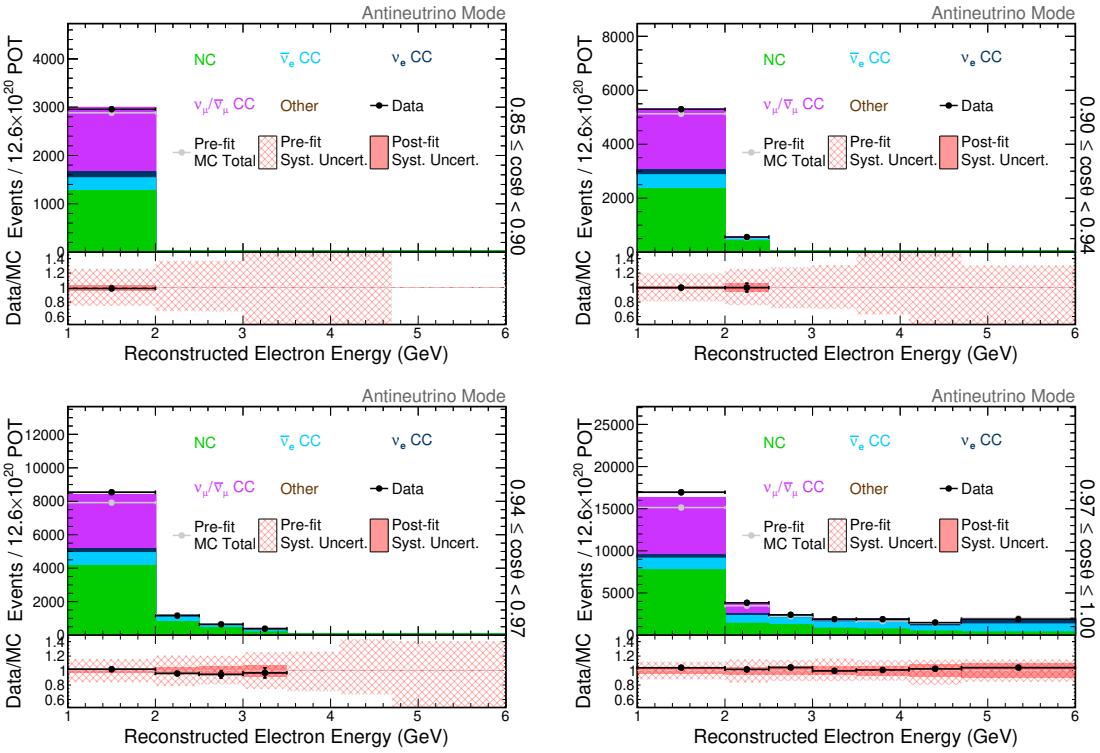

FIGURE 6.3. Renormalized event rates extracted from a template fit to NuMI data. The bottom panels each show the ratio between data and post-fit MC. Hashed red regions indicate shape-only uncertainties estimated from systematically modified simulation. Solid red regions indicate total uncertainty on the number of selected events constrained by data via template fit procedure.

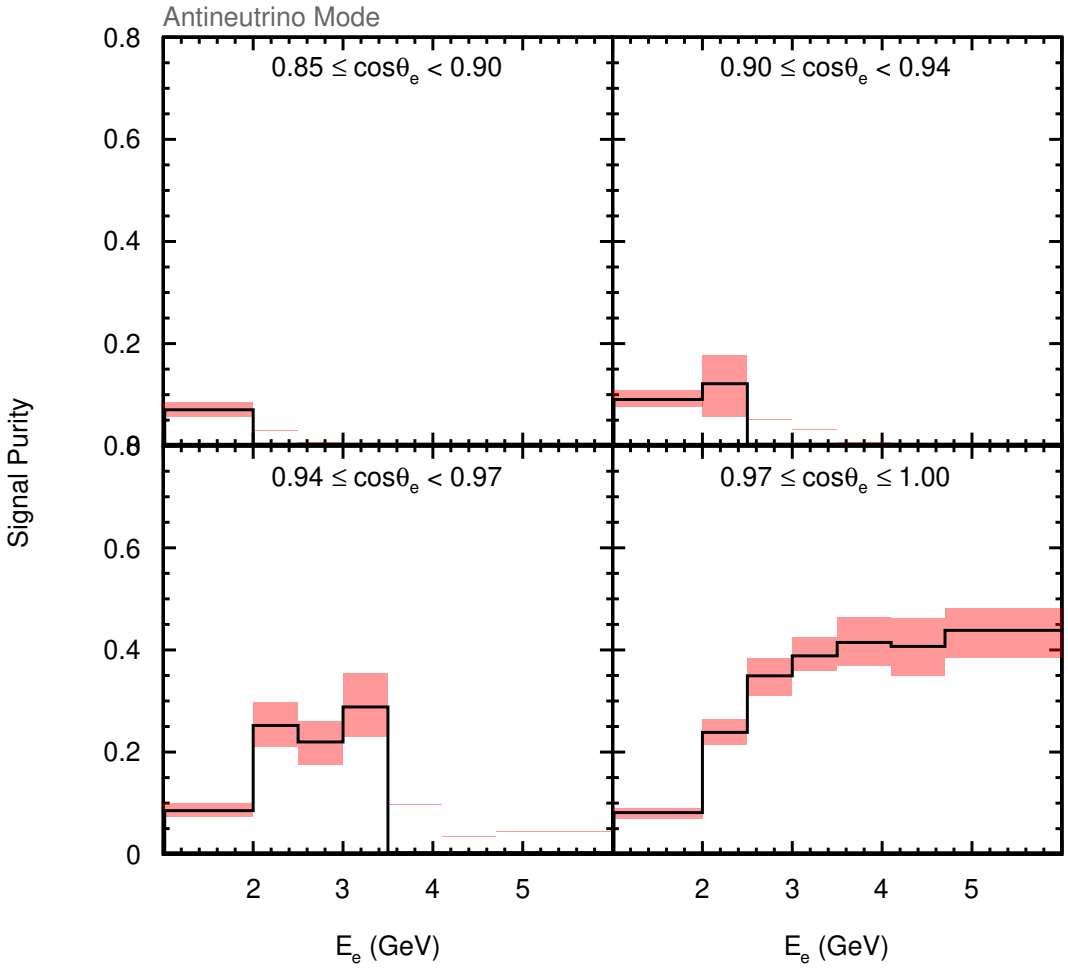

FIGURE 6.4. Sample purity estimated by template fit to NuMI data in bins of reconstructed electron energy and cosine of the scattering angle. Errors are derived from correlated uncertainties in the template fit normalization parameters.

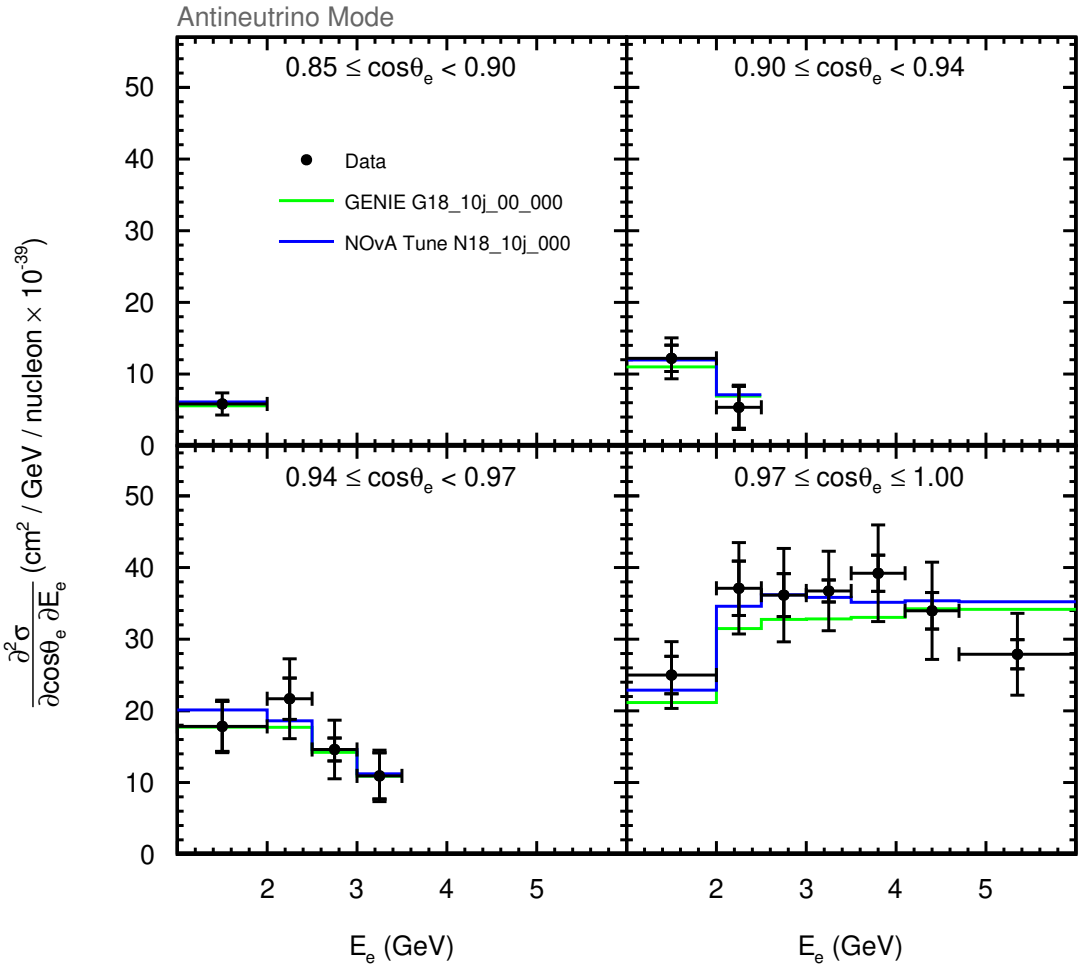

FIGURE 6.5. Measured double-differential $\bar{\nu}_e$-CC inclusive cross section using selected data from NuMI corresponding to 11.38×10^{20} POT (13.85×10^{20} POT) RHC (FHC) exposure. Results are compared to the NOvA (blue) and default (green) GENIE tunes.

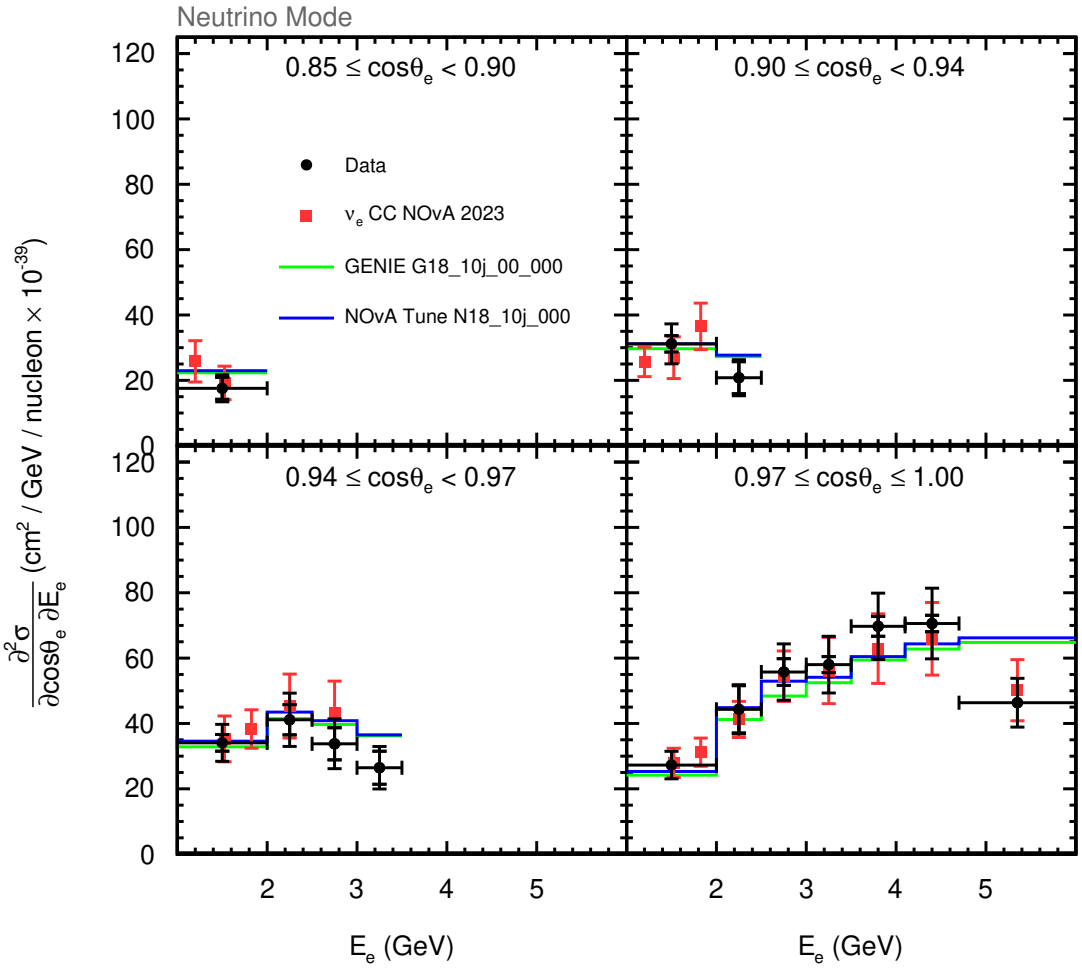

FIGURE 6.6. Measured double-differential ν_e-CC inclusive cross section using selected data from NuMI corresponding to 11.38×10^{20} POT (13.85×10^{20} POT) RHC (FHC) exposure. Results are compared to [5] (red squares) and the NOvA (blue line) and default (green line) GENIE tunes.

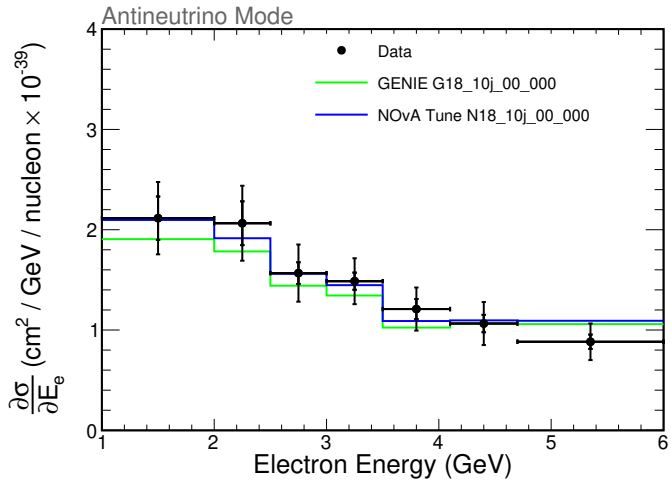

FIGURE 6.7. Measured single-differential $\bar{\nu}_e$-CC inclusive cross section as a function of electron angle using selected data from NuMI corresponding to 11.38×10^{20} POT (13.85×10^{20} POT) RHC (FHC) exposure. Results are compared to the NOvA (blue) and default (green) GENIE tunes.

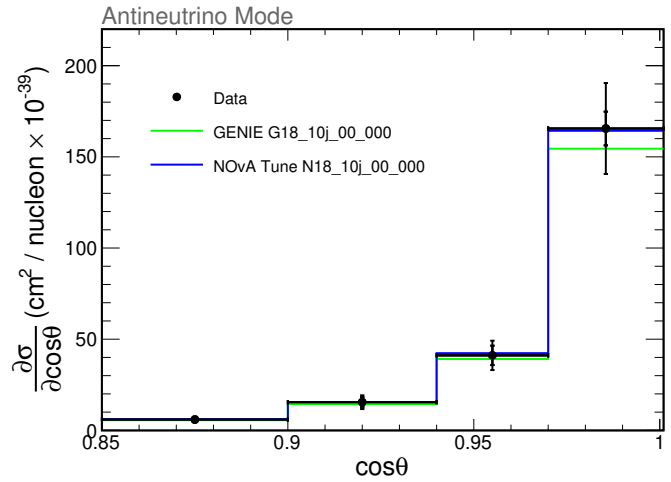

FIGURE 6.8. Measured single-differential $\bar{\nu}_e$-CC inclusive cross section as a function of the cosine of the electron scattering angle using selected data from NuMI corresponding to 11.38×10^{20} POT (13.85×10^{20} POT) RHC (FHC) exposure. Results are compared to the NOvA (blue) and default (green) GENIE tunes.

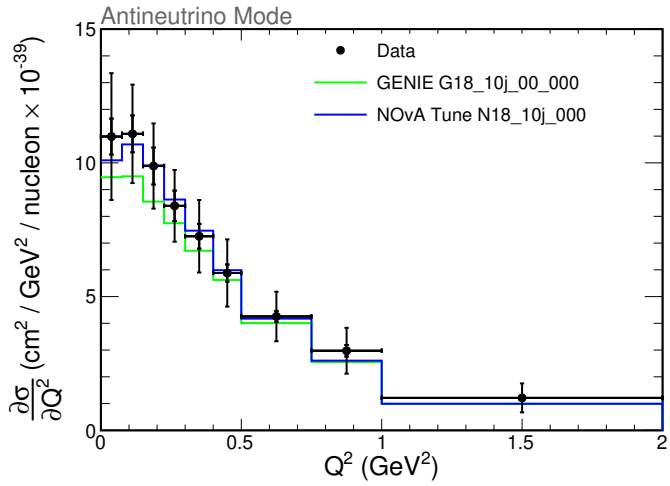

FIGURE 6.9. Measured single-differential $\bar{\nu}_e$-CC inclusive cross section as a function of Q^2 using selected data from NuMI corresponding to 11.38×10^{20} POT (13.85×10^{20} POT) RHC (FHC) exposure. Results are compared to the NOvA (blue) and default (green) GENIE tunes.

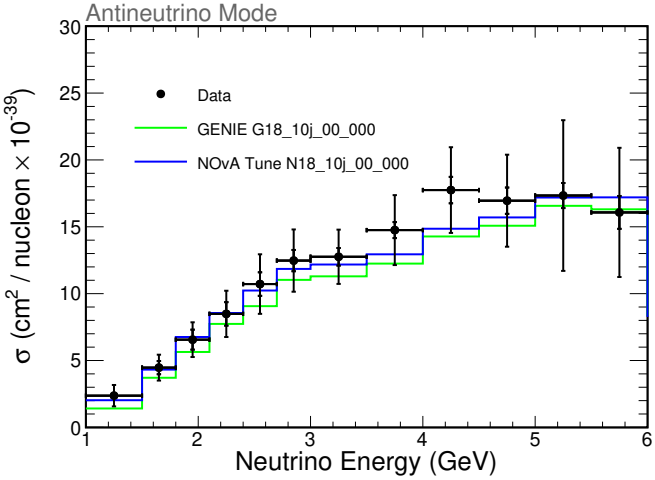

FIGURE 6.10. Measured total $\bar{\nu}_e$-CC inclusive cross section as a function of neutrino energy using selected data from NuMI corresponding to 11.38×10^{20} POT (13.85×10^{20} POT) RHC (FHC) exposure. Results are compared to the NOvA (blue) and default (green) GENIE tunes.

CHAPTER 7

The SciDAC Project and High Performance Computing

Next generation neutrino oscillation experiments [153, 154] promise to improve upon our understanding of neutrino physics using immensely powerful neutrino beams and unprecedented detection capabilities. These technological advances will require experiments to use High Performance Computing (HPC) to meet the computational demands. The SciDAC-4 collaboration aims to provide these experiments with the tools need to leverage these resources.

In this Chapter, a HEP analysis workflow developed by the SciDAC-4 collaboration is described, which aims to accelerate physics analyses using HPC. A study into the scaling of the workflow's file format is presented. Finally, the performance scaling of the workflow is demonstrated using a realistic neutrino analysis and the National Energy Research Scientific Computing Center (NERSC) Perlmutter system.

7.1. An Analysis Workflow for High Performance Computing

Neutrino event selection demands a significant amount of computational and human resources available on the NOvA collaboration due to the iterative nature of the development of an analysis. HPC systems can enable extremely computationally demanding physics results and interactive exploration of data. Both of these require expertise in the HPC standard parallel processing paradigm, Message Passing Interface (MPI), which is a barrier for analyzers using the C++ analysis framework described in Section 4.7. An alternative analysis workflow is developed to enable the analysis of HEP data using HPC. The workflow implements implicit parallelism, meaning no direct interaction with MPI is required on behalf of the analyzer. Though initially developed for the NOvA collaboration, the workflow is designed to be suitable for all HEP experiments.

The workflow consists of three major components to enable users to perform basic event selection using HPC systems. The first is a data schema stored in the Hierarchical Data Format, version 5 (HDF5) [155] file format. The second is the PandAna analysis framework [156] for ingesting, filtering, and transforming the data while leveraging the built-in and scalable parallel Input/Output (I/O) capabilities of HDF5. The third is the Llama histogram module for performing the final aggregation of histogrammed quantities. The workflow is designed to perform the parallel orchestration required for event selection without requiring the user to interact with MPI. It enables users to perform scalable event selection on HPC systems using the Python [157] programming language while utilizing the easy to use and performant h5py [158], mpi4py [159], NumPy [160], and pandas [161] libraries.

Data are organized in tables and stored in the HDF5 file format by flattening the CAF tree structure (Figure 4.14). Separate tables are constructed for each branch of the tree that contains leaves. Leaves are represented by columns in the table where each row represents a different event or branching product within a slice, for example, prongs. A complete set of indices is also stored in the tables that uniquely identify each row and are used to relate products from individual slices across tables. This columnar organization allows for users to query a subset of the data with the PandAna framework.

Like CAFAna, users implement PandAna `Cut` and `Var` objects to filter and transform the data, respectively, and `Weight` objects to calculate histogram weights for each event. In these `Cuts`, `Vars`, and `Weights`, users specify the columns needed for their analysis. PandAna reads only those columns and associated index information into pandas `DataFrames` for subsequent filtering and transformation operations.

PandAna distributes the work of reading data from a file by assigning each MPI process a subset of the data that it will read. For each file, processes are assigned an equal number of spills, and rows belonging to those spills are read from each column that is requested by the user. When the number of processes is greater than the total number of files, each file is assigned to a subset of all processes and those processes share the data to be read from that file. This significantly improves the read performance of PandAna by reducing the overall number of calls to the file system to request for the file to be opened. However, this makes the performance of PandAna heavily dependent on the data and MPI configuration.

7.1.1. Event Selection Scaling of the HDF5 Data Format. Scaling measurements were performed to investigate the I/O performance of the PandAna framework. Unlike the FermiGrid workflow, data are stored directly on the parallel file systems of the HPC system, alleviating the need to distribute data among many small files. Almost 3 TB of uncompressed NOvA data were distributed among a number of HDF5 files and 14 columns were read during the execution of a PandAna event selection program on the NERSC Cori system. The experiment was repeated to measure the total time of execution as a function of the number of MPI processes executing the program and the number of files that contain the data. Figure 7.1 shows the results of the scaling measurements. A consistent 10x speedup is achieved when data is contained in one HDF5 file when compared to the same data contained in 256 HDF5 files.

The Llama module aggregates events selected by each process executing a PandAna program into histograms. Using the Boost-histogram module [162] for performant histogramming of numpy arrays and built in propagation of errors, Llama provides encapsulation objects that aggregate histograms that are distributed among MPI ranks*. A Llama `Histogram` is constructed

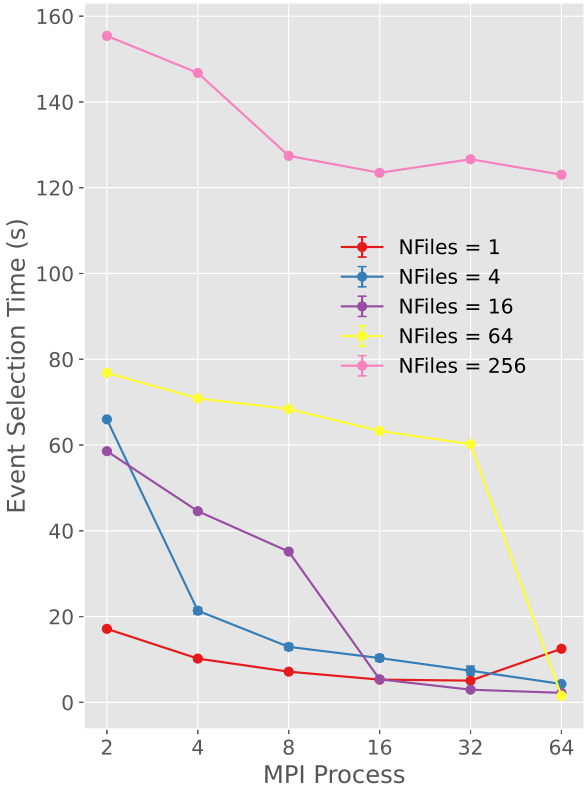

FIGURE 7.1. Event selection timing measurements as a function of the number of MPI ranks executing a PANDANA event selection program and the number of files among which 3 TB of uncompressed NOvA data is distributed. Measurements are performed using NERSC Cori system. A consistent 10x speedup is achieved when data is contained in one HDF5 file when compared to 256.

given a BOOST-HISTOGRAM `axis` object. Encapsulated histograms are filled from NUMPY data arrays and optional weight arrays. `Histograms` are aggregated by internal MPI `Reduce` operations that sum histogram contents and squared-errors among all processes. By convention, the rank 0 process is left with the aggregated results and all other processes posses empty `Histograms`.

Implicit parallelism is implemented as automatic aggregation triggered by `Histogram` methods that require aggregated results and that do not commute with aggregation. The aggregation step is a sum of histogram contents among all MPI processes using MPI `Reduce`. `Histogram` addition (`Histogram.__add__`) and subtraction (`Histogram.__sub__`) commute with addition

*The rank of an MPI process is the value used to index the process within a group of processes.

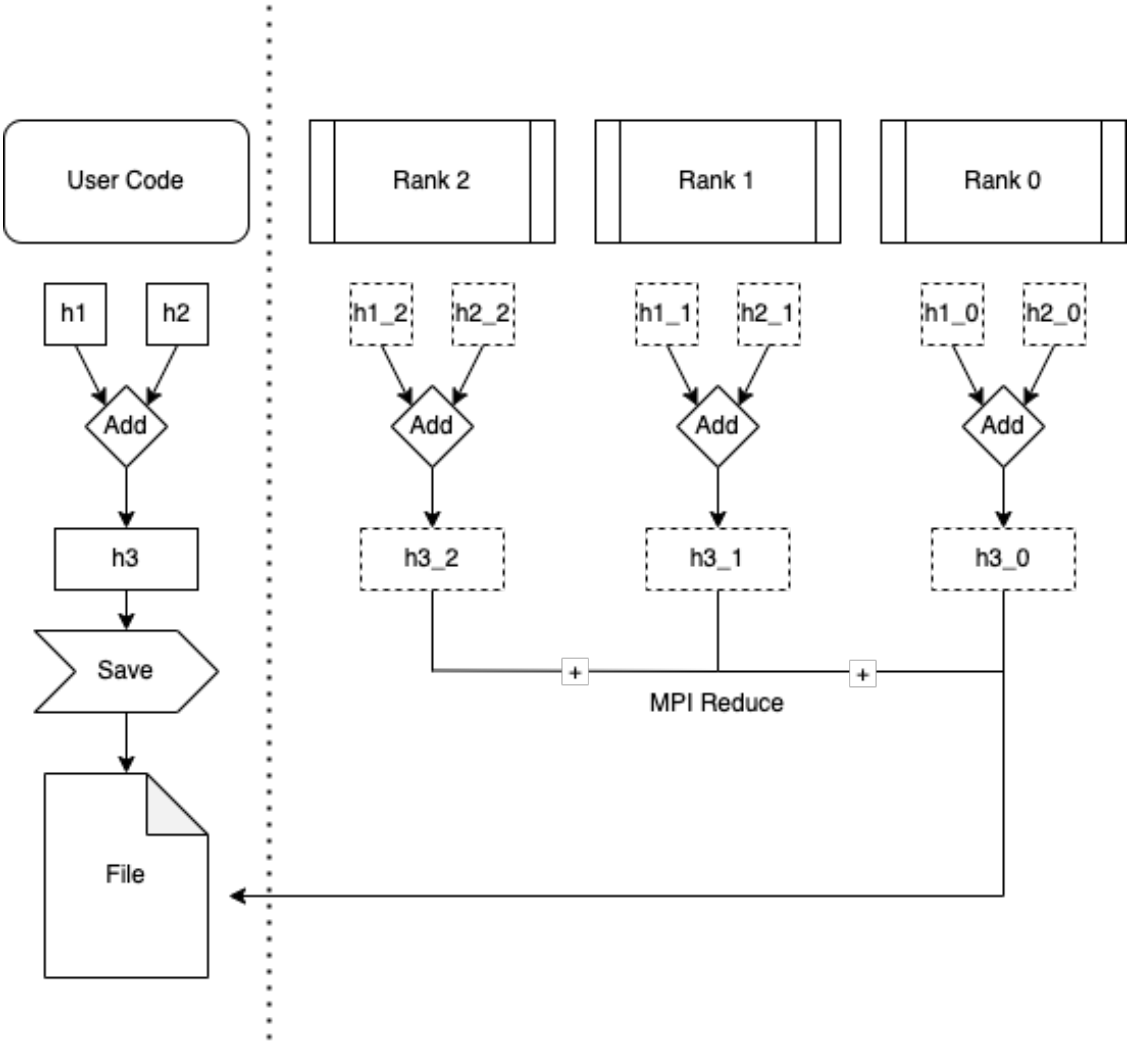

FIGURE 7.2. Diagram of LLAMA `Histogram` addition and automatic aggregation during parallel execution of a LLAMA program. Each rank posses a copy of two histograms, which are added together. Each rank then holds partial, but not complete, results of the addition operation. MPI `Reduce` is invoked automatically when the user attempts to save the resulting `Histogram` to a file.

and so no aggregation step is triggered. Multiplication (`Histogram.__mult__`) and division (`Histogram.__truediv__`) do not commute with addition and so an aggregation step is triggered. Finally, aggregation is triggered when the user attempts to save the `Histograms` to a file (`Histogram.saveto`). Figure 7.2 shows a diagram demonstrating this functionality. `Histogram` addition is executed in parallel where every process holds partial results. A final aggregation step is performed as the user saves the result to a file.

The following code example demonstrates the implicit parallelism implemented in Llama. In this example, an `axis` object is created using the `llama.AxisFactory` utility. The `axis` is used to create two histograms, which are randomly filled with data. Subsequent addition, multiplication, and division operations are performed. When executed in parallel, aggregation is performed before calculating `h3_mult` and `h3_div`. By convention, the results are held by the MPI process with rank 0 and all other processes hold empty results.

```
import llama
import numpy as np

d1 = np.random.uniform(0, 1, 100)
d2 = np.random.uniform(0, 1, 200)

axis = llama.AxisFactory.Regular("label", 4, 0, 1)
h1 = llama.Histogram(xaxis=axis)
h2 = llama.Histogram(xaxis=axis)

h1.fill(d1)
h2.fill(d2)

# Addition commutes with aggregation
# No aggregation is performed
h3_add = h1 + h2

# Multiplication does not commute with aggregation
# Aggregation is performed before calculating h3_mult
h3_mult = h1 * h2

# Division does not commute with aggregation
# Aggregation is performed before calculating h3_div
h3_div = h1 / h2
```

7.1.2. Demonstration of Workflow Scaling. The workflow described in Section 7.1 was used to carry out a realistic neutrino cross-section analysis on the NERSC Perlmutter system.

TABLE 7.1. Data analyzed to perform a realistic neutrino cross-section analysis using the HPC analysis workflow described in Section 7.1. The Nominal sample was used to predict the cross section. The $\pm 1\sigma$ Calibration samples were compared to the Reference Nominal to estimate error due to calibration uncertainty.

Data Sample	Beam Spills (10^6)	File Size (GB)
Nominal	104	432
Reference Nominal	25	74
$+1\sigma$ Calibration	25	74
-1σ Calibration	25	74

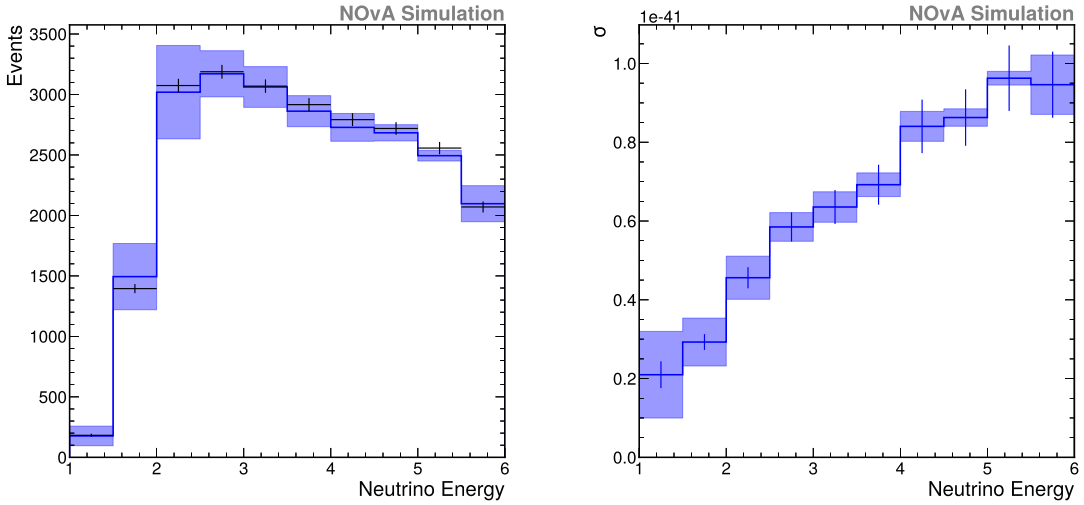

FIGURE 7.3. Demonstration of the HPC neutrino analysis workflow. Left: Distribution of selected events as a function of neutrino energy. Right: Predicted cross section as a function of neutrino energy with error bars. Error bars estimate uncertainties from detector calibration.

Data were selected from MC samples representing nominal and systematically shifted experimental conditions. Table 7.1 summarizes the data analyzed to perform the analysis. In total, 54 columns were read from each data sample using the PANDANA analysis framework.

Figure 7.3 demonstrates results of the analysis. Events were selected using the PANDANA event selection framework and aggregated using the LLAMA module. Fake data was generated by fluctuating the `Histograms` resulting from the nominal prediction within Poisson uncertainties.

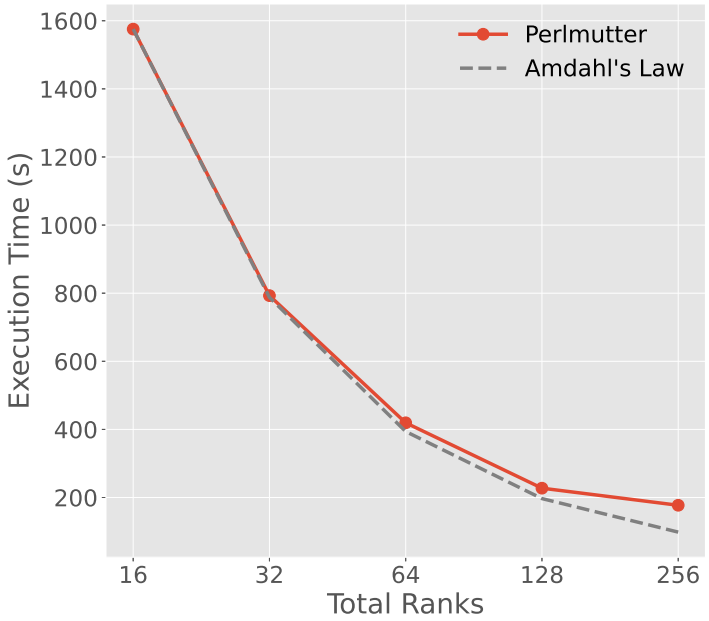

FIGURE 7.4. Runtime of the HPC analysis workflow as a function of the number of MPI processes (*i.e.* ranks) using the NERSC Perlmutter system. Results are compared to the theoretically most efficient (strong) scaling predicted by Amdahl's law [23].

Total runtime of the analysis was recorded as a function of total MPI processes (*i.e.* ranks) to measure the strong[†] scaling of the workflow. The runtime experiments were performed using the NERSC Perlmutter system. The analysis was repeated using an increasing number of total processes. Figure 7.4 shows the total execution time of the analysis program as a function of MPI processes. The workflow achieved close to the theoretically most efficient strong scaling predicted by Amdahl's law [23]. Moreover, these results demonstrate the total execution time of a realistic analysis performed using the HPC analysis workflow is on the order of a few minutes, enabling interactive exploration of neutrino data.

[†]Strong scaling is a measure of how total processing time changes as a function of the total number of processors for a fixed problem size.

CHAPTER 8

Conclusion

This thesis presents the first ever double-differential electron antineutrino charged-current inclusive cross section in the NOvA ND. It is estimated that $8{,}203.72 \pm 811.11$ signal event candidates are selected in the NuMI RHC sample with $(28 \pm 3)\,\%$ efficiency and $(24 \pm 4)\,\%$ purity using a simultaneous fit to RHC and FHC data. Good agreement is observed between data and the NOvA GENIE tune, N18_10j_00_000, with $\chi^2/d.o.f. = 5.02/14$. This measurement provides an experimental constraint for future models of antineutrino interactions, and the methods employed lay a foundation for a measurement of the ratio between ν_e-CC and $\bar{\nu}_e$-CC inclusive cross sections.

Finally, a workflow for neutrino data analysis using HPC is presented. The workflow implements implicit parallelism aimed at removing barriers of parallel-computing expertise between physicists and HPC systems. A realistic analysis is performed and near-perfect runtime scaling is measured using the NERSC Perlmutter system.

BIBLIOGRAPHY

[1] Shiqi Yu and Zelimir Djurcic. Energy Reconstruction for the 2020 nue Appearance Analysis. NOvA Document 43814-v3, May 2020.

[2] Leonidas Aliaga Soplin et al. Beam systematic uncertainties for third analyses. NOvA Document 17608-v5, July 2017.

[3] C. D. Ellis et al. The average energy of disintegration of radium E. *Proceedings of the Royal Society of London. Series A, Containing Papers of a Mathematical and Physical Character*, 117(776):109–123, December 1927.

[4] J. A. Formaggio and G. P. Zeller. From eV to EeV: Neutrino cross sections across energy scales. *Reviews of Modern Physics*, 84(3):1307–1341, September 2012.

[5] NOvA Collaboration et al. Measurement of the ν_e-Nucleus Charged-Current Double-Differential Cross Section at $<E_\nu> = 2.4$ GeV Using NOvA. *Physical Review Letters*, 130(5):051802, February 2023.

[6] K. Yonehara. Megawatt upgrade of NuMI target system. Technical Report FERMILAB-CONF-22-032-AD, Fermi National Accelerator Lab. (FNAL), Batavia, IL (United States), January 2022.

[7] Ashley Back and Jeremy Wolcott. Blessing Package for All-time POT Exposure for Ana2020. NOvA Document 46337-v3, June 2020.

[8] P. Adamson et al. The NuMI neutrino beam. *Nuclear Instruments and Methods in Physics Research Section A: Accelerators, Spectrometers, Detectors and Associated Equipment*, 806:279–306, January 2016.

[9] D. S. Ayres et al. The NOvA Technical Design Report. Technical Report FERMILAB-DESIGN-2007-01, Fermi National Accelerator Lab. (FNAL), Batavia, IL (United States), October 2007.

[10] Leonidas Aliaga Soplin. 2017-2018 Beam Plots. NOvA Document 20843-v12, May 2018.

[11] Hayes D Merritt. Blessed Near Detector Event Displays. NOvA Document 11404-v1, May 2014.

[12] Tyler Alion. Third Analysis: Absolute Calibration Technote. NOvA Document 23372-v2, September 2017.

[13] Leonidas Aliaga Soplin. PPFX tech-note for the 2017 analysis. NOvA Document 23441-v4, September 2017.

[14] Maria Martinez-Casales. Prod5.1 Cross section tuning blessing package. NOvA Document 55995-v5.

[15] Daniel Pershey et al. TDSlicer Technote. NOvA Document 27689-v5.

[16] E. Niner. *Observation of Electron Neutrino Appearance in the NuMI Beam with the NOvA Experiment.* PhD thesis, Indiana University, 2015.

[17] Matthew A. Judah. *Measurement of the Inclusive Electron-Neutrino Charged-Current Cross Section in the NOvA near Detector.* PhD thesis, Colorado State University, Fort Collins, Colorado, December 2019.

[18] Erika Catano-Mur et al. Prod5.1 Detector Systematics Executive Summary. NOvA Document 53225-v1.

[19] Juan M Carceller. Prod5.1 calibration shape systematic. NOvA Document 49986-v2.

[20] Miranda Elkins. 2019 Neutron Systematic Technical Note. NOvA Document 56061-v2, August 2022.

[21] Ryan Patterson. Attempts at scaling neutron energy distributions. NOvA Document 28556-v1, April 2018.

[22] Micah Groh. *Constraints on Neutrino Oscillation Parameters from Neutrinos and Antineutrinos with Machine Learning*. PhD thesis, Indiana University, Bloomington, Indiana, February 2021.

[23] K. Hwang and A. Faye. Computer architecture and parallel processing. January 1984.

[24] III. Atomic Stability and Conservation Laws. In R. Peierls, editor, *Niels Bohr Collected Works*, volume 9 of *Nuclear Physics (1929–1952)*, pp. 99–114. Elsevier, January 1986.

[25] K. Riesselmann. Neutrino invention. https://www.symmetrymagazine.org/article/march-2007/neutrino-invention.

[26] F. Reines and C. L. COWANjun. The Neutrino. *Nature*, 178(4531):446–449, September 1956.

[27] D. J. Griffiths. *Introduction to Elementary Particles; 2nd Rev. Version*. Physics Textbook. Wiley, New York, NY, 2008.

[28] M. Goldhaber et al. Helicity of Neutrinos. *Physical Review*, 109(3):1015–1017, February 1958.

[29] G. Backenstoss et al. Helicity of μ^- Mesons from π-Meson Decay. *Physical Review Letters*, 6(8):415–416, April 1961.

[30] J. H. Christenson et al. Evidence for the 2π Decay of the k_2^0 Meson. *Physical Review Letters*, 13(4):138–140, July 1964.

[31] KTeV Collaboration et al. Observation of Direct CP Violation in $k_{s,l} \to \pi\pi$ Decays. *Physical Review Letters*, 83(1):22–27, July 1999.

[32] V. Fanti et al. A new measurement of direct CP violation in two pion decays of the neutral kaon. *Physics Letters B*, 465(1):335–348, October 1999.

[33] A. Abashian et al. Measurement of the CP Violation Parameter $\sin 2\varphi_1$ in b^0_d Meson Decays. *Physical Review Letters*, 86(12):2509–2514, March 2001.

[34] B. Aubert et al. Measurement of CP -Violating Asymmetries in B 0 Decays to CP Eigenstates. *Physical Review Letters*, 86(12):2515–2522, March 2001.

[35] BABAR Collaboration et al. Direct cp Violating Asymmetry in $B^0 \to K^+\pi^-$ Decays. *Physical Review Letters*, 93(13):131801, September 2004.

[36] Belle Collaboration et al. Improved measurements of the partial rate asymmetry in $b \to hh$ decays. *Physical Review D*, 71(3):031502, February 2005.

[37] A. Riotto. Theories of Baryogenesis, July 1998.

[38] M. Fukugita and T. Yanagida. Barygenesis without grand unification. *Physics Letters B*, 174(1):45–47, June 1986.

[39] B. Pontecorvo. Mesonium and anti-mesonium. *Sov. Phys. JETP*, 6:429, 1957.

[40] B. Pontecorvo. Inverse beta processes and nonconservation of lepton charge. *Zh. Eksp. Teor. Fiz.*, 34:247, 1957.

[41] M. Gell-Mann and A. Pais. Behavior of Neutral Particles under Charge Conjugation. *Physical Review*, 97(5):1387–1389, March 1955.

[42] Z. Maki et al. Remarks on the Unified Model of Elementary Particles. *Progress of Theoretical Physics*, 28(5):870–880, November 1962.

[43] C. Giganti et al. Neutrino oscillations: The rise of the PMNS paradigm. *Progress in Particle and Nuclear Physics*, 98:1–54, January 2018.

[44] Y. Fukuda et al. Evidence for Oscillation of Atmospheric Neutrinos. *Phys. Rev. Lett.*, 81(8):1562–1567, August 1998.

[45] SNO Collaboration et al. Direct Evidence for Neutrino Flavor Transformation from Neutral-Current Interactions in the Sudbury Neutrino Observatory. *Physical Review Letters*, 89(1):011301, June 2002.

[46] V. Barger et al. Matter effects on three-neutrino oscillations. *Physical Review D*, 22(11):2718–2726, December 1980.

[47] S. P. Mikheev and A. Y. Smirnov. Resonance enhancement of oscillations in matter and solar neutrino spectroscopy. *Sov. J. Nucl. Phys. (Engl. Transl.); (United States)*, 42:6, December 1985.

[48] S. L. Glashow. The renormalizability of vector meson interactions. *Nuclear Physics*, 10:107–117, February 1959.

[49] S. L. Glashow. Partial-symmetries of weak interactions. *Nuclear Physics*, 22(4):579–588, February 1961.

[50] A. Salam and J. C. Ward. Electromagnetic and weak interactions. *Physics Letters*, 13(2):168–171, November 1964.

[51] S. Weinberg. A Model of Leptons. *Physical Review Letters*, 19(21):1264–1266, November 1967.

[52] C. S. Wu et al. Experimental Test of Parity Conservation in Beta Decay. *Physical Review*, 105(4):1413–1415, February 1957.

[53] H. A. Bethe. Energy Production in Stars. *Physical Review*, 55(5):434–456, March 1939.

[54] R. L. Workman and others. Review of Particle Physics. *PTEP*, 2022:083C01, 2022.

[55] C. W. Walter. Why understanding neutrino interactions is important for oscillation physics. *AIP Conference Proceedings*, 967(1):3–8, December 2007.

[56] O. Lalakulich et al. Neutrino energy reconstruction in quasielastic-like scattering in the MiniBooNE and T2K experiments. *Physical Review C*, 86(5):054606, November 2012.

[57] C. H. Llewellyn Smith. Neutrino reactions at accelerator energies. *Physics Reports*, 3(5):261–379, June 1972.

[58] N. Cabibbo. Unitary Symmetry and Leptonic Decays. *Physical Review Letters*, 10(12):531–533, June 1963.

[59] M. Kobayashi and T. Maskawa. CP-Violation in the Renormalizable Theory of Weak Interaction. *Progress of Theoretical Physics*, 49(2):652–657, February 1973.

[60] A. W. Thomas. CVC in Particle Physics, September 1996.

[61] K. Nakamura and P. D. Group). Review of Particle Physics. *Journal of Physics G: Nuclear and Particle Physics*, 37(7A):075021, July 2010.

[62] V. Bernard et al. Axial structure of the nucleon. *Journal of Physics G: Nuclear and Particle Physics*, 28(1):R1, November 2001.

[63] A. Bodek et al. Extraction of the Axial Nucleon Form Factor from Neutrino Experiments on Deuterium. *Journal of Physics: Conference Series*, 110(8):082004, May 2008.

[64] D. Rein and L. M. Sehgal. Neutrino-excitation of baryon resonances and single pion production. *Annals of Physics*, 133(1):79–153, April 1981.

[65] Ch. Berger and L. M. Sehgal. Lepton mass effects in single pion production by neutrinos. *Physical Review D*, 76(11):113004, December 2007.

[66] Ch. Berger and L. M. Sehgal. Partially conserved axial vector current and coherent pion production by low energy neutrinos. *Physical Review D*, 79(5):053003, March 2009.

[67] S. L. Adler. Tests of the Conserved Vector Current and Partially Conserved Axial-Vector Current Hypotheses in High-Energy Neutrino Reactions. *Physical Review*, 135(4B):B963–B966, August 1964.

[68] A. Bodek and U. K. Yang. Higher twist, Ξw scaling, and effective LO PDFs for lepton scattering in the few GeV region. *Journal of Physics G: Nuclear and Particle Physics*, 29(8):1899, July 2003.

[69] Single Particle Properties of Nuclei Through (e, e' p) Reactions - INSPIRE. https://inspirehep.net/literature/208355.

[70] R. A. Smith and E. J. Moniz. NEUTRINO REACTIONS ON NUCLEAR TARGETS. *Nucl. Phys. B*, 43:605, 1972.

[71] A. M. Ankowski and J. T. Sobczyk. Argon spectral function and neutrino interactions. *Physical Review C*, 74(5):054316, November 2006.

[72] J. Nieves et al. Inclusive quasielastic charged-current neutrino-nucleus reactions. *Physical Review C*, 70(5):055503, November 2004.

[73] J. Nieves et al. Inclusive charged-current neutrino-nucleus reactions. *Physical Review C*, 83(4):045501, April 2011.

[74] S. Dytman. Final State Interaction Models in Neutrino-Nucleus Cross Sections. *AIP Conference Proceedings*, 1189(1):51–59, November 2009.

[75] C. Andreopoulos et al. The GENIE neutrino Monte Carlo generator. *Nuclear Instruments and Methods in Physics Research Section A: Accelerators, Spectrometers, Detectors and Associated Equipment*, 614(1):87–104, February 2010.

[76] Y. Hayato. Neut. *Nuclear Physics B - Proceedings Supplements*, 112(1):171–176, November 2002.

[77] M. Day and K. S. McFarland. Differences in quasielastic cross sections of muon and electron neutrinos. *Physical Review D*, 86(5):053003, September 2012.

[78] M. Agostini et al. Comprehensive measurement of pp-chain solar neutrinos. *Nature*, 562(7728):505–510, October 2018.

[79] J. Blietschau et al. Total cross sections for ν_e and $\bar{\nu}_e$ interactions and search for neutrino oscillations and decay. *Nuclear Physics B*, 133(2):205–219, February 1978.

[80] MINERvA Collaboration et al. Measurement of Electron Neutrino Quasielastic and Quasielasticlike Scattering on Hydrocarbon at $<E_\nu> = 3.6$ GeV. *Physical Review Letters*, 116(8):081802, February 2016.

[81] R. Burns et al. Determination of Neutrino Flux. *Proceedings, CERN 65-32*, 97, 1965.

[82] Phys. Rev. D 105, L051102 (2022) - First measurement of inclusive electron-neutrino and antineutrino charged current differential cross sections in charged lepton energy on argon in MicroBooNE. https://journals-aps-org.ezproxy2.library.colostate.edu/prd/abstract/10.1103/PhysRevD.105.L051102.

[83] T. Golan et al. Effects of final-state interactions in neutrino-nucleus interactions. *Physical Review C*, 86(1):015505, July 2012.

[84] O. Buss et al. Transport-theoretical description of nuclear reactions. *Physics Reports*, 512(1):1–124, March 2012.

[85] K. Abe et al. Measurement of the charged-current electron (anti-)neutrino inclusive cross-sections at the T2K off-axis near detector ND280. *Journal of High Energy Physics*, 2020(10):114, October 2020.

[86] The NOvA Collaboration et al. Improved measurement of neutrino oscillation parameters by the NOvA experiment. *Physical Review D*, 106(3):032004, August 2022.

[87] K. Seiya et al. Slip Stacking. In *CARE-HHH-APD Workshop on Finalizing the Roadmap for the Upgrade of the CERN & GSI Accelerator Complex (BEAM'07)*, December 2007.

[88] R. Ainsworth et al. High intensity space charge effects on slip stacked beam in the Fermilab Recycler. *Physical Review Accelerators and Beams*, 22(2):020404, February 2019.

[89] N. None. The Fermilab Main Injector Technical Design Handbook. Technical Report FERMILAB-DESIGN-1994-01, Fermi National Accelerator Lab. (FNAL), Batavia, IL (United States), August 1994.

[90] Katsuya Yonehara. Status of NuMI Beam and Target System. NOvA Document 56522-v1.

[91] M. D. Messier. First neutrino oscillation measurements in NOvA. *Nuclear Physics B*, 908:151–160, July 2016.

[92] G. S. Davies. NOvA: Present and Future, October 2011.

[93] Michael Baird. A second look at ND Pileup. NOvA Document 8093-v2, October 2012.

[94] Christopher Backhouse et al. The Attenuation and Threshold Calibration of the NOvA detectors. NOvA Document 13579-v35. File: TA_Attenuation_and_threshold.pdf, September 2017.

[95] Luke Vinton. Calorimetric Energy Scale Calibration of the NOvA Detectors. NOvA Document 13579-v35. File: FA_Calorimetric_energy_scale.pdf, July 2015.

[96] Leonidas Aliaga Soplin. *Neutrino Flux Prediction for the NuMI Beamline*. PhD thesis, The College of William and Mary, Williamsburg, Virginia, March 2016.

[97] S. Agostinelli et al. Geant4—a simulation toolkit. *Nuclear Instruments and Methods in Physics Research Section A: Accelerators, Spectrometers, Detectors and Associated Equipment*, 506(3):250–303, July 2003.

[98] L. Alvarez-Ruso et al. Recent highlights from GENIE v3. *The European Physical Journal Special Topics*, 230(24):4449–4467, December 2021.

[99] A. S. Meyer et al. Deuterium target data for precision neutrino-nucleus cross sections. *Physical Review D*, 93(11):113015, June 2016.

[100] R. Gran et al. Neutrino-nucleus quasi-elastic and 2p2h interactions up to 10 GeV. *Physical Review D*, 88(11):113007, December 2013.

[101] L. A. Ahrens et al. Measurement of neutrino-proton and antineutrino-proton elastic scattering. *Physical Review D*, 35(3):785–809, February 1987.

[102] T. Sjostrand et al. PYTHIA 6.4 Physics and Manual. *Journal of High Energy Physics*, 2006(05):026–026, May 2006.

[103] T. Yang et al. A hadronization model for few-GeV neutrino interactions. *The European Physical Journal C*, 63(1):1–10, September 2009.

[104] L. L. Salcedo et al. Computer simulation of inclusive pion nuclear reactions. *Nuclear Physics A*, 484(3):557–592, July 1988.

[105] NOvA Collaboration. New constraints on oscillation parameters from ν_e appearance and ν_μ disappearance in the NOvA experiment. *ArXiv e-prints*, pp. arXiv:1806.00096, May 2018.

[106] GENIE Global Analysis of Neutrino Scattering Data & Comprehensive Model Tunes. http://tunes.genie-mc.org/.

[107] Aaron Mislivec. GENIE Skew Reweight and the FSI Tune. NOvA Document 53973-v1.

[108] Kirk Bays et al. NOvA 2020 cross-section tune tech note. NOvA Document 43962-v3, March 2020.

[109] Michael Dolce et al. GENIE 3.0.6 hN CV and uncertainties for 2020 analysis. NOvA Document 43724-v4, February 2020.

[110] A. Aurisano et al. The NOvA simulation chain. *Journal of Physics: Conference Series*, 664(7):072002, December 2015.

[111] L. A. F. Fernandes and M. M. Oliveira. Real-time line detection through an improved Hough transform voting scheme. *Pattern Recognition*, 41(1):299–314, January 2008.

[112] M. Messier. Vertex reconstruction based on elastic arms.

[113] R. Krishnapuram and J. Keller. A possibilistic approach to clustering. *IEEE Transactions on Fuzzy Systems*, 1(2):98–110, May 1993.

[114] N. H. Kuiper. Tests concerning random points on a circle. *Indagationes Mathematicae (Proceedings)*, 63:38–47, January 1960.

[115] R. E. Kalman. A New Approach to Linear Filtering and Prediction Problems. *Transactions of the ASME–Journal of Basic Engineering*, 82(Series D):35–45, 1960.

[116] Biswaranjan Behera. *Measurement of the Double Differential Inclusive Muon Neutrino Charged-current Cross-section in the NOvA Near Detector*. PhD thesis, Indian Institute of Technology Hyderabad, Telanganaa, India, August 2018.

[117] F. Psihas et al. Context-enriched identification of particles with a convolutional network for neutrino events. *Physical Review D*, 100(7):073005, October 2019.

[118] R. Brun and F. Rademakers. ROOT: An object oriented data analysis framework. *New computing techniques in physics research V. Proceedings, 5th International Workshop, AIHENP '96, Lausanne, Switzerland, September 2-6, 1996*, A389:81–86, 1997.

[119] K. Chadwick et al. FermiGrid—experience and future plans. *Journal of Physics: Conference Series*, 119(5):052010, July 2008.

[120] T. O. S. G. E. B. o. b. o. t. O. C. Pordes et al. The open science grid. *Journal of Physics: Conference Series*, 78(1):012057, July 2007.

[121] C. Backhouse. The CAFAna framework for neutrino analysis, March 2022.

[122] Leonidas Aliaga Soplin et al. Technical Note: Measurement of the Electron-Antineutrino Charged-Current Inclusive Cross Section in the NOvA Near Detector. NOvA Document 53691-v3.

[123] Louise Suter. Data quality tech note summary paper. NOvA Document 13628-v2, July 2015.

[124] Lisa Goodenough. Discussion on Beam Quality Cuts. NOvA Document 12474-v1, December 2014.

[125] Derek Doyle et al. Derivation of the Relative Cross-section Uncertainy Figure of Merit For Selection Criteria Cross Section Analyses. NOvA Document 49166-v2.

[126] Connor Johnson. MuonID for Prod5.1. NOvA Document 47420-v1, September 2020.

[127] J. Allison et al. Recent developments in Geant4. *Nuclear Instruments and Methods in Physics Research Section A: Accelerators, Spectrometers, Detectors and Associated Equipment*, 835:186–225, November 2016.

[128] GENIE Collaboration et al. Neutrino-nucleon cross-section model tuning in GENIE v3. *Physical Review D*, 104(7):072009, October 2021.

[129] Jeremy Wolcott et al. NOvARwgt.

[130] Oleg Samoylov and V Hewes. NOvA Production 5 Detector Simulation Changes and Systematics. NOvA Document 43935-v4, July 2021.

[131] Andrew Sutton. Technical Note: Neutron Transport Simulation. NOvA Document 56095-v2, August 2022.

[132] A. Aurisano et al. A convolutional neural network neutrino event classifier. *Journal of Instrumentation*, 11(09):P09001, September 2016.

[133] F. Psihas. *Measurement of Long Baseline Neutrino Oscillations and Improvements From Deep Learning*. PhD thesis, Indiana University, 2018.

[134] M. Sandler et al. MobileNetV2: Inverted Residuals and Linear Bottlenecks, March 2019.

[135] Aristeidis Tsaris. Single Particle Gen for CVN Prong. NOvA Document 28715-v1.

[136] Thomas Warburton. A truth containment filter and Parameters for Single Particle Generation. NOvA Document 45934-v1, June 2020.

[137] Francois Chollet. Keras. https://keras.io.

[138] Wilson Cluster-Institutional Cluster. https://computing.fnal.gov/wilsoncluster/.

[139] J. A. Hanley and B. J. McNeil. The meaning and use of the area under a receiver operating characteristic (ROC) curve. *Radiology*, 143(1):29–36, April 1982.

[140] J. Therhaag. TMVA - Toolkit for Multivariate Data Analysis in ROOT. In *Proceedings of 35th International Conference of High Energy Physics — PoS(ICHEP 2010)*, volume 120, pp. 510. SISSA Medialab, March 2011.

[141] Derek Doyle. A $\bar{\nu}_e$ Identifier for the $\bar{\nu}_e$ CC Inclusive Analysis. NOvA Document 49463-v2, March 2021.

[142] W. H. Press et al. *Numerical Recipes 3rd Edition: The Art of Scientific Computing*. Cambridge University Press, September 2007.

[143] F. James. *Statistical Methods in Experimental Physics*. World Scientific, second edition, 2006.

[144] M. L. Eaton. *Multivariate Statistics: A Vector Space Approach*. Institute of Mathematical Statistics, 2007.

[145] F. James and M. Winkler. *Minuit2 Manual*.

[146] NuebarCCInc: Template Fit Bias Update. NOvA Document 56092-v1, August 2022.

[147] S. Schmitt. Data Unfolding Methods in High Energy Physics. *EPJ Web of Conferences*, 137:11008, 2017.

[148] G. D'Agostini. A multidimensional unfolding method based on Bayes' theorem. *Nuclear Instruments and Methods in Physics Research Section A: Accelerators, Spectrometers, Detectors and Associated Equipment*, 362(2):487–498, August 1995.

[149] L. Brenner et al. Comparison of unfolding methods using RooFitUnfold, May 2020.

[150] Matthew Strait. Geometry and Composition Updates; Fiducial Mass Systematics. NOvA Document 15421-v6, May 2016.

[151] Matthew Strait. Tech Note: 2016 geometry and composition changes. NOvA Document 23132-v4, August 2018.

[152] Matthew Strait. Tech Note: Muon Energy Scale Systematic. NOvA Document 20816-v24, June 2017.

[153] H.-K. Proto-Collaboration et al. Hyper-Kamiokande Design Report, November 2018.

[154] B. Abi et al. Deep Underground Neutrino Experiment (DUNE), Far Detector Technical Design Report, Volume II: DUNE Physics, March 2020.

[155] The HDF Group. Hierarchical Data Format, version 5, 1997.

[156] M. Groh et al. PandAna: A Python Analysis Framework for Scalable High Performance Computing in High Energy Physics. *EPJ Web of Conferences*, 251:03033, 2021.

[157] G. Van Rossum and F. L. Drake. *Python 3 Reference Manual*. CreateSpace, Scotts Valley, CA, 2009.

[158] HDF5 for Python.

[159] L. Dalcin and Y.-L. L. Fang. Mpi4py: Status Update After 12 Years of Development. *Computing in Science & Engineering*, 23(4):47–54, July 2021.

[160] C. R. Harris et al. Array programming with NumPy. *Nature*, 585(7825):357–362, September 2020.

[161] W. McKinney. Pandas: A Foundational Python Library for Data Analysis and Statistics.

[162] H. Schreiner et al. Boost-histogram: High-Performance Histograms as Objects. *Proceedings of the 19th Python in Science Conference*, pp. 63–69, 2020.

LIST OF ACRONYMS

ADC Analog-to-Digital Converter

APD Avalanche Photo Diode

AUC Area Under the Curve

BDT Boosted Decision Tree

BR Branching Ratio

CAF Common Analysis File

CC Charged-Current

CKM Cabibbo-Kobayashi-Maskawa

CMC Comprehensive Model Configuration

CNN Convolutional Neural Network

COH Coherent Pion Production

CVC Conserved Vector Current

CVN Convolutional Vision Network

DAQ Data Acquisition

DIS Deep Inelastic Scattering

DL Deep Learning

ECM Efficiency Confusion Matrix

FD Far Detector

FHC Forward Horn Current

FSI Final State Interactions

HDF5 Hierarchical Data Format, version 5

HEP High Energy Physics

HPC High Performance Computing

I/O Input/Output

LArTPC Liquid-Argon Time Projection Chamber

LFG Local Fermi Gas

MC Monte Carlo

MEC Meson-Exchange Current

MI Main Injector

MIP Minimum Ionizing Particle

ML Machine Learning

MLE Maximum Likelihood Estimator

MPI Message Passing Interface

MSE Mean-squared Error

MSW Mikheev-Smirnov-Wolfenstein

NC Neutral-Current

ND Near Detector

NERSC National Energy Research Scientific Computing Center

NOvA NuMI Off-axis ν_e Appearance

NuMI Neutrinos at the Main Injector

PCAC Partially Conserved Axial Current

PCM Purity Confusion Matrix

PID Particle Identification

PM Pixel Map

PMNS Pontecorvo-Maki-Nakagawa-Sakata

POT Protons on Target

PPFX Package to Predict the Flux

QCD Quantum Chromo-Dynamic

QE Quasi-Elastic

RES Resonant

RFG Relativistic Fermi Gas

RHC Reverse Horn Current

ROC Receiver Operating Characteristic

RPA Random Phase Approximation

SciDAC-4 Scientific Discovery through Advanced Computing: High Energy Physics Data Analytics on High Performance Computing

SGD Stochastic Gradient Descent

SM Standard Model

SR Standard Record